URANIUM AND ZIRCONIUM ELECTROCHEMICAL STUDIES IN LiCl-KCl EUTECTIC FOR FUNDAMENTAL APPLICATIONS IN USED NUCLEAR FUEL REPROCESSING

A Dissertation

Presented in Partial Fulfillment of the Requirements for the

Degree of Doctorate of Philosophy

with a

Major in Chemical Engineering

in the

College of Graduate Studies

University of Idaho

by

Robert Oaks Hoover

May 2014

Major Professor: Supathorn Phongikaroon, Ph.D.

Authorization to Submit Dissertation

This dissertation of Robert Oaks Hoover, submitted for the degree of Doctorate of Philosophy with a major in Chemical Engineering and titled "Uranium and Zirconium Electrochemical Studies in LiCl-KCl Eutectic for Fundamental Applications in Used Nuclear Fuel Reprocessing," has been reviewed in final form. Permission, as indicated by the signatures and dates below, is now granted to submit final copies to the College of Graduate Studies for approval.

Major Professor: _____ Date:_____
Supathorn Phongikaroon, Ph.D.

Committee Members: _____ Date:_____
Kerry Allahar, Ph.D.

_____ Date:_____
Patricia Paviet, Ph.D.

_____ Date_____
Vivek Utgikar, Ph.D.

Department Administrator: _____ Date_____
Wudneh Admassu, Ph.D.

Discipline's College Dean: _____ Date_____
Larry Stauffer, Ph.D.

Final Approval and Acceptance

Dean of the College of Graduate Studies: _____ Date_____
Jie Chen, Ph.D.

Abstract

Measurement and analysis of uranium (U) and zirconium (Zr) electrochemistry in the molten salt system are extremely important to the fundamental understanding of electrochemical processing of used nuclear fuel currently operated at the Idaho National Laboratory. Few studies have been performed in the past with U and Zr at concentrations approaching those in the electrorefiner. For this main reason, a set of experiments, including cyclic voltammetry (CV), chronopotentiometry, and anodic stripping voltammetry (ASV), has been performed to explore different parameters in a system that are common to the electrorefiner's conditions. U experiments were performed at 773 K with concentrations from 1.0 to 10.0 wt% UCl_3 in the LiCl-KCl, while Zr behavior was studied under three different temperature (723, 773, and 823 K) and at varying concentrations from 0.5 to 5 wt% $ZrCl_4$. An additional set of experiments with UCl_3-$ZrCl_4$-LiCl-KCl was also performed to explore the behavior of these two species together. ASV and CV were analyzed as possible *in-situ* methods for analyzing concentration, with CV cathodic data showing the most promise.

From these experiments, diffusivity (D), apparent standard reduction potential (E^{0*}), and activity coefficients (γ) were calculated. The values for D and E^{0*} versus the Cl_2/Cl^- reference were determined to be:

773 K:	$D_{U(IV)} = 1.26 \times 10^{-5}$ cm^2/s	$E^{0*}_{U(IV)/U(III)} = -1.453$ V
	$D_{U(III)} = 2.16 \times 10^{-5}$ cm^2/s	$E^{0*}_{U(III)/U} = -2.552$ V
723 - 823 K:	$D_{Zr(IV)} = 4.60 \times 10^{-4}\exp(-3716/T)$	$E^{0*}_{Zr(IV)/Zr(II)} = 0.002T - 3.508$
	$D_{Zr(II)} = 0.027\exp(-5619/T)$	$E^{0*}_{Zr(II)/Zr} = 0.0007T - 2.908$

Calculation of the E^{0*} values required the standard rate constant (k_s) which was not known for Zr. The results reveal that there is a weak effect of k_s on E^{0*}; for the current purpose, the value for U(III)/U has been used to facilitate the discussion. It appears that γ values vary significantly depending on different used thermodynamic databases. Results from the combined UCl_3-$ZrCl_4$ study provide some insight to Zr recovery in the presence of UCl_3. The CV data appear to show that Zr(II) may not fully reduce to Zr metal, forming instead ZrCl, which may be a possible impediment to electrorefining pure Zr metal.

Acknowledgements

This work was supported through an International Nuclear Energy Research Initiative project (I-NERI 2010-001-K), a collaboration with University of Idaho, Idaho National Laboratory (INL), Seoul National University (SNU), and Korea Atomic Energy Research Institute (KAERI).

There are many people and organizations to thank, without whom, this work could not have been done:

- First, and foremost, my wife Rebecca for being supportive and understanding as I have spent many long days and late nights in the lab.
- Dr. Supathorn Phongikaroon for advising and supporting me throughout this research and my studies.
- My committee: Drs. Kerry Allahar, Patricia Paviet, and Vivek Utgikar for taking the time to review this work and provide invaluable input and suggestions.
- Michael Shaltry for help with performing many of the experiments, for being my "Rad Buddy", and for training and advice on glovebox use and maintenance.
- University of Idaho and CAES staff including Debbie Lacroix, Joanna Taylor, Bryan Forsmann, and Alice Allen.
- Collaborators at INL: Dr. Michael Simpson and Dr. Tae-Sic Yoo.
- Collaborators at SNU: Prof. Il-Soon Hwang, Jaeyeong Park and Sungjune Sohn.
- Collaborator at KAERI: Dr. Kwang-Rag Kim.
- Last but not least, my fellow students: Ammon Williams, Joshua Versey, Dalsung Yoon, and Sean Martin from University of Wisconsin.

Table of Contents

List of Figures

List of Tables

List of Symbols

Symbol	Physical Quantity	Unit
C	Concentration	mol/cm^3
D	Diffusion coefficient	cm^2/s
D_0	Pre-exponential factor for diffusivity	cm^2/s
E	Equilibrium potential	V
E^0	Standard reduction potential	V
E^{0*}	Apparent standard reduction potential	V
E_D	Activation energy of diffusion	J/mol
$E_{p/2}$	Half peak potential in voltammetry	V
E_{pa}	Anodic peak potential in voltammetry	V
E_{pc}	Cathodic peak potential in voltammetry	V
f_i	Fugacity of the pure species i	Pa
$\hat{f}_i$	Fugacity of species i in solution	Pa
F	Faraday's constant	C/eq
g	Gibbs free energy	J/mol
g^{0*}	Experimental standard Gibbs free energy	J/mol
$g_{id}{}^0$	Theoretical ideal state Gibbs free energy	J/mol
g^E	Excess Gibbs energy of a solution	J/mol
i_0	Exchange current density	A/cm^2
i_c	Capacitive current density	A/cm^2
i_{pc}	Cathodic peak current density in voltammetry	A/cm^2
I_d	Driving current in chronopotentiometry	A

I_i	Initial current in chronopotentiometry	A
I_p	Peak current in voltammetry	A
I_{pa}	Anodic peak current in voltammetry	A
I_{pc}	Cathodic peak current in voltammetry	A
k_s	Standard rate constant	cm/s
n	Number of electrons transferred per mole	eq/mol
N	Molar flux	$mol/(cm^2 \cdot s)$
R	Universal gas constant	J/(mol·K)
R^2	Coefficient of determination	
R_{CT}	Charge transfer resistance	ohms
S	Working electrode surface area	cm^2
T	Absolute temperature	K
x_i	Mass fraction of species i in solution	
X	Mole fraction	

Greek

α	Transfer coefficient	
γ	Activity coefficient	
ν	Scan rate in voltammetry	V/s
τ	Transition time in chronopotentiometry	s
Δ	Change in a property	

Subscripts

ox	oxidized species	
red	reduced species	

Chapter 1: Introduction

Worldwide, at the end of 2012, the global nuclear power generating capacity was 372.1 GW(e) with 437 operating power reactors and 247 research reactors [1]. The International Atomic Energy Agency (IAEA) estimates that growth in the use of nuclear energy worldwide is predicted to be 23% to 100% by 2030, with the majority of the growth projected in Asia, with 47 of the 67 reactors under construction at the end of 2012 [1].

In the United States, as of November 2013, there are 62 commercially operating nuclear power plants with 100 nuclear reactors producing approximately 20% of electricity [2]. The prospects of nuclear power growth in the US include 28 proposed nuclear power plants [2]. The US has a long history of nuclear reactors with over 3800 operating years of experience [1]. This history of nuclear reactor operation has produced approximately 69,000 metric tons of commercial spent fuel as of the end of 2012, which is currently stored in either spent fuel pools (~78%) or dry casks (~22%) [2]. This amount is expected to increase by approximately 2400 metric tons per year [2], with no current permanent geological storage site.

Beyond commercial light water reactors, there are many different reactor designs being researched as part of the Generation IV International Forum, an international collaboration between the United States, United Kingdom, Switzerland, South Korea, South Africa, Japan, France, Canada, Brazil, Argentina, and the European Union [3]. These systems include the Very High Temperature Reactor, Supercritical Water Cooled Reactor, Gas Cooled Fast Reactor, Lead Cooled Fast Reactor, Sodium Cooled Fast Reactor, and the Molten Salt Reactor [3]. As the future is to move towards one or several of these reactor types, development of associated fuel cycles is an indispensable part of the reactor

development process. It has been proposed that electrochemical processing, with an additional head-end step, could be applied to many of the different fuel types being studied for both these new Gen IV reactors or conventional light water reactor oxide fuel [4-7].

1.1 Electrochemical Processing

Electrochemical processing, pyroprocessing, pyrochemical processing, and electrometallurgical processing are all different names for the same general process in used nuclear fuel reprocessing technology. Electrochemical processing was first developed by Argonne National Laboratory (ANL) as part of the Integral Fast Reactor program to treat used metallic sodium-bonded fuel from the Experimental Breeder Reactor-II (EBR-II) at Argonne National Laboratory-West, now part of Idaho National Laboratory (INL) and demonstrate the possibility of on-site reprocessing [8-10]. Electrochemical processing has some advantages when compared with the more conventional aqueous processes (i.e. PUREX) especially when treating sodium bonded metallic fuel. During irradiation, the metallic sodium bond material is incorporated into the fuel [10], which limits the disposal options, due to the highly exothermic reaction with water [7].

From the beginning, electrochemical processing was designed to be a compact, on-site used fuel processing method. It is a dry process, using molten metals and salts, in lieu of water, which provides some safety benefits regarding criticality margins and treatment of the metallic sodium. Studies of the electrorefiner (ER), the heart of the process, have shown that, due to the lack of water, which is a great moderator, the criticality safety margin is very large, even for highly enriched fuel [11]. Within the ER, sodium passivation occurs through

a chemical redox reaction, which converts the problematic sodium metal to more easily manageable NaCl (see Eq. (1.2)).

1.1.1 Uranium Electrochemical History

The first demonstration of electrochemical uranium purification appears in 1930, when Driggs and Lilliendahl of the Westinghouse Lamp Co. reported preparing pure uranium metal by electrolysis of KUF_5 in equimolar NaCl-$CaCl_2$ [12]. Following this initial work, several different molten salts were investigated as an electrolyte for purifying metallic uranium including UCl_3-$BaCl_2$-KCl-NaCl at Los Alamos National Laboratory [13], UF_4-$BaCl_2$ and UCl_3-$CaCl_2$ at Knolls Atomic Power Laboratory [14], UCl_3-$CaCl_2$-$BaCl_2$-LiCl-NaCl at Argonne National Laboratory [15], until eventually ANL developed the current process in UCl_3-LiCl-KCl due partially to the relatively low melting point of the LiCl-KCl eutectic composition (~59 mol% LiCl-41 mol% KCl, 621-634 K [16]).

1.1.2 Current Electrochemical Process at Idaho National Laboratory

The electrochemical process originally developed by ANL (Figure 1.1) is currently used at INL to treat used metallic fuel from the Experimental Breeder Reactor-II (EBR-II). The driver fuel, post-irradiation, contains approximately 80.6 wt% uranium and 10.8 wt% zirconium, with the remainder fission products as listed in Table 1.1 [17-24]. It should be noted that the terms "noble" and "active" are commonly used in electrochemical processing to describe elements that have standard reduction potentials (E^0) more and less positive, respectively, than the U(III)/U redox couple.

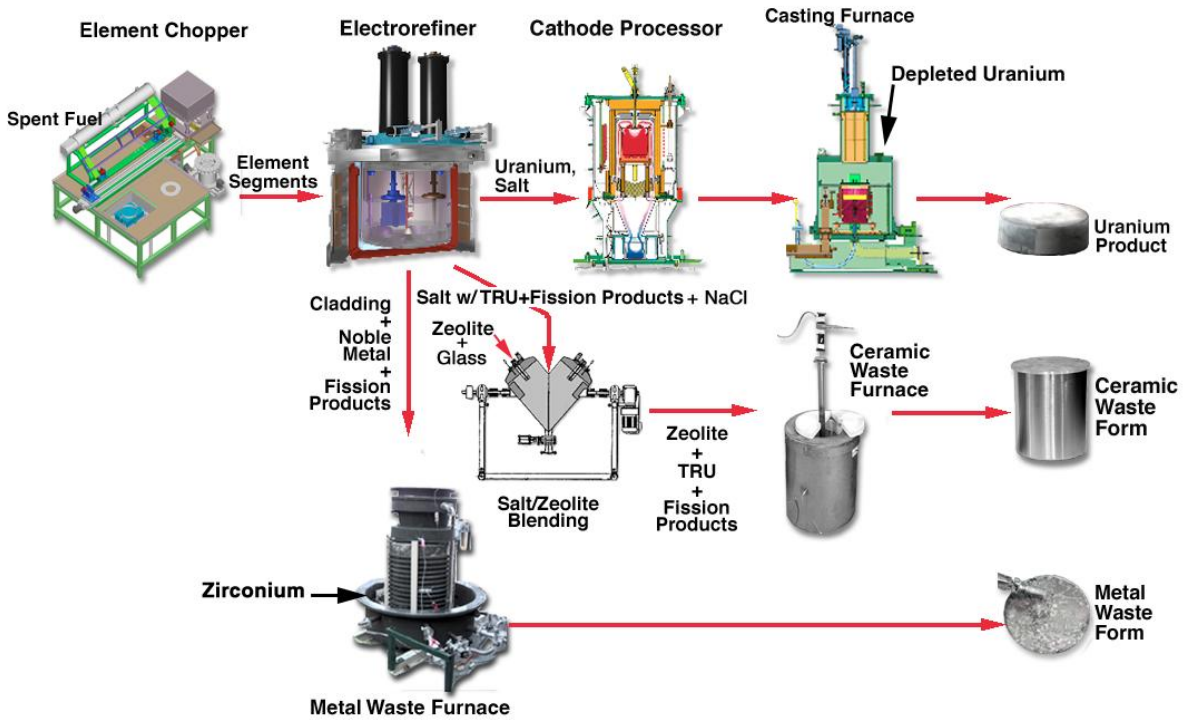

Figure 1.1 The electrochemical process for EBR-II used driver fuel treatment at INL.

The heart of this process, which takes place in a shielded argon hot cell at the Fuel Conditioning Facility of the Materials and Fuels Complex at INL is the Mark-IV electrorefiner (shown in Figure 1.2). The used EBR-II driver fuel rods are chopped and loaded into stainless steel fuel dissolution baskets (FDB) (Figure 1.3), which are lowered into a molten LiCl-KCl eutectic salt electrolyte containing nominally 10 wt% UCl_3 at 773 K [17]. The ER vessel itself is constructed of stainless steel, has a 1 m inside diameter containing a 10 cm deep layer of molten cadmium metal below a 32 cm layer of the UCl_3-LiCl-KCl salt electrolyte [17]. The top lid of the ER contains four ports, into which any combination of anode(s) and cathode(s) can be loaded.

Table 1.1 Representative used driver fuel composition and general location of species post electrorefining along with the standard reduction potential (E^0).

Element	Weight % in used fuel [17]	E^0 (V vs. Ag/AgCl) @ 723 K	
Bromine	0.007	0.920 [18]	Noble Species† (Remain in Anode basket)
Tellurium	0.112	0.64 [19]	
Ruthenium	0.407	0.615 [19]	
Rhodium	0.111	0.526 [19]	
Palladium	0.090	0.513 [19]	
Iodine	0.048	0.473 [19]	
Arsenic	0.005	0.283 [19]	
Molybdenum	0.771	0.119 [19]	
Antimony	0.004	0.087 [19]	
Silver	0.004	0.000 [19]	
Copper	0.003	0.295 [20]	
Tin	0.015	-0.355 [19]	
Niobium	0.002	-0.41 [19]	
Selenium	0.019	-0.459 [21]	
Cadmium	0.007	-0.589 [19]	
Vanadium	0.003	-0.806 [19]	
Titanium	0.077	-1.010 [19]	
Zirconium	10.805	-1.088 [19]	
Neptunium	0.041	-1.311 [19]	
Europium	0.011	-1.471* [22]	
Uranium	80.596	-1.496 [19]	Collected at solid cathode
Plutonium	0.413	-1.570 [23]	Active Species† (Accumulate in salt)
Gadolinium	0.005	-2.066 [19]	
Neodymium	0.930	-2.097 [19]	
Yttrium	0.126	-2.109 [19]	
Lanthanum	0.284	-2.126 [19]	
Samarium	0.177	-2.147* [24]	
Promethium	0.011	-2.147* [22]	
Cerium	0.542	-2.183 [19]	
Praseodymium	0.269	-2.316* [22]	
Sodium	2.160	-2.50 [19]	

*Value at 773 K.

†The terms “noble" and "active" are used to describe elements that have E^0 more and less positive, respectively, than the U(III)/U redox couples.

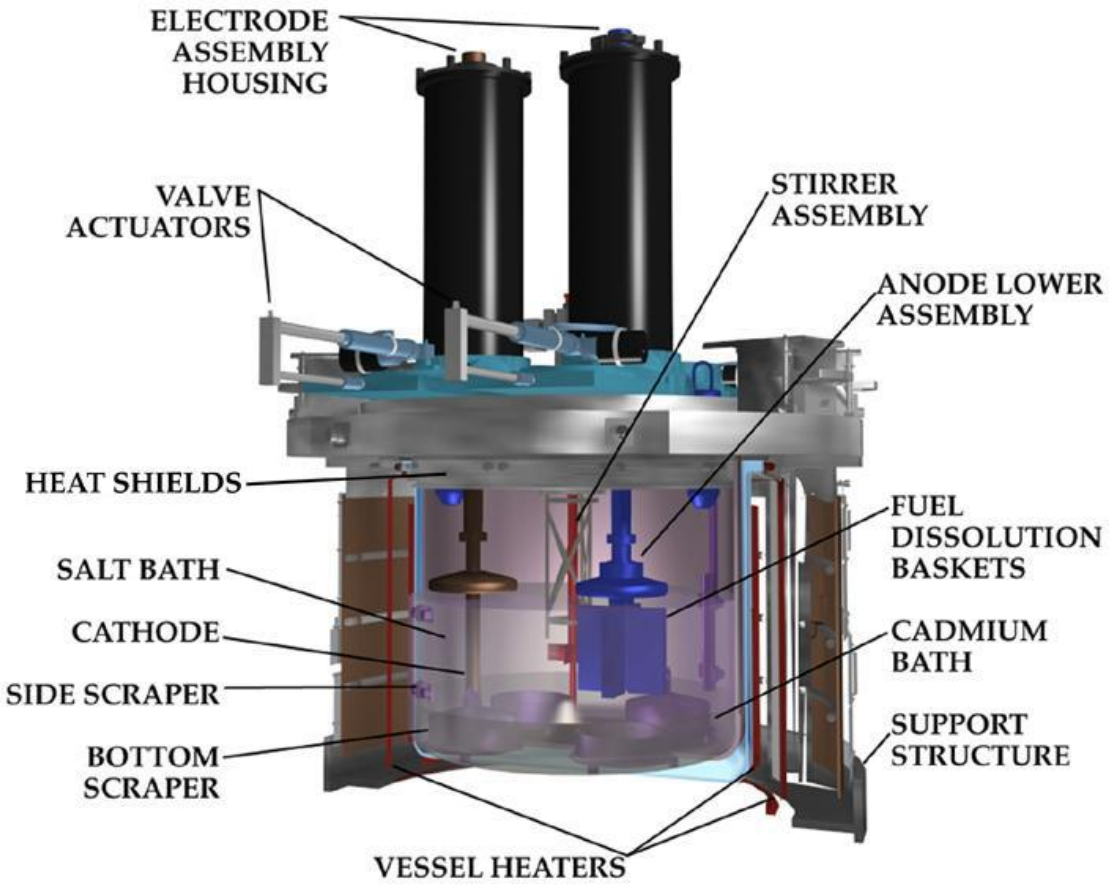

Figure 1.2 The Mark-IV electrorefiner used at INL to treat EBR-II metallic fuel.

Four of the FDBs are combined into a cruciform arrangement (Figure 1.3 [25]) and act as an anode. When the FDBs are lowered into the molten electrolyte, the more active constituents (listed in Table 1.1) chemically react with the UCl_3, including plutonium and sodium metals to form chlorides, which dissolve into the salt [26]:

$$UCl_3 + Pu \rightarrow U + PuCl_3 \text{ and} \quad (1.1)$$

$$UCl_3 + 3Na \rightarrow U + 3NaCl\ . \quad (1.2)$$

Other active species will react thermodynamically similarly to those shown in Eqs. (1.1) and (1.2).

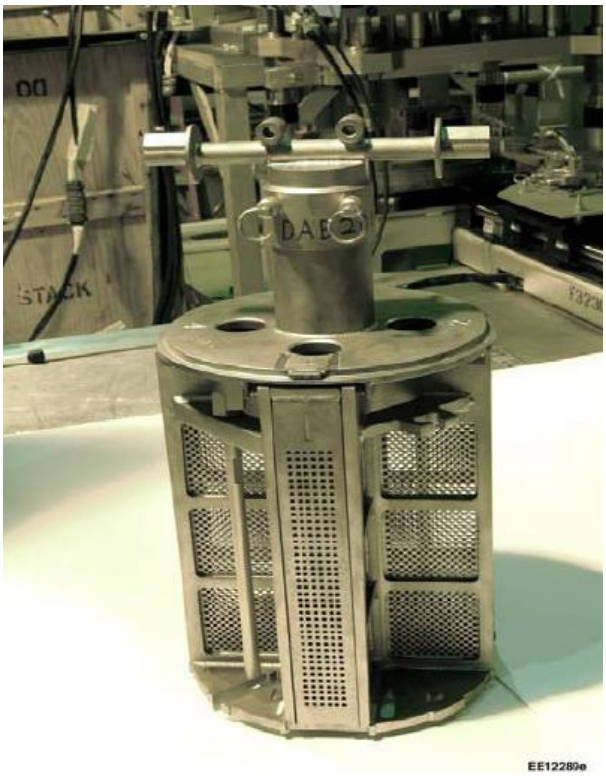

Figure 1.3 Cruciform geometry of four fuel dissolution baskets [25].

The ER is generally operated in a galvanostatic mode, so a current is applied with a cutoff voltage, to electrochemically oxidize and dissolve the uranium into the electrolyte, while ideally retaining zirconium and the noble metal fission products (listed in Table 1.1) in the FDBs [27]. For any electrochemical cell, there have to be corresponding oxidation and reduction reactions occurring at the anode and cathode, respectively. While uranium and the more active species are being oxidized at the anode, U(III) and any noble species that may be present in the electrolyte are reduced to metal at the solid steel cathode. Uranium is generally deposited as metal dendrites as shown in Figure 1.4 [25].

Figure 1.4 Uranium deposits on solid steel cathode [25].

The goal of the electrochemical process is to anodically dissolve uranium and retain zirconium and the other noble species, while collecting pure uranium at the cathode [5, 28] as shown in Eqs. (1.3) to (1.5),

$$\text{Anode:} \quad U(\text{anode}) \rightarrow U^{3+}(\text{salt}) + 3e^- \tag{1.3}$$

$$\text{Cathode:} \quad U^{3+}(\text{salt}) + 3e^- \rightarrow U(\text{cathode}) \tag{1.4}$$

$$\text{Net:} \quad U(\text{anode}) \rightarrow U(\text{cathode}) \tag{1.5}$$

1.2 Purpose

The purpose of this dissertation is to study the effect of concentrations on thermodynamic and electrochemical properties for uranium and zirconium in molten LiCl-KCl salt at 773 K. To develop a fundamental understanding of these electrochemical

systems, we have explored the behavior of low to high uranium (1 - 10 wt%) and zirconium (0.5 - 5 wt%) concentrations in molten salt and a mixture of high uranium with low and moderate zirconium concentrations for similitude with the actual situation in the Mark-IV ER. In addition, the effect of temperature on these properties for zirconium in the molten salt is explored. Emphasis is placed on the following two points. First, the focus is on the electrochemical measurement and analysis of uranium and zirconium electrochemistry from the collected data. Second, for the different systems, thermodynamic and electrochemical properties (i.e., apparent standard reduction potential, diffusion coefficient, and activity coefficient) are determined, described, and reported to help explain their influence on the electrochemical separation process.

1.3 Motivation

Ideally, the zirconium should remain unoxidized in the anode basket along with the other noble metals listed in Table 1.1; however, due to the small difference in oxidation potentials between uranium and zirconium (-1.496 V and -1.088 V vs. Ag/AgCl at 773 K, respectively), some zirconium is unavoidably oxidized along with uranium [17]. The amounts of uranium and zirconium oxidized are directly related. Uranium dissolution and zirconium retention are at odds with each other. In the early years of ER operation at INL (during the U.S. Department of Energy demonstration program) zirconium retention was the primary goal, while during the Advanced Fuel Cycle Initiative (AFCI) more emphasis was put on achieving complete actinide dissolution [29]. The zirconium buildup in the ER (primarily in the cadmium pool) during these times is illustrated in Figure 1.5 along with the total amount of zirconium present in the processed used fuel [29], while Table 1.2 [29] lists

the average uranium and zirconium dissolution percentages during these two stages of operation [29]. From the figure and data in the table, it is clear that during the AFCI program, the rate of zirconium accumulation was similar to the overall rate of zirconium being processed, while during the DOE demonstration program, zirconium accumulation was limited.

Due to this behavior, it is clear that zirconium has been building up in the ER at INL and must be periodically collected. To develop a method of collecting zirconium in a pure (free from uranium contamination) state, the electrochemical behaviors of uranium and zirconium, both separately and together, in the LiCl-KCl eutectic molten salt must be known. The electrochemical behavior in LiCl-KCl of zirconium as a constituent of zircaloy is of great interest regarding the treatment of oxide fuel cladding hulls, which could greatly reduce the amount of high-level waste from used oxide fuel [30].

The above discussions yield two important motivations for this study. First, although electrochemical research with uranium has been relatively widespread, these substantial experimental studies on the electrochemical behavior of uranium in the molten LiCl-KCl eutectic have been focused at low concentrations [4, 31-42] up to ~4.7 wt% UCl_3 with one exception in 1961 at ~6.16 wt% [43], as listed in Appendices A to C. Second, research studies on zirconium electrochemistry in molten LiCl-KCl eutectic are scarce. Therefore, it is important to study and develop a fundamental understanding of both uranium and zirconium behavior relevant to electrochemical separations and to better reflect the conditions in an operating used nuclear fuel ER, as the Mark-IV contains nominally 10 wt% UCl_3 [17].

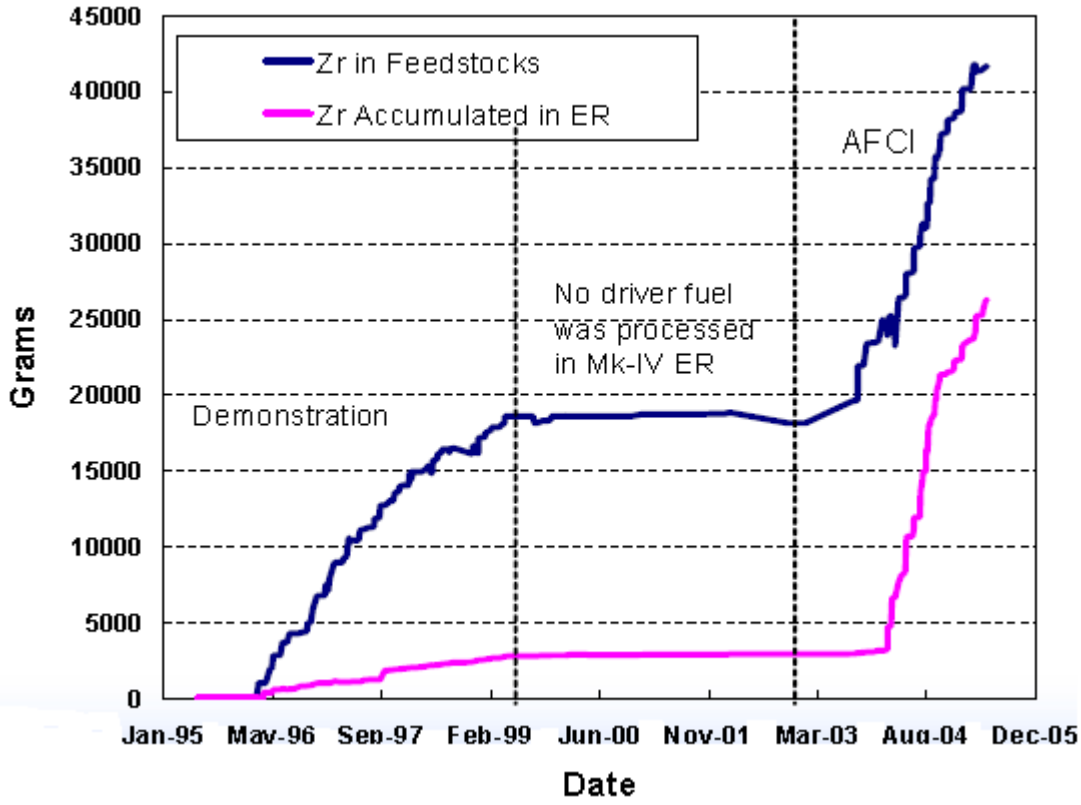

Figure 1.5 Zirconium inventory buildup in the Mark-IV ER [29].

Table 1.2 Average anode dissolution percentage (wt% dissolved relative to feed) [29].

Demonstration (1996-1999)		AFCI (post 2003)	
Uranium	**Zirconium**	**Uranium**	**Zirconium**
95.8 ± 0.7	19.7 ± 14.1	99.72 ± 0.16	87.85 ± 6.55

1.4 Approach

This work was supported by the International Nuclear Energy Research Initiative (INERI) program with the Republic of Korea (ROK) and the United States (US) government through the Korea Atomic Energy Research Institute (KAERI) with Seoul National University (SNU) and the INL with University of Idaho (UI). The focus on the US side is on the experimental programs, working in parallel with KAERI and SNU—focusing on computational modeling development—in order to improve a method to electrochemically

collect zirconium from a used nuclear fuel electrorefiner, such as at INL or treat zircaloy cladding hulls in ROK.

The goal of this approach was first to conduct a thorough and extensive literature review of electrochemical properties of zirconium and uranium as well as experimental methods that can be used to better understand the electrochemical behavior of these two important elements. Next, all of the experiments were planned and conducted in a glovebox with an inert argon atmosphere located in the Radiochemistry Laboratory at the Center for Advanced Energy Studies (CAES). The studies focused on performing electrochemical experiments including cyclic voltammetry, chronopotentiometry, and anodic stripping voltammetry on various concentrations of UCl_3 (1.0 - 10.0 wt%) in the molten LiCl-KCl eutectic salt at 773 K and on several concentrations of $ZrCl_4$ (0.5 - 5 wt%) in the molten salt at 723, 773, and 823 K. The combination of these methods allow the calculation of the desired thermodynamic and electrochemical properties by using the theories obtained from the literature survey. Then, additional CV experiments were performed in mixtures of UCl_3-$ZrCl_4$-LiCl-KCl to analyze the behavior of these species together in the same salt.

1.5 Organization of the Dissertation

The dissertation continues with Chapter 2, which presents the electrochemical and thermodynamic parameters that are important to the electrochemical processing of used nuclear fuel, including standard reduction potential, diffusion coefficient, and activity coefficient. Previous work determining these parameters for U and Zr are compared and discussed. The various experimental electrochemical methods used in this dissertation are discussed along with the methods used to analyze the data and calculate the desired

parameters. Chapter 3 presents the experimental program, beginning with the materials and equipment used and followed by the preparation methods for the reference electrode and salt mixtures. The chapter is closed out by discussing the detailed data collection methods used for all experiments and the lessons learned (failures and successes). Chapter 4 provides the electrochemical experimental results for U and Zr, including an analysis of several different molten salt concentration detection methods. These data sets are used to calculate the important thermodynamic and electrochemical properties for uranium and zirconium, which are then compared to previous work. The combined behavior of both species in the molten salt is then presented and qualitatively discussed. The final chapter summarizes the presented work and discusses the recommended next steps. All appendices are given to provide additional data for the entire body of this work.

Chapter 2: Literature Survey

An understanding of previous uranium (U) and zirconium (Zr) electrochemical studies is an important building block for the development of any experimental plan and design for a separation process inside an electrorefiner. Mainly, different electrolyte mediums and compositions may yield different thermodynamic and electrochemical properties. These dynamic values and conditions can greatly affect the operational schemes, separation processes, and modeling simulations of the electrochemical process. Different experimental schemes and electrochemical methods have been developed and selected, respectively, in order to understand these effects and measure the relevant values in the system. The purpose of this chapter is to explain importance of these parameters and different techniques that will be used to measure them. The outline of this chapter can be summarized as follows: first, the general description of important parameters considered in this research is presented along with previous work in determining these parameters. Second, the discussion of various electrochemical techniques and their methods are explained in detail.

2.1 Uranium and Zirconium Studies

Several research studies have been previously performed on the thermodynamic and electrochemical properties of U and Zr in the LiCl-KCl eutectic salt. A complete understanding of this existing body of work is essential in development of the experimental program that will be discussed later in Chapter 3. The most important parameters consist of the standard reduction potential, E^0, the diffusion coefficient, D, and the activity coefficient, γ. It can be seen that U electrochemistry has a long history in the United States. Driggs and Lilliendahl [12] first demonstrated the electrolytic preparation of pure U in different molten

salt mediums in 1930. In their studies, either uranium trioxide or uranyl chloride was electrochemically dissolved in various electrolytes: sodium chloride (NaCl), sodium fluoride (NaF), potassium chloride (KCl), potassium fluoride (KF), and calcium chloride ($CaCl_2$). Because of their work, over the following years, much work has been performed in an attempt to better understand the electrochemical behavior of U in molten salts resulting in a large amount of reported electrochemical data, primarily in the LiCl-KCl eutectic molten salt at 723 K and 773 K.

On the contrary, little attention has been paid to the electrochemical behavior of Zr in molten salt. Early work in 1965 by Baboian, et al. [44] provided a specific study and report on the potentials and stabilities of zirconium chlorides ($ZrCl_4$ and $ZrCl_2$) in molten LiCl-KCl. Since then, there have been several other experiments and computational models focusing on understanding Zr behavior in molten salt systems [30, 45-47].

A complete review of the available standard reduction potential, diffusivity, and activity coefficient values for U and Zr is given in Appendices A, B, and C, and summarized below in Sections 2.1.1 through 2.1.3.

2.1.1 Standard Reduction Potential, E^0

E^0 is the equilibrium potential of a reduction reaction at a given temperature and standard conditions, i.e. pure substance ($\gamma = 1$) at 1 atm pressure. This value can be used to determine the equilibrium potential of the reaction, E, at any concentration through the Nernst equation,

$$E = E^0 + \frac{RT}{nF} \ln\left(\frac{\gamma_{ox} X_{ox}}{\gamma_{red} X_{red}}\right), \tag{2.1}$$

where R is the universal gas constant (8.314 J/mol·K), T is the absolute temperature, n is the number of electrons transferred per mole, F is the Faraday's constant (96,485 C/eq), X is the mole fraction of the species at the electrode surface, and subscripts $_{ox}$ and $_{red}$ are for the oxidized and reduced species of the redox couple, respectively. Potential can be directly related to the Gibbs free energy change, Δg, of the redox reaction through

$$\Delta g = -nFE. \tag{2.2}$$

The standard reduction potentials of both U and Zr in LiCl-KCl eutectic have been reported by several researchers at different temperatures, concentrations, reference electrodes, and experimental methods. A complete overview of E^0 values available in literature for uranium and zirconium at 723 K and 773 K can be found in Appendix A, along with the reference electrode and method used, which will be discussed later in Section 2.2. The average value at each temperature along with the standard deviation is shown in Figure 2.1. Data from Baboian et al. [44] on the reduction potentials of zirconium was omitted from the average and standard deviation calculations as they are clear outliers from the other data, but they can be seen in Appendix A. This was published in 1965 and was the first publication providing discussion on zirconium's behavior in the LiCl-KCl eutectic. The results may differ from the more recently published data due to the improvement in electrochemical experimental capabilities. To better compare the reported values, all reduction potentials are converted to the Cl_2/Cl^- reference electrode. For values that were originally reported versus the Ag/AgCl reference, data from Yang and Hudson [48] was used to convert to the Cl_2/Cl^- reference, while the Pt^{2+}/Pt values were converted using data from Laitinen and Liu [20].

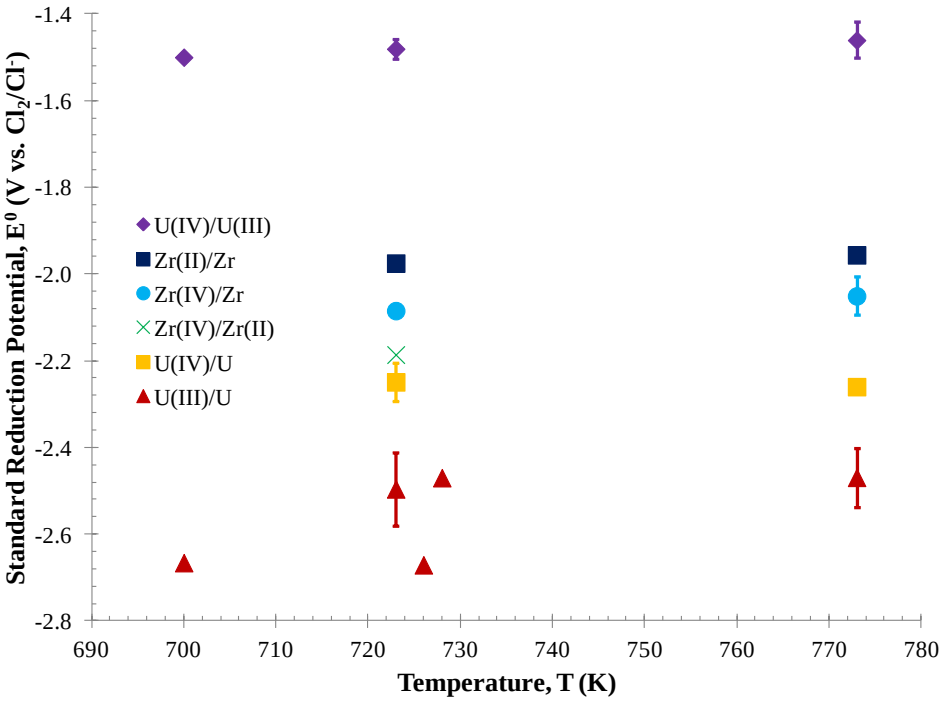

Figure 2.1 Average standard reduction potential values (with standard deviations) reported in literature [4, 18-19, 21-22, 32, 35-39, 41, 43, 45, 49-53]. A complete list of the reported data values can be found in Appendix A.

As can be seen, the general trend from easiest to hardest to reduce (or most stable as the oxidized chloride salt), in terms of applied potential required, goes in the following order: U(IV)/U(III) → Zr(II)/Zr → Zr(IV)/Zr → Zr(IV)/Zr(II) → U(IV)/U → U(III)/U.

2.1.2 Diffusion Coefficient, D

D is a proportionality constant between molar flux, N, and concentration gradient, ∇C,

$$N = -D\nabla C. \tag{2.3}$$

Diffusivity is used to determine the mass transfer to and from the electrodes in an electrochemical cell and generally follows an Arrhenius temperature dependence, which can be expressed as

$$D = D_0 \exp\left(\frac{-E_D}{RT}\right), \tag{2.4}$$

where D_0 is a pre-exponential factor and E_D is the activation energy of diffusion. Literature values of the pre-exponential factor and activation energy for U and Zr ions are listed in Appendix B along with the diffusion values (calculated and reported) at 723 K and 773 K and the method used by the various authors. The geometric mean diffusivity of the reported values at ten degree increments is shown in Figure 2.2 along with the standard deviations. It should be noted that no Zr(II) diffusivity data was found and only one source was found for Zr(IV) leading to no error bars.

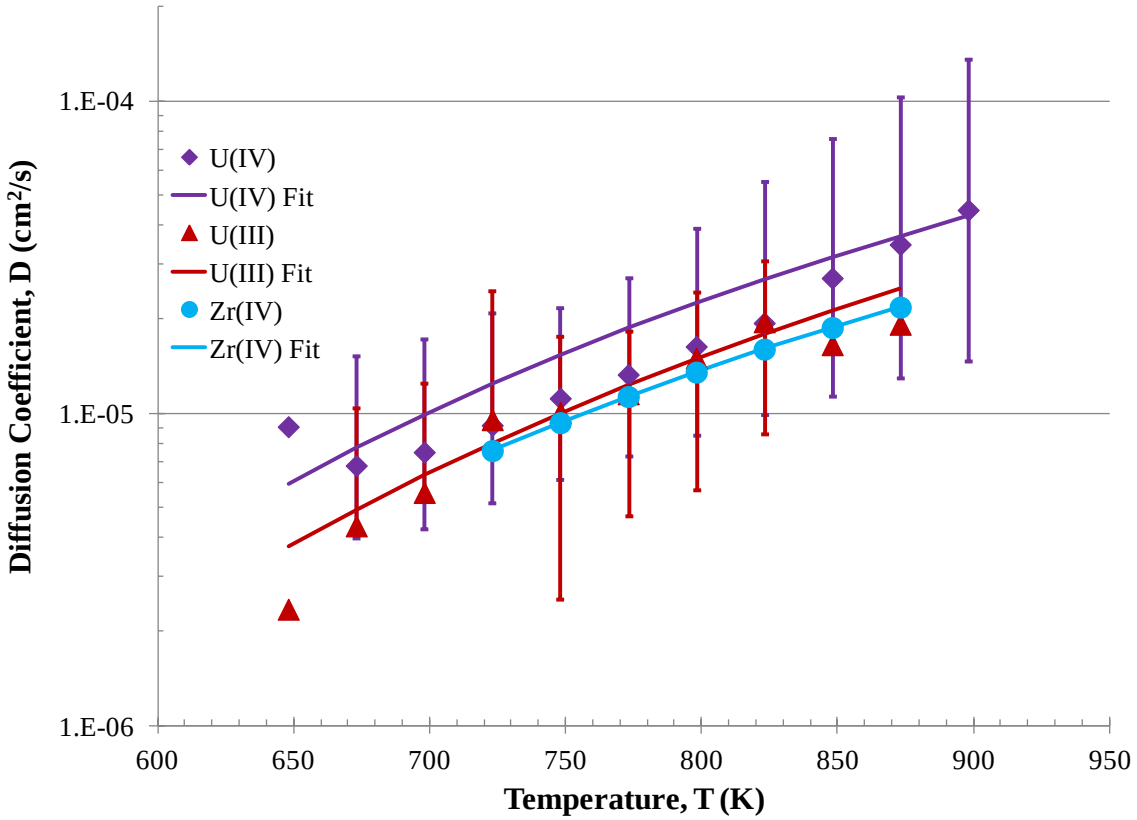

Figure 2.2 Geometric mean of the diffusion coefficient values reported in literature [31, 33-34, 37-42, 49, 52-56] along with standard deviations. A complete list of the available data is listed in Appendix B.

Figure 2.2 also reveals that the diffusion coefficients for the three ions increase in this general order: Zr(IV) → U(III) → U(IV). Figure 2.2 shows the accuracy of the fit to each data set. The fitted pre-exponential factors and activation energies were calculated and listed in Table 2.1, along with the coefficient of determination, R^2, for each fit. For the diffusivity of Zr(IV) only one source of values was available, leading to $R^2 = 1$.

Table 2.1 Pre-exponential factors, D_0, and activation energy of diffusion, E_D, values for the Arrhenius equation (Eq. 2.4) fitted to diffusion coefficients reported in literature [31, 33-34, 37-42, 49, 52-56].

	D_0 (cm^2/s)	E_D (J/mol·K)	R^2	References
U(IV)	0.00709	38,200	0.854	[33-34, 38-39, 53-56]
U(III)	0.00596	39,700	0.841	[31, 34, 37-42, 49, 52-55]
Zr(IV)	0.00358	37,000	1.000	[55]

2.1.3 Activity Coefficient, γ

The activity coefficient of a species in solution, γ, is a measure of the nonideality of the mixture, which is related to the excess Gibbs energy, g^E, of a solution. The excess Gibbs energy is the difference between the actual and ideal Gibbs energy of the solution,

$$g^E = RT\sum_i x_i \ln \gamma_i \,. \tag{2.5}$$

where x_i is the mass fraction of species i in the solution. Generally, γ is defined as the ratio of the species' fugacity in solution and its mass fraction in solution times its pure species fugacity,

$$\gamma_i \equiv \frac{\hat{f}_i}{x_i f_i}, \tag{2.6}$$

where $\hat{f}_i$ is the fugacity in solution and f_i is the fugacity of the pure species i. In a completely ideal solution, each species has γ of unity. The geometric mean and standard deviation of published γ values in the molten LiCl-KCl eutectic are shown in Figure 2.3, while the full table of data is summarized in Appendix C. It should be noted that one set of published values for the Zr(II) ion are not included in the calculations and figure as they are approximately eleven orders of magnitude larger than the other values. Here, both uranium and zirconium chlorides tend to have activity coefficients much less than unity in the LiCl-KCl eutectic system, thus increasing their stability in the molten salt.

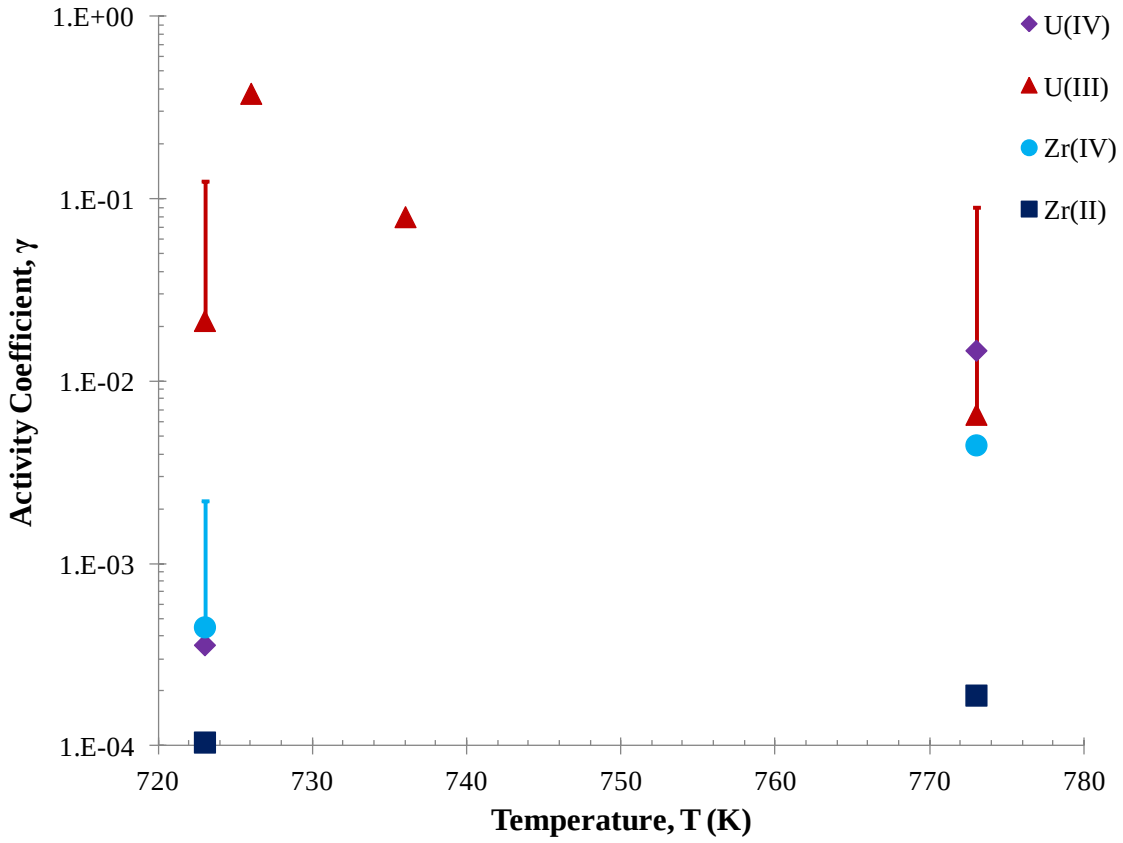

Figure 2.3 Geometric mean activity coefficient values (with standard deviations) reported in literature [31, 35, 39, 43-46, 53, 57]. A complete list of the available data can be found in Appendix C.

The results of the literature survey in Figures 2.1to 2.3 and Appendices A through C reveal that available electrochemical values either vary greatly as in the case of U or are very sparse, as with Zr. To better understand the electrochemical behavior of these species and accurately determine the electrochemical and thermodynamic parameters, more detailed experimental studies must be performed.

2.2 Review of Electrochemical Experimental Techniques

There are many different experimental electrochemical methods that could be used to help determine the behavior of species in an electrolyte. Of these methods, cyclic voltammetry (CV), chronopotentiometry (CP), and anodic stripping voltammetry (ASV) are three widely used techniques that together can be used to better understand the behavior of U and Zr in the molten LiCl-KCl eutectic. Short descriptions of these methods along with how they may be used to determine the desired electrochemical parameters are given in the next subsection.

2.2.1 Cyclic Voltammetry (CV)

CV is a common electrochemical technique that can be used to determine information about the reactions that can, and do, occur in an electrochemical cell [58]. In CV, the potential is repeatedly ramped from one vertex potential to another at a constant scan rate, ν, as shown in Figure 2.4. As the potential is changed, both reduction and oxidation reactions can occur at the electrode surface resulting in cathodic (negative current) and anodic (positive current) peaks, respectively, in the measured current as shown in Figure 2.5 [59].

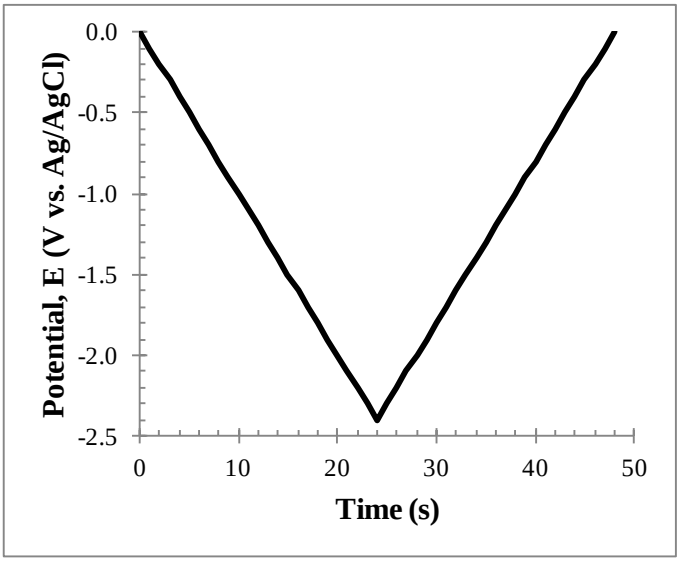

Figure 2.4 Example of a potential waveform at a scan rate of 100 mV/s.

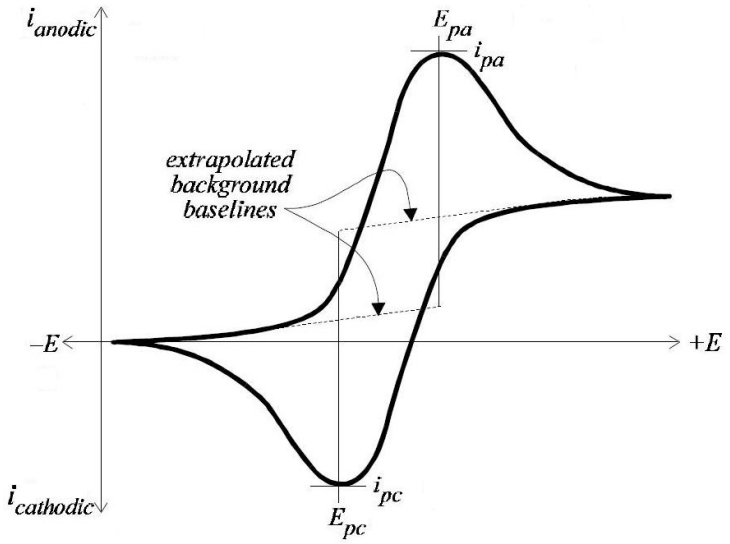

Figure 2.5 A typical cyclic voltammogram [59].

From the resulting cyclic voltammogram (Figure 2.5), the equilibrium potential, E, can be found by averaging the potentials of the cathodic and corresponding anodic peaks (E_{pc} and E_{pa} respectively),

$$E = \frac{E_{pa} + E_{pc}}{2}. \tag{2.7}$$

2.2.1.1 Reversible Redox Reactions

The simplest test for reversibility of a reaction using CV is to examine the cathodic peak potential, E_{pc}, as a function of scan rate. For an irreversible reaction the peak potential shifts in the negative direction with increasing scan rate, while for a reversible there is no shift. For a reversible reaction, the number of electrons transferred in the reaction, n, can be found from the difference between E_{pa} and E_{pc}, which can be related by

$$E_{pa} - E_{pc} = 2.22\frac{RT}{nF}, \tag{2.8}$$

The diffusion coefficients, D, of the species involved in a reversible soluble/soluble reaction can be found by using the cathodic and anodic peak currents, I_{pc} and I_{pa}, for the oxidized and reduced species, respectively, from any given CV data through two different forms of the Randles-Sevcik equation [19],

$$\frac{I_{pc}}{\sqrt{\nu}} = -0.4463nFSC\sqrt{\frac{nFD_{ox}}{RT}}, \tag{2.9}$$

$$\frac{I_{pa}}{\sqrt{\nu}} = 0.4463nFSC\sqrt{\frac{nFD_{red}}{RT}}. \tag{2.10}$$

For a reversible soluble/soluble redox couple, the equilibrium potential obtained by using Eq. (2.7) can be related to the apparent standard reduction potential and the diffusivity of each species [38-39]; that is,

$$E = E^{0*} + \frac{RT}{nF}\ln\left(\sqrt{\frac{D_{red}}{D_{ox}}}\right). \tag{2.11}$$

The apparent standard reduction potential, E^{0}*, includes the activity coefficients and is defined as

$$E^{0*} = E^{0} + \frac{RT}{nF}\ln\left(\frac{\gamma_{ox}}{\gamma_{red}}\right), \tag{2.12}$$

where γ_{ox} and γ_{red} are the activity coefficients for the oxidized and reduced species, respectively.

For a soluble/insoluble reversible process, the equilibrium potential can be plotted versus the ratio of oxidized/reduced species mole fractions, X_{ox} and X_{red}, through the Nernst equation,

$$E = E^{0*} + \frac{RT}{nF}\ln\left(\frac{X_{ox}}{X_{red}}\right). \tag{2.13}$$

When the reduced species is a metal, $X_{red} = 1$. From the resulting Nernst plot, the apparent standard reduction potential can then be determined from the y-intercept and the number of electrons transferred from the slope of the line.

2.2.1.2 Irreversible Redox Reactions

For an irreversible redox reaction, the number of electrons transferred can be calculated from the difference between the cathodic peak potential, E_{pc}, and the half peak potential, $E_{p/2}$, which is the potential at the point where the current is half of the peak current. This relationship can be expressed as

$$\left|E_{pc} - E_{p/2}\right| = 1.857\frac{RT}{n\alpha F}, \tag{2.14}$$

where α is the transfer coefficient (generally considered to be 0.5).

For these irreversible reactions, the peak current is related to the scan rate, ν, by an equation similar to Eqs. (2.9) and (2.10), which is known as the Delahay equation [58]:

$$\frac{I_{pc}}{\sqrt{\nu}} = -0.4958nFSC\sqrt{\frac{n\alpha FD_{ox}}{RT}}\,. \qquad (2.15)$$

For a soluble/insoluble irreversible redox couple, the following equation relates the cathodic peak potential, E_{pc}, to the apparent standard potential [38],

$$E_{pc} = E^{0*} - \frac{RT}{n\alpha F}\left[0.78 - \ln k_s + \ln\left(\sqrt{\frac{n\alpha F\nu D_{ox}}{RT}}\right)\right], \qquad (2.16)$$

where k_s is the standard rate constant.

2.2.2 Chronopotentiometry (CP)

CP is a current-controlled technique used to study time-dependent concentration change in a solution. Here, a driving current, I_d, is applied to the working electrode from an initial current, I_i, and the resulting potential is measured as a function of time. The large current step (Figure 2.6) causes the oxidized species to be reduced at the electrode surface at a constant rate. When the interfacial surface concentration is depleted, the potential of the electrode will rapidly drop toward a more negative value in order to start a second reduction process [58]. The time of this potential transition is referred to as the transition time, τ. From the resulting chronopotentiogram (Figure 2.7), the transition time can be found and used to calculate the diffusion coefficient, D_{ox}, with the Sand equation,

$$I_d\sqrt{\tau} = \frac{nFSC\sqrt{\pi D_{ox}}}{2}\,. \qquad (2.17)$$

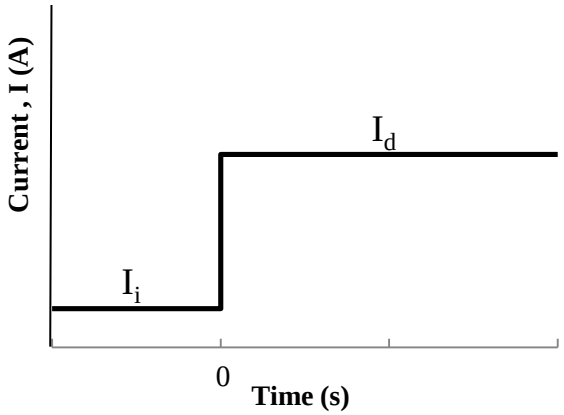

Figure 2.6 Applied current in chronopotentiometry.

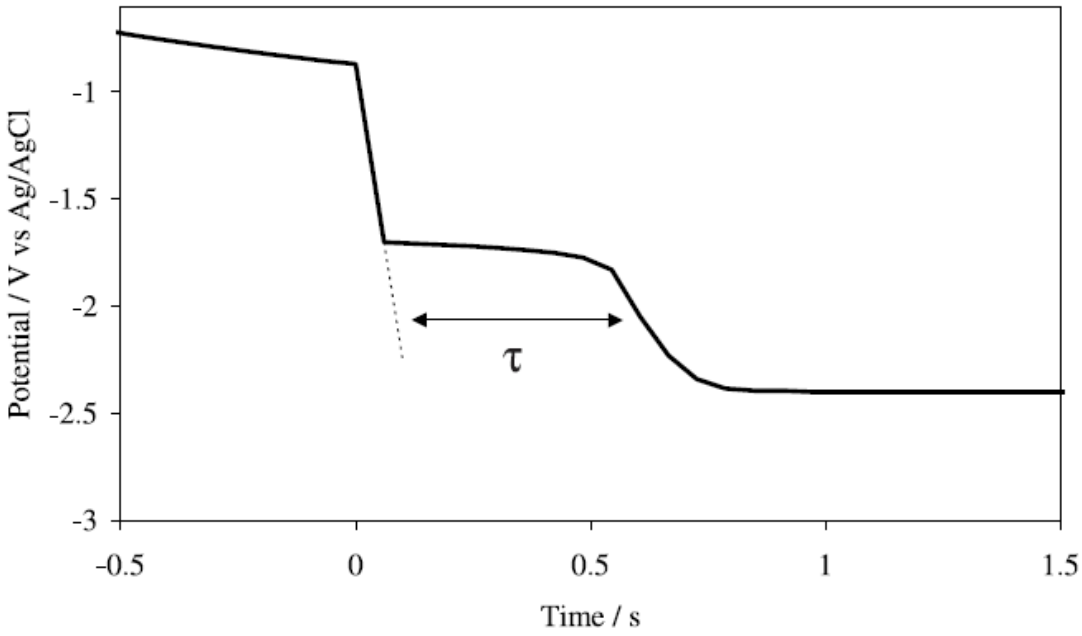

Figure 2.7 Example of a chronopotentiogram of $PuCl_3$ in LiCl-KCl [23].

2.2.3 Anodic Stripping Voltammetry (ASV)

ASV is an electrochemical technique that can be used to take advantage of the relationship between concentration and peak current in linear sweep voltammetry. A reducing potential is applied at the working electrode, plating the analyte onto the electrode

surface, for a known period of time. Following the plating step, the potential is linearly ramped to a higher anodic potential. During this linear sweep, the analyte is oxidized from the working electrode, resulting in a current peak. This process is similar to the anodic sweep in cyclic voltammetry (discussed previously in Section 2.2.1) and is illustrated in Figure 2.8. As in CV, the height of the current peak should be proportional to the concentration of the analyte in the bulk salt as seen in Eqs. (2.9), (2.10), and (2.15).

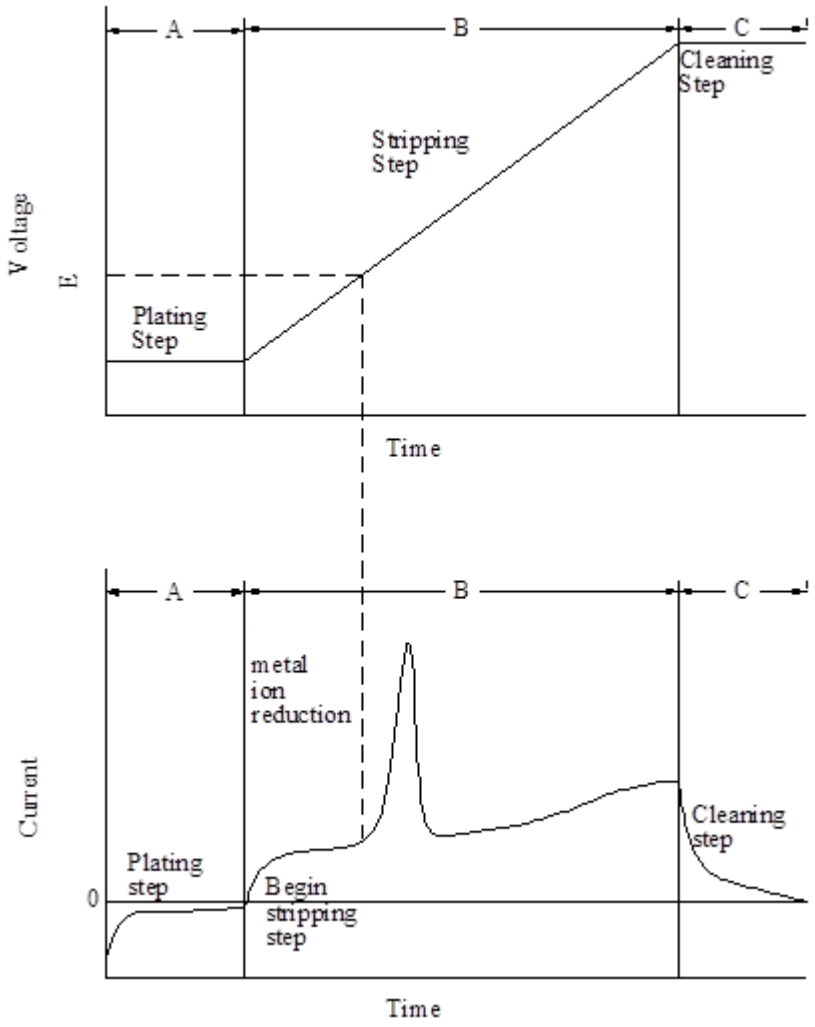

Figure 2.8 Example of the applied potential and resulting current during anodic stripping voltammetry [60].

2.3 General Summary

For this research, the definition of the standard reduction potential, diffusion coefficient, and activity coefficient were presented. Discussion on these values reported in literature for U and Zr electrochemical experiments were provided and indicated these values were varied greatly and scarce, respectively. It is evident that specific design must be acquired in order to obtain accurate data sets for scale-up and modeling. Here, three different electrochemical techniques, CV, CP, and ASV were chosen for the analysis. Reversible and irreversible redox reactions were discussed and explanation was given of how to characterize the observed reactions from CV data. CP was chosen to also use for determining diffusion coefficients. ASV was selected to provide possible direction in concentration detection towards material accountability and safeguards routines. The given information is valuable in planning out the experimental program, which will be discussed in the next chapter.

Chapter 3: Experimental Program and Data Collection

Understanding the mechanisms that are responsible for electrochemical reactions of compounds such as uranium (U) and zirconium (Zr) in a molten salt system requires several fundamental experiments. Each particular experiment is designed to verify and test the effects of electrochemical parameters on the ultimate behavior and characteristics for such a system. The main purpose of this chapter is to (1) discuss the fundamental experiments which help to determine how the physical variables influence the behavior of either a UCl_3-LiCl-KCl, $ZrCl_4$-LiCl-KCl, or UCl_3-$ZrCl_4$-LiCl-KCl system and (2) explain the data collection method that ensures consistency of the collected measurements based on several test runs for a given experiment.

First, the focus will be on the experimental materials and equipment. Second, experimental preparation and details are discussed. Third, the experimental program is given along with a matrix of all performed experiments. Finally, data collection techniques are explained in detail.

3.1 Experimental Materials and Equipment

All U experiments were conducted in the MBraun argon atmosphere glovebox (as shown in Figure 3.1) in the Center for Advanced Energy Studies (CAES) Radiochemistry Laboratory (RL), while the Zr experiments were conducted in a similar MBraun glovebox. It should be mentioned that prior to working with uranium samples and operating inside the laboratory, all users must take the CAES Radiation Safety Training course and pass a test with a score of 80% or above along with the CAES Glovebox training course.

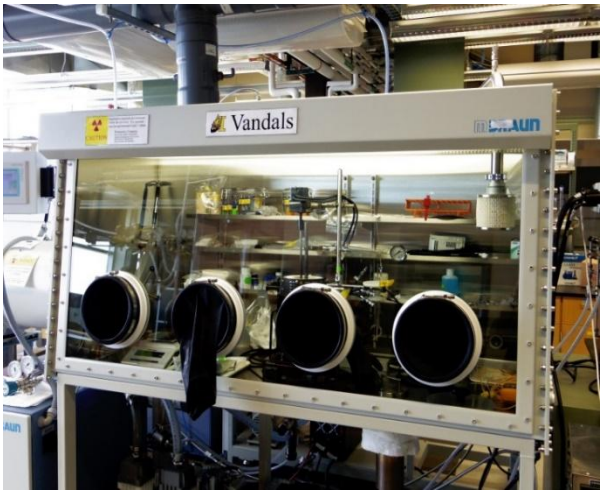

Figure 3.1 MBraun argon atmosphere glovebox in which all uranium experiments were conducted.

The LiCl-KCl eutectic salt is highly hygroscopic and, at the temperatures studied, will react with both O_2 and H_2O to form oxides. The gloveboxes were maintained at a slightly negative pressure to avoid the ingress of any oxygen and/or moisture. The O_2 and H_2O concentrations in the inert atmosphere were both less than 0.1 ppm for the experiments involving uranium, and less than 3.0 ppm throughout the duration of the zirconium experiments (Figure 3.2). Within the glovebox was a Kerrlab melting furnace (Figure 3.3) used to melt and maintain the salt at the desired temperature.

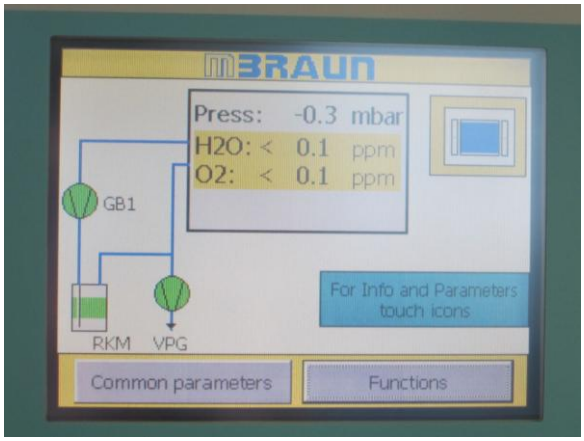

Figure 3.2 Oxygen and moisture sensor readings from the glovebox in which all depleted uranium experiments were performed.

Figure 3.3 Kerrlab furnace within glovebox used in all experiments.

The salt mixtures were composed of LiCl-KCl eutectic from AAPL (99.99%) and depleted uranium trichloride (UCl_3) and/or zirconium tetrachloride ($ZrCl_4$). The depleted UCl_3 was provided by INL as a 75 wt% mixture in LiCl-KCl eutectic (Figure 3.4). The $ZrCl_4$ was reactor grade, 99.5+% from Alfa Aesar. The salt was loaded into a tapered glassy carbon crucible (Sigradur®, HTW-Germany) that was 16.8 cm tall, had outside diameters of 4.1 cm and 4.5 cm at the bottom and top, respectively, and a wall thickness of 0.3 cm. This glassy carbon crucible was then placed into a magnesia (MgO) secondary crucible to contain any molten salt upon possible breakage of the crucible before loading it into the furnace. The working electrodes were tungsten (diameter of 2.0 mm and length of 30 cm, Alfa Aesar, 99.95%) and the counter electrode leads were glassy carbon (diameter of 3.0 mm and length of 30 cm, Sigradur®, HTW-Germany). The glassy carbon rod was in contact with the glassy carbon crucible making the entire crucible and rod in contact with the electrolyte the counter electrode. A 5.0 mol% AgCl (Alfa Aesar, ultra dry, 99.997%) Pyrex® body reference electrode was used. The salt temperature was monitored with an alumina (Al_2O_3)

sheathed thermocouple connected to a Fluke 52II thermometer. A diagram of the experimental setup is shown in Figure 3.5.

Figure 3.4 75 wt% UCl_3 in LiCl-KCl eutectic used in the experiments provided by INL.

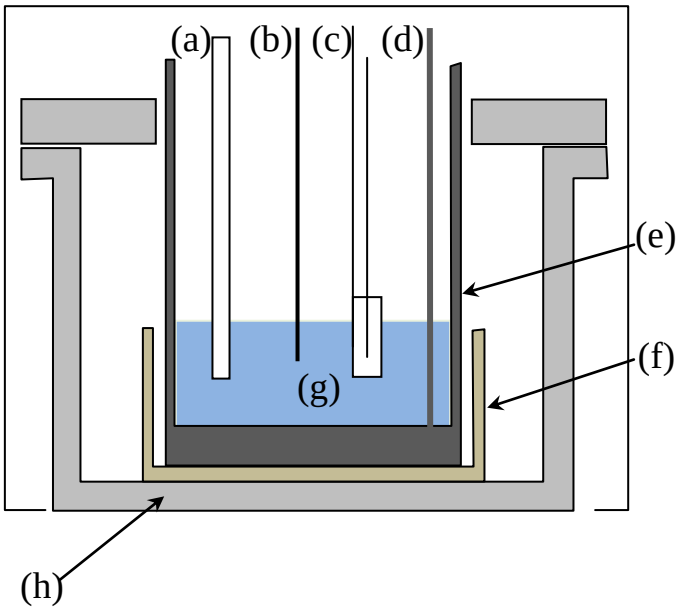

Figure 3.5 Experimental setup within the glovebox with (a) Al_2O_3 sheathed thermocouple, (b) tungsten working electrode, (c) Ag/AgCl reference electrode, (d) glassy carbon counter electrode lead, (e) glassy carbon crucible/counter electrode, (f) MgO secondary crucible, (g) eutectic LiCl-KCl salt containing UCl_3 and/or $ZrCl_4$, and (h) Kerrlab furnace.

A quartz electrode assembly (Figure 3.6) designed by a University of Wisconsin-Madison team [60] was used to position the electrodes and thermocouple at the desired

depths in the molten electrolyte and to keep them electrically insulated from each other. The assembly has a fixed location for each electrode providing reproducibility for each experimental run (see Figure 3.7). A Princeton Applied Research VersaSTAT 4-400 potentiostat (Figure 3.8) with *VersaStudio* software was used for all electrochemical experiments and data collection (version 1.33 [61] for U experiments and version 2.02 [62] for Zr experiments).

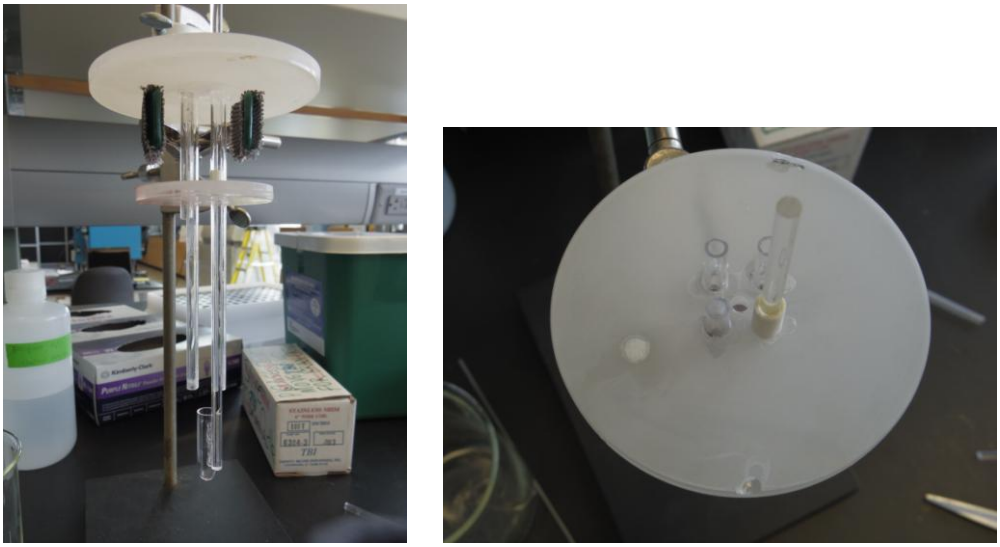

Figure 3.6 Quartz electrode assembly used in all the experiments.

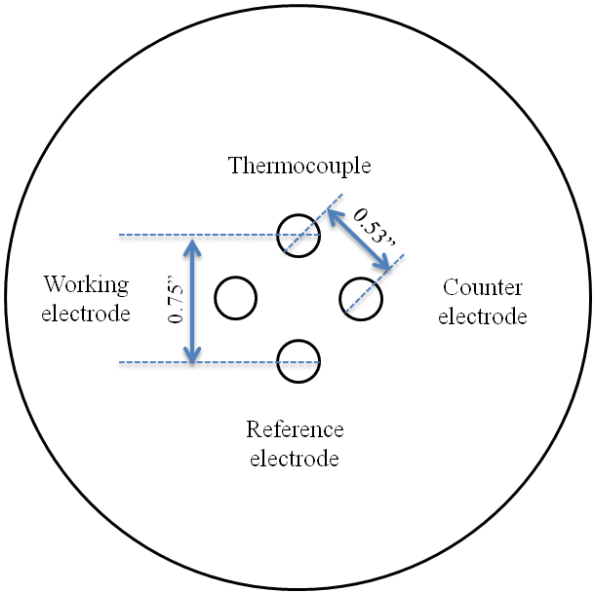

Figure 3.7 Quartz assembly electrode separation dimensions.

Figure 3.8 Computer and VersaSTAT 4-400 potentiostat used to apply potential or current to the cell and record data.

3.2 Experimental Preparation

3.2.1 Reference Electrode Preparation

Prior to performing any electrochemical experiments, a reference electrode must be prepared (see Figure 3.9). For the current studies, a 5.0 mol% Ag/AgCl in LiCl-KCl eutectic reference electrode was chosen. This is a higher concentration than many researchers used previously (commonly 1 wt%) [22, 35, 45]; but as will be discussed later in Section 4.2.2, the value can be converted to a standard reference for direct comparison. The 5.0 mol% concentration was chosen to take advantage of its long term stability as compared with lower concentrations. Work by Shirai and co-workers [63] has reported that the higher concentrations allow for a more stable potential reading. At low concentrations, any reaction of the AgCl alters the concentration by a relatively large degree, whereas at higher concentrations, this same change results in less of an overall effect.

Figure 3.9 5.0 mol% Ag/AgCl reference electrode in a Pyrex® body used in the electrochemical experiments.

To prepare the reference electrode, 0.135 g of AgCl beads were added to 1.00 g of the LiCl-KCl eutectic, creating a 5.0 mol% mixture. This mixture was loaded into a small (1.0 cm outside diameter) Pyrex® tube with 1 mm wall thickness. This is thin enough to allow ionic conduction between the solution and the electrolyte; yet it is thick enough to prohibit electronic conduction. A silver wire (diameter of 1.0 mm, Acros Organics, 99.9%) was then immersed into the salt mixture. An image of the reference electrode is shown in Figure 3.9 following the 1.0 wt% UCl_3 experiments.

3.2.2 UCl_3-LiCl-KCl Preparation

For all experiments performed with U, a minimum of two people were present. Whenever any work was occurring in the uranium glovebox, a second person who went

through and passed both the CAES Glovebox and Radiation Safety Training courses must be present. Initially, approximately 85 g LiCl-KCl was added to the glassy carbon crucible and the 75 wt% UCl_3-LiCl-KCl mixture was incrementally added to achieve each desired concentration as calculated and shown in Table 3.1.

Table 3.1 Incremental additions of 75 wt% UCl_3-LiCl-KCl.

	U1	U2.5	U5	U7.5	U10
LiCl-KCl (g)	84.569	---	---	---	---
UCl_3(75%)-LiCl-KCl (g)	1.143	1.773	3.130	3.357	3.615
UCl_3 Concentration (wt%)	1.00	2.50	5.00	7.50	10.0
U Concentration (mol/cm^3)	4.71×10^{-5}	1.18×10^{-4}	2.35×10^{-4}	3.53×10^{-4}	4.71×10^{-4}

The furnace was heated at 4 K/min to avoid thermal shock on the glassy carbon crucible, up to a temperature of approximately 813 K, taking approximately two hours. During this heat-up time, the quartz structure containing the electrodes and thermocouple were positioned over the top of the crucible to be pre-heated. Prior to initiating the electrochemical tests, the electrodes and assembly were lowered into the molten salt resulting in working electrode surface areas ranging from 0.583 cm^2 to 0.785 cm^2. Banana clips were used to connect the assembly to the potentiostat system, as shown in Figure 3.10.

Once the molten salt temperature was steady at 773 K ± 2 K, which would generally take approximately ninety minutes, the electrochemical tests were performed and recorded as will be described in Section 3.3. Typically, the entire preparation process would take a minimum of four hours prior to running each experiment.

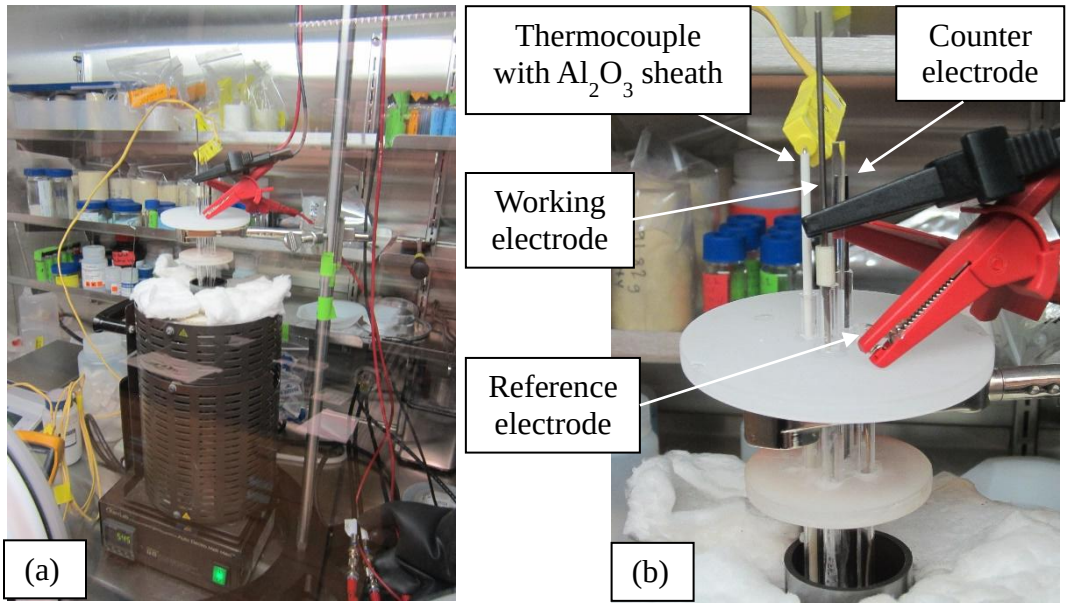

Figure 3.10 (a) Experimental setup in the glovebox with (b) up close view of the electrodes and connections.

3.2.3 $ZrCl_4$-LiCl-KCl Preparation

While $ZrCl_4$ is soluble and stable in the molten eutectic, pure $ZrCl_4$ sublimes at 604 K [64], which is lower than the melting point of the LiCl-KCl eutectic from 621 K to 634 K °C [16]. Initially, $ZrCl_4$ was added directly to the LiCl-KCl eutectic and heated to the operating temperature of 773 K. When this was done, white vapor was seen rising out of the crucible and depositing on the electrodes above the furnace, as shown in Figure 3.11.

To overcome this challenge, a modified process was developed to trap $ZrCl_4$ underneath the LiCl-KCl until the salt melts and all $ZrCl_4$ can be all dissolved into the eutectic by working with a tapered glassy carbon crucible. The pure LiCl-KCl eutectic was first melted and consolidated into a single ingot in the tapered glassy carbon crucible, taking approximately 3.5 hours. When cooled overnight, the LiCl-KCl ingot was removed from the crucible and approximately 1 cm was cut off the bottom of the salt ingot using a hacksaw (Figure 3.12). The powdered $ZrCl_4$ was added to the crucible and the ingot with the bottom

cut off was placed over the top of the $ZrCl_4$ powder in the crucible. Due to the taper, the salt ingot sits tightly against the walls of the crucible and above this powder, as illustrated in Figure 3.13. The sawing and measuring processes would take an average of one hour.

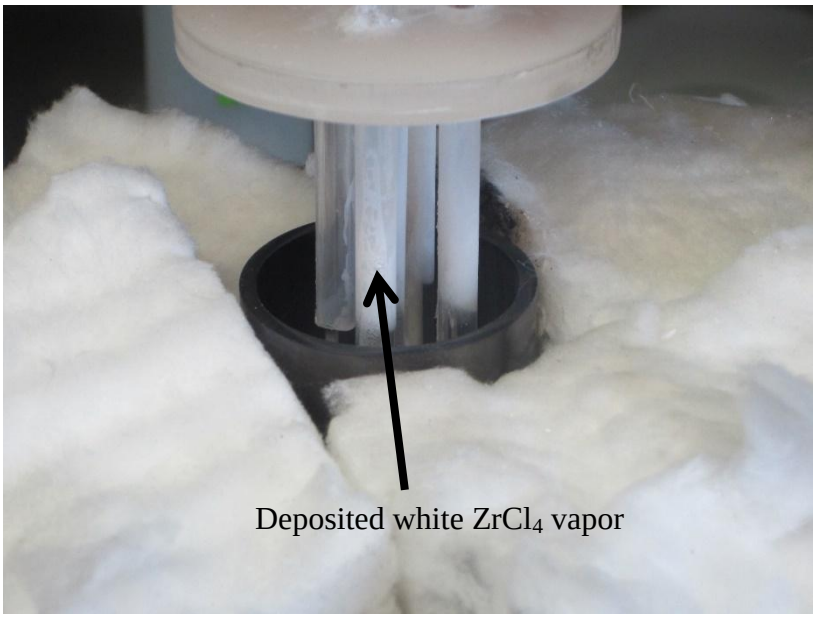

Figure 3.11 White $ZrCl_4$ deposits on quartz electrode structure following initial $ZrCl_4$-LiCl-KCl mixture attempts.

Figure 3.12 The bottom of the LiCl-KCl ingot is cut off as part of a method to ensure $ZrCl_4$ is dissolved into the eutectic.

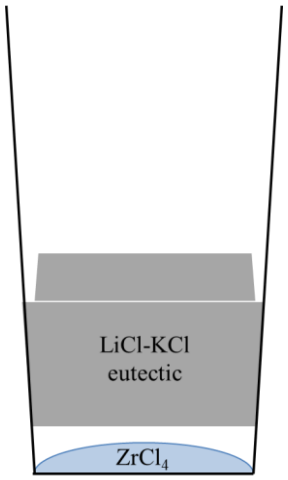

Figure 3.13 Diagram of the $ZrCl_4$ trapping method developed for this experimental study. (Not drawn to scale).

When this method was performed there was no evidence of $ZrCl_4$ vaporization and ICP-MS analysis of the salt mixtures following each experiment showed that all the $ZrCl_4$ that was added to the mixture remained in the crucible. As with the UCl_3-LiCl-KCl experiments, $ZrCl_4$ was incrementally added for each experiment to approximately 83 g LiCl-KCl eutectic in a glassy carbon crucible as shown in Table 3.2. It is important to point out that the negative values listed in Table 3.2 indicate a decrease in the total amount due to loss of salt powder during the sawing procedure . Following the addition of $ZrCl_4$, a similar heating method as described in the previous section for UCl_3 was performed. The furnace was heated at 4 K/min to a temperature of 603 K to achieve a temperature in the salt just below the sublimation point of $ZrCl_4$. The furnace was held at this temperature for approximately one hour allowing the contents to reach equilibrium prior to heating the furnace up (again at 4 K/min) to the desired working temperature. Following this heating procedure, which would take approximately five hours, all electrochemical methods were performed.

Table 3.2 Incremental additions of $ZrCl_4$ with an initial LiCl-KCl mass of 83.25 g.

	Zr0.5	Zr1	Zr2.5	Zr5
LiCl-KCl Loss (g)	0	-1.91	-0.98	-0.94
$ZrCl_4$ (g)	0.48	0.41	1.18	2.14
$ZrCl_4$ Concentration (wt%)	0.57	1.07	2.49	4.98
Zr Concentration (mol/cm^3)	3.99×10^{-5}	7.43×10^{-5}	1.73×10^{-4}	3.46×10^{-4}

3.2.4 UCl_3-$ZrCl_4$-LiCl-KCl Preparation

The behavior of $ZrCl_4$ together with UCl_3 in the LiCl-KCl eutectic is important as there is nominally 10 wt% UCl_3 in the LiCl-KCl electrolyte during the pyrochemical treatment of used nuclear fuel [17] in the Mark-IV electrorefiner. For similitude with this ER, UCl_3 concentration was slightly less than 10 wt% (9.80 and 8.34 wt%) with two experiments containing a low (0.497 wt%) and a high (4.17 wt%) concentration of $ZrCl_4$.

To minimize depleted uranium waste, the UCl_3-$ZrCl_4$-LiCl-KCl salt mixtures were prepared by adding $ZrCl_4$ to the 10.0 wt% UCl_3-LiCl-KCl mixture prepared for the pure uranium experiments. The cutting of the salt ingot as described in Section 3.2.2 would spread UCl_3 sawdust throughout the glovebox, so a modified method was undertaken in preparing the salt mixture. A 25.1 wt% mixture of $ZrCl_4$-LiCl-KCl was prepared utilizing the vapor trapping method described previously, maintaining the salt at temperature for five hours to allowing for a complete dissolution. This salt with the $ZrCl_4$ pre-dissolved in the LiCl-KCl eutectic was then added to the 10.0 wt% UCl_3-LiCl-KCl mixture to achieve the desired $ZrCl_4$ concentration. The amounts of these salts used in each experiment are listed in Table 3.3. The heating process was the same as with the UCl_3-LiCl-KCl experiments; that is, the furnace was heated at 4 K/min to approximately 813 K and when the salt mixture

reached the desired temperature of 773 K (approximately 4 hours after the heating process began), the electrochemical experiments were initiated.

Table 3.3 Incremental additions of 25.1 wt% $ZrCl_4$-LiCl-KCl.

		U10-Zr0.5	U10-Zr5
UCl_3-LiCl-KCl		95.189	---
25.1 wt% $ZrCl_4$		1.922	16.899
Concentration:	**UCl_3**	9.80 wt% 4.61×10^{-4} mol/cm^3	8.34 wt% 3.92×10^{-4} mol/cm^3
	$ZrCl_4$	0.497 wt% 3.45×10^{-5} mol/cm^3	4.17 wt% 2.90×10^{-4} mol/cm^3

3.3 Experimental Program and Data Collection Methods

Once the molten salt temperature was steady at the desired temperature ± 2 K, the electrochemical tests including CV, CP, and ASV were performed. The combination of these methods allows the calculations of the desired electrochemical properties (apparent standard reduction potential, diffusion coefficient, and activity coefficient) using the theory discussed in Chapter 2. These properties can be used to better understand the behavior of both uranium and zirconium in the LiCl-KCl molten salt and be used to improve the system models. A matrix of the experiments performed is presented in Table 3.4.

Typically, the entire process—preparing the salts, heating and melting, performing the electrochemical experiments, and collecting a sample—would take between 11 and 14 hours for each uranium concentration studied and a total of 26 to 32 hours for each zirconium concentration at the three temperatures.

Table 3.4 Experimental Program

Exp. No.	Concentration (wt%)		Electrochemical Methods			Temperature (K)
	U	Zr	CV	CP	ASV	
1	0	0	Yes	Yes	Yes	773
2	1.0	0	Yes	Yes	Yes	773
3	2.5	0	Yes	Yes	Yes	773
4	5.0	0	Yes	Yes	Yes	773
5	7.5	0	Yes	Yes	Yes	773
6	10.0	0	Yes	Yes	Yes	773
7	0	0.5	Yes	Yes	No	723
8	0	0.5	Yes	Yes	Yes	773
9	0	0.5	Yes	Yes	No	823
10	0	1.0	Yes	Yes	No	723
11	0	1.0	Yes	Yes	Yes	773
12	0	1.0	Yes	Yes	No	823
13	0	2.5	Yes	Yes	No	723
14	0	2.5	Yes	Yes	Yes	773
15	0	2.5	Yes	Yes	No	823
16	0	5.0	Yes	Yes	No	723
17	0	5.0	Yes	Yes	Yes	773
18	0	5.0	Yes	Yes	No	823
19	10.0	0.5	Yes	No	No	773
20	10.0	5.0	Yes	No	No	773

3.3.1 Cyclic Voltammetry (CV) Method

All CV experiments were performed using the Princeton Applied Research VersaSTAT 4-400 and *VersaStudio* software [61-62]. In the software, the user provides the following inputs: (1) the desired initial potential, (2) the potential at which to reverse the scan, (3) the final potential, (4) the scan rate, and (5) the number of cycles to run with 2000 data points per cycle recorded. For the uranium experiments, the scans were started at -2.4 V versus the Ag/AgCl reference, reversed at 0.0 V, ending back at -2.4 V. The zirconium

experiments went up to 0.5 V to ensure that all relevant peaks were captured. For these potential windows, resulting current was recorded at approximately every 2.4 mV for uranium and 2.9 mV for zirconium. These potential scan windows were chosen to be wide enough to capture the possible analyte reactions, but avoid reactions involving the base LiCl-KCl salt. The standard potential for the lithium ion reduction is -2.561 V vs. Ag/AgCl, while the standard potential for the oxidation of chloride ions is +1.065 V vs. Ag/AgCl [20]. These settings are shown as an example for the 1.0 wt% UCl_3 experiment with a 100 mV/s scan rate in Figure 3.14.

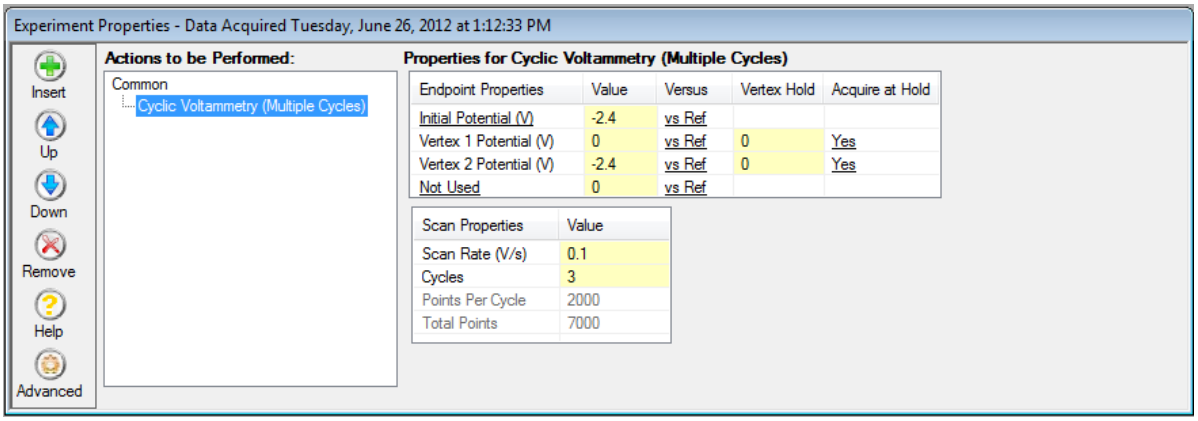

Figure 3.14 Example of *VersaStudio* user interface for setting up a set of cyclic voltammograms.

Three cycles were performed to ensure repeatability. The second and third cycles were generally identical, as illustrated in Figure 3.15, and the third cycle was used for the analysis methods discussed in Chapter 2.

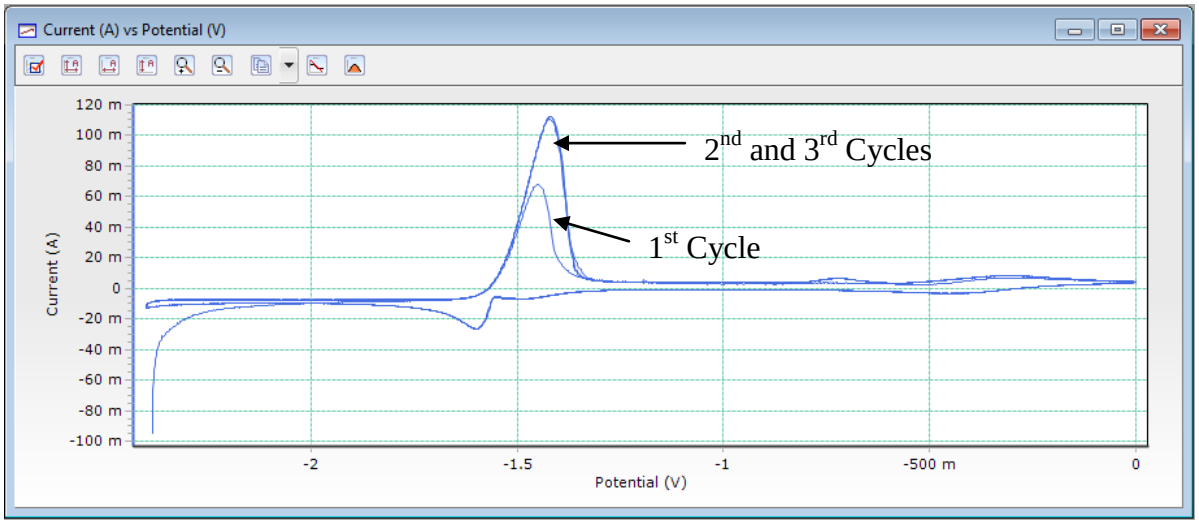

Figure 3.15 An example of three cycles of CVs for the 1.00 wt% UCl_3 experiment at a scan rate of 100 mV/s.

The scan rates were chosen to give clear oxidation and reduction peaks—generally beginning with 100 mV/s and increasing or decreasing from there as necessary. Anything slower than an optimal scan rate would cause too much time at reducing potentials yielding a large amount of the species to deposit onto the surface of the electrode. This situation would further create an uneven surface area, which was clearly evident during the runs as shown in Figure 3.16 (a). At faster than optimal scan rates, the peaks would broaden and shift with subsequent cycles (see Figure 3.16 (b)). A minimum of five acceptable scan rates was required for each experimental procedure listed in Table 3.4. Between each cyclic voltammetry run, an oxidizing potential of 0.0 V was applied to the working electrode for a minimum of 30 sec to strip off any uranium that may have deposited during the CVs. This helps to ensure an accurate, repeatable working electrode surface area.

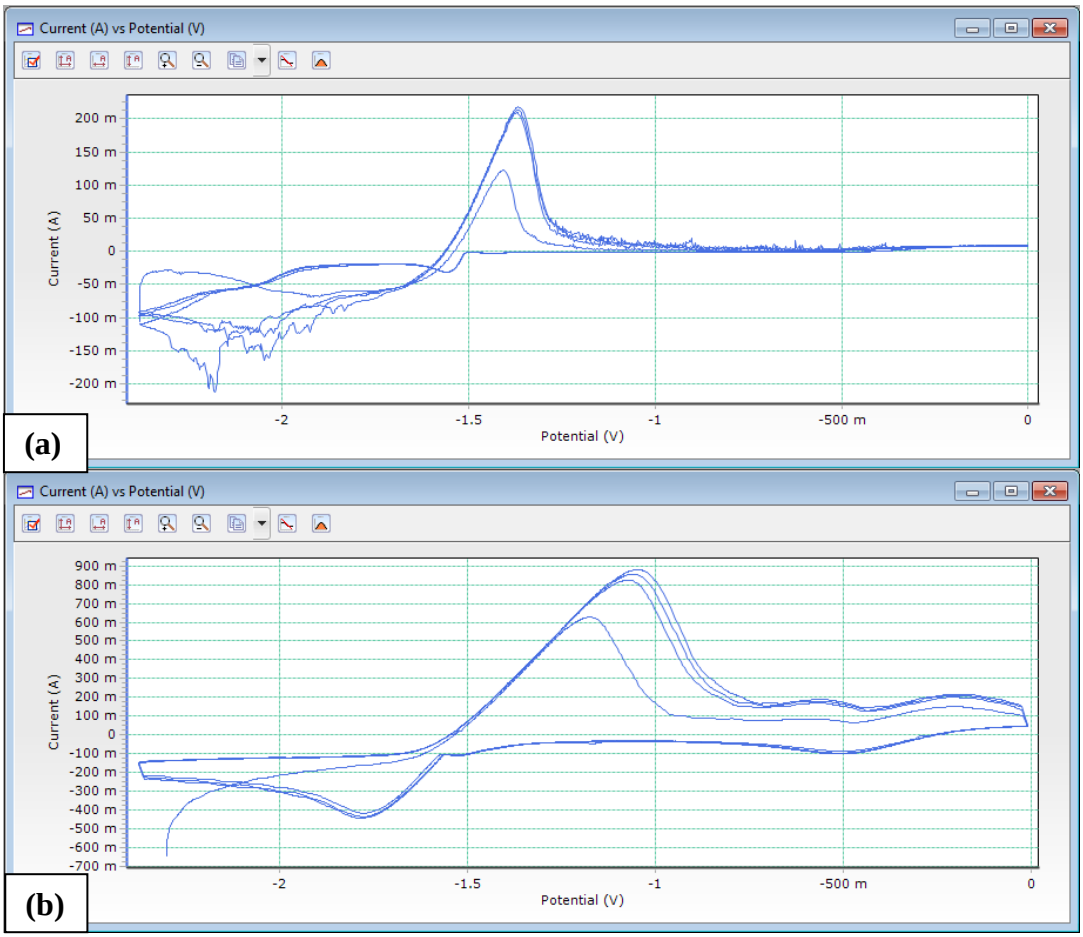

Figure 3.16 Example of (a) slower than optimal scan rate (20 mV/s in 2.50 wt% UCl_3) and (b) faster than optimal scan rate (2.0 V/s in 5.00 wt% UCl_3) at 773 K.

3.3.2 Chronopotentiometry (CP) Method

CP experiments were also all performed with the VersaSTAT 4-400 potentiostat and *VersaStudio* software [61-62]. For the CP runs, a series of potentiostatic (constant potential) and galvanostatic (constant current) steps was performed leading up to and following the actual CP step. First, an oxidizing potential of 0.0 V was applied for a minimum of 20 sec to oxidize any active material that may have deposited onto the working electrode. Then, 0.0 A was applied for 20 seconds to bring everything to equilibrium, ensuring no reaction is occurring at the electrode surface. The third step was the actual CP experiment, in which a

driving current was applied to the working electrode for 20 sec, reducing the active species onto the electrode surface. User inputs are shown in Figure 3.17 (a) as an illustration. During this step, potential was recorded every 0.01 sec to accurately determine the transition time. After the CP step, 0.0 V was again applied for 20 sec to strip off all deposited material. If an adequate driving current was applied, this procedure would result in very clean chronopotentiograms, with a clear plateau representing the diffusion of the analyte to the surface, followed by a drop in potential to the reduction of lithium when the species was exhausted at the electrode surface as shown in Figure 3.17 (b). This procedure was repeated to record a minimum of four chronopotentiograms with clear plateaus.

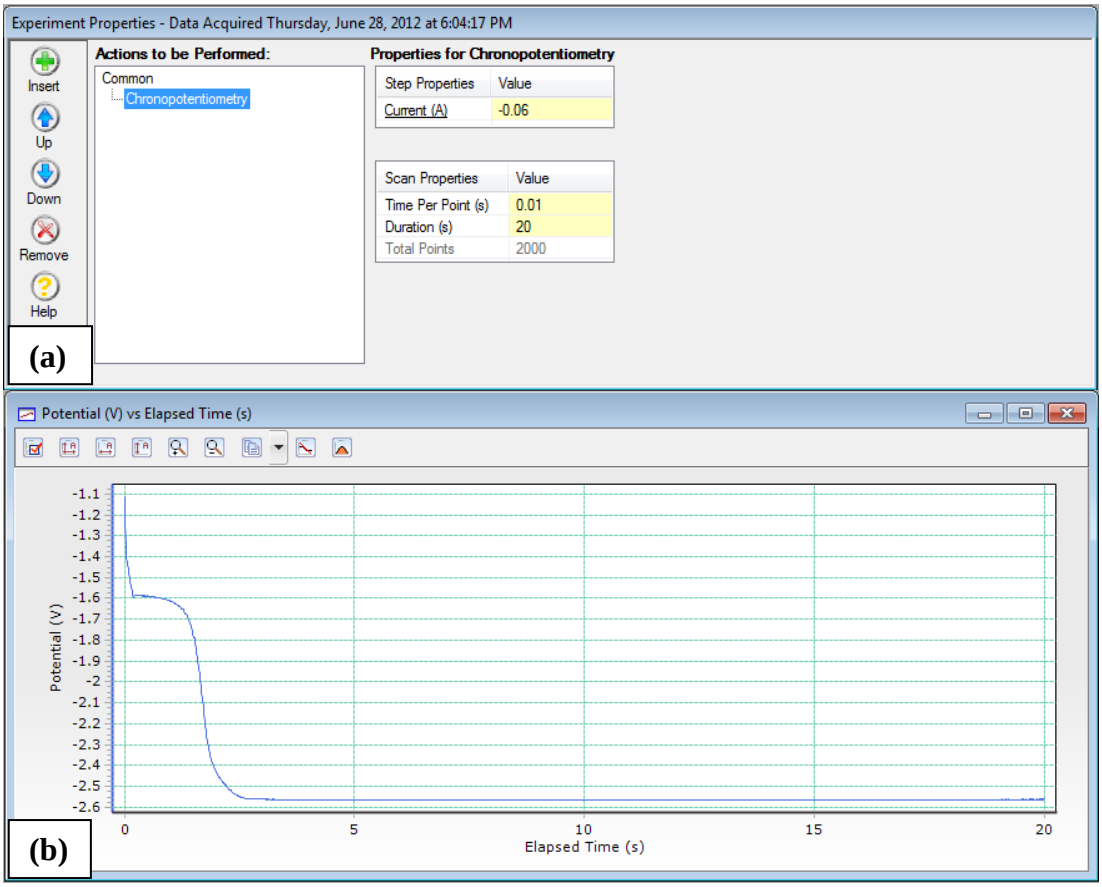

Figure 3.17 (a) Chronopotentiometry settings in *VersaStudio* and (b) the resulting chronopotentiogram for 2.50 wt% UCl_3 in LiCl-KCl at 773 K and applied current of 60 mA.

As mentioned, in order to collect good CP data, the correct driving current(s) must be applied. A smaller than optimal driving current would not be large enough to reduce the analyte at the surface fast enough to create a diffusion limited reaction; that is, there would be no clear plateau and the potential would not drop to reduce lithium, as illustrated in Figure 3.18 (a), which was performed in the 2.50 wt% UCl_3 with a driving current of 10 mA. Applying a driving current larger than optimal would rapidly exhaust the analyte at the electrode surface, causing the potential to almost immediately drop to reduce lithium. An example of this is shown in Figure 3.18 (b). The reason for the eventual rise in potential after approximately 20 sec is unclear.

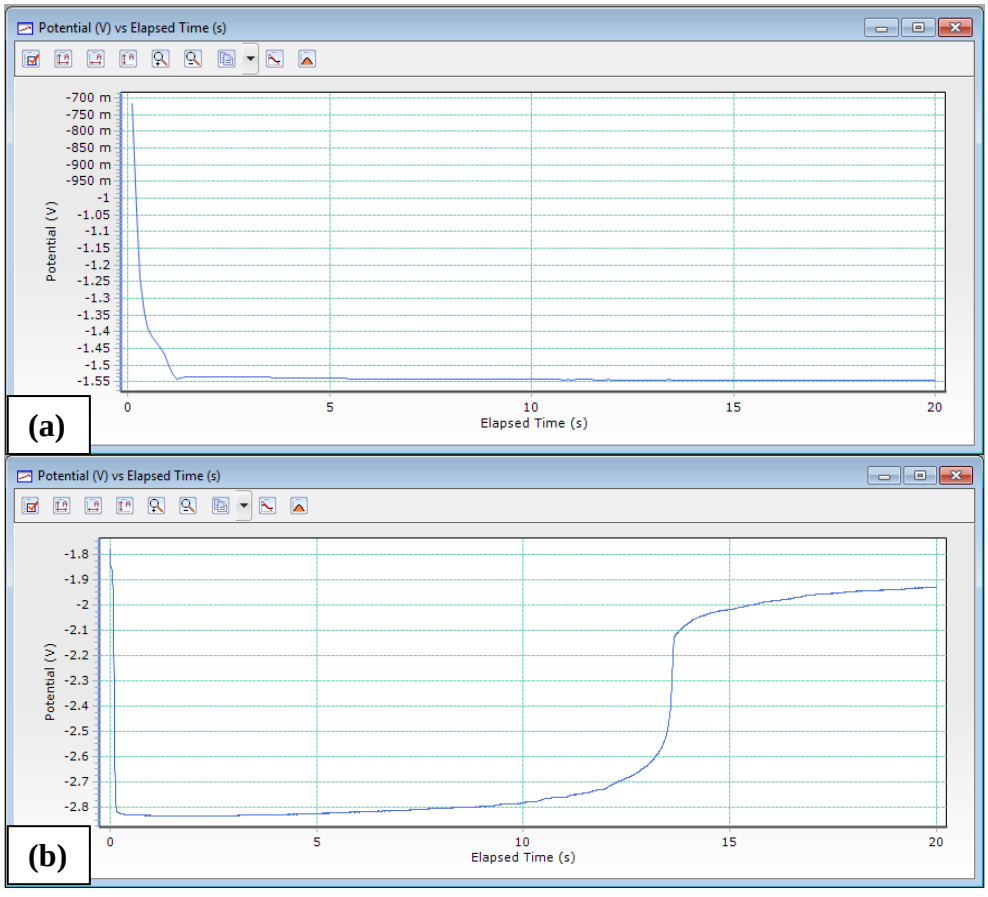

Figure 3.18 Example of (a) smaller than optimal driving current (10 mA in 2.50 wt% UCl_3) and (b) larger than optimal driving current (700 mA in 7.50 wt% UCl_3) at 773 K.

3.3.3 Anodic Stripping Voltammetry (ASV) Method

ASV was performed with the Princeton Applied Research VersaSTAT 4-400 potentiostat and *VersaStudio* software [61-62] for all experiments listed in Table 3.4. To properly perform anodic stripping voltammetry, the following procedure was followed: (1) 0.0 V vs. Ag/AgCl was applied for 20 sec to the working electrode to strip any material that may be deposited onto the surface, (2) a reducing potential of -2.3 V vs. Ag/AgCl was applied for 5 or 60 sec (will be discussed later in Chapter 4) to reduce a large amount of material onto the working electrode, (3) the voltage was linearly ramped at 50 mV/s from -2.3 V up to 0.0 V, and (4) 0.0 V was applied for 20 seconds to fully remove the electroplated material. Often, especially with the higher concentration experiments, longer than 20 sec at 0.0 V was required during the last step. This procedure (shown in Figure 3.19 (a) for 1.00 wt% UCl_3) was repeated ten times to obtain a mean peak height value. Figure 3.19 (b) illustrates the recorded current as a function of time for the ASV procedure described. Further discussion on difficulties performing ASV in varying concentrations will be given in Section 4.1.3.

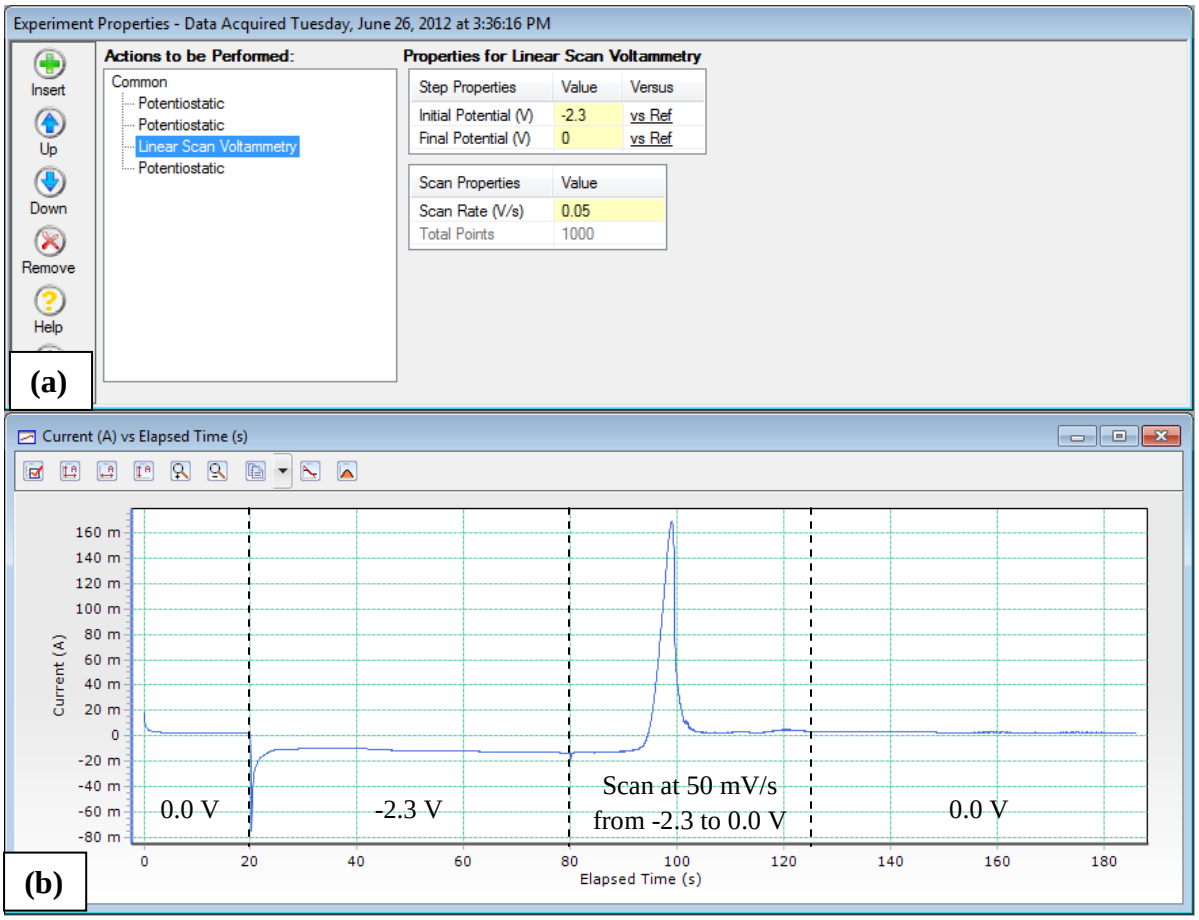

Figure 3.19 (a) Anodic Stripping Voltammetry settings in *VersaStudio* and (b) the resulting current for 1.00 wt% UCl_3 in LiCl-KCl at 773 K.

3.3.4 Working Electrode Surface Area Measurement Method

The electroactive surface area of the working electrode is incredibly important in each of the three electrochemical techniques as shown in Eqs. (2.9), (2.10), (2.15), and (2.17). Careful steps must be followed to provide accurate determination of the surface area. Following each experiment, the working electrode was removed from the salt and furnace. The immersion depth of the electrode was evident as a line of adhered salt (see Figure 3.20). This wetted length was measured and used along with the electrode diameter to calculate the working electrode surface area, ranging from 0.6 cm^2 to 2.5 cm^2.

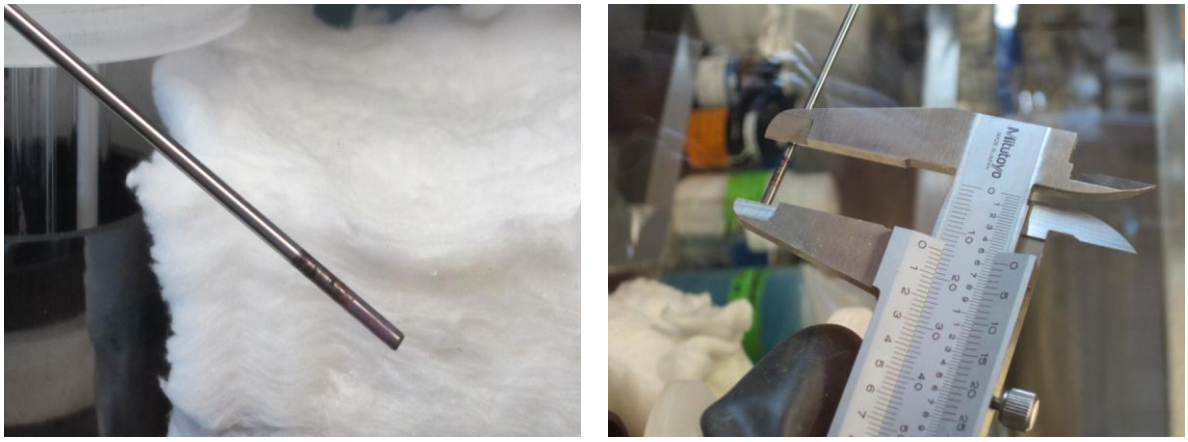

Figure 3.20 Example of working electrode immersion depth measurement from 1.00 wt% UCl_3 in LiCl-KCl at 773 K.

3.4 General Summary

In this chapter, the experimental work performed in this dissertation was described. The materials and equipment used were first presented and discussed. This was followed by a discussion of the experimental preparation required including the reference electrode construction and the salt mixing and melting process. Next, a matrix of the experiments performed was presented. Lastly, details were provided describing each experimental method performed (CV, CP, and ASV), and how the data sets were recorded and collected indicating all applied electrochemical software routines, lessons learned, and data dissemination. This given information all leads into the next chapter, in which the results from experimental methods will be presented, analyzed and discussed.

Chapter 4: Results and Discussion

The results for the fundamental studies described in the previous chapter are presented here. The main focus of the discussion is on the electrochemical results, the calculated properties, and analysis. The purpose of this chapter is to consider the important parameters that may affect or influence the electrochemical results of an ER system. Experimental results are given to show relative effects of these influential factors. Furthermore, on a fundamental basis, these electrochemical methods help us to gain insight into the significance of different factors responsible for electrochemical separations and their behaviors.

The outline of this chapter is as follows. First, the results for uranium (U) electrochemistry are presented showing resulting ingots and their appearance along with CV, CP, and ASV studies. Second, the results for the U thermodynamic and electrochemical properties are given. Here, different electrochemical methods have been applied to the experimental data to show the possible range of confidence in these equations. Furthermore, a comparison with the earlier work reported in literature is presented and discussed. Third, the results and discussion of zirconium (Zr) electrochemistry are provided yielding significant thermodynamic and electrochemical information. And lastly, the combined U and Zr electrochemistry is presented to provide an insight into actual ER electrochemical behavior.

4.1 Uranium Electrochemistry

Uranium experiments were performed at five different concentrations (1.00, 2.50, 5.00, 7.50, and 10.0 wt%). Photos of these five salt ingots following the experiments are shown in Figure 4.1. All ingots appear dark purple in color.

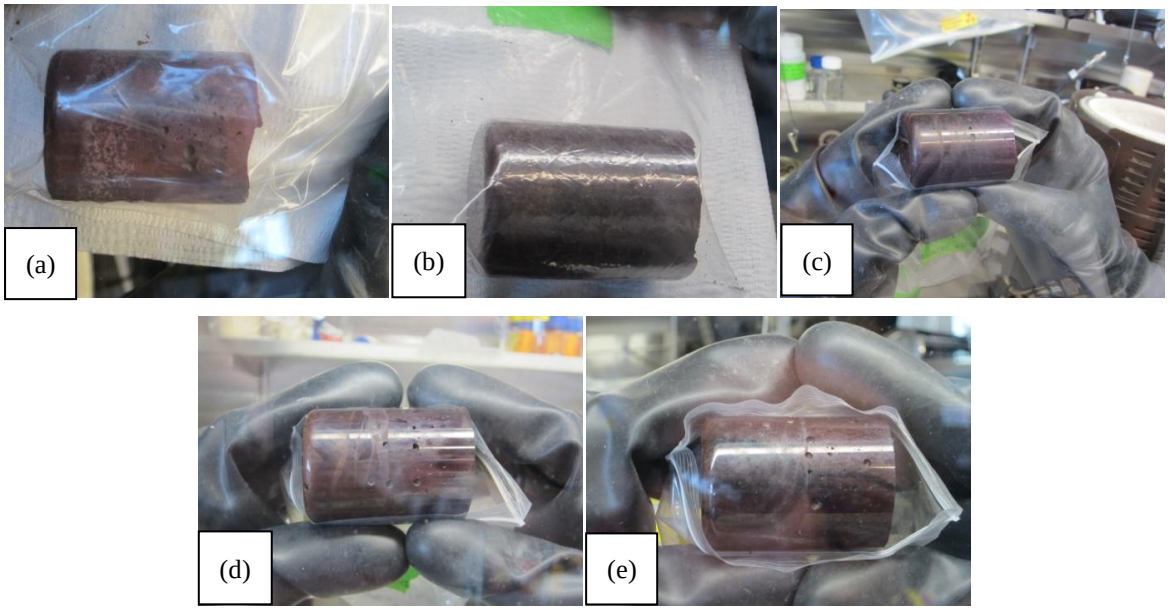

Figure 4.1 Images of the five UCl_3 salt ingots following electrochemical experiments: (a) 1.00 wt% UCl_3, (b) 2.50 wt% UCl_3, (c) 5.00 wt% UCl_3, (d) 7.50 wt% UCl_3, and (e) 10.0 wt% UCl_3. The ingots are approximately 5 cm tall with a diameter of 3.3 cm.

4.1.1 Uranium Cyclic Voltammetry (CV)

Cyclic voltammograms were recorded for the pure LiCl-KCl eutectic and the five UCl_3 concentrations. Figure 4.2 shows the results for 1.00 wt% UCl_3 at various scan rates (20 mV/s to 200 mV/s) along with the CV for the pure LiCl-KCl eutectic at 200 mV/s. The CVs for the other experiments are shown in Figures 4.3 to 4.6.

The cyclic voltammogram of the pure LiCl-KCl eutectic clearly shows no reactions of importance in the potential scan range of (-2.4 to 0.0) V vs. Ag/AgCl as seen in Figure 4.2. Three cathodic peaks (A_c, B_c, and C_c) and three anodic peaks (A_a, B_a, and C_a) can be observed.

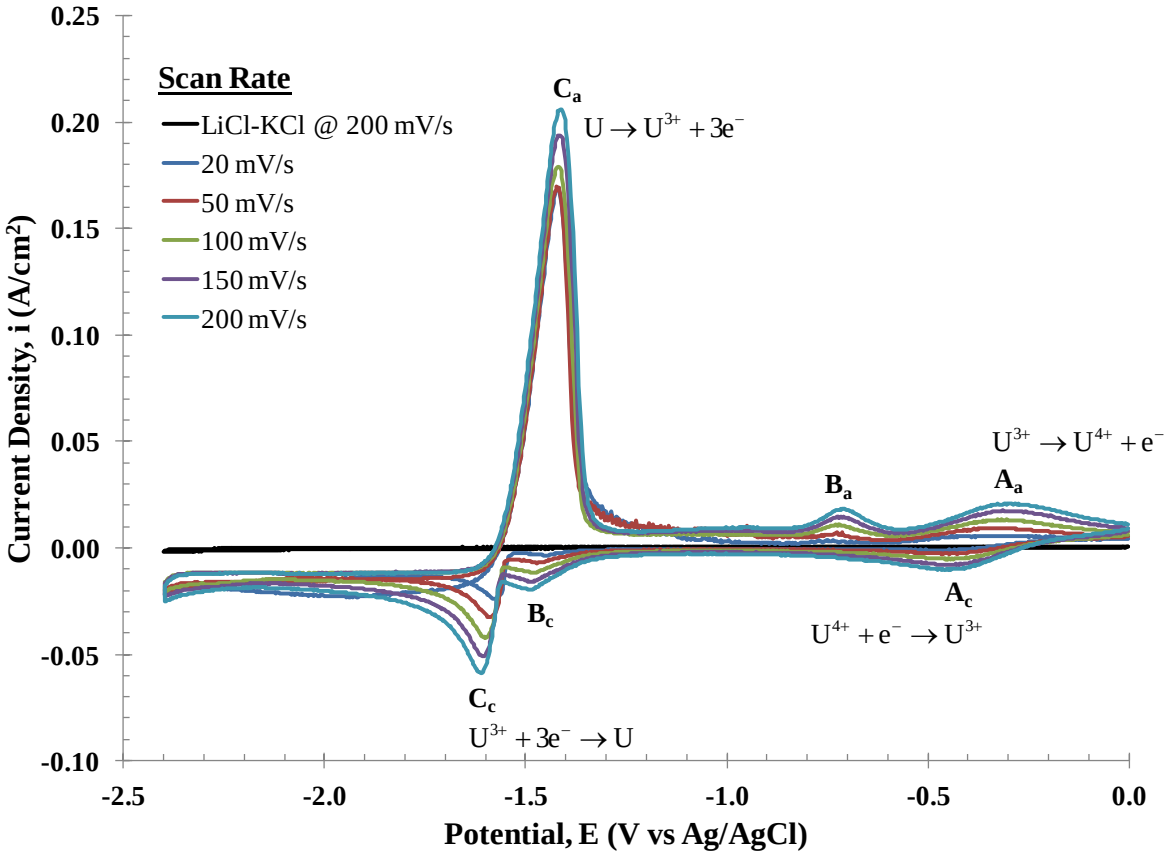

Figure 4.2 Cyclic voltammograms for 1.00 wt% UCl_3 in LiCl-KCl eutectic at 773 K.

The major anodic peak C_a potential does not appear to shift with scan rate at 1.00 wt%; however, the major cathodic peak C_c shows a shift of peak potential in the negative direction with increasing scan rates. The shift of these peaks (C_c and C_a) is more prevalent at the higher range of concentrations studied, as seen in Figures 4.3 to 4.6. The A peaks do not appear to shift at any concentration. From this observation, the reaction represented by Peaks C can be considered irreversible, while that represented by Peaks A is considered reversible.

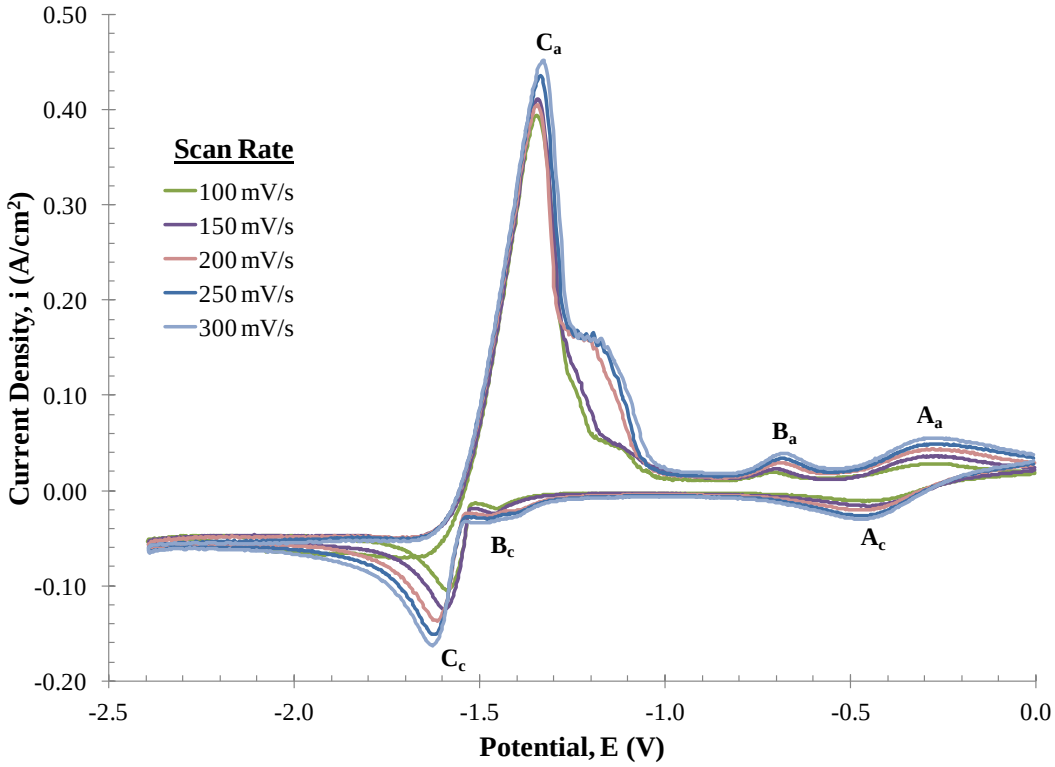

Figure 4.3 Cyclic voltammograms of 2.50 wt% UCl_3 in LiCl-KCl eutectic at 773 K.

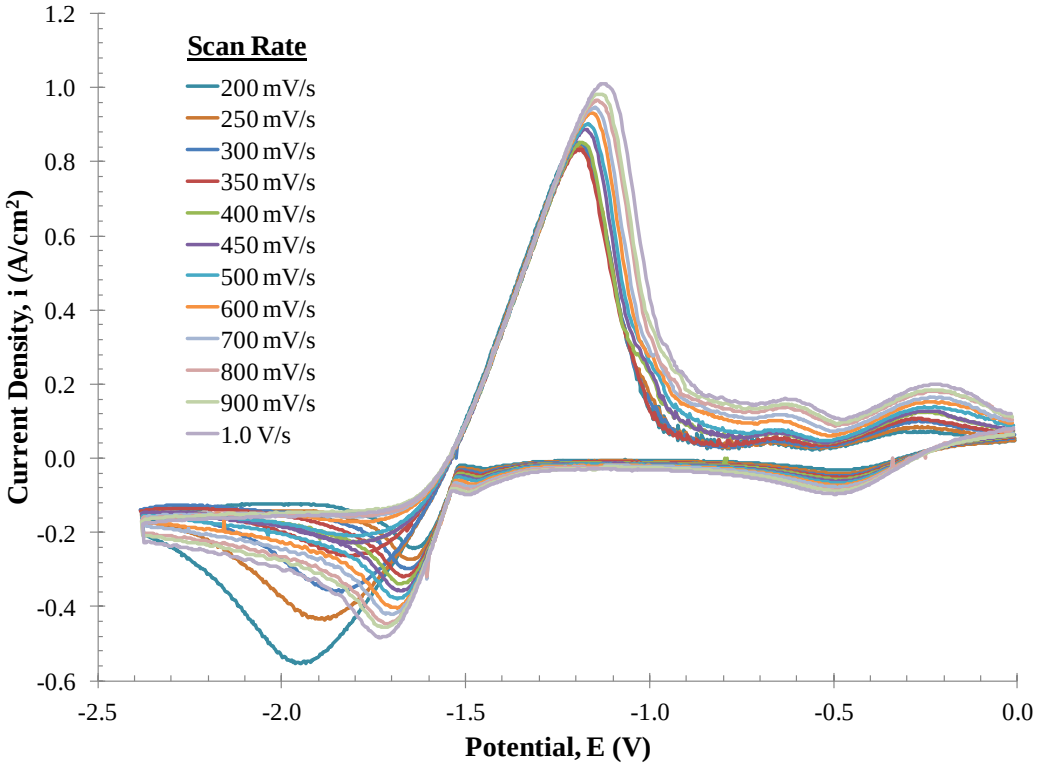

Figure 4.4 Cyclic voltammograms of 5.00 wt% UCl_3 in LiCl-KCl eutectic at 773 K.

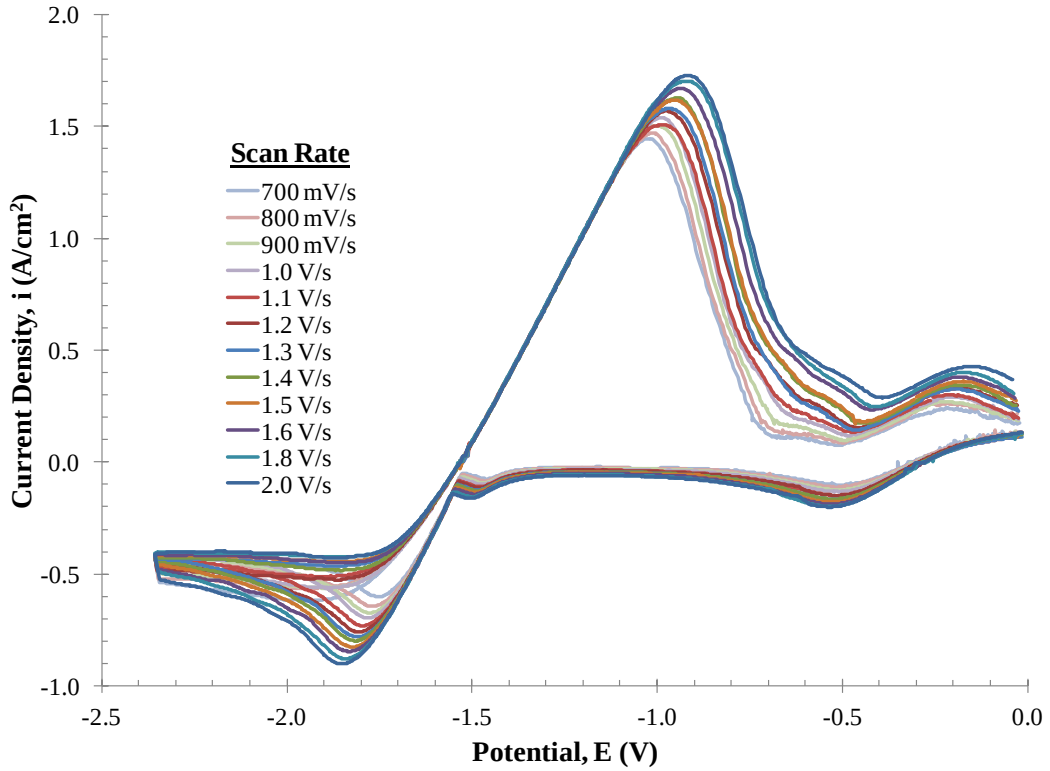

Figure 4.5 Cyclic voltammograms of 7.50 wt% UCl_3 in LiCl-KCl eutectic at 773 K.

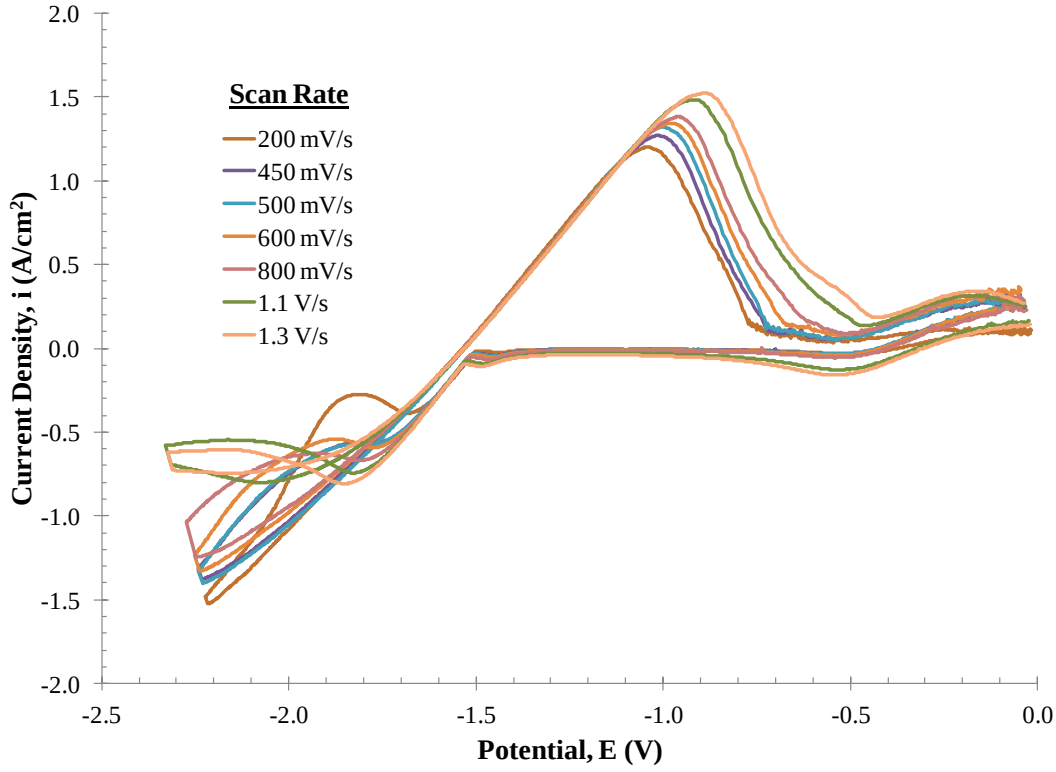

Figure 4.6 Cyclic voltammograms of 10.0 wt% UCl_3 in LiCl-KCl eutectic at 773 K.

The reactions likely represented by each peak as shown in the figures are determined through studies reported in the literature [37-39]. As the potential is scanned from 0.0 V vs. Ag/AgCl in the negative direction, the first reaction to occur is U(IV) being reduced to U(III), resulting in Peak A_c at approximately -0.5 V; that is,

$$A_c: \ U^{4+} + e^- \rightarrow U^{3+} \tag{4.1}$$

As the potential is scanned further in the negative direction, the U(III) present in the salt is most likely adsorbed to the working electrode surface resulting in Peak B_c at approximately -1.5 V [37]. Continuing further in the negative direction, the U(III) is reduced to uranium metal at approximately -1.6 V, which is

$$C_c: \ U^{3+} + 3e^- \rightarrow U, \tag{4.2}$$

At -2.4 V, the potential scan was reversed and the first oxidation reaction that occurs is shown by the large Peak C_a at approximately -1.4 V, which represents the oxidation of uranium metal to U(III); that is,

$$C_a: \ U \rightarrow U^{3+} + 3e^-. \tag{4.3}$$

Peak B_a at approximately -0.7 V corresponds to the adsorption Peak B_c. At the high end of the potential range, a final oxidation peak can be seen at approximately -0.3 V. This oxidation peak corresponds to the reduction Peak A_c and the oxidation of U(III) to U(IV) is represented by

$$A_a: \ U^{3+} \rightarrow U^{4+} + e^-. \tag{4.4}$$

Based on Eqs. (2.9), (2.10) and (2.15), in CV, the peak current should increase with increasing concentration for the same scan rate. This is evident in Figure 4.7, showing the cyclic voltammograms for different UCl_3 concentrations at two different scan rates.

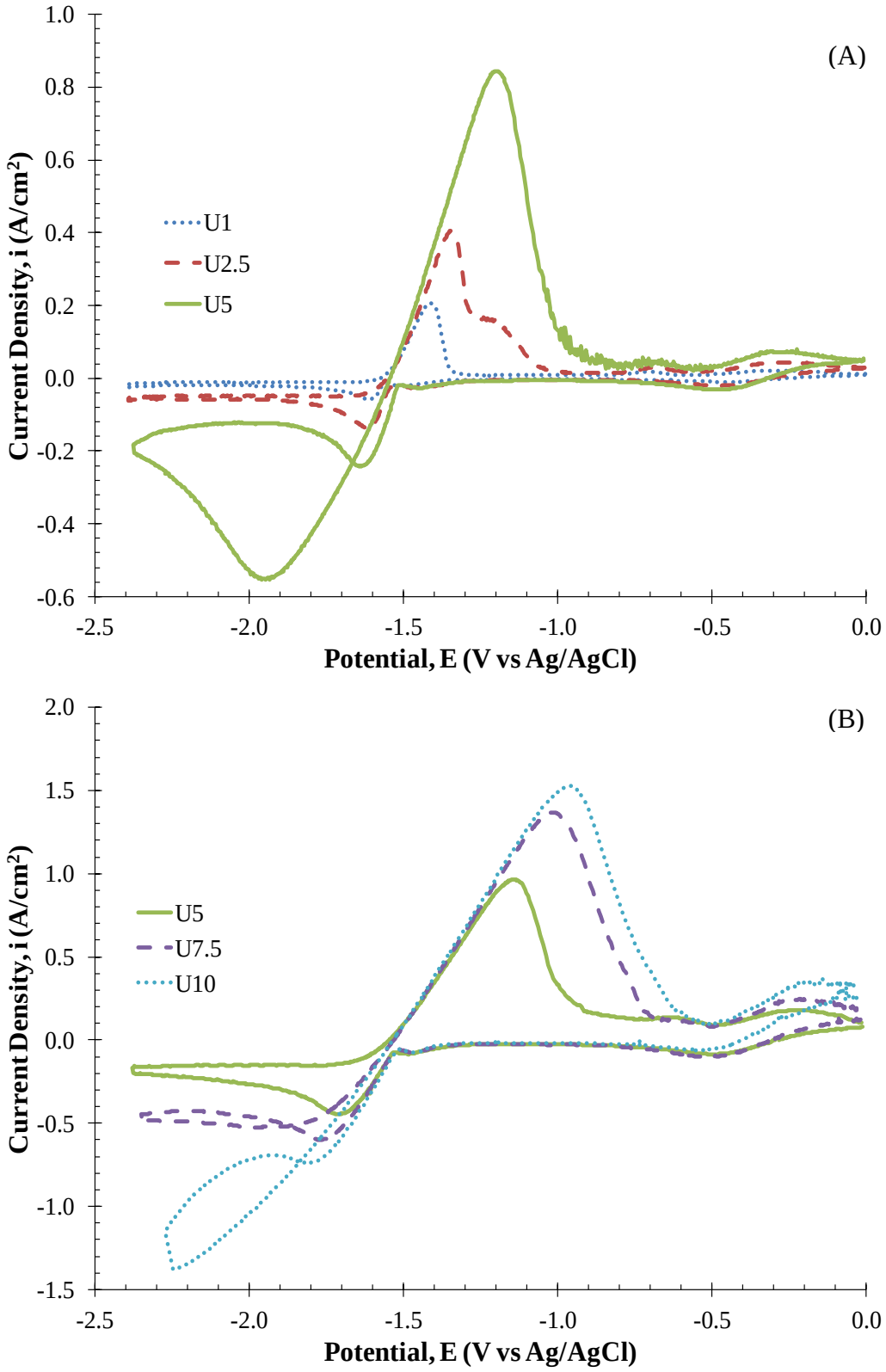

Figure 4.7 Effect of UCl_3 concentration on cyclic voltammograms at 773 K and scan rates of (A) 200 mV/s and (B) 800 mV/s.

4.1.2 Uranium Chronopotentiometry (CP)

CP was also performed on the five different UCl_3 salt compositions to determine the diffusion coefficient using the Sand Eq. (2.17). The resulting chronopotentiograms from the 2.50 wt% UCl_3 experiment at varying applied current densities are shown in Figure 4.8.

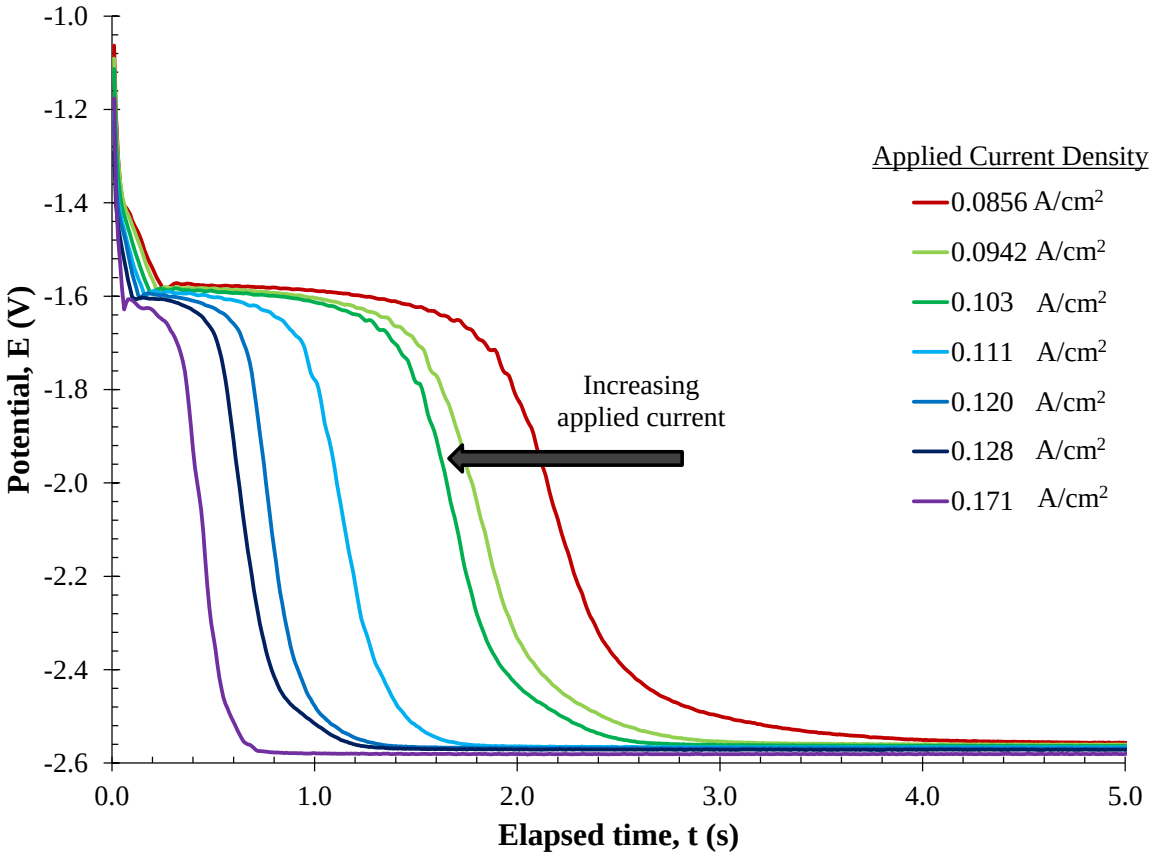

Figure 4.8 Chronopotentiograms for 2.50 wt% UCl_3 in LiCl-KCl eutectic salt at 773 K.

All chronopotentiograms have one clear plateau at approximately -1.6 V, which corresponds to Peak C_c in Figure 4.2. This plateau represents the diffusion and reduction of U(III) at the working electrode surface. The chronopotentiograms for the other UCl_3 concentrations studied exhibit similar behavior and appearances; therefore, the resulting plots are shown in Appendix D.

4.1.3 Uranium Anodic Stripping Voltammetry (ASV) and Concentration Detection Methods

Three different methods were examined to determine their usefulness in developing an *in-situ* electrochemical probe for molten salt concentration measurements: ASV peak height, CV anodic peak height, and CV cathodic peak height. In the ASV tests, plating time had a large effect on the peak heights, and the same plating times were not possible at all concentrations. At the higher concentrations (7.50 and 10.0 wt%), a 60 second plating time at -2.3 V vs. Ag/AgCl produced large deposits with no distinct stripping peak; therefore, a 5 second plating time was used. At the lower concentrations (1.00 and 2.50 wt%), a plating time of 5 seconds did not allow for enough reduction of material onto the working electrode to give a clear stripping peak. Due to these issues, a 60 second plating time was used for the 1.00, 2.50, and 5.00 wt% UCl_3 salt mixtures and a 5 second plating time was used for the 5.00, 7.50, and 10.0 wt% UCl_3 experimental runs. At least ten runs were performed at each concentration to develop a good average peak height. Figures of these peaks at each concentration are shown in Appendix E. The peak height was divided by the square root of the scan rate and plotted against UCl_3 concentration as shown in Eqs. (2.9), (2.10), and (2.15) in order to normalize the data at different scan rates. The anodic and cathodic U(III)/U redox couple CV peaks were also analyzed in the same manner. The adjusted peak current density at different concentrations for the ASV method is shown in Figure 4.9 while that for the CV anodic and cathodic peak height methods is shown in Figure 4.10.

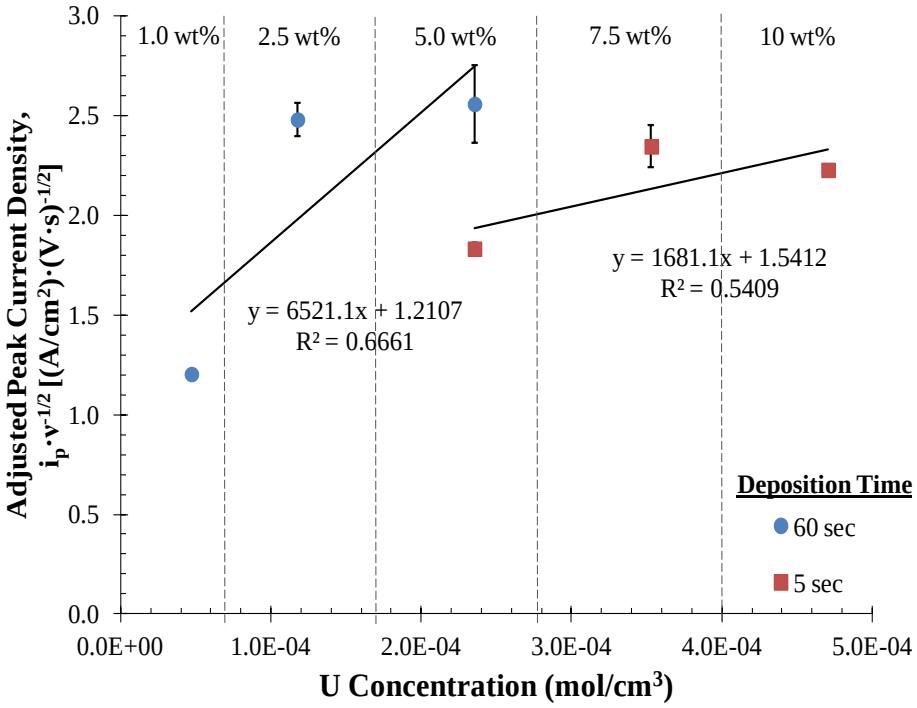

Figure 4.9 Peak current density divided by square root of the scan rate for the U(III)/U redox couple from ASV data at 773 K.

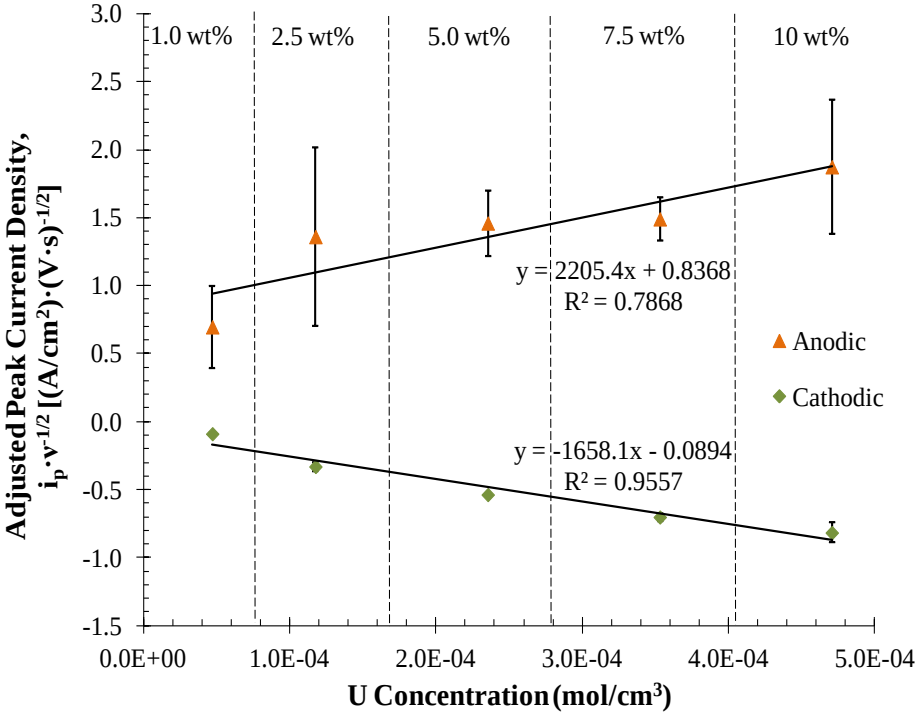

Figure 4.10 Peak current density divided by square root of the scan rate for the U(III)/U redox couple from CV anodic and cathodic peaks at 773 K.

The ASV peak data in Figure 4.9 is not linear, with coefficients of determination, R^2, of 0.666 and 0.541 for the low and high concentrations, respectively. Although the standard deviations are relatively low, the best linear fits clearly do not fit within these values. For these reasons, the ASV peak heights would be difficult to use as a predictor of UCl_3 concentration in the molten LiCl-KCl eutectic. The CV data in Figure 4.10, however, appears to be easier to use as a concentration detection method. Both the anodic and cathodic peaks fit a linear trend better than the ASV data, with higher R^2 values (0.787 and 0.956, respectively). Of the three sets of data, the cathodic peak current density from CV could be most accurately used to determine concentration, with a higher R^2 value and smaller standard deviations over the concentration range.

4.2 Uranium Thermodynamic and Electrochemical Properties

4.2.1 Uranium Diffusion Coefficient

Transition times, τ, related to the diffusion of U(III) ions were calculated for different concentrations and applied driving currents from the CP data sets (as shown in Figure 4.8 and Appendix D). To determine the applicability of the Sand equation, Eq. (2.17), and whether the reaction is mass transfer limited, the applied driving current density is plotted versus the inverse square root of the transition time in Figure 4.11.

The data results in straight lines for all the concentrations, as predicted by the Sand equation; therefore, it can be used to analyze the data. The average diffusion coefficient for each concentration was calculated showing no discernible trend with concentration, as listed in Table 4.1. To determine an approximate diffusivity, which can be used over the entire concentration range studied (1.0 - 10.0 wt% UCl_3), the mean diffusivity is calculated to be $(1.04 \pm 0.173) \times 10^{-5}$ cm^2/s for U(III).

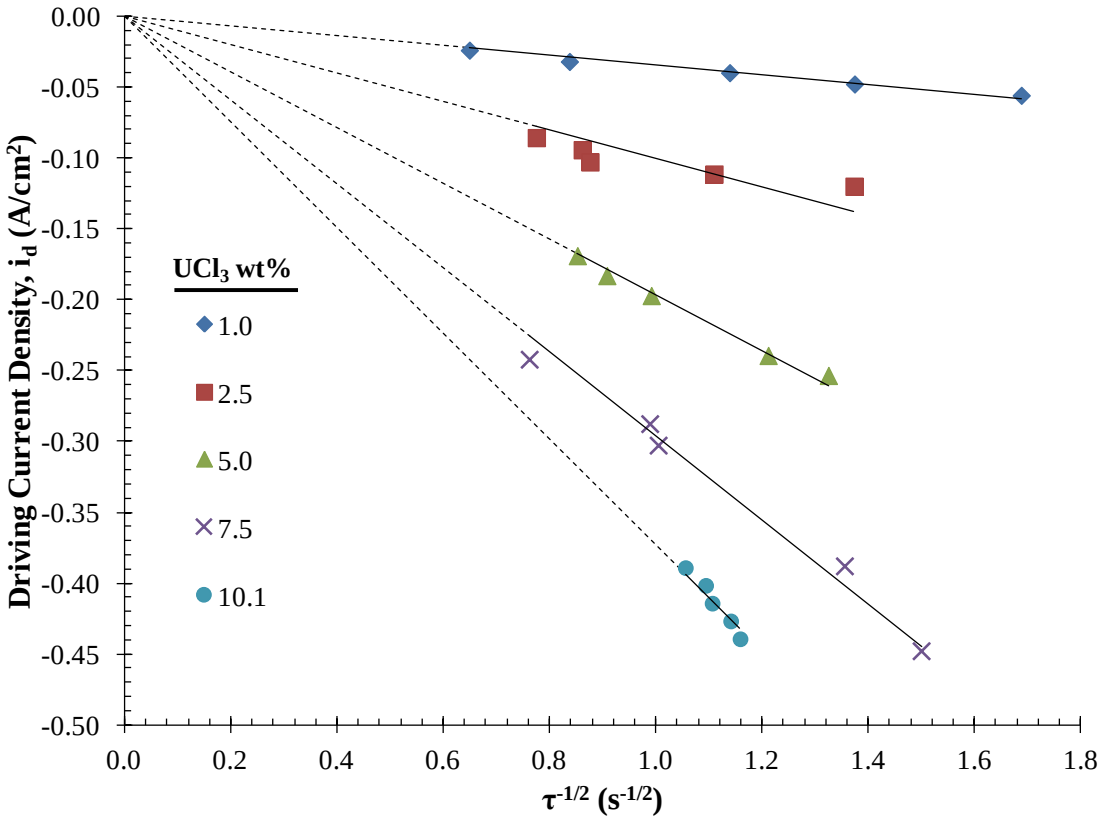

Figure 4.11 Analysis of chronopotentiograms using the Sand equation, Eq. (2.17).

The CV data can also be used to calculate the diffusivity of U(III) using Eq. (2.10) and the peak current density of Peak A_a. To determine the validity of the equation, the anodic peak current density, i_{pa}, is plotted against the square root of the scan rate, as shown in Figure 4.12, for the 1.00 wt% experiments. The data for Peak A_a is fairly linear with R^2 value of 0.987. Thus, the U(III)/U(IV) oxidation reaction can be considered mass transfer limited and Eq. (2.10) can be applied to calculate the diffusivity of U(III). This same analysis is shown in Appendix F for all concentrations. The calculated diffusion coefficients using Eq. (2.10) and the fitted slopes of the lines in Figure 4.12 with an assumption of one electron transfer are summarized in Table 4.1. The average $D_{U(III)}$ over the concentrations studied is $(3.28 \pm 0.849) \times 10^{-5}$ cm^2/s, which compares well with the value calculated from

the CP data. The resulting overall average $D_{U(III)}$ is $(2.16 \pm 0.430) \times 10^{-5}$ cm^2/s. This value falls within the previously published values ranging from 6.86×10^{-6} [54] to 1.0×10^{-4} cm^2/s [49] (see the listed values in Appendix B). A graphical comparison of the experimental results with those previously published values is shown in Figure 4.13.

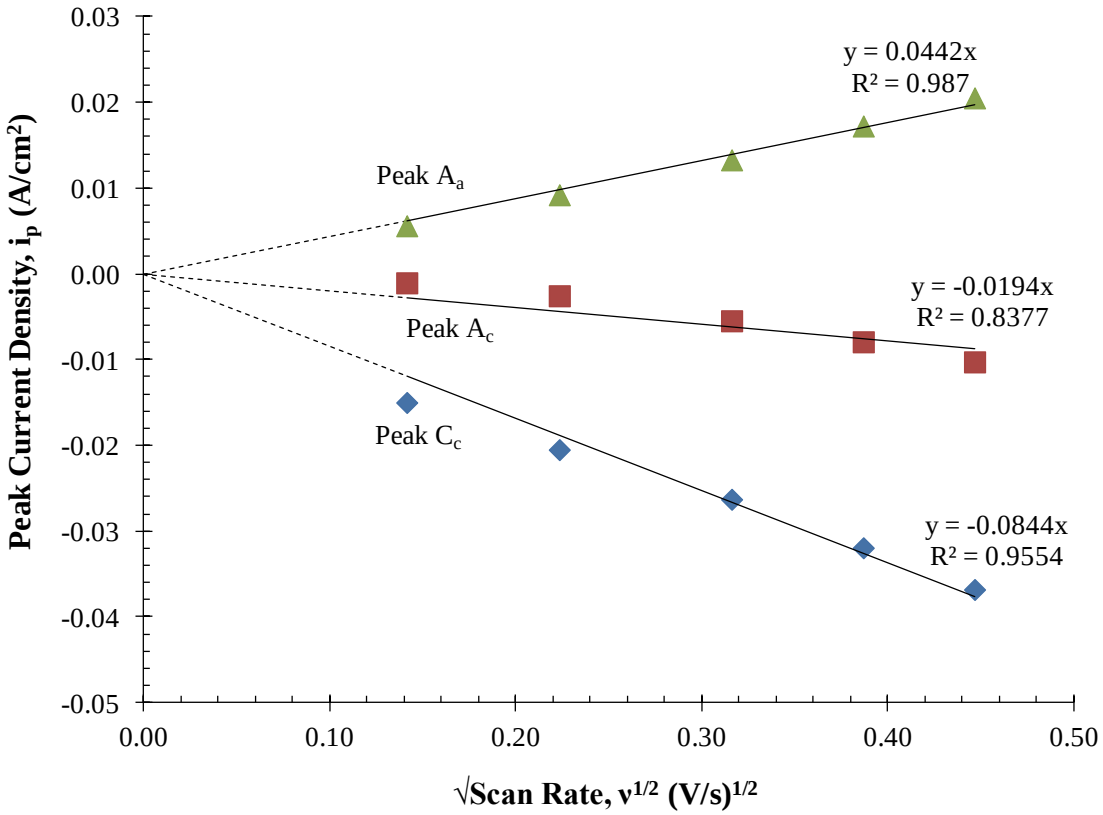

Figure 4.12 Peak current versus square root of scan rate for anodic and cathodic peaks in the 1.00 wt% UCl_3 CVs at 773 K.

The CP data set only provides information for the U(III)/U redox couple as the U(IV)/U(III) reaction occurs at a potential more positive than the open circuit potential. To determine the diffusivity of the U(IV) ion in the LiCl-KCl eutectic, the cyclic voltammogram data shown in Figures 4.2 through 4.6 can also be analyzed using the

Randles-Sevcik equation, Eq. (2.9), for the reversible U(IV)/U(III) redox couple. To determine the validity of the equation, the cathodic peak current densities, i_{pc}, are plotted against the square root of the scan rate, as seen in Figure 4.12, for the 1.00 wt% experiments. As the data is fairly linear with R^2 of 0.838 for the U(IV)/U(III) couple and R^2 value of 0.955 for the U(III)/U couple, the reactions can be considered mass transfer limited, and the Randles-Sevcik or Delahay equation can be applied. The linearity of the data is maintained at the higher concentrations as can be seen in Appendix F.

Table 4.1 U(III) diffusion coefficients at 773 K calculated from CP and CV experiments.

Concentration (wt%)	**Diffusion, $D_{U(III)}$ ($\times 10^5$ cm^2/s)**		
	CP, Eq. (2.17)	**CV, Eq. (2.10)**	**Average**
1.00	0.861 ± 0.0958	4.19	2.53 ± 2.35
2.50	1.23 ± 0.260	3.45	2.34 ± 1.57
5.00	1.07 ± 0.0409	3.77	2.42 ± 1.91
7.50	1.09 ± 0.0893	3.01	2.05 ± 1.36
10.0	0.944 ± 0.0246	1.97	1.46 ± 0.725
Average	**1.04 ± 0.173**	**3.28 ± 0.849**	**2.16 ± 0.430**

Using Eq. (2.9), the peak current density information for Peak A_c, with an assumption that one electron is transferred for the reaction, the diffusion coefficient for U(IV) in the LiCl-KCl eutectic at 773 K was calculated at each concentration as shown in Table 4.2. The resulting average value of $D_{U(IV)}$ was calculated to be $(1.26 \pm 0.6) \times 10^{-5}$ cm^2/s. This is a reasonable value for the liquid phase diffusion and is close to those reported in literature, ranging from 7.29×10^{-6} [39] to 2.73×10^{-5} [33] (all values are listed in Appendix B).

Table 4.2 U(IV) diffusion coefficients at 773 K calculated from cyclic voltammetry experiments.

Concentration (wt%)	1.00	2.50	5.00	7.50	10.0	Average
$D_{U(IV)}$ ($\times 10^5$ cm^2/s)	1.92	1.89	0.930	0.942	0.620	**1.26 ± 0.604**

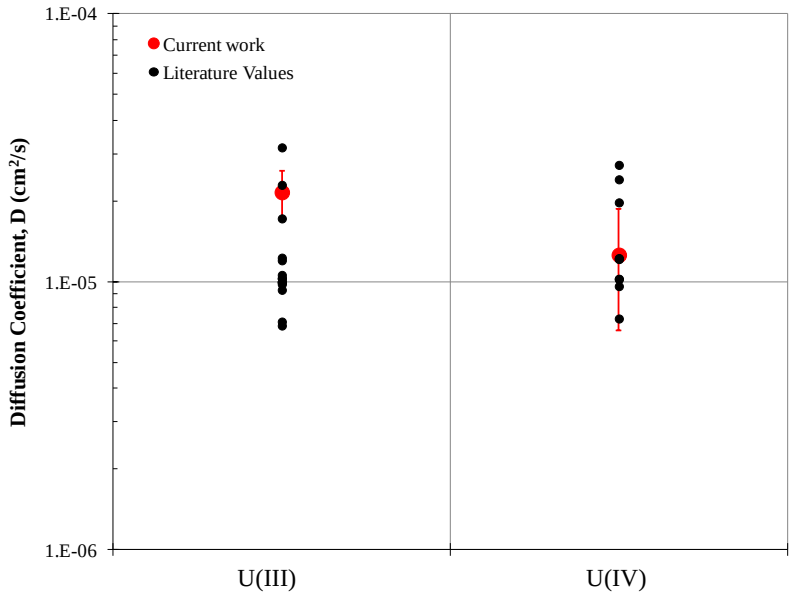

Figure 4.13 Comparison of experimental and previously published values for the diffusivity of uranium ions in the LiCl-KCl eutectic at 773 K.

4.2.2 Uranium Apparent Standard Reduction Potential

As discussed previously in Section 2.2.1, from the CV data, the equilibrium potential, E, can be calculated using the average peak potential of a given pair of anodic/cathodic peaks. This was done for the A peaks (U(IV)/U(III) redox couple) for all concentrations (1.00 wt & to 10.0 wt%) and scan rates (20 mV/s to 2 V/s). Then the diffusion coefficients calculated previously were substituted into Eq. (2.11) to find the apparent standard reduction potential of the U(IV)/U(III) couple. From this analysis, the mean apparent standard potential of the U(IV)/U(III) couple is found to be (-0.386 ± 0.012) V vs. 5 mol% Ag/AgCl. To better compare with published data using different reference

electrodes, this is converted to the Cl_2/Cl^- reference. Using the Ag/AgCl data from Yang and Hudson [48], the apparent standard reduction potential of the U(IV)/U(III) redox couple is (-1.453 ± 0.012) V vs. the Cl_2/Cl^- reference. This compares well with published data, which range from -1.428 V [53] to -1.51 V [38]. Figure 4.14 shows a graphical comparison between the experimental and the reported literature values.

For the U(III)/U couple the Peak C_c potentials from the CV, the average diffusion coefficient and Eq. (2.16) were used to calculate the apparent standard reduction potential. The standard rate constant value of $k_s = 2.6 \times 10^{-4}$ cm/s from Kuznetsov and co-workers [38] was also used in this calculation. For all scan rates and concentrations, the mean value of the apparent standard potential for the U(III)/U redox couple is (-1.486 ± 0.075) V vs. 5 mol% Ag/AgCl. When converted using the data from Ref. [48], this becomes (-2.552 ± 0.075) V vs. the Cl_2/Cl^- reference electrode. Literature values of the U(III)/U couple vary from -2.31 to -2.532 V [39, 51] at 773 K (see Figure 4.14).

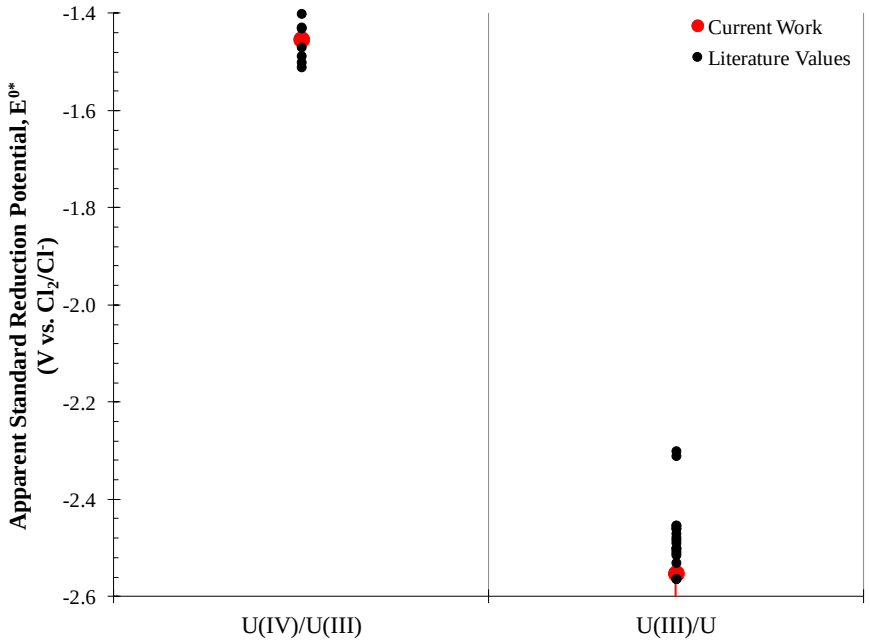

Figure 4.14 Comparison of experimental and previously published values for the apparent standard reduction potentials of uranium in the LiCl-KCl eutectic at 773 K.

4.2.3 Uranium Activity Coefficient

The activity coefficient, γ, is a 'correction factor' used in order to take account of deviations from solution ideality in the liquid phase. It is a measure of the excess energy of a solution. The activity coefficient in solution can be determined through a comparison of the actual, or experimental, Gibbs free energy, Δg^{0*}, of the oxidation reaction and the theoretical ideal Gibbs free energy, Δg_{id}^{0}, of the same reaction,

$$\Delta g^{0*} - \Delta g_{id}^{0} = RT \ln \gamma , \tag{4.5}$$

which is related to the excess Gibbs energy of the solution, Eq. (2.5). The Gibbs free energy and potential are directly related through

$$\Delta g = -nFE . \tag{4.6}$$

The results of this depend largely upon the thermodynamic data used for the theoretical Gibbs free energy. Reported ideal state thermodynamic data for uranium chlorides is summarized in Table 4.3 along with the corresponding activity coefficient calculated from the experimental data and Eq. (4.5).

Table 4.3 Ideal state thermodynamic data for uranium [24, 35, 39, 65] and corresponding calculated activity coefficients.

UCl_4			**UCl_3**		
Δg^{0*} (kJ/mol)	Δg_{id}^{0} (kJ/mol)	γ	Δg^{0*} (kJ/mol)	Δg_{id}^{0} (kJ/mol)	γ
-140.2 ± 1.158	-110.6 [39]	0.0100 ± 0.00180	-738.7 ± 21.71	-683.95 [39]	$(2.00 \pm 6.75) \times 10^{-4}$
	-100.793 [65]	0.00218 ± 0.000392		-693.798 [65]	$(9.26 \pm 31.3) \times 10^{-4}$
	-106.326 [24]	0.00515 ± 0.000927		-679.6 [35]	$(1.02 \pm 3.43) \times 10^{-4}$
				-721.901 [24]	0.0734 ± 0.248

As can be seen, these activity coefficient values vary greatly depending on the ideal state thermodynamic data used in Eq. (4.5). The possible values for both UCl_4 and UCl_3 range several orders of magnitude depending on the data used, from 0.00234 to 0.0108 and 4.94×10^{-5} to 0.0358, respectively. The values for UCl_4 generally compare well with the published value of 0.0148 [39]. For UCl_3, most of the experimental values are slightly smaller than published values, ranging from 0.00139 [39] to 0.169 [66]. The values shown in Table 4.3 are compared to the published values in Figure 4.15. Due to the large range of possible activity coefficient values, it is recommended that the experimental apparent standard reduction potential, E^{0*}, which includes the effect of the activity coefficient as shown in Eq. (2.12), to be used as well. Using the apparent standard reduction potential in place of the standard reduction potential and activity coefficient removes any uncertainty in the thermodynamic database used to calculate the activity coefficient.

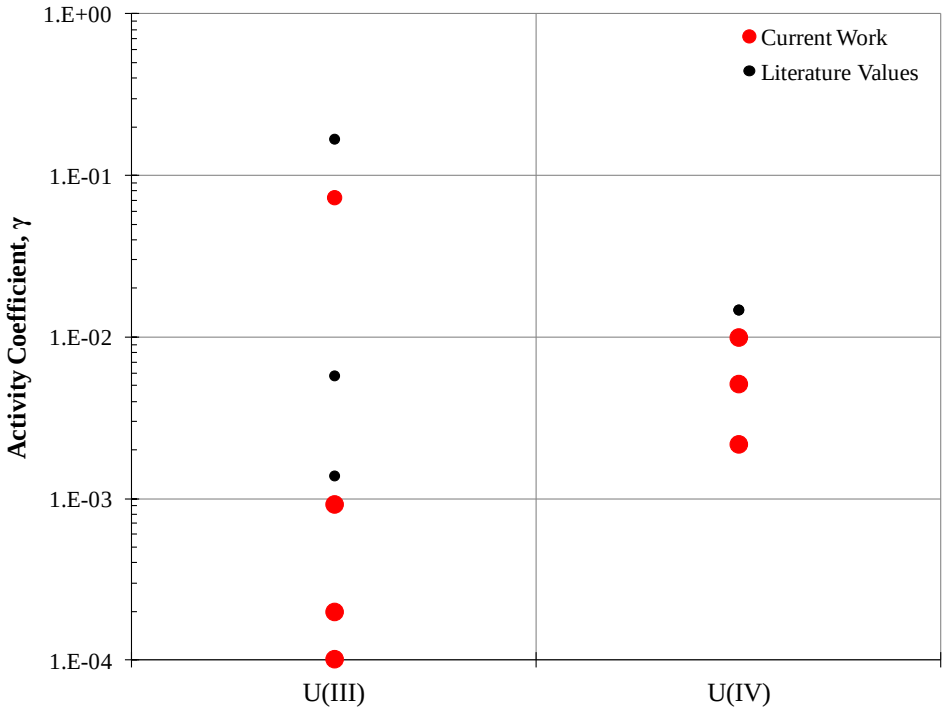

Figure 4.15 Comparison of experimental and previously published values for the activity coefficients of uranium in the LiCl-KCl eutectic at 773 K.

4.3 Zirconium Electrochemistry

Electrochemical experiments were also performed with $ZrCl_4$ at various concentrations (0.57, 1.07, 2.49, and 4.98 wt%) and temperatures (723, 773, and 823 K) to determine the effects of both concentration and temperature on the behavior of Zr in the molten LiCl-KCl eutectic salt. The four zirconium concentration studies are summarized in Table 3.2. Photos of the four salt ingots following the experiments are shown in Figure 4.16. The ingots are all light brown in color, approximately 5 cm tall, with a diameter of 3.3 cm.

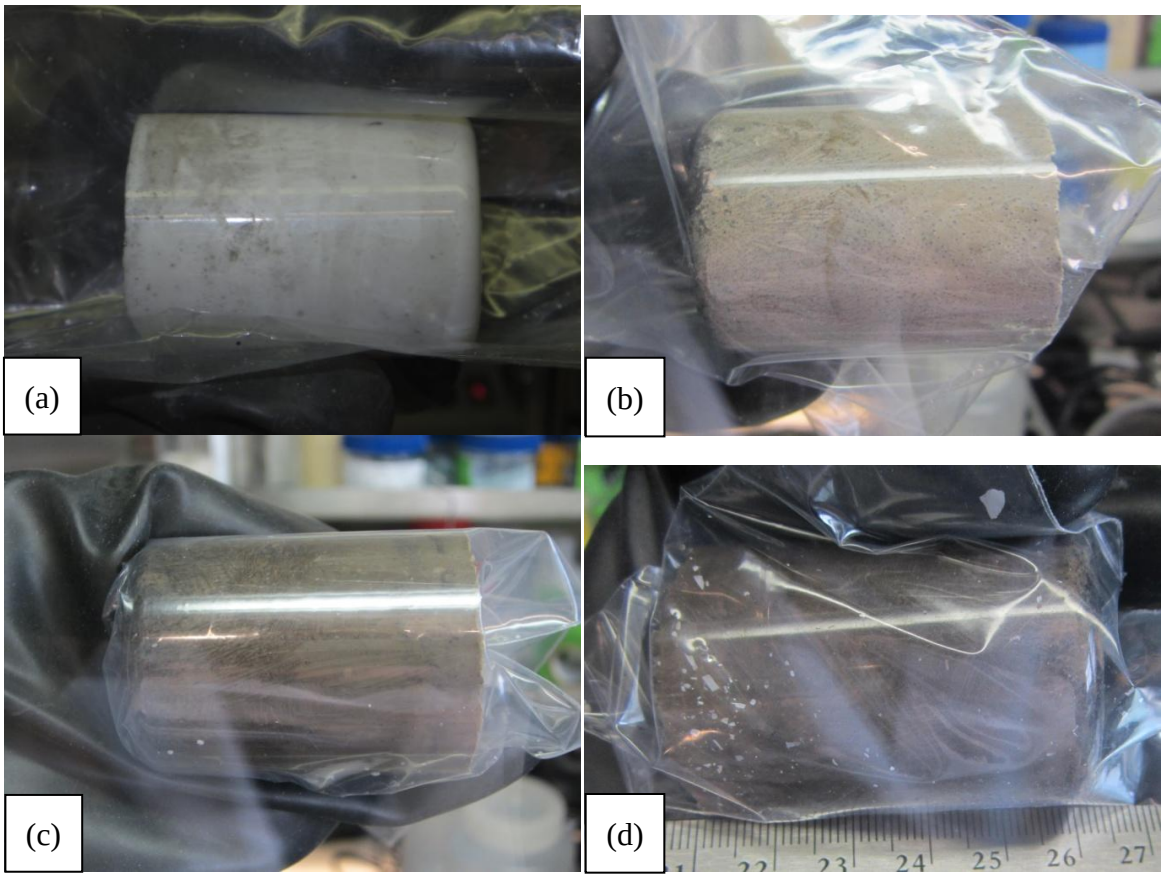

Figure 4.16 Photos of the four $ZrCl_4$ salt ingots following electrochemical experiments: (a) 0.57 wt% $ZrCl_4$, (b) 1.07 wt% $ZrCl_4$, (c) 2.49 wt% $ZrCl_4$, and (d) 4.98 wt% $ZrCl_4$.

4.3.1 Zirconium Cyclic Voltammetry (CV)

Cyclic voltammograms of 1.07 wt% $ZrCl_4$ at 723, 773, and 823 K and scan rates of 300 and 350 mV/s were recorded as shown in Figure 4.17. CVs for all concentrations (0.57, 1.07, 2.49, and 4.98 wt% $ZrCl_4$) and temperatures (723, 773 and 823 K) show similar complex behavior; these plots are shown in Appendix G.

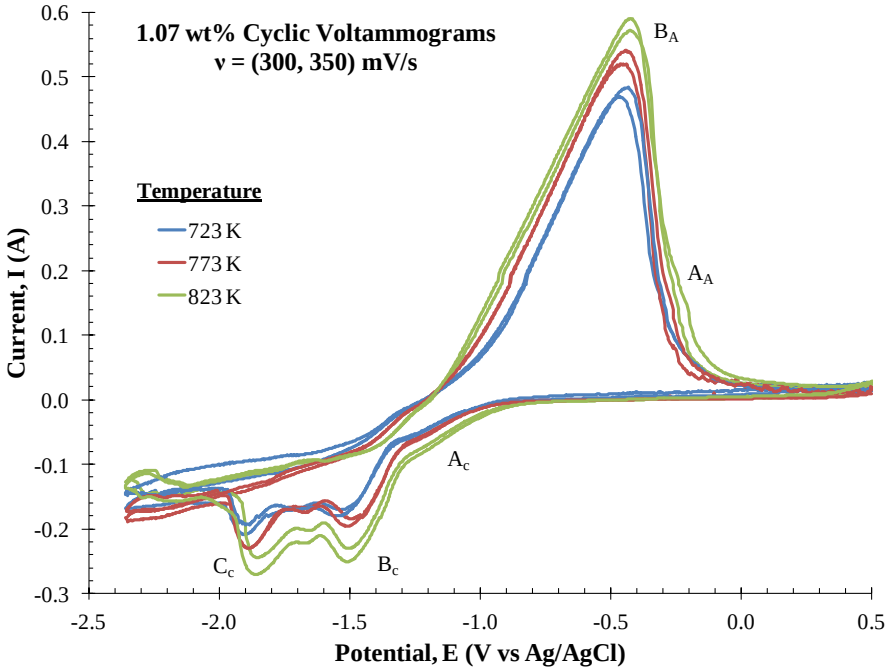

Figure 4.17 Cyclic voltammograms of 1.07 wt% $ZrCl_4$ in the molten LiCl-KCl eutectic at 723, 773, and 823 K.

The 1.07 wt% $ZrCl_4$ CVs show three cathodic peaks (A_c, B_c, and C_c) and two anodic peaks (A_a and B_a). It is clear that the peak potential shifts slightly negative for the reduction peaks and positive for the oxidation peaks with increasing scan rate. This shows that the reactions must be considered irreversible.

Peak identification has been performed through a review of the literature [30, 47]. As the potential is scanned from 0.5 V in the negative direction, the first reaction to occur is Zr(IV) being reduced to Zr(II), resulting in Peak A_c at approximately -1.06 V, which is

$$A_c: \quad Zr^{4+} + 2e^- \rightarrow Zr^{2+}. \tag{4.7}$$

As the potential is scanned further in the negative direction Zr(II) may be reduced to Zr metal while some remaining Zr(IV) may be reduced to insoluble ZrCl, resulting in Peak B_c at approximately -1.5 V; these are

$$B_c: \quad Zr^{2+} + 2e^- \rightarrow Zr \tag{4.8}$$

$$Zr^{4+} + 3e^- + Cl^- \rightarrow ZrCl. \tag{4.9}$$

Continuing further in the negative direction, both ZrCl and Zr(IV) are fully reduced to Zr metal at approximately -1.85 V,

$$C_c: \quad ZrCl + e^- \rightarrow Zr + Cl^- \tag{4.10}$$

$$Zr^{4+} + 4e^- \rightarrow Zr. \tag{4.11}$$

At -2.4 V, the potential scan was reversed and the first oxidation reactions that may occur are shown by the large Peak B_a at approximately -0.5 V.

$$B_a: \quad Zr \rightarrow Zr^{4+} + 4e^- \tag{4.12}$$

$$Zr \rightarrow Zr^{2+} + 2e^-. \tag{4.13}$$

The small hump on the shoulder of Peak B_a, marked A_a, is likely the oxidation of Zr(II) to Zr(IV).

$$A_a: \quad Zr^{2+} \rightarrow Zr^{4+} + 2e^-. \tag{4.14}$$

Some work in the past has shown up to three distinct anodic peaks [30] depending upon the scan range used. If a narrower potential range was used, not all ZrCl is fully reduced to Zr metal and an anodic peak just negative of Peak B_a is seen corresponding to:

$$ZrCl \rightarrow Zr^{4+} + 3e^- + Cl^- \tag{4.15}$$

$$ZrCl \rightarrow Zr^{2+} + e^- + Cl^-. \tag{4.16}$$

The effects of concentration at the three different temperatures can be seen in Figures 4.18 to 4.20. It can be seen that, as expected, with increasing concentration, the peak heights increase and cathodic peak potentials shift in the negative direction. That is, higher current density results from higher bulk concentration due to increased mass transfer rates. Peak C_c is not clearly observed at 0.57 wt% $ZrCl_4$ in comparison to the other concentrations. This leads to the conclusion that, at this low concentration, ZrCl is either not formed at the electrode surface as in Eq. (4.9), or ZrCl is formed, but it is not reduced to Zr metal via Eq. (4.10). The effect of temperature can also be examined in Figures 4.21 to 4.23. As temperature is increased, the effect appears qualitatively similar to increasing concentration—peak heights increase and peak potentials shift in the negative direction. It can be seen that temperature may be used to enhance the peak detection for low concentration studies. For example, Peak A_c becomes more prominent as temperature increases (see Figure 4.21).

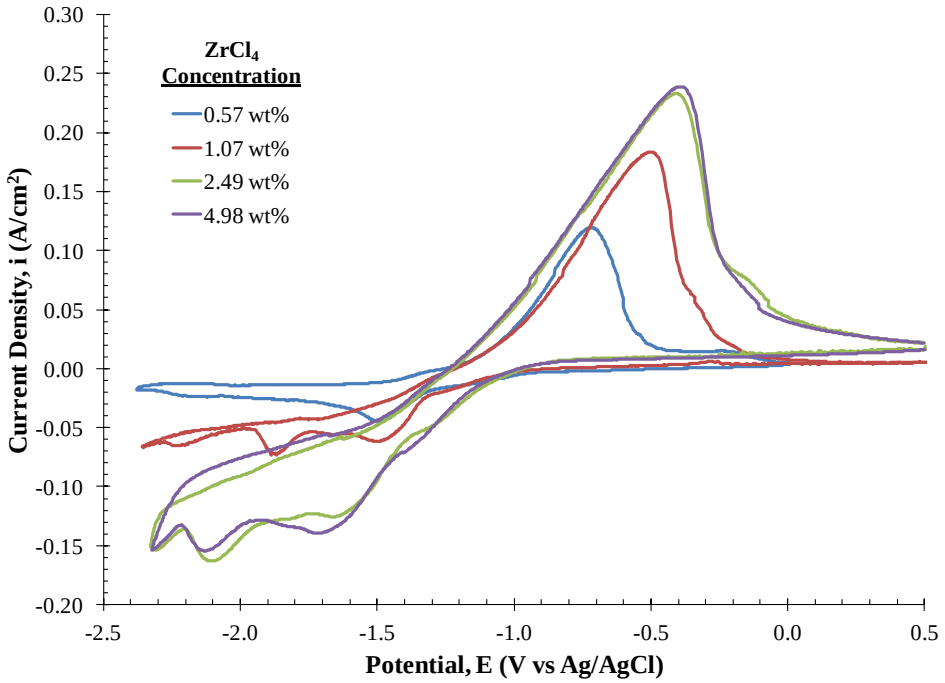

Figure 4.18 The effect of concentration on CV at T = 723 K and ν = 200 mV/s.

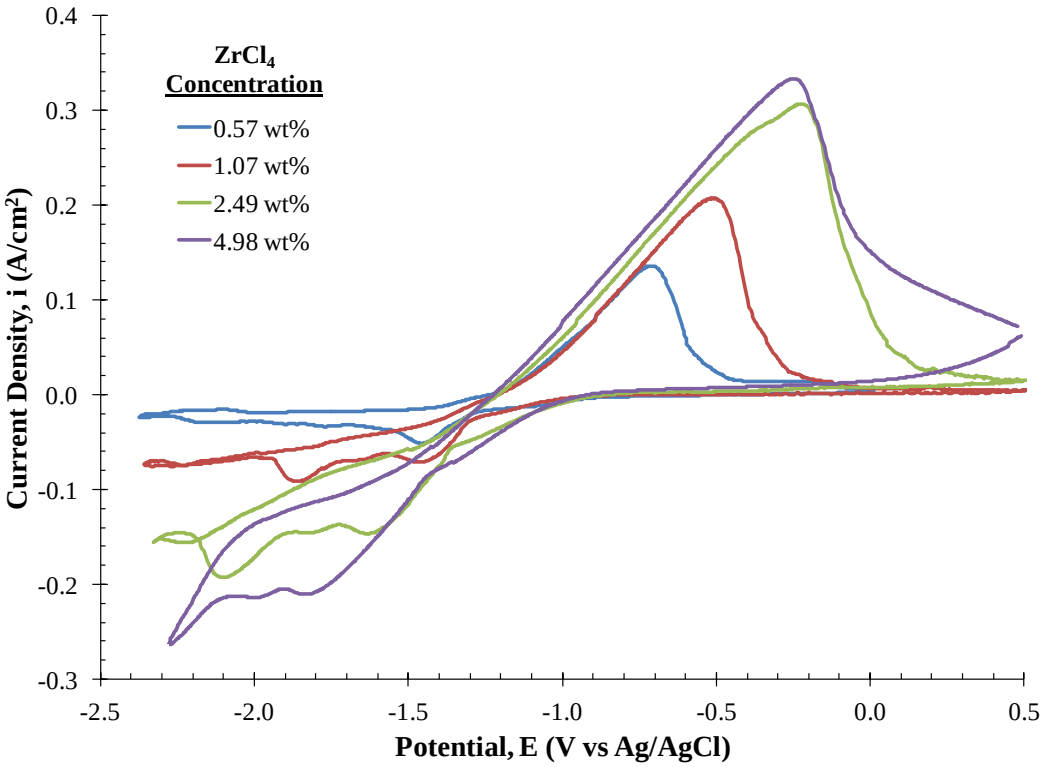

Figure 4.19 The effect of concentration on CV at T = 773 K and ν = 200 mV/s.

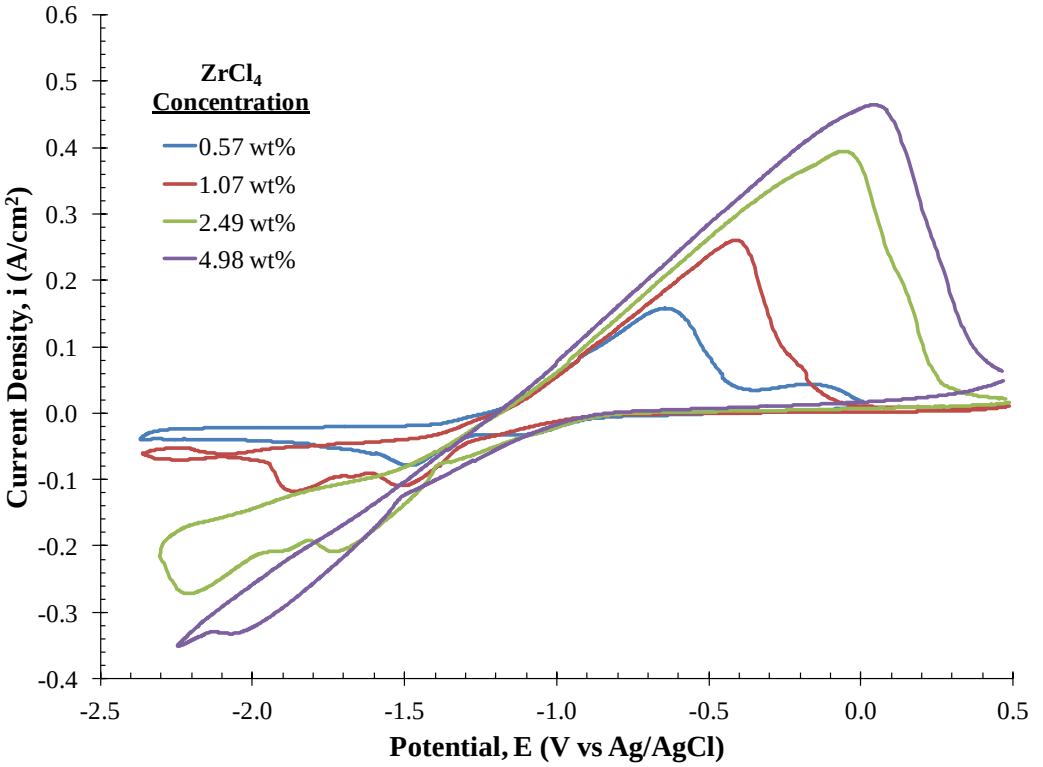

Figure 4.20 The effect of concentration on CV at T = 823 K and ν = 400 mV/s.

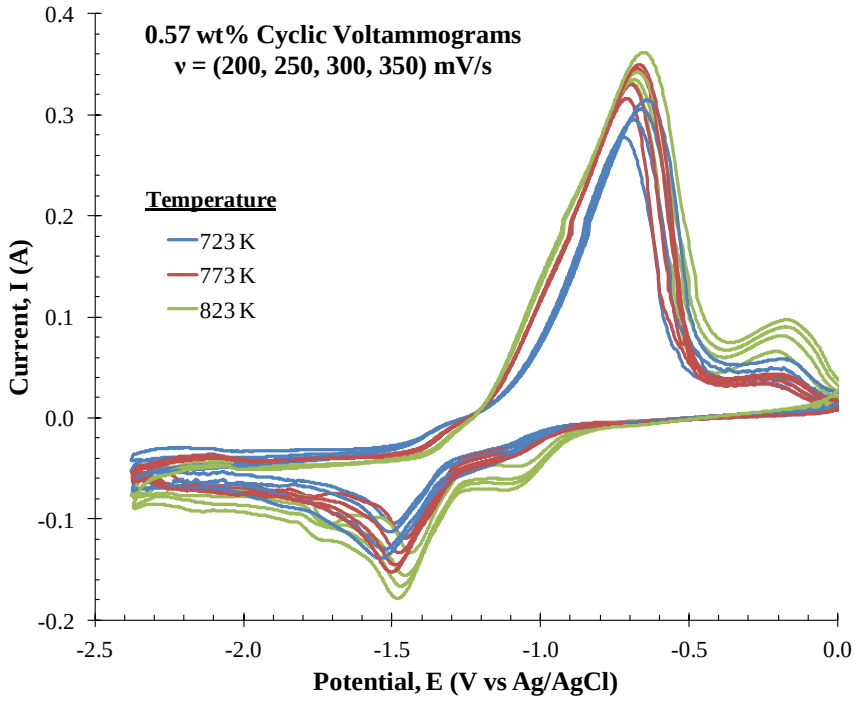

Figure 4.21 CVs of 0.57 wt% $ZrCl_4$ in LiCl-KCl eutectic at 723, 773, and 823 K and scan rates, ν = (200, 250, 300, and 350) mV/s.

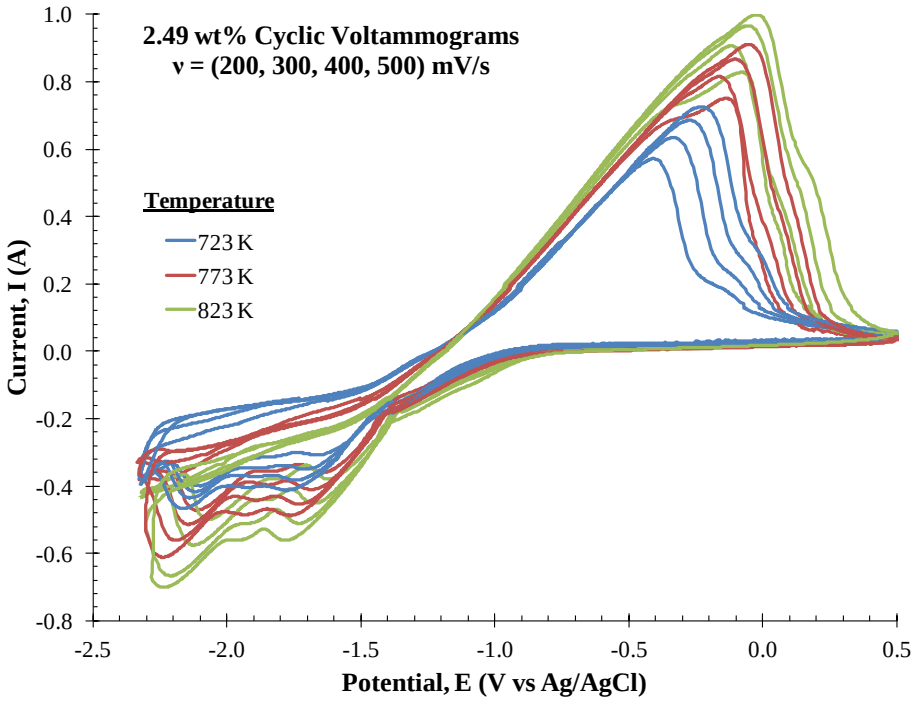

Figure 4.22 CVs of 2.49 wt% $ZrCl_4$ in LiCl-KCl eutectic at 723, 773, and 823 K and scan rates, ν = (200, 300, 400 and 500) mV/s.

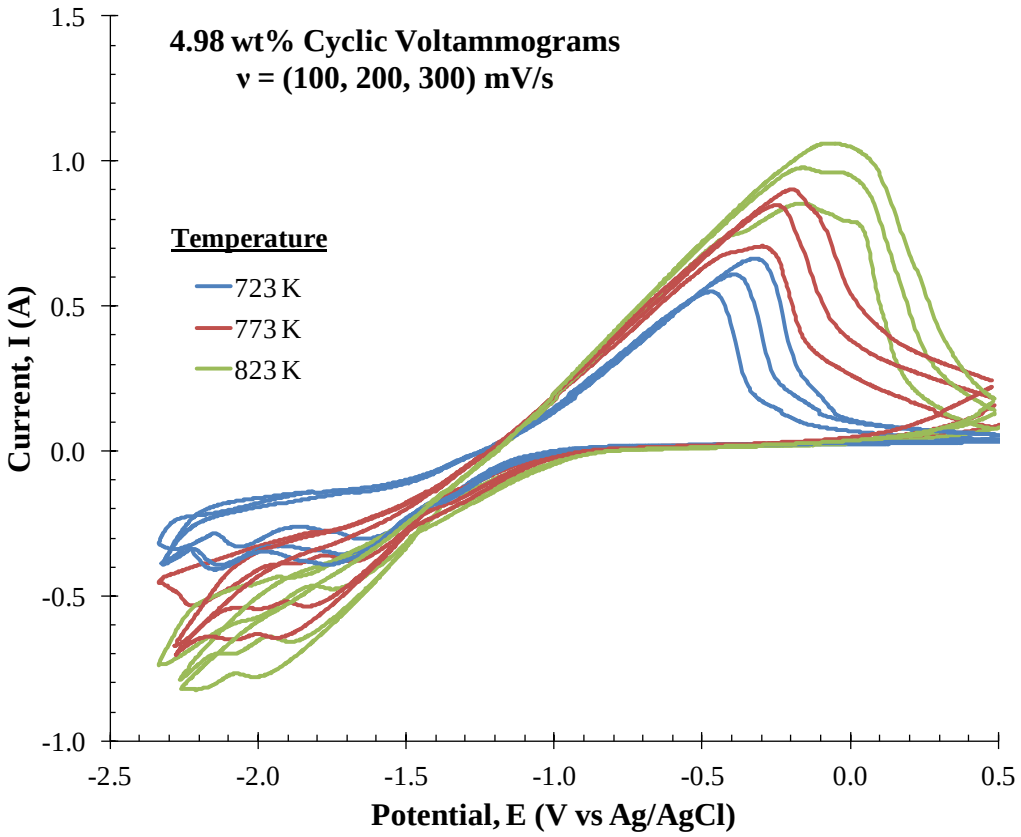

Figure 4.23 CVs of 4.98 wt% $ZrCl_4$ in LiCl-KCl eutectic at 723, 773, and 823 K and scan rates, ν = (100, 200 and 300) mV/s.

4.3.2 Zirconium Chronopotentiometry (CP)

CP was also performed on the four different $ZrCl_4$ salt compositions at three temperatures. As a typical example, the resulting chronopotentiograms for the 0.57 wt% $ZrCl_4$ salt mixture at 823 K and various applied driving current densities are shown in Figure 4.24.

As can be seen in the chronopotentiograms, there are several plateaus corresponding to the different reactions that can occur in the LiCl-KCl eutectic. The first plateau at approximately -1.3 V likely corresponds to Peak B_c in the cyclic voltammograms as shown in Figure 4.17, and therefore likely represents the diffusion limited reaction of Zr(II)/Zr, and

thus the diffusion of Zr(II). The second plateau at approximately -1.7 V most likely corresponds to Peak C_c in the CVs (see Figure 4.17), and the reduction of ZrCl to Zr. The chronopotentiograms for the other $ZrCl_4$ concentrations are similar and are shown in Appendix H. It is important to note that larger driving currents were required for the higher concentrations and higher temperatures. For both of these situations, the mass transfer is increased and faster reaction rates are required at the electrode surface to ensure diffusion limited reduction.

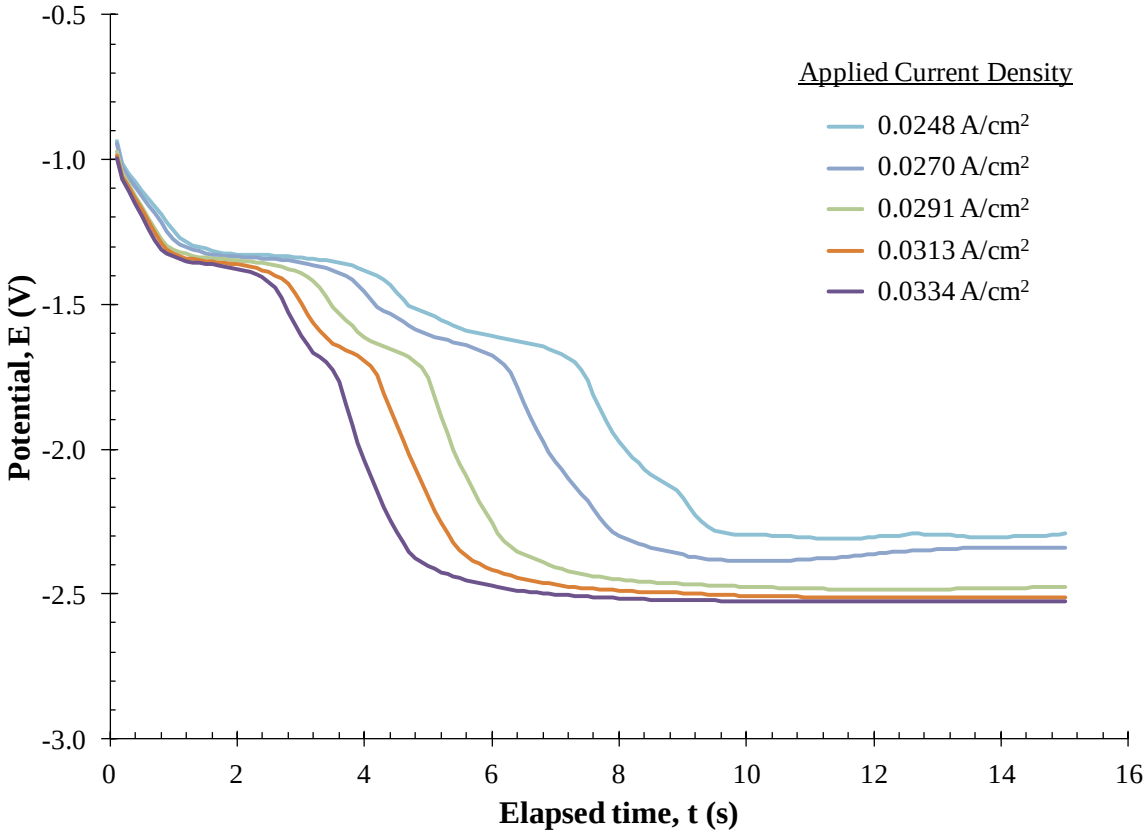

Figure 4.24 Chronopotentiograms for 0.57 wt% $ZrCl_4$ in LiCl-KCl eutectic salt at 823 K.

4.3.3 Zirconium Anodic Stripping Voltammetry (ASV) and Concentration Detection Methods

As with the uranium concentration studies, zirconium concentration measurements were studied using ASV peak height and anodic and cathodic CV peak heights at 773 K. Due to the smaller range of concentrations studied with zirconium, one single plating time of 60 seconds was sufficient for each concentration. For each of the four concentrations ten ASV tests were performed, from which an average and standard deviation were determined. The anodic stripping voltammograms are available and shown in Appendix I. Plots of the peak current divided by square root of the scan rate versus the zirconium concentration at 773 K for ASV and CV peaks are illustrated in Figures 4.25 and 4.26.

Similar to the U experimental results, cathode peak data from cyclic voltammetry appears to be the most precise method with smaller standard deviations and a larger coefficient of determination for the studied concentration range. For this reason, ASV data was not prepared and analyzed for 723 and 823 K. Our focus has been emphasized on the concentration curves using CV anode and cathode peaks for these two temperatures. The results are displayed in Figures 4.27 and 4.28, respectively.

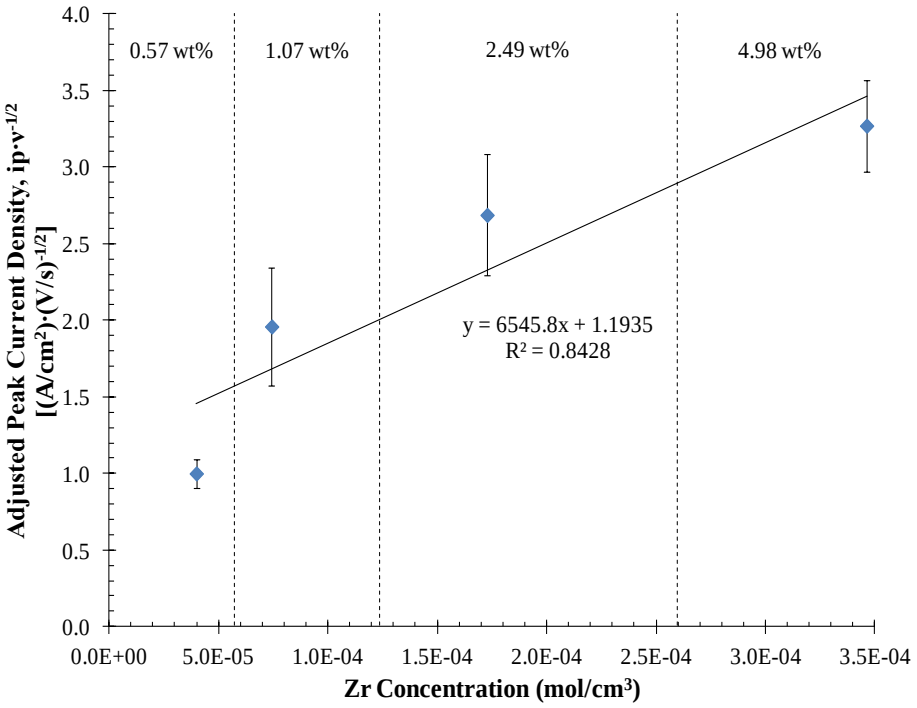

Figure 4.25 Peak current density divided by square root of the scan rate for the Zr(II)/Zr redox couple from ASV data at 773 K.

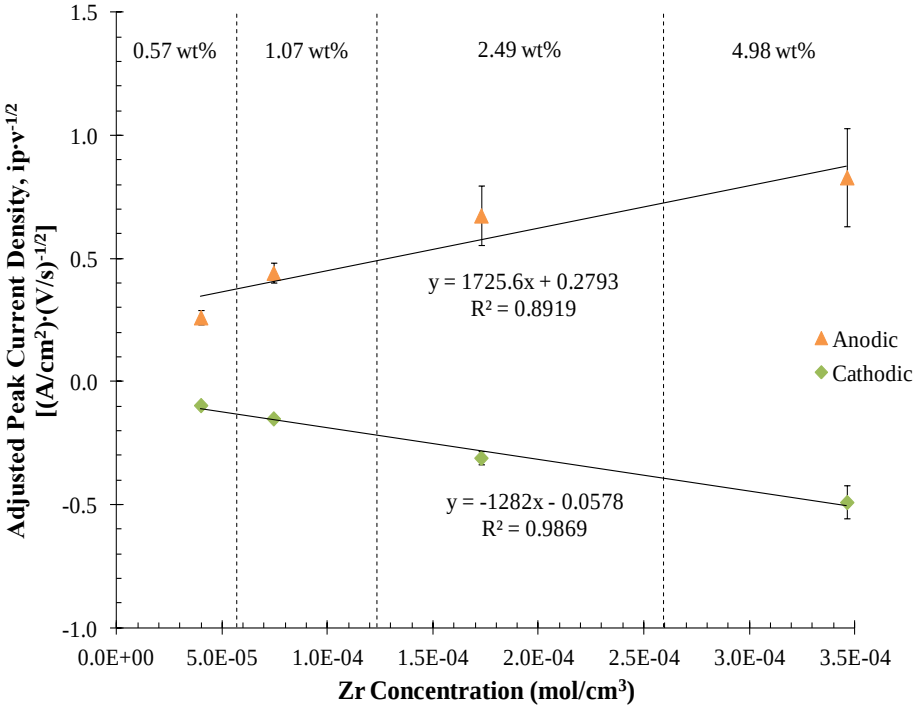

Figure 4.26 Peak current density divided by square root of the scan rate for the Zr(II)/Zr redox couple from CV anodic and cathodic peaks at 773 K.

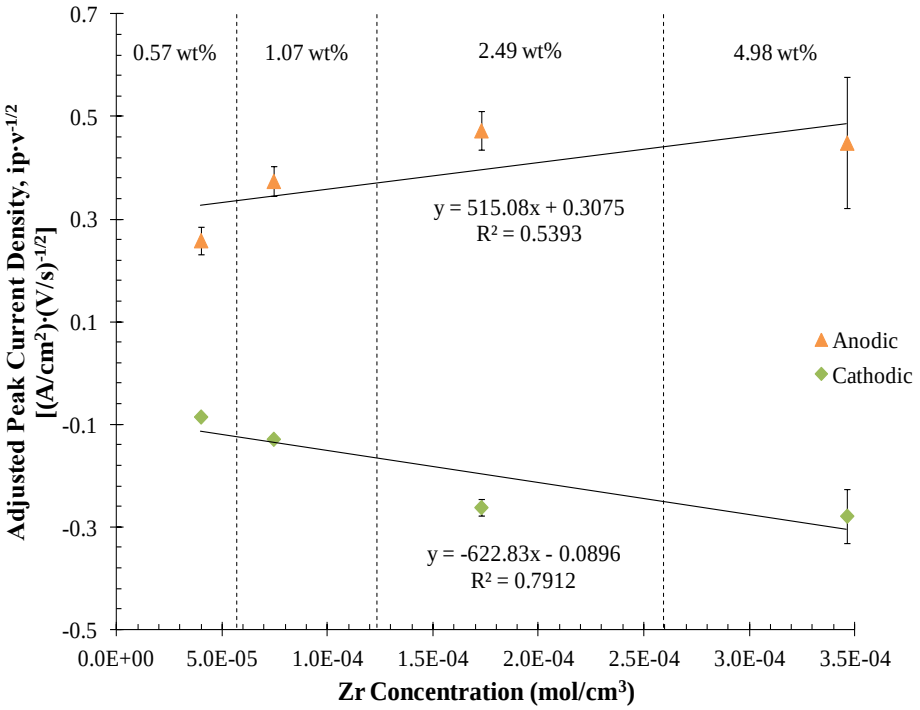

Figure 4.27 Peak current density divided by square root of the scan rate for the Zr(II)/Zr redox couple from CV anodic and cathodic peaks at 723 K.

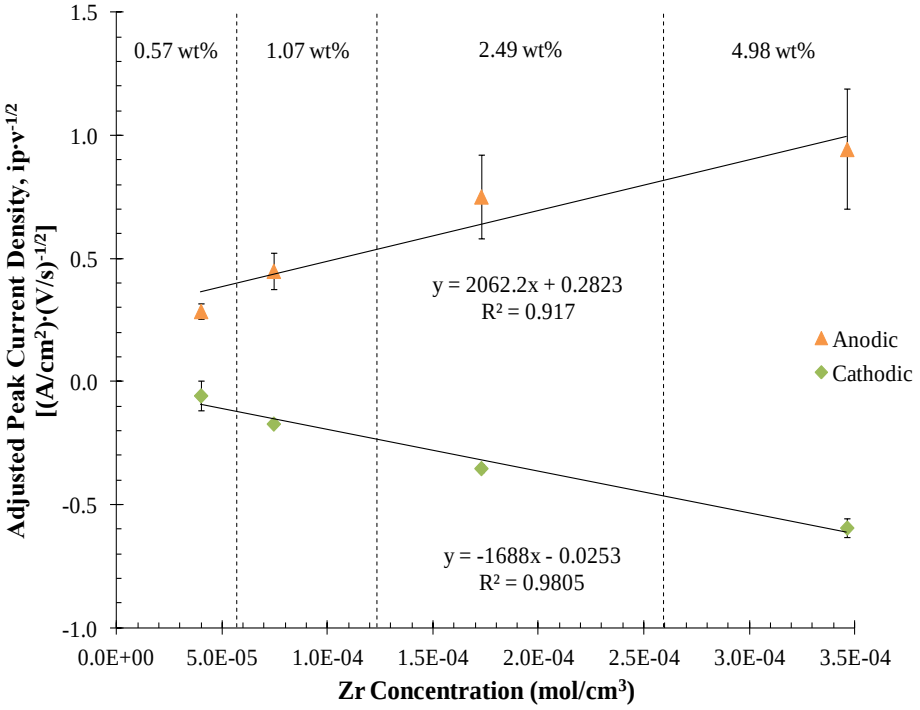

Figure 4.28 Peak current density divided by square root of the scan rate for the Zr(II)/Zr redox couple from CV anodic and cathodic peaks at 823 K.

The calibration lines for zirconium concentration tend to change with temperature as seen in Figures 4.26 to 4.28 and Eqs. (4. 17) to (4.19).

$$723\text{ K:}\quad \frac{i_{pc}}{\sqrt{\nu}} = -622.83C - 0.0896, \tag{4.17}$$

$$773\text{ K:}\quad \frac{i_{pc}}{\sqrt{\nu}} = -1282C - 0.0578, \text{ and} \tag{4.18}$$

$$823\text{ K:}\quad \frac{i_{pc}}{\sqrt{\nu}} = -1688C - 0.0253. \tag{4.19}$$

4.4 Zirconium Thermodynamic and Electrochemical Properties

4.4.1 Zirconium Diffusion Coefficient

As the zirconium system is irreversible, Eq. (2.15) has been chosen to determine information about the reactions occurring in the system. Figure 4.29 shows a plot of peak current versus square root of the scan rate for the 1.07 wt% $ZrCl_4$ mixture at 773 K. The data was similarly linear for all concentrations and temperatures. All resulting plots are shown in Appendix J. From the slope of this line, if the number of electrons transferred during the reaction is known, the diffusivity of the oxidized species can be determined.

The product of the number of electrons transferred and the transfer coefficient, $n\alpha$, as calculated using Eq. (2.14) for the cathodic peaks can be seen in Table 4.4. If the transfer coefficient is assumed to be 0.5 (a commonly accepted assumption), this results in values for Peaks A_c and B_c close to two electrons transferred, which corroborates the likely redox couples of Zr(IV)/Zr(II) and Zr(II)/Zr for the peaks, respectively. A transfer coefficient of 0.4, which has also been used for reactions in the molten LiCl-KCl for modeling purposes [67-68] results in values that are much closer to the expected number of electrons transferred. An accurate baseline for Peak C_c was not possible, and therefore the half peak

potential, $E_{p/2}$, could not be determined and the same analysis using Eq. (2.14) could not be performed. Assuming two electrons transferred for Peaks A_c and B_c and a transfer coefficient of 0.4, the diffusion coefficients of Zr(IV) and Zr(II) were calculated from the slopes indicated by the Delahay Eq. (2.15) at each temperature as listed in Table 4.4. These values are compared with the one published [55] value for the diffusivity of Zr(IV), as shown in Figure 4.30. For Peak C_c, the likely oxidized species is the insoluble ZrCl. This implies that it does not diffuse in the molten LiCl-KCl eutectic; therefore, there is no diffusivity value associated to it. Though, Eq. (2.15) leads to the assumption that the data should have an intercept of zero, the experimental data does not fully fit this assumption. In reality, a non-zero intercept can exist when a capacitive current is present in the system, as appears to be the case with zirconium. The capacitive current densities, i_c, can be seen for all concentrations and temperatures in Appendix J as the y-intercept.

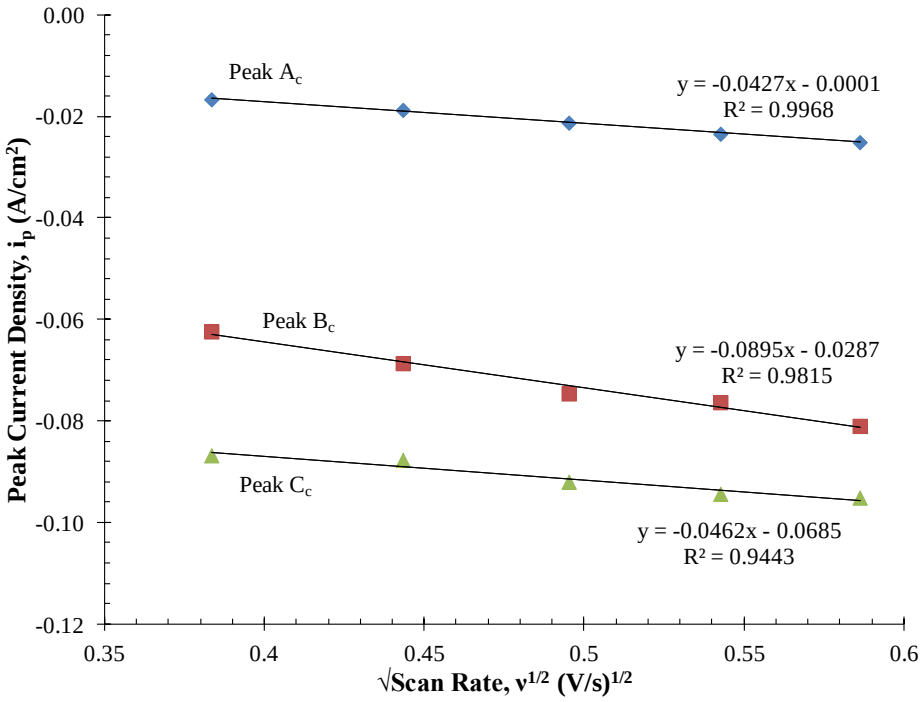

Figure 4.29 Peak current versus square root of scan rate for cathodic peaks in the 1.07 wt% $ZrCl_4$ cyclic voltammogram at 773 K.

Table 4.4 Calculated product of number of electrons transferred and transfer coefficient and diffusion coefficients for Zr(IV) and Zr(II) at 723, 773, and 823 K in the molten LiCl-KCl eutectic.

Peak: Species	**Product of electrons transferred and transfer coefficient, nα**			**Diffusion Coefficient, D (cm^2/s)**		
	723 K	**773 K**	**823 K**	**723 K**	**773 K**	**823 K**
A_c: Zr(IV)	0.85	0.825	0.93	3.06×10^{-6}	2.86×10^{-6}	5.82×10^{-6}
B_c: Zr(II)	0.75	0.65	0.875	1.27×10^{-5}	1.47×10^{-5}	3.33×10^{-5}

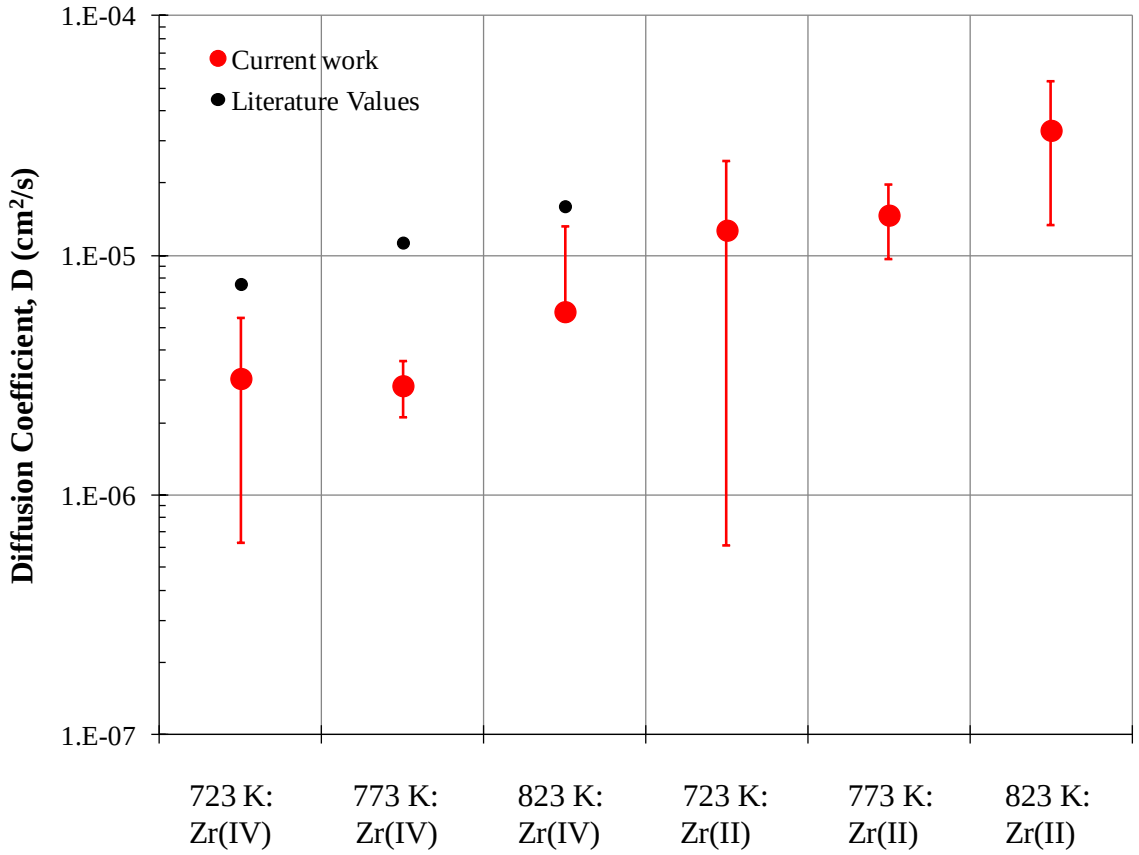

Figure 4.30 Comparison of experimental and previously published values [55] for the diffusivity of zirconium ions in LiCl-KCl eutectic at 723, 773, and 823 K.

The calculated diffusion coefficients are reasonable values for liquid phase diffusion and are in the same general range as those reported by Lee, et al. [30]. Diffusivity tends to follow an Arrhenius temperature dependence of

$$D = D_0 \exp\left(\frac{-E_D}{RT}\right). \tag{4.20}$$

The natural log of the calculated diffusivities of Zr(IV) and Zr(II) are plotted against the inverse temperature to determine the pre-exponential factor, D_0, and the diffusion activation energy, E_D (see Figure 4.31).

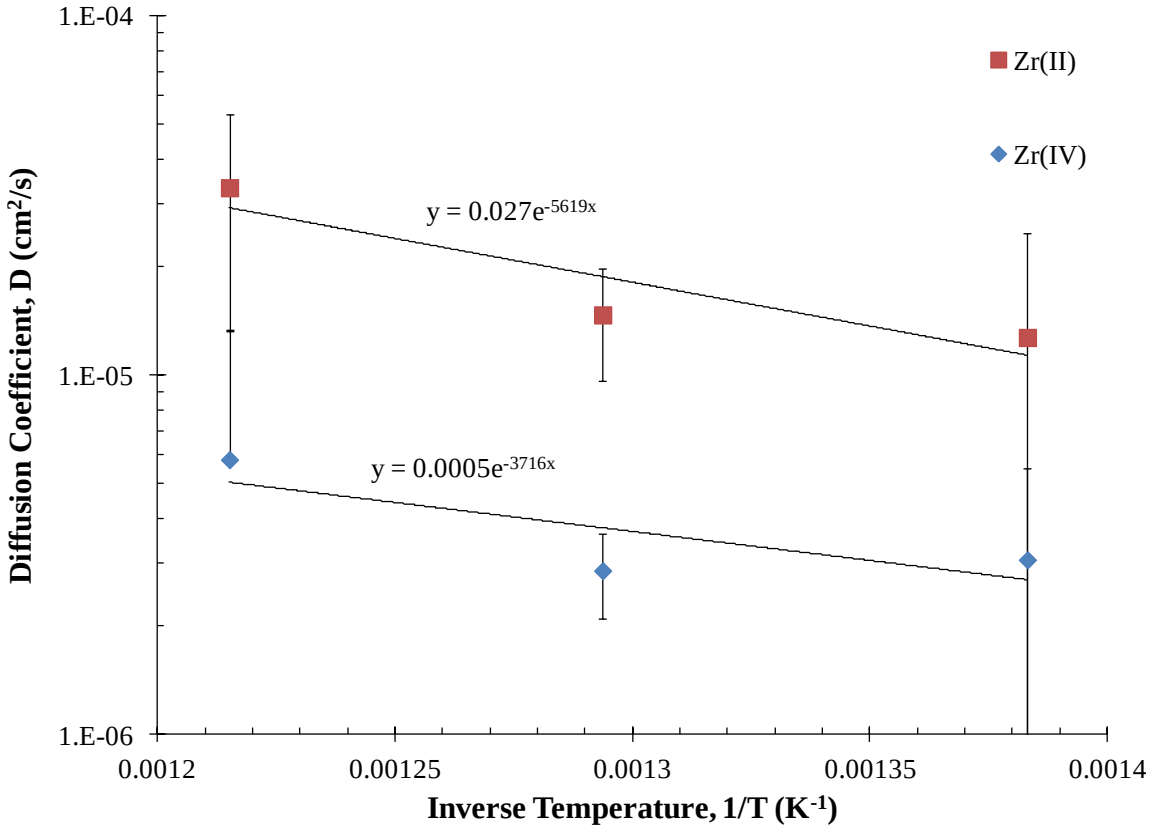

Figure 4.31 Arrhenius plot of Zr(IV) and Zr(II) diffusivities in the LiCl-KCl eutectic.

From the line fit to the data, the pre-exponential factor and diffusion activation energy were calculated. These values are indicated in Table 4.5 along with the published values of pre-exponential factor and activation energy [55].

Table 4.5 Zr(IV) and Zr(II) diffusion Arrhenius temperature dependence factors.

	D_0 (cm^2/s)		E_D (kJ/mol)	
	Current Work	**Literature Ref. [55]**	**Current Work**	**Literature Ref. [55]**
Zr(IV)	4.60×10^{-4}	3.58×10^{-3}	30.9	37.0
Zr(II)	0.0270	N/A	46.7	N/A

4.4.2 Zirconium Apparent Standard Reduction Potential

To calculate the apparent standard reduction potentials of the zirconium system, Eq. (2.16) for irreversible redox reactions was used along with the cathodic peak potentials. Since the value of the standard rate constant, k_s, is not known, the value for uranium of 2.6×10^{-4} cm/s [38] is used as an estimate. Due to the uncertainty of this value, the effect of standard rate constant on the calculated apparent standard reduction potential should be known. Figure 4.32 shows the effect of k_s, with values one-half and twice that of uranium, on the apparent standard reduction potentials of Zr(IV)/Zr(II) and Zr(II)/Zr versus the Cl_2/Cl^- reference. Conversion to the Cl_2/Cl^- reference was performed as discussed in Section 4.2.2. As shown, the calculated data fits a logarithmic trend, as expected by Eq. (2.16). Figure 4.32 reveals that there is not a great difference in the resulting apparent standard reduction potential value by changing the estimated k_s value in the order relative to the uranium k_s value. The average difference is about 5.3% between the lowest and highest predicted values. To provide a meaningful relationship of this resulting plot, the equations relating apparent standard reduction potential, E^{0*}, to standard rate constant, k_s, are

Peak A_c: Zr(IV)/Zr(II) 723 K: $E^{0*} = -0.078\ln(k_s) - 2.7415$, (4.21)

773 K: $E^{0*} = -0.083\ln(k_s) - 2.7364$, (4.22)

823 K: $E^{0*} = -0.089\ln(k_s) - 2.6377$, (4.23)

Peak B_c: Zr(II)/Zr 723 K: $E^{0*} = -0.078\ln(k_s) - 3.0283$, (4.24)

773 K: $E^{0*} = -0.083\ln(k_s) - 3.0203$, (4.25)

823 K: $E^{0*} = -0.089\ln(k_s) - 3.0441$. (4.26)

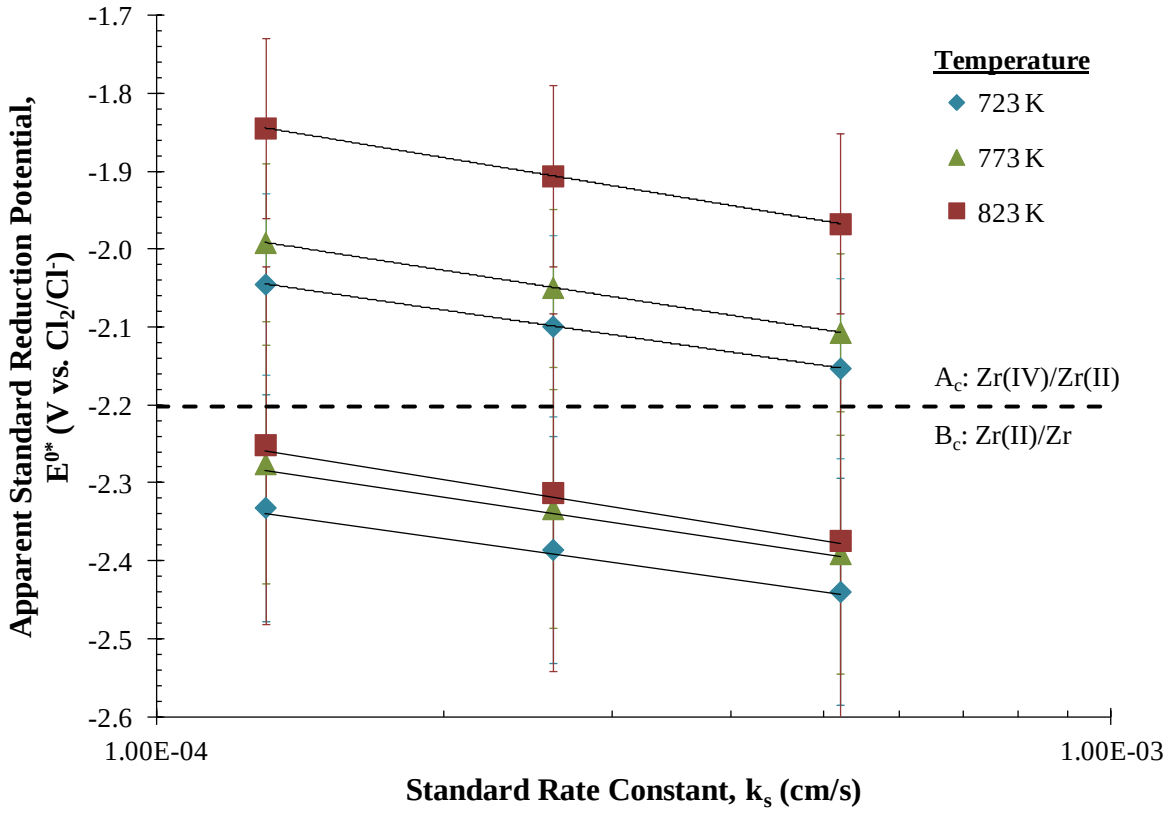

Figure 4.32 Effect of standard rate constant on apparent standard reduction potential for Zr(IV)/Zr(II) and Zr(II)/Zr in LiCl-KCl.

The standard rate constant can be experimentally determined by analyzing potentiostatic-electrochemical impedance spectroscopy (EIS) data. Though this analysis is

beyond the scope of the current work, EIS data was experimentally collected and future work should include its analysis. The calculated apparent standard reduction potentials are shown in Table 4.6 using $k_s = 2.6 \times 10^{-4}$ cm/s against both the Ag/AgCl and Cl_2/Cl^- reference. Conversion to the Cl_2/Cl^- reference was performed as discussed in Section 4.2.2. The calculated values are compared with the few published values available in Figure 4.33.

Table 4.6 Apparent standard reduction potentials for Zr at 723, 773, and 823 K in the LiCl-KCl eutectic, assuming standard rate constant, $k_s = 2.6 \times 10^{-4}$ cm/s.

Peak	**Apparent Standard Reduction Potential, E^{0*} (V vs. Ag/AgCl)**			**Apparent Standard Reduction Potential, E^{0*} (V vs. Cl_2/Cl^-)**		
	723 K	**773 K**	**823 K**	**723 K**	**773 K**	**823 K**
A_C: Zr(IV)/Zr(II)	-1.031	-0.982	-0.841	-2.099	-2.049	-1.906
B_C: Zr(II)/Zr	-1.317	-1.266	-1.247	-2.385	-2.333	-2.312

The apparent standard reduction potential for Peak C_c, likely representing the reduction of ZrCl/Zr was not calculated, as Eq. (2.16) contains the diffusion coefficient of the oxidized species based on the previous discussion. Because of this, the ZrCl/Zr reaction is likely not mass transfer limited. In addition, the temperature dependence of the apparent standard reduction potentials was examined, assuming standard rate constant, $k_s = 2.6 \times 10^{-4}$ cm/s (see Figure 4.34) resulting in the following fitted equations:

$$\text{Zr(IV)/Zr(II):} \quad E^{0*}(\text{vs. } Cl_2/Cl^-) = 0.002T(K) - 3.508, \text{ and} \tag{4.22}$$

$$\text{Zr(II)/Zr:} \quad E^{0*}(\text{vs. } Cl_2/Cl^-) = 0.0007T(K) - 2.908\ . \tag{4.23}$$

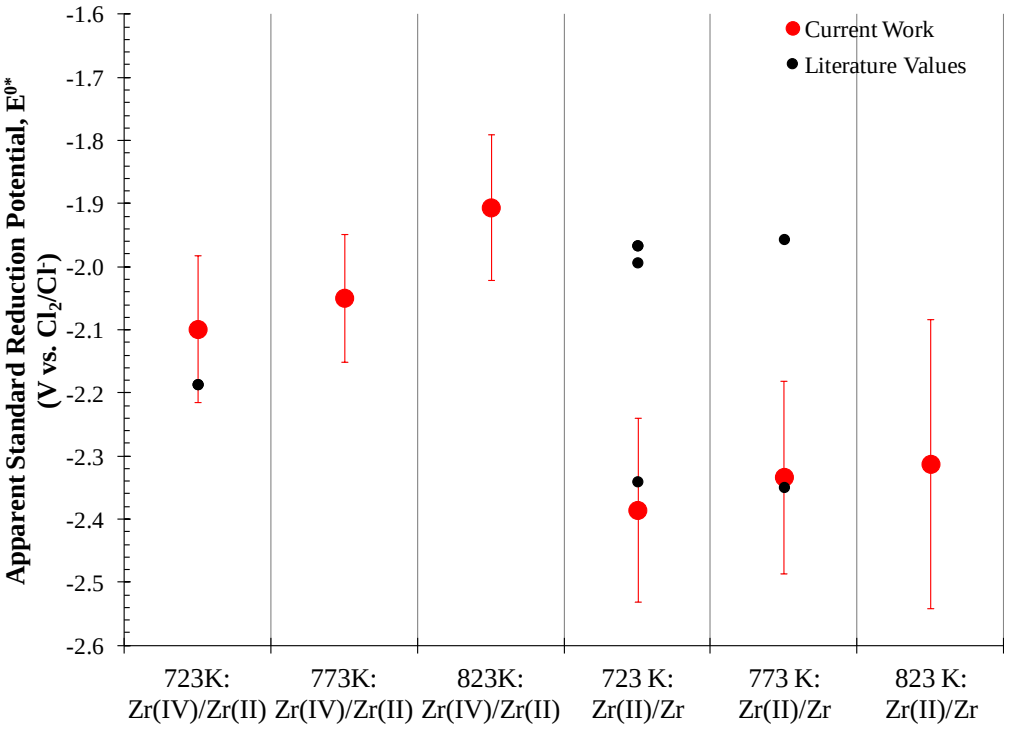

Figure 4.33 Comparison of experimental and previously published values for E^{0*} of zirconium in LiCl-KCl eutectic assuming $k_s = 2.6 \times 10^{-4}$ cm/s.

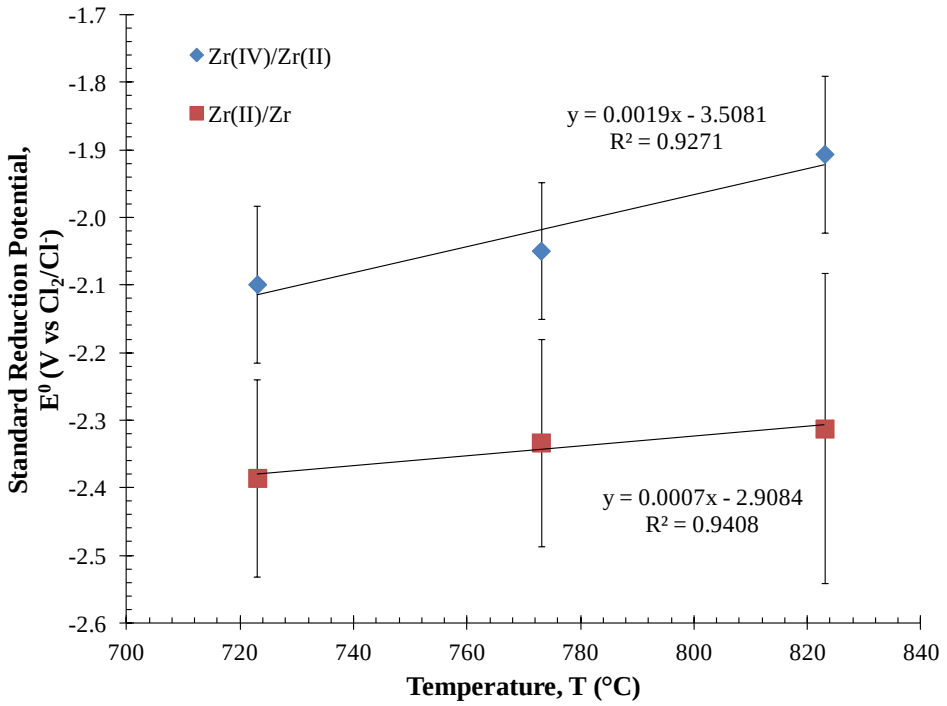

Figure 4.34 Temperature dependence of E^{0*} for the Zr(IV)/Zr(II) and Zr(II)/Zr redox couples, assuming $k_s = 2.6 \times 10^{-4}$ cm/s.

4.4.3 Zirconium Activity Coefficient

By using the same method for U electrochemical experiments, γ of Zr(IV) and Zr(II) can be found by comparing the theoretical and actual Gibbs energy change for the reactions oxidation reactions using Eq. (4.5). As with the uranium activity coefficient calculations, the result depends greatly on the theoretical thermodynamic data used to compare with the experimental. Two sources of theoretical Gibbs energy for zirconium have been found in the literature, which differ by a large amount. This outcome results in values that differ by as much as 14 orders of magnitude (see Table 4.7). Again, similar to the uranium data, it is recommended that the experimentally determined apparent standard reduction potential be used in place of the theoretical standard reduction potential and activity coefficient. A comparison with published values of activity coefficient is shown in Figure 4.35.

Table 4.7 Ideal state thermodynamic data for zirconium [24, 65] and corresponding calculated γ.

T (K)	$ZrCl_4$			$ZrCl_2$		
	Δg^{0*} (kJ/mol)	Δg_{id}^{0} (kJ/mol)	γ	Δg^{0*} (kJ/mol)	Δg_{id}^{0} (kJ/mol)	γ
723	-405.0 ± 22.40	–441.304 [65]	420.8 ± 1568	-460.3 ± 28.11	–323.877 [65]	$(1.388 \pm 6.489) \times 10^{-10}$
		–258.385 [24]	$(2.560 \pm 9.541) \times 10^{-11}$		–500.564 [24]	808.9 ± 3782
773	-395.4 ± 19.56	–434.245 [65]	420.5 ± 1280	-450.2 ± 29.54	–316.880 [65]	$(9.784 \pm 44.98) \times 10^{-10}$
		–251.732 [24]	$(1.951 \pm 5.936) \times 10^{-10}$		–494.003 [24]	911.7 ± 4191
823	-367.8 ± 22.35	–427.338 [65]	6025 ± 19,680	-446.2 ± 44.29	–309.984 [65]	$(2.255 \pm 14.60) \times 10^{-9}$
		–245.080 [24]	$(1.629 \pm 5.321) \times 10^{-8}$		–487.442 [24]	413.7 ± 2678

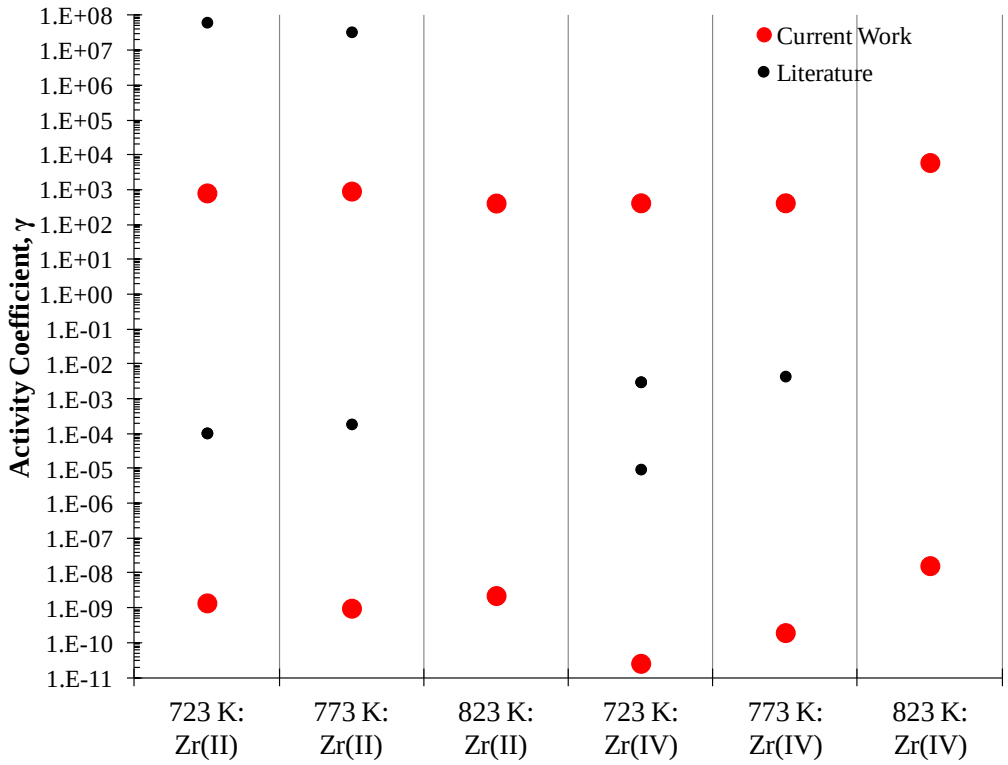

Figure 4.35 Comparison of experimental and previously published values for the activity coefficients of zirconium ions in the LiCl-KCl eutectic at 723, 773, and 823 K.

4.5 Uranium and Zirconium Electrochemistry

Results obtained from both uranium and zirconium experiments can independently be used to help gain insights into the quaternary salt electrochemical experiments, UCl_3-$ZrCl_4$-LiCl-KCl mixture at 773 K.

4.5.1 Uranium and Zirconium Cyclic Voltammetry

CV experiments were performed on two LiCl-KCl-$ZrCl_4$-UCl_3 mixtures at 773 K. The CVs for the 0.497 wt% $ZrCl_4$ - 9.80 wt% UCl_3 are shown in Figure 4.36. When comparing this plot with the 0.57 wt% $ZrCl_4$ CVs and the 10.0 wt% UCl_3 CVs, it is clear that the relatively high concentration of UCl_3 hides some of the features of the smaller concentration of $ZrCl_4$, which are overlaid and shown in Figure 4.37.

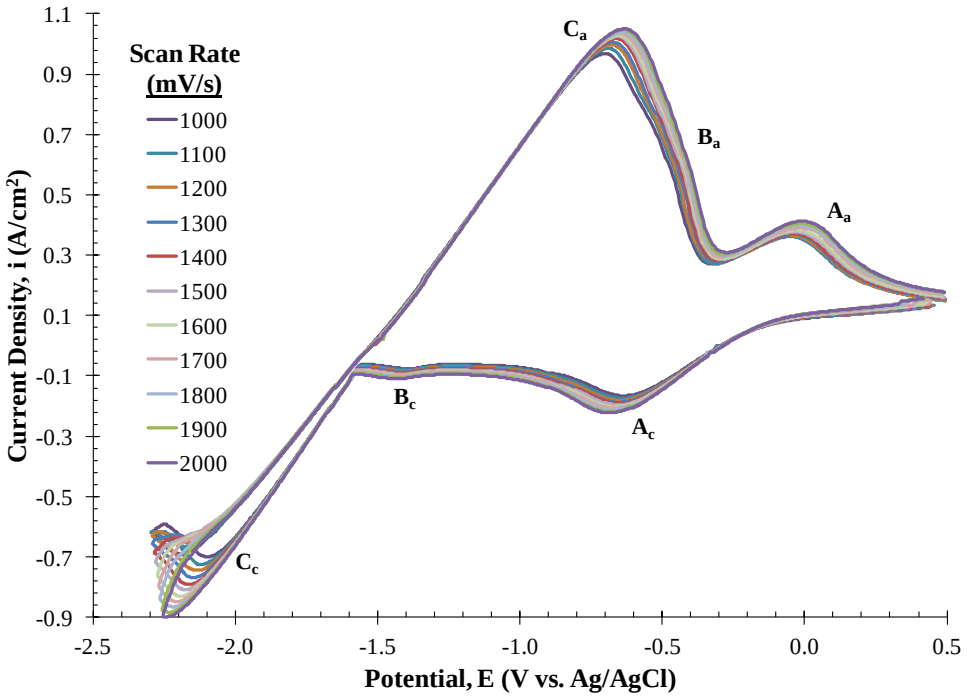

Figure 4.36 Cyclic voltammograms of 0.497 wt% $ZrCl_4$ and 9.80 wt% UCl_3 mixture in the LiCl-KCl eutectic at 773 K.

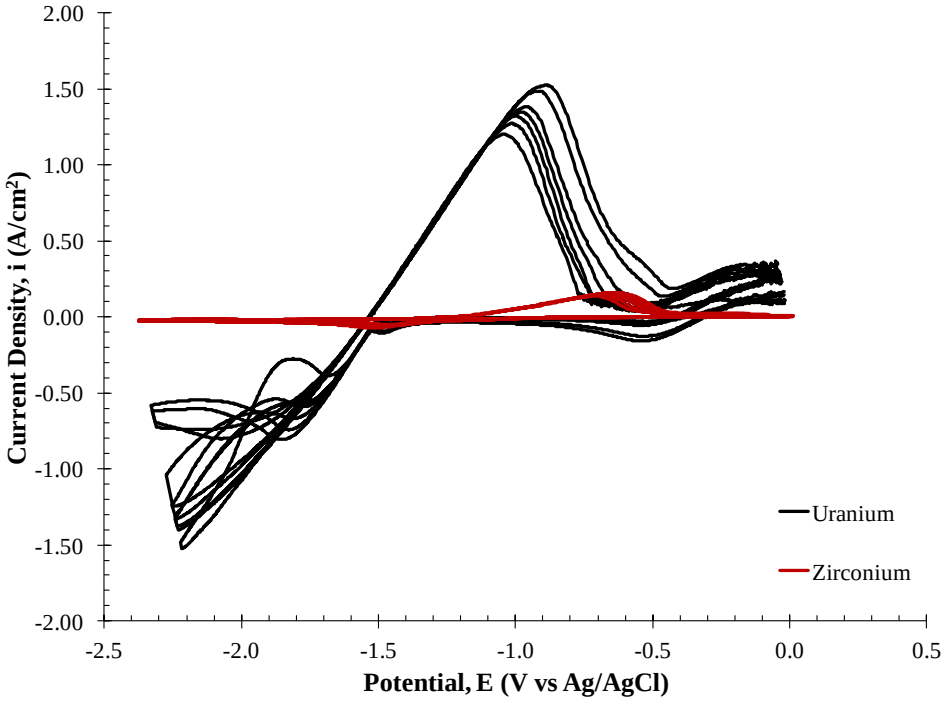

Figure 4.37 Cyclic voltammograms of 0.57 wt% $ZrCl_4$ and 10.0 wt% UCl_3 in the LiCl-KCl eutectic at 773 K overlaid upon each other.

The main location where any effect of $ZrCl_4$ is evident is on the positive potential side of the large anodic Peak C_a. At approximately -0.5 V (see Figure 4.36), there is a small hump, labeled B_a, on the large anodic peak, which is likely caused by the Zr/Zr(II) oxidation peak as seen in Figure 4.37. The presence of $ZrCl_4$ is more prominent in the CVs from the 4.17 wt% $ZrCl_4$ - 8.34 wt% UCl_3 mixture as seen in Figure 4.38.

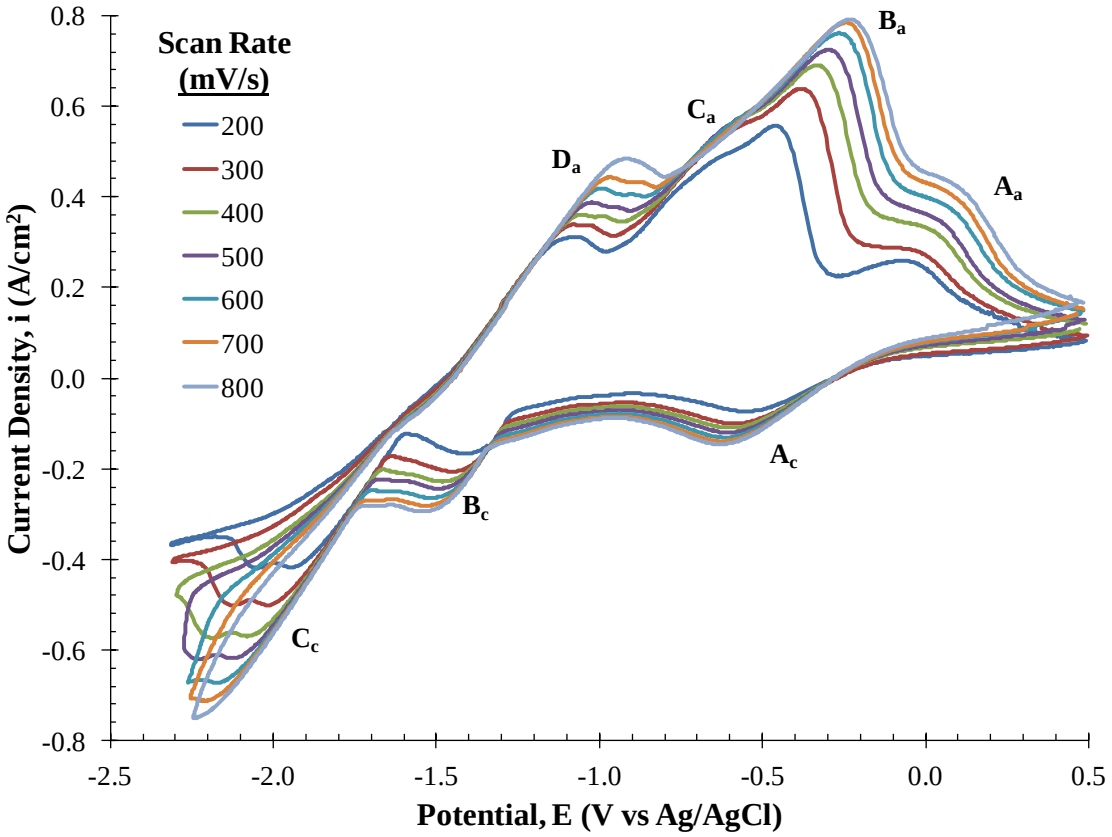

Figure 4.38 Cyclic voltammograms of 4.17 wt% $ZrCl_4$ and 8.34 wt% UCl_3 mixture in the LiCl-KCl eutectic at 773 K.

Through a comparison of the data shown in Figures 4.38 and 4.39, it is clear that zirconium has a substantial effect on the appearance of the CVs in the 4.17 wt% $ZrCl_4$ - 8.34 wt% UCl_3 mixture. The large anodic peak B_a at -0.3 V is most likely due to the Zr/Zr(II) oxidation. There is also the appearance of an anodic peak at approximately -1.0 V, labeled

D_a in Figure 4.38. As discussed previously, some researchers showed an anodic peak corresponding to the oxidation of ZrCl if it wasn't fully reduced to metal during the cathodic sweep as shown in Eqs. (4.15) and (4.16). This peak is likely evidence of that oxidation reaction. With the large amount of uranium present in the mixture, the ZrCl is likely not fully reduced to metal during the cathodic sweep leaving some ZrCl to oxidize during the following anodic sweep. This could be a possible impediment to electrorefining pure Zr metal in the presence of large UCl_3 concentrations.

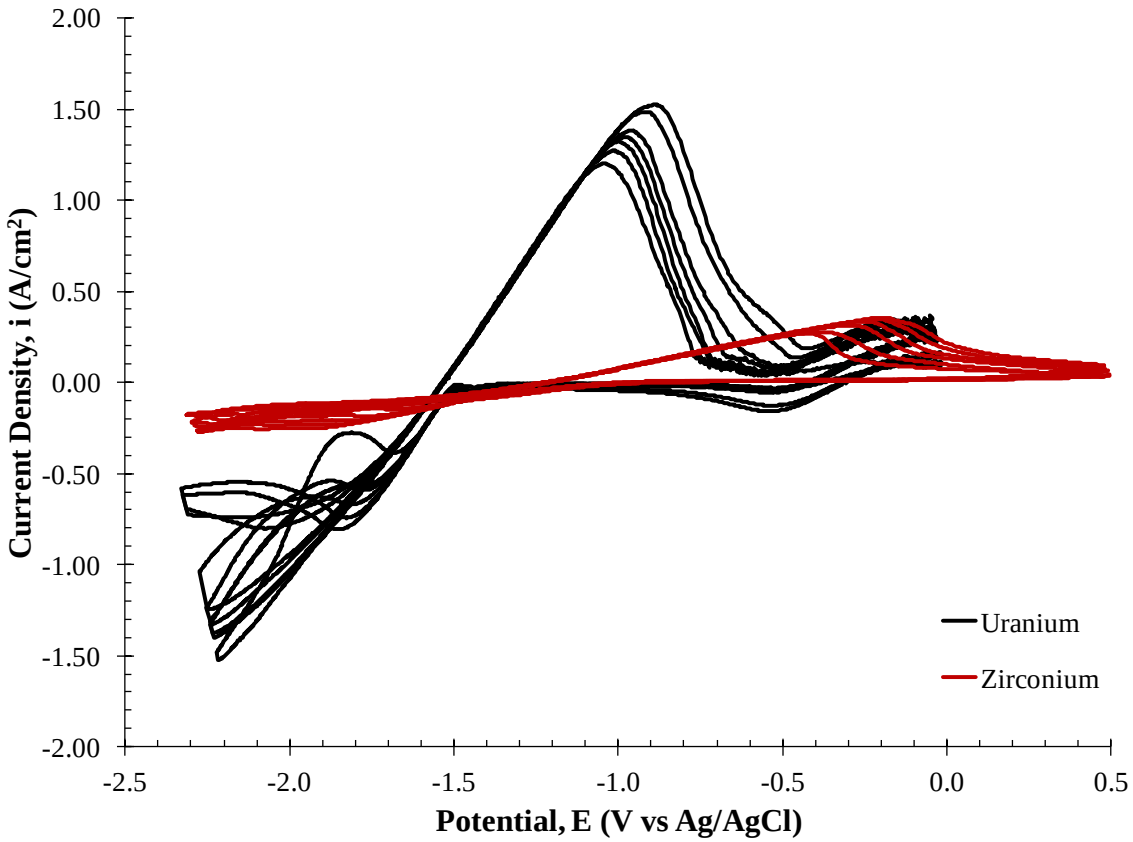

Figure 4.39 Cyclic voltammograms of 4.98 wt% $ZrCl_4$ and 10.0 wt% UCl_3 in the LiCl-KCl eutectic at 773 K overlaid upon each other.

4.5.2 Analysis of UCl_3-$ZrCl_4$-LiCl-KCl Mixtures

To determine whether the combinations of reduction reactions occurring at the cathode peaks are diffusion limited, the peak currents are shown versus the square root of the scan rate in Figures 4.40 and 4.41 for the 0.497 wt% $ZrCl_4$ - 9.80 wt% UCl_3 and 4.17 wt% $ZrCl_4$ - 8.34 wt% UCl_3 mixtures, respectively. The high degrees of linearity ($R^2 > 0.98$) lead to the conclusion that these reactions are indeed diffusion limited. These figures show a non-zero intercept, likely due to the effect of the capacitive current present with the reactions of zirconium as discussed in Section 4.4.1.

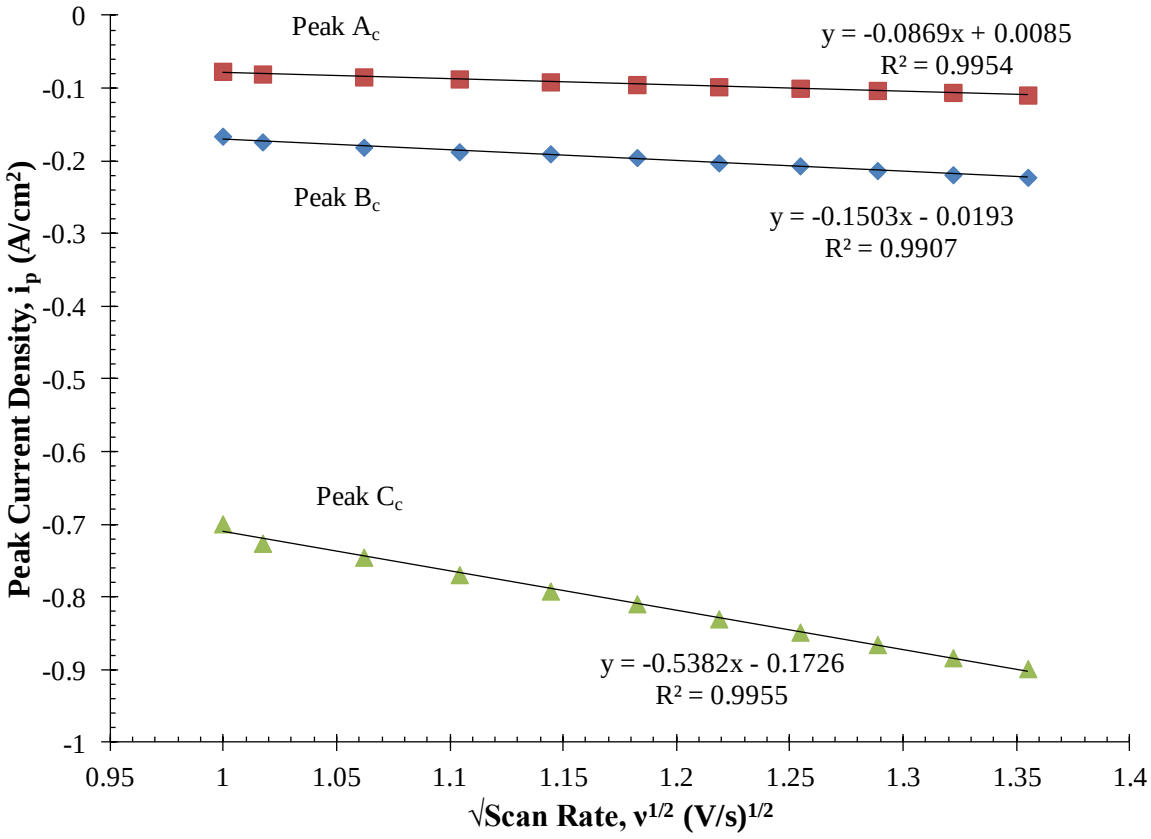

Figure 4.40 Peak current versus square root of scan rate for cathodic peaks in the 0.497 wt% $ZrCl_4$ - 9.80 wt% UCl_3 cyclic voltammograms at 773 K.

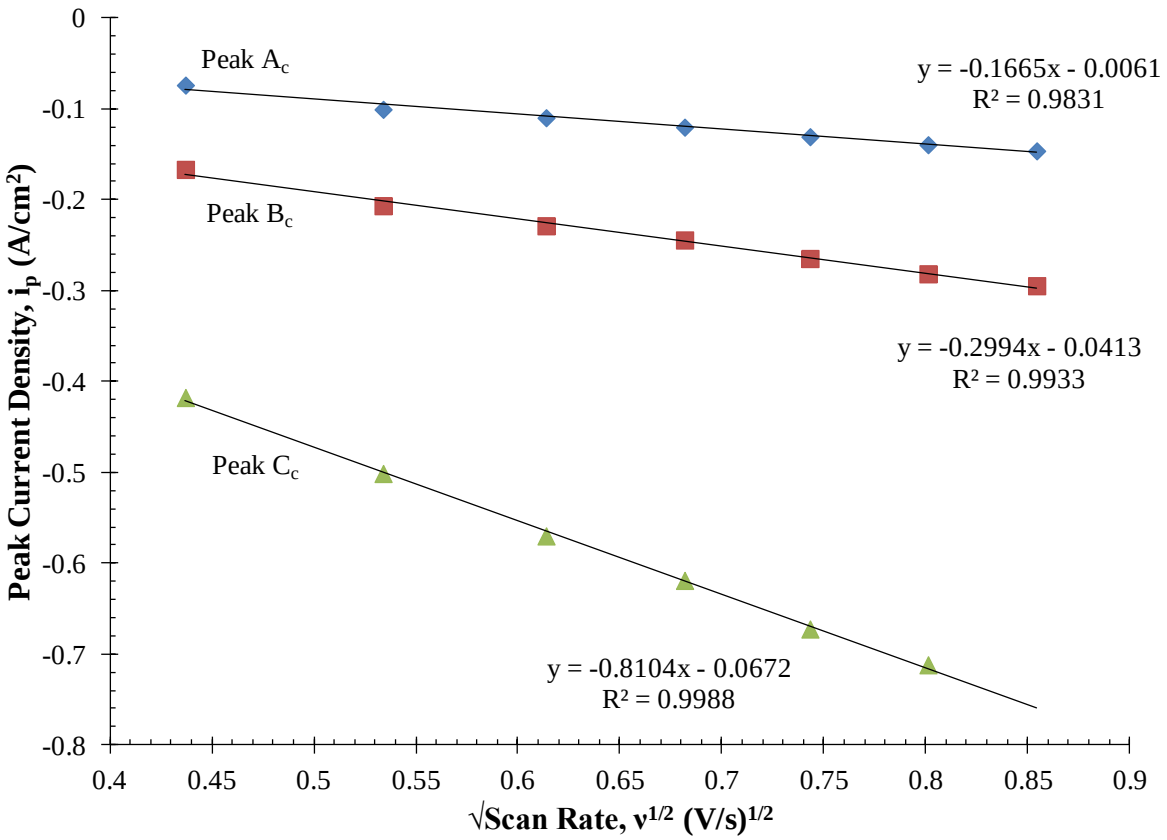

Figure 4.41 Peak current versus square root of scan rate for cathodic peaks in the 4.17 wt% $ZrCl_4$ - 8.34 wt% UCl_3 cyclic voltammograms at 773 K.

To further examine the effect of $ZrCl_4$ additions on the electrochemical behavior of UCl_3, the slopes of the UCl_3-$ZrCl_4$-LiCl-KCl data shown in Figures 4.40 and 4.41 are compared with those for the UCl_3-LiCl-KCl mixtures (Figure 4.12 and Appendix F). As exhibited in Eq. (2.9) and discussed in Section 4.1.3, the slopes should become more negative with increasing concentration, which is seen in Figure 4.42.

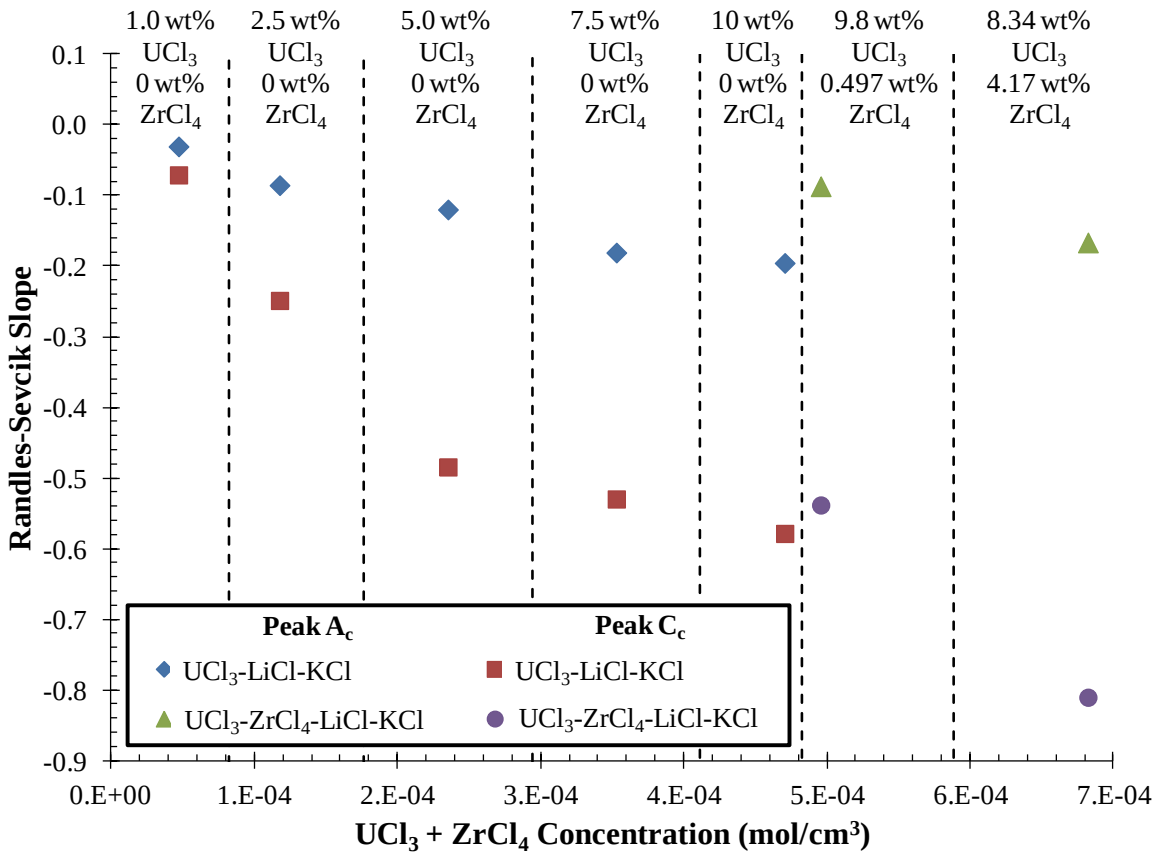

Figure 4.42 Slope of the peak current versus square root of scan rate for cathodic peaks as a function of total concentration for the UCl_3-LiCl-KCl and UCl_3-$ZrCl_4$-LiCl-KCl salt mixture cyclic voltammograms at 773 K.

Figure 4.42 shows the slope of the Randles-Sevcik Eq. (2.9), repeated as Eqn. 4.24, versus the total analyte concentration (UCl_3 + $ZrCl_4$) for the pure UCl_3-LiCl-KCl and UCl_3-$ZrCl_4$-LiCl-KCl salt mixtures. As seen in the figure, with the addition of $ZrCl_4$ to the salt mixture, there is a decrease in the slope from the UCl_3-LiCl-KCl trend. This decrease is likely caused by two different phenomena. First, the addition of $ZrCl_4$ changes two of the parameters in the Randles-Sevcik equation,

$$\frac{I_{pc}}{\sqrt{\nu}} = -0.4463nFSC\sqrt{\frac{nFD_{ox}}{RT}}\,. \qquad (4.24)$$

The reactions occurring at Peaks A_c and C_c involve Zr(IV)/Zr(II) and Zr(II)/Zr, respectively, along with the uranium reactions. The decrease in the expected slope for Peak A_c can likely be partially attributed to the diffusivity of Zr(IV), which is an order of magnitude smaller than the diffusivity of U(IV), the other species being reduced (2.86×10^{-6} and 1.26×10^{-5} cm^2/s, respectively). Similarly for peak C_c, the diffusivity of Zr(II) is slightly smaller than the value for U(III) (1.47×10^{-5} versus 1.26×10^{-5} cm^2/s); but primarily the number of electrons transferred is two, compared with three for the UCl_3 reduction.

The second explanation for a reduced peak height with the mixture has to do with the location of the peaks themselves. If the reduction reactions don't occur at the same potential (as is reported in Sections 4.2.2 and 4.4.2), a form of destructive interference between the two peaks would occur, decreasing the height of the resultant measured peak. Due to this effect, to determine parameters (potential and diffusivity) for each analyte contributing to the peaks, a deconvolution method for the individual peaks from the measured peaks would be required, and could be an area of additional future research.

Chapter 5: Summary and Future Work

5.1 Basic Concept

The electrochemical processing of used nuclear fuel is a promising method for nuclear fuel treatment that is currently being considered worldwide. The heart of this process is the electrorefiner, within which uranium and transuranics are electrochemically separated from the fission products. This technology is best suited to metallic fuel, and has been used at INL to treat used U-Zr alloy fuels from the Experimental Breeder Reactor-II. The used driver fuel is approximately 80% uranium and 10% zirconium, which makes the behavior of these two species important to the entire treatment process.

5.2 Electrochemical Studies on Uranium and Zirconium

In Chapter 2, a literature survey was presented. Three important electrochemical and thermodynamic parameters (standard reduction potential, diffusion coefficient, and activity coefficient) were introduced and discussed along with previous studies that have been performed in this field. Then the discussion of three selected electrochemical techniques and their methods were given in detail. The following conclusions can be drawn from this chapter:

- The standard reduction potential is significant for determination of the equilibrium potential of the reaction of interest. This value can be calculated based on the Nernst equation, Eq. (2.1). This information is fruitful in helping to directly determine the Gibbs free energy of the redox reaction.
- The diffusion coefficient of each species is vital in helping researchers to examine the mass transfer to and from the electrodes in an electrochemical system. An

Arrhenius form of equation can be used to identify temperature dependency of the diffusivity values. This value is significant in computational modeling of the electrorefiners.

- The activity coefficient is the thermodynamic property that identifies the nonideality of the mixture within the system. The stability of a species within the molten salt can be determined based on this value.
- There has been substantial prior electrochemical work reported on uranium worldwide, but the published parameter values vary by a large degree, depending on different researchers.
- It is also evident that there has been limited work reported on the behavior of zirconium in the LiCl-KCl eutectic. Of the few papers that do report zirconium parameters, many research teams do not discuss the method that was used to determine these values.
- The summary of reported values for zirconium shows parameters with large variations (i.e. E^{0*} and γ) and gaps where no values are reported (i.e. $D_{Zr(II)}$). The results of the literature survey on these electrochemical values are listed in Appendices A to C.
- Three electrochemical techniques can be applied to obtain these important values. CV can be used to determine information about the reactions that may occur within the electrochemical cell. By performing this technique, reversible and/or irreversible redox reactions can be identified.
    - For the reversible reactions, two different forms of the Randles-Sevcik equation, Eqs. (2.9) and (2.10) can be applied to calculate the diffusion

coefficient. Furthermore, information can be used to obtain insight into the apparent standard reduction potential.

    - For the irreversible reactions, the Delahay equation, Eq. (2.15) can be used to obtain the diffusion coefficient. Then, Eq. (2.16) is used to calculate the apparent standard reduction potential, where the standard rate constant must be known or estimated.

- CP is often used to study time-dependent concentration change in a solution. This is the standard electrochemical method to determine the diffusion coefficient by use of the Sand equation, Eq. (2.17). CP techniques can be used to cross-validate the CV technique. The number of electrons transferred for the reactions of interest can be calculated from information obtained using the CP technique.
- ASV can be applied to take advantage of the relationship between concentration and peak current in linear sweep voltammetry. This method can be utilized as a possible electrochemical detection method. This technique can be compared and contrasted with the other concentration detection methods, including both CV anodic and cathodic peak heights.

5.3 Experimental Plan and Data Collection

To fill in the aforementioned gaps and better understand the behavior of uranium and zirconium together, an experimental program was developed and discussed in Chapter 3. The experimental materials and equipment were presented along with the preparation methods used for the salt mixtures. Then, the individual experimental techniques and data collection methods were discussed. The following summary can be given:

- All uranium related experiments were conducted in a MBraun argon atmosphere glovebox with O_2 and H_2O concentrations in the inert atmosphere at less than 0.1 ppm. Experiments were performed at five different UCl_3 concentrations ranging from 1.00 wt% to 10.0 wt%. Typically, the entire experimental routine—preparing the salts, heating and melting, performing the electrochemical techniques and collecting a sample for analysis—would take between 11 and 14 hours for each uranium concentration.
- All zirconium experiments were conducted in a similar MBraun glovebox with the O_2 and H_2O concentrations in the inert atmosphere at less than 3.0 ppm. Experiments were performed at four different concentrations between 0.50 wt% and 5.0 wt%. The preparation process for each zirconium experiment, including the trapping method, electrochemical runs and sample collections would take a total of 26 to 32 hours for each zirconium concentration at three different temperature settings.
- Two UCl_3-$ZrCl_4$-LiCl-KCl quaternary salt experiments were performed at 9.8 UCl_3 – 0.49 $ZrCl_4$ and 8.34 UCl_3 – 4.2 $ZrCl_4$ compositions (all numbers represent wt%) to mock-up the actual ER salt. The total experimental processing time for each experiment is the same as that for zirconium experiments.
- The experimental setup is equipped with a quartz electrode assembly (based on the design by a University of Wisconsin research team [60]) connected with a Princeton Applied Research VersaSTAT 4-400 pontentiostat with *VersaStudio* software (see Figures 3.5, 3.6, and 3.7).

- The reference electrode must be prepared in advance for all experimental runs. Here, 5.0 mol% Ag/AgCl in LiCl-KCl eutectic has been selected to take advantage of its long term stability as compared with lower concentrations reported in the literature [22, 36, 45].
- A matrix of the experimental program was given in Table 3.4.
- For all CV experiments, several important inputs must be entered: (1) the desired initial potential, (2) the potential at which to reverse the scan, (3) the final potential, (4) the scan rate, and (5) the number of cycles to run with 2000 data points per cycle recorded. Three cycles were tested to ensure repeatability where the third cycle would be used for theoretical analysis. A minimum of five acceptable scan rates was required for each experimental run listed in Table 3.4 to achieve reliable and accurate data.
- For all CP runs, a series of constant potential and constant current steps was applied. To achieve this task, several parameters must be identified and entered: (1) step current, (2) time per point, and (3) duration. An accurate driving current must be applied in order to achieve a clean chronopotentiogram plot. The process was monitored and recorded at a minimum of four chronopotentiograms with clear plateaus for repeatability and accuracy of obtained data sets.
- For all ASV studies, the following procedure was conducted: (1) 0.0 V vs. Ag/AgCl was applied for 20 sec to the working electrode to strip any material that may be deposited onto the surface, (2) a reducing potential of -2.3 V vs. Ag/AgCl was applied for 5 or 60 sec to reduce a large amount of material onto the working electrode, (3) the voltage was linearly ramped at 50 mV/s from -2.3 V up to 0.0 V,

and (4) 0.0 V was applied for 20 seconds to fully remove the electroplated material. This procedure was repeated ten times for identifying and calculating a mean peak height value.

5.4 Electrochemical Results

Three types of studies to measure and interpret the collected data for fundamental electrochemical separations have been completed during this research: (1) uranium, (2) zirconium, and (3) uranium and zirconium in combination.

5.4.1 Uranium Electrochemistry—Thermodynamic and Electrochemical Properties

Based on the results of the first study, the following conclusions can be drawn:

- The CV plot exhibits three cathodic and three anodic peaks. These peaks are summarized in Table 5.1.

Table 5.1 Cathodic and anodic peaks for uranium CV.

Peak	Cathodic Reaction, Location	Anodic Reaction, Location
A	$U^{4+} + e^- \rightarrow U^{3+}$, –0.5 V	$U^{3+} \rightarrow U^{4+} + e^-$, –0.3 V
B	Adsorption U^{3+}, –1.5 V	Desorption U^{3+}, –0.7 V
C	$U^{3+} + 3e^- \rightarrow U$, –1.6 V	$U \rightarrow U^{3+} + 3e^-$, –1.4 V

- The major anodic peak potential, $U \rightarrow U^{3+} + 3e^-$, does not shift at low concentration; this is not true for the major cathodic peak, $U^{3+} + 3e^- \rightarrow U$. The shift of these peaks is more distinctive at high concentration range. Therefore, the reaction would be considered irreversible.

- The reaction represented by Peak A was considered reversible due to no shift at all concentrations.
- All CP plots have one common feature of having one clear plateau at approximately -1.6 V, which corresponds to the major cathodic Peak C. This plateau represents the diffusion and reduction of U(III) at the working electrode surface.
- Plating time had a strong effect on the peak heights for the ASV method. In addition, the same plating time was not possible at all concentrations. There was no direct relationship between the adjusted peak current density and uranium concentration from the ASV method. However, the cathodic peak current density from CV could be most accurately used to determine concentration because of its strong linear relationship with R^2 values of greater than 0.9.
- Transition times were calculated from all CP data sets. The Sand equation, Eq. (2.17), was applied and the resulting average diffusivity for U(III) was calculated to be $1.04 \times 10^{-5} \pm 0.173 \times 10^{-5} cm^2/s$. By using the CV method, the average diffusivity for U(III) was calculated to be $3.28 \times 10^{-5} \pm 0.849 \times 10^{-5} cm^2/s$. It is proven that CP is a better method for determining the diffusion value because the standard deviation of $D_{U(III)}$ from CP is about 8 times smaller than that of $D_{U(III)}$ from CV. We chose to report the value based on averaging between these two values.
- There was no observed plateau for peak A. Strictly speaking, higher resolution study near that potential is necessary in the future to obtain that plateau. Thus, the CV method was used to determine the diffusion value. Here, the average value of the diffusion for U(IV) was $1.26 \times 10^{-5} \pm 0.604 \times 10^{-5} cm^2/s$.

- For the reversible redox reaction, the mean apparent standard reduction potential of U(IV)/U(III) was calculated to be -1.453 V ± 0.012 V vs. the Cl_2/Cl^- reference electrode at 773K (based on Eq. (2.11) and conversion method). For the U(III)/U irreversible reaction, the standard rate constant value of $k_s = 2.6 \times 10^{-4}$ cm/s from Kuznetsov and co-workers [38] was also used in this calculation and the apparent standard reduction potential was calculated to be -2.552 V ± 0.075 V vs. Cl_2/Cl^- reference electrode at 773 K. Both calculated values were in a reasonable range to those reported in literature [38-39, 51, 53].
- The activity coefficient varies with the theoretical ideal state Gibbs free energy values obtained from the literature [24, 35, 39, 65]. All calculated results are shown in Table 4.3. The possible values for both UCl_4 and UCl_3 range several orders of magnitude, from 0.00234 - 0.0108 and 4.94×10^{-5} - 0.0358, respectively. The values for UCl_4 compared well with the published value of 0.0148 [39]. For UCl_3, most of the experimental values were slightly smaller than published values, ranging from 0.00139 [39] to 0.169 [66].

5.4.2 Zirconium Electrochemistry—Thermodynamic and Electrochemical Properties

Based on the results of the second study, the following conclusions can be drawn:

- CV plots show three cathodic and two anodic peaks, which are summarized in Table 5.2.

Table 5.2 Cathodic and anodic peaks for zirconium CV.

Peak	Cathodic Reaction, Location	Anodic Reaction, Location
A	$Zr^{4+} + 2e^- \rightarrow Zr^{2+}$, –1.06 V	$Zr^{2+} \rightarrow Zr^{4+} + 2e^-$, shoulder near B_a
B	$Zr^{2+} + 2e^- \rightarrow Zr$ and $Zr^{4+} + 3e^- + Cl^- \rightarrow ZrCl$, –1.5 V	$Zr \rightarrow Zr^{4+} + 4e^-$ and $Zr \rightarrow Zr^{2+} + 2e^-$, –0.5 V
C	$ZrCl + e^- \rightarrow Zr + Cl^-$ and $Zr^{4+} + 4e^- \rightarrow Zr$, –1.85 V	NONE

- If a narrower potential range was to be used, it appears that not all ZrCl is fully reduced to Zr metal and an anodic peak just negative of Peak B_a can be considered to represent these two reactions: $ZrCl \rightarrow Zr^{4+} + 3e^- + Cl^-$ and $ZrCl \rightarrow Zr^{2+} + e^- + Cl$.
- The results show that peak heights increase and peak potentials shift in the negative direction as temperature increases. Thus, it appears that temperature may be used as a tool for enhanced peak detection for any low concentration studies.
- Two distinct plateaus can be observed in the CP plots at -1.3 V for peak B_c and -1.7 V for peak C_c.
- Similar to the uranium experimental results, cathode peak data from cyclic voltammetry appears to be the most precise method with smaller standard deviations and a larger R^2 for the studied concentration range. The results indicate that ASV is not a good tool to use for the detection analysis of the zirconium system either. The slope of calibration lines for zirconium becomes more negative as temperature increases while the y-intercept becomes less negative as temperature increases.
- The product of the number of electrons transferred and the transfer coefficient was used in Eq. (2.14). A transfer coefficient of 0.4, which has also been used for reactions in the molten LiCl-KCl for modeling purposes [67-68] results in values that

are much closer to the expected number of electrons transferred. Diffusion as a function of temperature has been determined for both Zr(IV) and Zr(II), which are listed in Table 5.3. The value of D_0 and E_D for Zr(IV) are in agreement with the values reported in the literature [55].

- The k_s value was assumed to be within the range of the value reported for uranium electrochemistry [38]. The effect of k_s was studied and observed to provide minimal impact to the calculation of the apparent standard reduction potential. Therefore, k_s of 2.6×10^{-4} cm/s was chosen for all calculations of apparent standard reduction potentials. It appears that the values become less negative as temperature increases. All results are listed in Table 5.3.

Table 5.3 Summary of electrochemical and thermodynamic properties of zirconium calculated from experimental data in LiCl-KCl eutectic.

	Diffusion coefficient, D (cm^2/s)			**Apparent standard reduction potential, E^{0*} (V vs Cl_2/Cl^-)**		
	723 K	**773 K**	**823 K**	**723 K**	**773 K**	**823 K**
Zr(IV), Zr(IV)/Zr(II)	3.06×10^{-6}	2.86×10^{-6}	5.82×10^{-6}	-2.099	-2.049	-1.906
	$D = 4.60 \times 10^{-4} \exp\left(\frac{-30{,}900}{RT}\right)$			$E^{0*} = 0.002T - 3.508$		
Zr(II), Zr(II)/Zr	1.27×10^{-5}	1.47×10^{-5}	3.33×10^{-5}	-2.385	-2.333	-2.312
	$D = 0.0270 \exp\left(\frac{-46{,}700}{RT}\right)$			$E^{0*} = 0.0007T - 2.908$		

- The activity coefficient result depends greatly on the theoretical thermodynamic data used to compare with the experimental. Two sources of theoretical Gibbs energy for zirconium have been found in the literature, which differ by a large amount. This

outcome results in values that differ by as much as 14 orders of magnitude (see Table 4.7).

5.4.3 Uranium and Zirconium Electrochemistry

Based on the results of the third study, the following conclusions can be drawn:

- The CV results reveal that high concentration of UCl_3 hide some of the important features of the smaller concentration of $ZrCl_4$. There is no distinctive feature of zirconium that can be observed from the low concentration CV data sets.
- Careful examination indicates that there is a small hump on the large anodic peak at approximately -0.5 V showing a small sign of the Zr/Zr(II) oxidation process. The presence of zirconium becomes prominent as the concentration of $ZrCl_4$ increases.
- It is possible to expect that the ZrCl is likely not fully reduced to metal during the cathodic sweep leaving some ZrCl to oxidize during the following anodic sweep. This would be possible with large amounts of uranium present in the mixture. This can be used to explain a possible impediment to electrorefining pure Zr metal in the presence of large UCl_3 concentrations.
- The addition of $ZrCl_4$ to UCl_3-LiCl-KCl mixtures shows a decrease in the expected peak height. This is likely due to the smaller diffusivities of zirconium ions with respect to the uranium ions along with destructive interference of the multiple peaks contributing to the measure cathodic peaks.

5.4.4 Plots of All Important Calculated Values

All experimental data can be summarized and plotted as shown in Figures 5.1, 5.2, and 5.3 for comparison to previously published values.

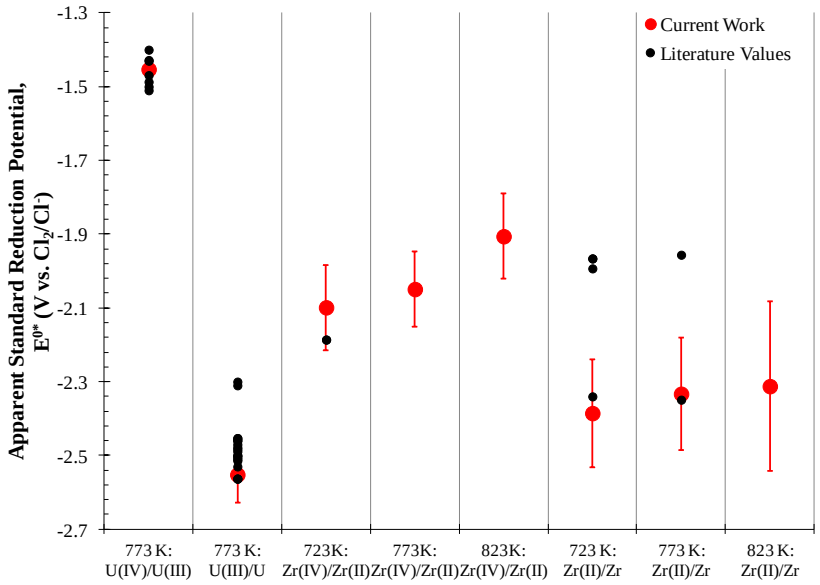

Figure 5.1 Comparison of experimental and previously published values for the apparent standard reduction potentials of uranium and zirconium in the LiCl-KCl eutectic [4, 18-19, 21-22, 32, 35-39, 41, 43, 45, 49-53].

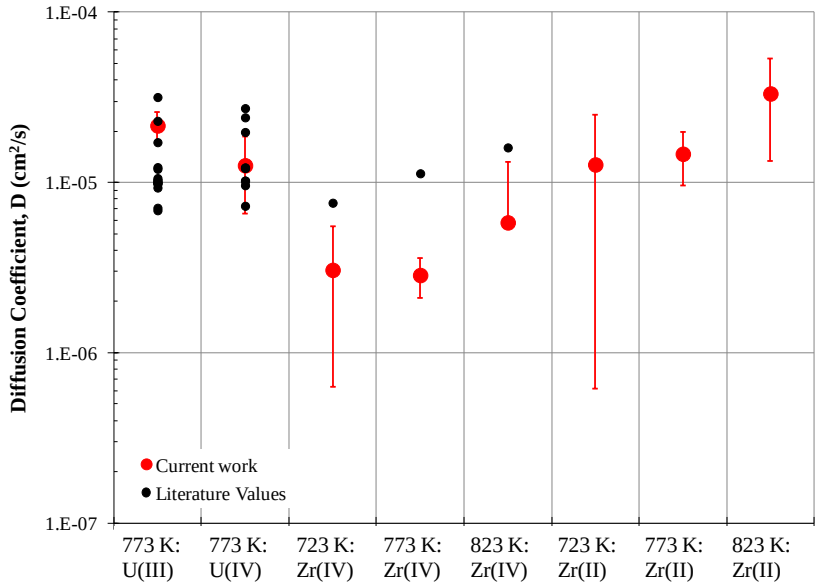

Figure 5.2 Comparison of experimental and previously published values for the diffusivity of uranium and zirconium ions in the LiCl-KCl eutectic [31, 33-34, 37-42, 49, 52-56].

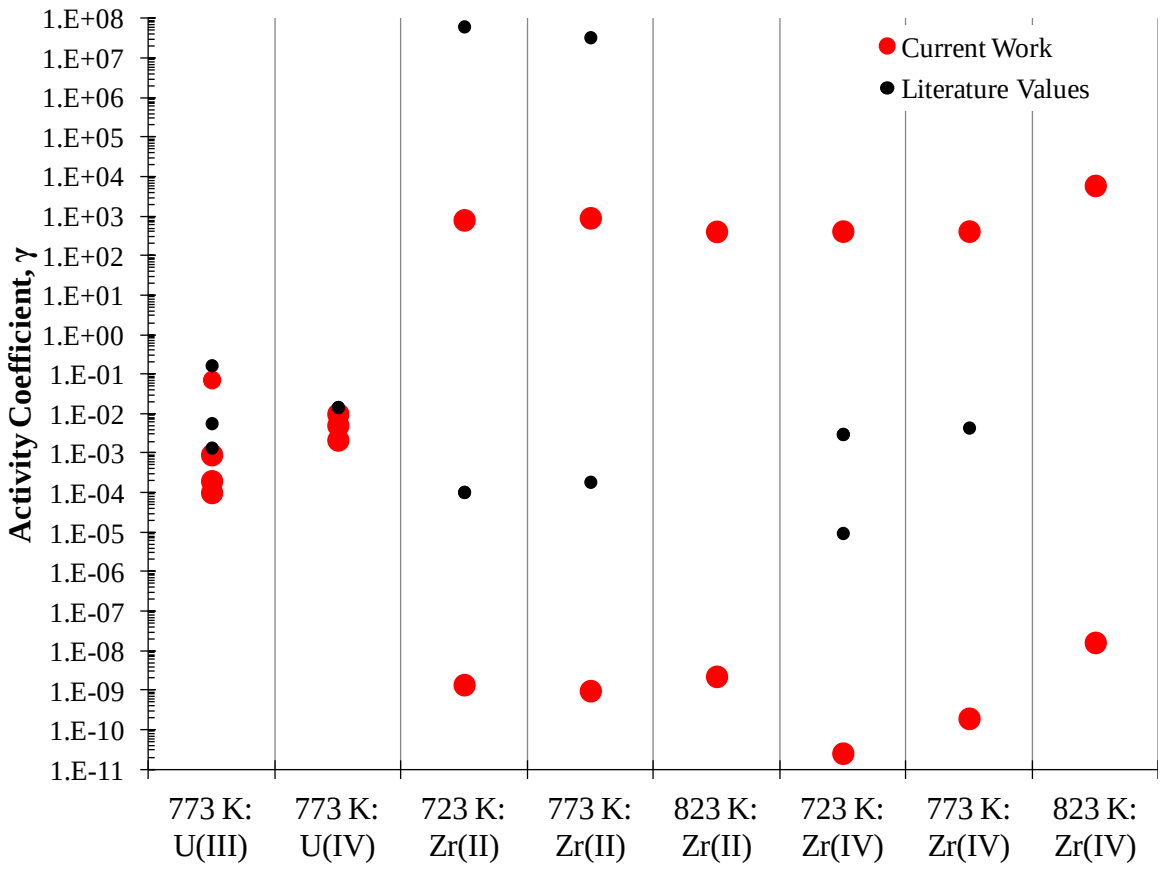

Figure 5.3 Comparison of experimental and previously published values for the activity coefficients of uranium and zirconium in the LiCl-KCl eutectic [31, 35, 39, 43-46, 53, 57].

5.5 Future Work

Several recommendations for future work based on this study can be made as follows:

- Computational modeling is necessary for testament of a successful project. Currently, this work has been handled by SNU and KAERI in a collaborative effort with UI and INL. Development of the computational model based on these experimental parameters is recommended.
- An analysis of the exchange current density, i_0, and standard rate constant, k_s, is necessary for modeling. This study will be applicable with the potentiostatic-

electrochemical impedance spectroscopy (P-EIS) data, which provides the necessary information for the calculation of k_s and $i_{0.}$ Several P-EIS data sets were experimentally recorded for the zirconium experiments. Detailed analysis is required on those measured data sets, and is recommended as a future study. Data was collected in triplicate at the peak cathodic potentials shown in the CVs in Chapter 4 and at a potential at which no reaction occurred. This impedance data can be fit to an equivalent electrical circuit, from which a charge transfer resistance, R_{CT}, is determined, which is related to k_s and i_0 by [38]

$$R_{CT} = \frac{RT}{nFi_0} = \frac{RT}{n^2F^2k_sC_{ox}^{1-\alpha}}. \quad (5.1)$$

From this data, k_s and i_0 can be calculated for the zirconium reactions as a function of temperature, improving the accuracy of the calculated apparent standard reduction potentials and allowing for the calculation of i_0.

- A deconvolution method for the $ZrCl_4$-UCl_3-LiCl-KCl cyclic voltammetry data could be a useful tool in determining the contribution of each species to the overall measured CV peaks. A successful implementation of this technique will provide an important benefit in determining individual species concentrations via electrochemical methods.

References

[1] Nuclear Technology Review 2013, International Atomic Energy Agency, July 22, 2013.

[2] 2013-2014 Information Digest, NUREG-1350, United States Nuclear Regulatory Commission, July 2013.

[3] W.D. Magwood, "Generation IV: Looking Back," 2012 American Nuclear Society Winter Meeting; San Diego, CA, November 11-15, 2012. available at: https://www.gen-4.org/gif/upload/docs/application/pdf/2013-10/ans_-_gen_iv_session_2013-10-07_13-55-18_733.pdf

[4] O. Shirai, H. Yamana, and Y. Arai, "Electrochemical Behavior of Actinides and Actinide Nitrides in LiCl-KCl Eutectic Melts," *Journal of Alloys and Compounds*, **408-412**, 1267-1273 (2006).

[5] J.J. Laidler, J.E. Battles, W.E. Miller, J.P. Ackerman and E.L. Carls, "Development of Pyroprocessing Technology," *Progress in Nuclear Energy*, **31**, 131-140 (1997).

[6] C.C. McPheeters, J.P. Ackerman, E.C. Gay and G.K. Johnson, "Application of Spent Fuel Treatment Technology to Plutonium Immobilization," *Proceedings of the 1996 DOE Spent Nuclear Fuel and Fissile Management Embedded Topical Meeting*; Reno, NV, June 16-20, 1996.

[7] C.C. McPheeters, E.C. Gay, E.J. Karell, and J.P. Ackerman, "Electrometallurgically Treating Metal, Oxide, and Al Alloy Spent Nuclear Fuel Types," *Journal of the Minerals, Metals and Materials Society*, **49(7)**, 22-25 (1997).

[8] Y.I. Chang, "The Integral Fast Reactor," *Nuclear Technology*, **88**, 129-138 (1989).

[9] J.P. Ackerman, “Chemical Basis for Pyrochemical Reprocessing of Nuclear Fuel,” *Industrial and Engineering Chemistry Research*, **30**, 141-145 (1991).

[10] C.E. Till and Y.I. Chang, *Plentiful Energy - The Story of the Integral Fast Reactor*, p. 41, self-published, (2011).

[11] R.D. Mariani, R.W. Benedict, R.M. Lell, R.B. Turski, and E.K. Fujita, "Criticality Safety Strategy and Analysis Summary for the Fuel Cycle Facility Electrorefiner at Argonne National Laboratory West," *Nuclear Technology*, **114(2)**, 224-234 (1996).

[12] F.H. Driggs and W.C. Lilliendahl, “Preparation of Metal Powders by Electrolysis of Fused Salts: I – Ductile Uranium,” *Industrial and Engineering Chemistry*, **22(5)**, 516-519 (1930).

[13] M. Kolodney, “Preparation of the First Electrolytic Plutonium and of Uranium from Fused Chlorides,” *Journal of the Electrochemical Society: Electrochemical Science and Technology*, **129(11)**, 2438-2442 (1982).

[14] L.W. Niedrach and A.C. Glamm, “Uranium Purification by Electrorefining,” *Journal of the Electrochemical Society*, **103(9)**, 521-528 (1956).

[15] L. Burris, R.K. Steunenberg and W.E. Miller, “The Application of Electrorefining for Recovery and Purification of Fuel Discharged from the Integral Fast Reactor,” *Proceedings of the AIChE Annual Meeting*; Miami, FL, November 2-7, 1986.

[16] J. Sangster and A.D. Pelton, “Phase Diagrams and Thermodynamic Properties of the 70 Binary Alkali Halide Systems Having Common Ions,” *Journal of Physical and Chemical Reference Data*, **16(3)**, 509-561 (1987).

[17] S.X. Li and M.F. Simpson, "Anodic Process of Electrorefining Spent Driver Fuel in Molten LiCl-KCl-UCl_3/Cd System," *Minerals and Metallurgical Processing*, **22(4)**, 192-198 (2005).

[18] J.A. Plambeck, "Electromotive Force Series in Molten Salts," *Journal of Chemical and Engineering Data*, **12(1)**, 77-82 (1967).

[19] A.J. Bard, *Encyclopedia of Electrochemistry of the Elements, Vol. X, Fused Salt Systems*, p. 68, Marcel Dekker, Inc., New York (1976).

[20] H.A. Laitinen and C.H. Liu, "An Electromotive Force Series in Molten Lithium Chloride - Potassium Chloride Eutectic," *Journal of the American Chemical Society*, **80(5)**, 1015-1020 (1958).

[21] M. Iizuka, T. Inoue, O. Shirai, T. Iwai, and Y. Arai, "Application of Normal Pulse Voltammetry to On-line Monitoring of Actinide Concentrations in Molten Salt Electrolyte," *Journal of Nuclear Materials*, **297**, 43-51 (2001).

[22] R.K. Ahluwalia and T.Q. Hua, "Electrotransport of Uranium from a Liquid Cadmium Anode to a Solid Cathode," *Nuclear Technology*, **140**, 41-50 (2002).

[23] J. Serp, R.J.M. Konings, R. Malmbeck, J. Rebizant, C. Scheppler, and J.P. Glatz, "Electrochemical Behaviour of Plutonium Ion in LiCl-KCl Eutectic Melts," *Journal of Electroanalytical Chemistry*, **561**, 143-148 (2004).

[24] W.J. Hamer, M.S. Malmberg, and B. Rubin, "Theoretical Electromotive Forces for Cells Containing a Single Solid or Molten Chloride Electrolyte," *Journal of the Electrochemical Society*, **103(1)**, 8-16 (1956).

[25] S.X. Li, T.A. Johnson, B.R. Westphal, K.M. Goff, and R.W. Benedict, "Electrorefining Experience for Pyrochemical Processing of Spent EBR-II Driver Fuel," *Proceedings of Global 2005*; Tsukuba, Japan, October 9-13, 2005.

[26] S.X. Li, D. Vaden, B.R. Westphal, G.L. Fredrickson, R.W. Benedict, and T.A. Johnson, "Integrated Efficiency Test for Pyrochemical Fuel Cycles," *Proceedings of GLOBAL 2007*; Boise, Idaho, September 9-13, 2007.

[27] B.R. Westphal and R.D. Mariani, "Uranium Processing during the Treatment of Sodium-Bonded Spent Nuclear Fuel," *Journal of the Minerals, Metals and Materials Society*, **52(9)**, 21-25 (2000).

[28] R.W. Benedict, H.F. McFarlane, "EBR-II Spent Fuel Treatment Demonstration Project Status," *RADWASTE*, **5**, 23 (1998).

[29] S.X. Li, "Electrorefining Theory and Applications in Pyrochemical Processing of Spent Nuclear Fuel - An Integral Part of a Closed Nuclear Fuel Cycle," University of New Mexico Seminar; Albuquerque, NM, November 7, 2005.

[30] C.H. Lee, K.H. Kang, M.K. Jeon, C.M. Heo, and Y.L. Lee, "Electrorefining of Zirconium from Zircaloy-4 Cladding Hulls in LiCl-KCl Molten Salts," *Journal of the Electrochemical Society*, **159(8)**, D463-D468 (2012).

[31] D. Inman, G.J. Hills, L. Young, and J. O'M. Bockris, "Electrode Reactions in Molten Salts: The Uranium + Uranium Trichloride System," *Transactions of the Faraday Society*, **55**, 1904-1914 (1959).

[32] D.L. Hill, J. Perano, and R.A. Osteryoung, "An Electrochemical Study of Uranium in Fused Chlorides," *Journal of the Electrochemical Society*, **107(8)**, 698-705 (1960).

[33] C.E. Thalmayer, S. Bruckenstein, and D.M. Gruen, "Chronopotentiometric Determination of Interdiffusion Coefficients and Heats of Interdiffusion in Molten Salts," *Journal of Inorganic Nuclear Chemistry*, **26**, 347-357 (1964).

[34] F. Caligara, L. Martinot, and G. Duyckaerts, "Contribution to the Knowledge of the Electrochemistry of Uranium in Molten LiCl-KCl Eutectic. II. Chronopotentiometric Study of the Reaction U(IV)+e↔U(III) and Measurement of the Diffusion Coefficient," *Bulletin des Sociétés Chimique Belges*, **76**, 15-25 (1967).

[35] J.J. Roy, L.F. Grantham, D.L. Grimmett, S.P. Fusselman, C.L. Krueger, T.S. Storvick, T. Inoue, Y. Sakamura, and N. Takahashi, "Thermodynamic Properties of U, Np, Pu, and Am in Molten LiCl-KCl Eutectic and Liquid Cadmium," *Journal of the Electrochemical Society*, **143(8)**, 2487-2492 (1996).

[36] Y. Sakamura, T. Hijikata, K. Kinoshita, T. Inoue, T.S. Storvick, C.L. Krueger, J.J. Roy, D.L. Grimmett, S.P. Fusselman, and R.L. Gay, "Measurement of Standard Potentials of Actinides (U, Np, Pu, Am) in LiCl-KCl Eutectic Salt and Separation of Actinides from Rare Earths by Electrorefining," *Journal of Alloys and Compounds*, **271-273**, 592-596 (1998).

[37] B.P. Reddy, S. Vandarkuzhali, T. Subramanian, and P. Venkatesh, "Electrochemical Studies on the Redox Mechanism of Uranium Chloride in Molten LiCl-KCl Eutectic," *Electrochimica Acta*, **49**, 2471-2478 (2004).

[38] S.A. Kuznetsov, H. Hayashi, K. Minato, and M. Gaune-Escard, "Electrochemical Behavior and Some Thermodynamic Properties of UCl_4 and UCl_3 Dissolved in a LiCl-KCl Eutectic Melt," *Journal of the Electrochemical Society*, **152(4)**, C203-C212 (2005).

[39] P. Masset, D. Bottomley, R. Konings, R. Malmbeck, A. Rodrigues, J. Serp, and J.Glatz, “Electrochemistry of Uranium in Molten LiCl-KCl Eutectic”, *Journal of the Electrochemical Society*, **152(6)**, A1109-A1115 (2005).

[40] I. Choi, "Determination of Exchange Current Density of U^{3+}/U Couple in LiCl-KCl Eutectic Mixture," *Proceedings of Global 2009*; Paris, France, Sept. 6-11, 2009.

[41] F. Gao, C. Wang, L. Liu, J. Guo, S. Chang, L. Chang, R. Li, and Y. Ouyang, "Electrode Processes of Uranium Ions and Electrodeposition of Uranium in Molten LiCl-KCl," *Journal of Radioanalytical and Nuclear Chemistry*, **280(1)**, 207-218 (2009).

[42] S. Kim, D. Yoon, Y. You, S. Paek, J. Shim, S. Kwon, K. Kim, H. Chung, D. Ahn, and H. Lee, "In-situ Observation of a Dendrite Growth in an Aqueous Condition and a Uranium Deposition into a Liquid Cadmium Cathode in an Electrowinning System," *Journal of Nuclear Materials*, **385**, 196-199 (2009).

[43] D. Inman and J.O’M. Bockris, “The Reversible Electrode Potential of the System U/UCl_3 in Molten Chloride Solvents,” *Canadian Journal of Chemistry*, **39**, 1161-1163 (1961).

[44] R. Baboian, D.L. Hill, and R.A. Bailey, "Electrochemical Studies on Zirconium and Hafnium in Molten LiCl-KCl Eutectic, *Journal of the Electrochemical Society*, **112(12)**, 1221-1224 (1965).

[45] R. Ahluwalia, T.Q. Hua, and H.K. Geyer, "Behavior of Uranium and Zirconium in Direct Transport Tests with Irradiated EBR-II Fuel," *Nuclear Technology*, **126**, 289-302 (1999).

[46] R.K. Ahluwalia, T.Q. Hua, and H.K. Geyer, "Removal of Zirconium in Electrometallurgical Treatment of Experimental Breeder Reactor II Spent Fuel," *Nuclear Technology*, **133**, 103-118 (2001).

[47] Y. Sakamura, "Zirconium Behavior in Molten LiCl-KCl Eutectic," *Journal of the Electrochemical Society*, **151(3)**, C187-C193 (2004).

[48] L. Yang and R.G. Hudson, "Some Investigations of the Ag/AgCl in LiCl-KCl Eutectic Reference Electrode," *Journal of the Electrochemical Society*, **106(11)**, 986-990 (1959).

[49] T. Kobayashi, R. Fujita, M. Fujie, and T. Koyama, "Polarization Effects in the Molten Salt Electrorefining of Spent Nuclear Fuel," *Journal of Nuclear Science and Technology*, **32(7)**, 53-63 (1995).

[50] T. Murakami and T. Kato, "Electrochemical Behavior of Zr on a Liquid Cd Electrode in LiCl-KCl Eutectic Melts," *Journal of the Electrochemical Society*, **155(7)**, E90-E95 (2008).

[51] A.V. Bychkov, O.V. Skiba, S.K. Vavilov, S. Kormilitzyn, and A.G. Osipenco, "Overview of RIAR Activity on Pyroprocess Development and Application to Oxide Fuel and Plans in the Coming Decade," *Proceedings of the Workshop on Pyrochemical Separations*; Avignon, France, March 14-16, 2000.

[52] K.R. Kim, S.Y. Choi, D.H. Ahn, S. Paek, B.G. Park, H.S. Lee, K.W. Yi, and I.S. Hwang, "Computational Analysis of a Molten-Salt Electrochemical System for Nuclear Waste Treatment," *Journal of Radioanalytical and Nuclear Chemistry*, **282**, 449-453 (2009).

[53] P. Masset, R.J.M. Konings, R. Malmbeck, J. Serp, and J.P. Glatz, “Thermochemical Properties of Lanthanides (Ln = La, Nd) and Actinides (An = U, Np, Pu, Am) in Molten LiCl-KCl Eutectic,” *Journal of Nuclear Materials*, **344**, 173-179 (2005).

[54] G.J. Janz and N.P. Bansal, "Molten Salts Data: Diffusion Coefficients in Single and Multi-Component Salt Systems," *Journal of Physical and Chemical Reference Data*, **11(3)**, 505-693 (1982).

[55] D. Yamada, T. Murai, K. Moritani, T. Sasaki, I. Takagi, H. Moriyama, K. Kinoshita, and H. Yamana. “Diffusion Behavior of Actinide and Lanthanide Elements in Molten Salt for Reductive Extraction,” *Journal of Alloys and Compounds*, **444-445**, 557-560 (2007).

[56] L. Martinot, and G. Duyckaerts, “Chronopotentiometric Study of the Reaction Pu(IV) + e → Pu(III) in Molten LiCl-KCl Eutectic,” *Inorganic and Nuclear Chemistry Letters*, **6(6)**, 587-593 (1970).

[57] T. Koyama, T.R. Johnson, and D.F. Fischer, "Distribution of Actinides in Molten Chloride Salt/Cadmium Metal Systems," *Journal of Alloys and Compounds*, **189**, 37-44 (1992).

[58] A.J. Bard and L.R. Faulkner, *Electrochemical Methods: Fundamentals and Applications Second Edition*, John Wiley & Sons, Inc., New Jersey (2001).

[59] *Educator's Reference Guide for Electrochemistry*, Pine Instrument Company, Grove City, Pennsylvania (2000).

[60] K. Sridharan, T. Allen, M. Anderson, M. Simpson, L. Olson, M. Mohammadian, S. Martin, J. Sager, and A. Boyle, "Thermal Properties of LiCl-KCl Molten Salt for Nuclear Waste Separation," US DOE, NEUP Final Report Project No. 09-780 (2012).

[61] VersaStudio Electrochemical software, *Princeton Applied Research*, version 1.33 (2012).

[62] VersaStudio Electrochemical software, *Princeton Applied Research*, version 2.02 (2013).

[63] O. Shirai, T. Nagai, A. Uehara, and H. Yamana, "Electrochemical Properties of the Ag+|Ag and Other Reference Electrodes in the LiCl-KCl Eutectic Melts," *Journal of Alloys and Compounds*, **456**, 498-502 (2008).

[64] W.B. Blumenthal, *The Chemical Behavior of Zirconium*, pp. 1-45, D. Van Nostrand Company, Inc., Princeton, NJ (1958).

[65] HSC Chemistry—Chemical reaction and equilibrium software with extensive thermochemical database, *Outokumpu Research*, version 7.00 (2009).

[66] DeeEarl Vaden, "Fuel Conditioning Facility Electrorefiner Process Model," *Separation Science and Technology*, **41**, 2003-2012 (2006).

[67] R.O. Hoover, S. Phongikaroon, M.F. Simpson, S.X. Li, and T.-S. Yoo, "Development of Computational Models for the Mark-IV Electrorefiner - Effect of Uranium, Plutonium, and Zirconium Dissolution at the Fuel Basket-Salt Interface," *Nuclear Technology*, **171(3)**, 276-284 (2010).

[68] R.O. Hoover, "Development of a Computational Model for the Mark-IV Electrorefiner," M.S. Thesis, University of Idaho, Idaho Falls, ID (2010).

Appendix A

Standard Reduction Potentials

Table A.1 Uranium and zirconium standard reduction potentials in the LiCl-KCl eutectic from literature.

Redox Couple	Standard Reduction Potential as reported			Standard Reduction Potential vs. Cl_2/Cl^-		Experimental Method	Conc. (wt%)	Ref.	Note
	723 K	773 K	Ref. Elect.	723 K	773 K				
U	-2.500	---	Cl_2/Cl^-	-2.500	---	Unk.	---	[21]	1
U(III)/U	---	-1.249	Ag/AgCl, 1 wt%	---	-2.483	Unk.	---	[22]	3
U(III)/U	-2.498	---	Cl_2/Cl^-	-2.498	---	EMF	0.04 - 1.61	[35]	
U(III)/U	-2.253	---	Pt^{2+}/Pt	-2.469	---	Lit.	---	[19]	2
U(III)/U	-2.48	-2.4533	Cl_2/Cl^-	-2.48	-2.4533	CV	0.54	[4]	
U(III)/U	-1.283	---	Ag/AgCl, 1 wt%	-2.163	---	CV	0.11 - 1.93	[36]	2
U(III)/U	---	-1.1	Ag/AgCl	---	-2.3	Lit.	---	[49]	
U(III)/U	---	-2.5	Cl_2/Cl^-	---	-2.5	Lit.	---	[50]	
U(III)/U	---	-2.31	Cl_2/Cl^-	---	-2.31	Unk.	---	[51]	
U(III)/U	-2.55	-2.53	Cl_2/Cl^-	-2.55	-2.53	Lit., EMF	---	[39]	
U(III)/U	-2.49	-2.46	Cl_2/Cl^-	-2.49	-2.46	Lit., EMF	---	[39]	
U(III)/U	-2.49	-2.47	Cl_2/Cl^-	-2.49	-2.47	Lit., EMF	---	[39]	
U(III)/U	-2.55	-2.51	Cl_2/Cl^-	-2.55	-2.51	Lit., CV	---	[39]	
U(III)/U	-2.6	-2.5	Cl_2/Cl^-	-2.6	-2.5	Lit., CV	---	[39]	
U(III)/U	-2.5	---	Cl_2/Cl^-	-2.5	---	Lit., EMF	---	[39]	
U(III)/U	-2.543	-2.505	Cl_2/Cl^-	-2.543	-2.505	CV, CP, Conv.	2.10	[39]	
U(III)/U	---	-1.244	Ag/AgCl	---	-2.478	Lit.	---	[52]	
U(III)/U	-1.271	-1.225	Ag/AgCl, 1 wt%	-2.496	-2.459	Unk.	---	[45]	
U(III)/U	-2.541	-2.514	Cl_2/Cl^-	-2.541	-2.514	CV, CP	0.43 - 1.33	[38]	

U(III)/U	-2.484	-2.453	Cl_2/Cl^-	-2.484	-2.453	Lit.	---	[38]	
U(III)/U	-2.540	---	Cl_2/Cl^-	-2.540	---	Lit.	---	[38]	
U(III)/U	-2.520	-2.489	Cl_2/Cl^-	-2.520	-2.489	Lit.	---	[38]	
U(III)/U	-2.498	---	Cl_2/Cl^-	-2.498	---	Lit.	---	[38]	
U(III)/U	-1.61	---	Ag/AgCl, 100 mol%	-2.47	---	EMF	0.01 - 0.08	[32]	
U(III)/U	-2.253	---	Pt/Pt^{2+}	-2.469	---	Lit., EMF	---	[18]	4
U(III)/U	-2.563	-2.563	Cl_2/Cl^-	-2.563	-2.563	CV, CP	---	[53]	
U(III)/U	-1.638 (726 K)	---	Ag/AgCl, 0.73 mol%	-2.671 (726 K)	---	EMF	0.69 - 6.16	[43]	
U(III)/U	-2.666 (700 K)	---	Cl_2/Cl^-	-2.666 (700 K)	---	Unk.	1.35 - 4.70	[37]	
U(III)/U	-2.47 (728 K)	---	Cl_2/Cl^-	-2.47 (728 K)	---	Unk.	0.19 - 1.37	[41]	
U(IV)/U	-1.190	---	Pt/Pt^{2+}	-1.406	---	Lit.	---	[18]	4
U(IV)/U	-2.28	-2.26	Cl_2/Cl^-	-2.28	-2.26	CV, CP	---	[38]	
U(IV)/U	-2.002	---	Pt/Pt^{2+}	-2.218	---	Lit.	---	[19]	4
U(IV)/U(III)	---	-1.40	Cl_2/Cl^-	---	-1.40	Unk.	---	[51]	
U(IV)/U(III)	-1.51	-1.50	Cl_2/Cl^-	-1.51	-1.50	Lit., CV	---	[39]	
U(IV)/U(III)	-1.461	-1.430	Cl_2/Cl^-	-1.461	-1.430	CV, CP, Conv.	2.10	[39]	
U(IV)/U(III)	-1.250	---	Pt/Pt^{2+}	-1.466	---	Lit., EMF	---	[18]	4
U(IV)/U(III)	-1.52	-1.51	Cl_2/Cl^-	-1.52	-1.51	Volt., CP	0.43 - 1.33	[38]	
U(IV)/U(III)	-1.495	-1.487	Cl_2/Cl^-	-1.495	-1.487	Lit.	---	[38]	
U(IV)/U(III)	-1.466	---	Cl_2/Cl^-	-1.466	---	Lit.	---	[38]	
U(IV)/U(III)	-1.492	-1.469	Cl_2/Cl^-	-1.492	-1.469	Lit.	---	[38]	
U(IV)/U(III)	-1.250	---	Pt/Pt^{2+}	-1.466	---	Lit.	---	[19]	4
U(IV)/U(III)	-1.460	-1.428	Cl_2/Cl^-	-1.460	-1.428	CV, CP	---	[53]	

U(IV)/U(III)	-1.47	---	Cl_2/Cl^-	-1.47	---	EMF	0.01 - 0.08	[32]	
U(IV)/U(III)	-1.500 (700 K)	---	Cl_2/Cl^-	-1.500 (700 K)	---	Unk.	1.35 - 4.70	[37]	
Zr(II)/Zr	-1.12	-1.115	Ag/AgCl	-2.34	-2.349	EMF	---	[44]	4
Zr(II)/Zr	-1.75	---	Pt/Pt^{2+}	-1.966	---	Lit., EMF	---	[18]	4
Zr(II)/Zr	-0.768	-0.722	Ag/AgCl, 1 wt%	-1.993	-1.956	Unk.	---	[45]	
Zr(II)/Zr	-1.75	---	Pt/Pt^{2+}	-1.966	---	Lit.	---	[19]	4
Zr(IV)/Zr	-1.860	---	Pt/Pt^{2+}	-2.076	---	Lit.	---	[19]	4
Zr(IV)/Zr	---	-2.0	Cl_2/Cl^-	---	-2.0	Lit.	---	[50]	
Zr(IV)/Zr	---	-2.08	Cl_2/Cl^-	---	-2.08	Unk.	---	[51]	
Zr(IV)/Zr	-1.22	---	Ag/AgCl	-2.45	---	EMF	---	[44]	4
Zr(IV)/Zr	-1.860	---	Pt/Pt^{2+}	-2.076	---	Lit., EMF	---	[18]	4
Zr(IV)/Zr	-0.877	-0.838	Ag/AgCl, 1 wt%	-2.102	-2.072	Unk.	---	[45]	
Zr(IV)/Zr(II)	-1.970	---	Pt/Pt^{2+}	-2.186	---	Lit.	---	[18]	4
Zr(IV)/Zr(II)	-1.970	---	Pt/Pt^{2+}	-2.186	---	Lit.	---	[19]	4

Notes:

1 Temperature not specified. Through comparison with other sources, values assumed to be reported at 723 K.

2 Value reported is E^0_M, based on molarity.

4 Value reported is E^0_x, based on mole fraction.

Conv. Convolution

CP Chronopotentiometry

CV Cyclic Voltammetry

EMF Electromotive Force

Lit. Literature

Unk. Unknown

Volt. Voltammetry

Appendix B

Diffusion Coefficients

Table B.1 Uranium and zirconium diffusion coefficients in the LiCl-KCl eutectic from literature.

Ion	D_0 (cm^2/s)	E_D (J/mol)	Temperature Range (K)	D × 10^5 @ 723 K (cm^2/s)	D × 10^5 @ 773 K (cm^2/s)	Method	Conc. (wt%)	Ref.	Note
U(III)	0.001739	35,600	650-810	0.468	0.686	Lit.	---	[54]	
U(III)	2.64	14,000	723-823	1.02	1.45	CV, CP, CA	0.43 - 1.33	[38]	1
U(III)	---	36,000	---	0.48	---	Lit.	---	[38]	
U(III)	---	39,000	---	0.68	---	Lit.	---	[38]	
U(III)	0.0032	37,100	670-870	0.668	0.992	Lit.	---	[55]	
U(III)	---	---	---	---	10 (775 K)	Lit.	---	[49]	
U(III)	0.00137	24,200	673-823	2.44	3.17	CV, CP, Conv.	2.10	[39]	
U(III)	0.02486	46,750	723-823	1.042	1.723	Lit., CV	---	[39]	
U(III)	0.02277	48,500	723-823	0.7133	1.202	Lit., CV	---	[39]	
U(III)	0.307	66,410	673-798	0.489	0.999	Lit., CV, CP	---	[39]	1
U(III)	0.002046	39,400	673-823	0.4798	0.7098	Lit., CP	---	[39]	
U(III)	0.001216	31,300	673-823	0.666	0.933	Lit., CP	---	[39]	
U(III)	---	---	---	---	1.0	CV	---	[42]	
U(III)	---	---	---	---	1.06	CP	3.27	[40]	
U(III)	---	---	---	---	1.03	Lit.	---	[52]	
U(III)	---	---	---	6	---	EMF	~1.04 - 3.39	[31]	
U(III)	---	---	---	0.680	1.031	CP	0.8 - 1.83	[34]	
U(III)	---	---	---	2.7	---	CV, CP	---	[54]	
U(III)	---	---	---	---	0.98	Unk.	1.35 - 4.70	[37]	
U(III)	---	---	---	8.1 (728 K)	---	Unk.	0.19 - 1.37	[41]	
U(IV)	0.00113	26,000	640-880	1.41	1.87	Lit.	---	[54]	
U(IV)	0.462	32,300	693-894	1.23	2.73	CP	1.84	[33]	1
U(IV)	0.00971	42,900	670-870	0.772	1.23	Lit.	---	[55]	

U(IV)	0.00111	32,300	693-893	0.515	0.729	Lit., CP	---	[39]	
U(IV)	0.000934	29,400	673-823	0.702	0.963	Lit., CP	---	[39]	
U(IV)	0.006048	41,000	673-823	0.6597	1.026	Lit., CP	---	[39]	
U(IV)	0.000525	19,800	673-823	1.95	2.41	CV, CP, Conv.	2.10	[39]	
U(IV)	---	---	---	0.8	1.22	CP	---	[56]	
U(IV)	---	---	---	0.801	1.215	CP	0.8 - 1.83	[34]	
U(IV)	---	---	---	2.1	---	CV, CP	---	[53]	
U(IV)	-2.46	16,260	723-823	0.75	1.02	CV, CP, CA	---	[38]	1
U(IV)	---	41,000	---	0.66	---	Lit.	---	[38]	
U(IV)	---	46,000	---	0.80	---	Lit.	---	[38]	
Zr(IV)	0.00358	37,000	723-873	0.759	1.13	Capillary	---	[55]	

Notes:

1 D_0 and E_A values reported for $\log D = -D_0 - E_D/(RT)$, not Arrhenius equation.

CA Chronoamperometry

Conv. Convolution

CP Chronopotentiometry

CV Cyclic Voltammetry

EMF Electromotive Force

Lit. Literature

Appendix C

Activity Coefficients

Table C.1 Uranium and zirconium ion activity coefficients in the LiCl-KCl eutectic from literature.

Ion	γ (723 K)	γ (773 K)	Method	Conc. (wt%)	Reference
U(III)	0.150	---	Unk.	---	[45]
U(III)	---	0.00579	Unk.	---	[57]
U(III)	---	0.169	Unk.	---	[66]
U(III)	0.0031	---	EMF	0.04 - 1.61	[35]
U(III)	---	0.00139	CP, CV, Conv.	2.10	[39]
U(III)	---	0.00139	CP, CV	---	[53]
U(III)	0.08 (736 K)	---	Unk.	~1.04 - 3.39	[31]
U(III)	0.38 (726 K)	---	Unk.	0.69 - 6.16	[43]
U(IV)	0.0003587	---	Unk.	---	[45]
U(IV)	---	0.0148	CV, Conv.	2.10	[39]
U(IV)	---	0.0148	CV, CP	---	[53]
Zr(II)	0.000105	---	Unk.	---	[45]
Zr(II)	64000000	34000000	EMF	---	[44]
Zr(II)	0.000105	0.00019	Unk.	---	[46]
Zr(IV)	0.003081	---	Unk.	---	[45]
Zr(IV)	0.0000096	---	EMF	---	[44]
Zr(IV)	0.00308	0.00448	Unk.	---	[46]

Notes:

CP Chronopotentiometry

Conv. Convolution

CV Cyclic Voltammetry

EMF Electromotive Force

Unk. Unknown

Appendix D

Uranium Chronopotentiograms (CP)

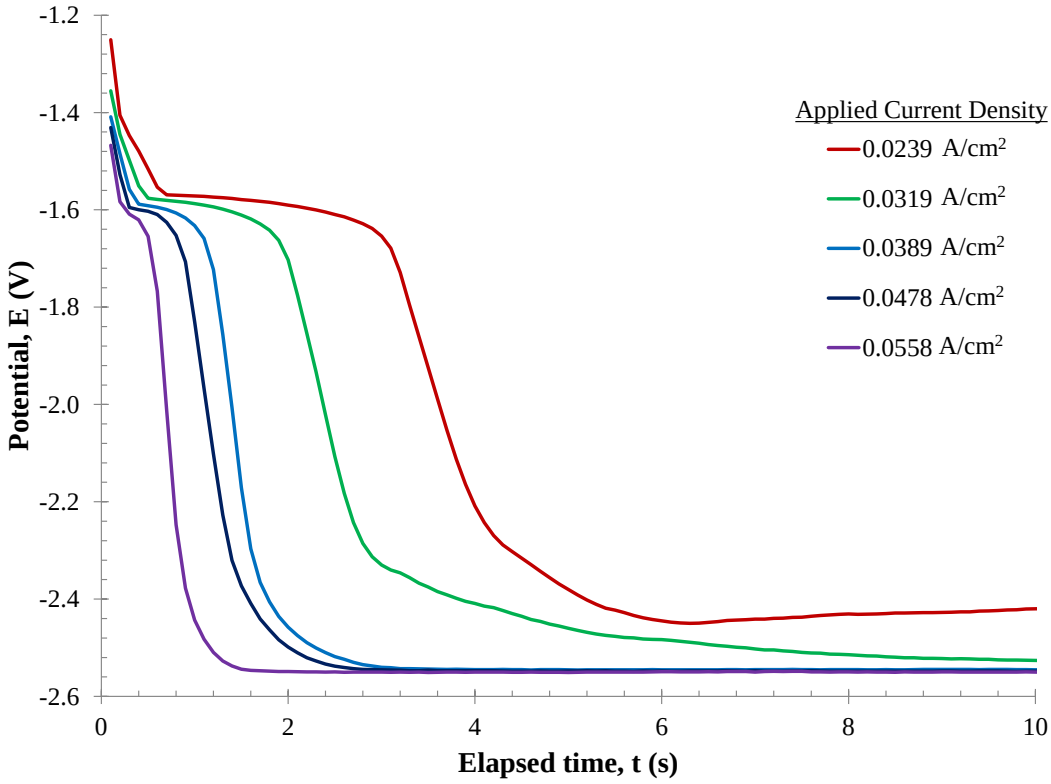

Figure D.1 Chronopotentiograms of 1.00 wt% UCl_3 in LiCl-KCl eutectic at 773 K.

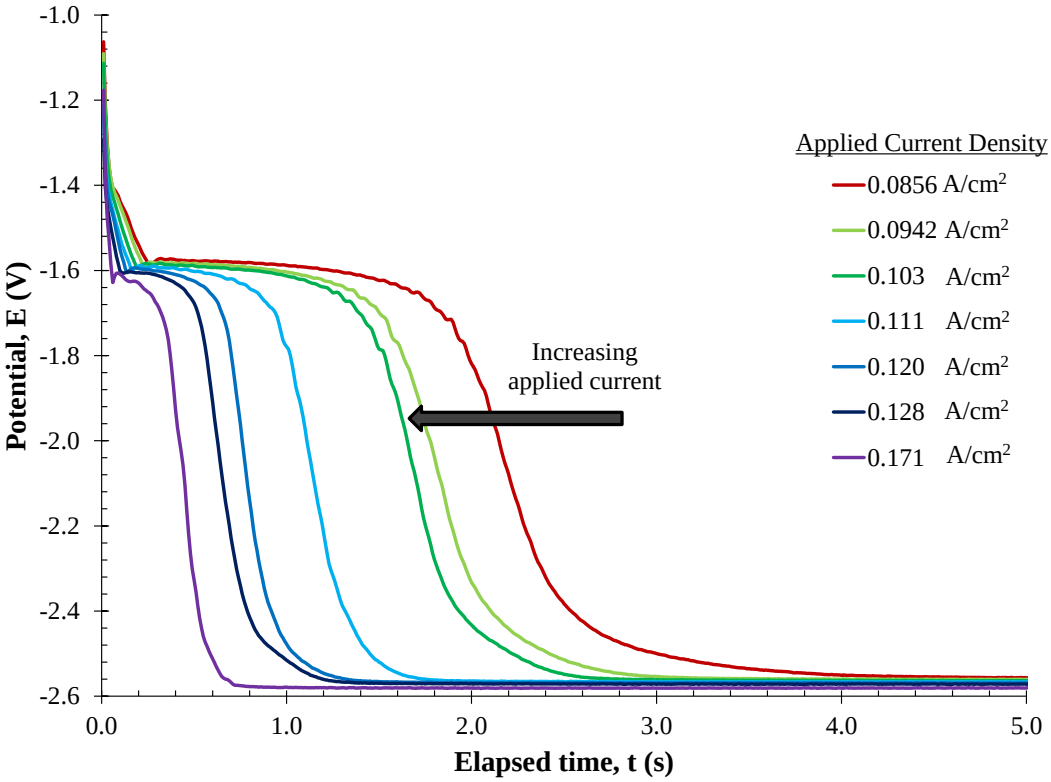

Figure D.2 Chronopotentiograms for 2.50 wt% UCl_3 in LiCl-KCl eutectic at 773 K.

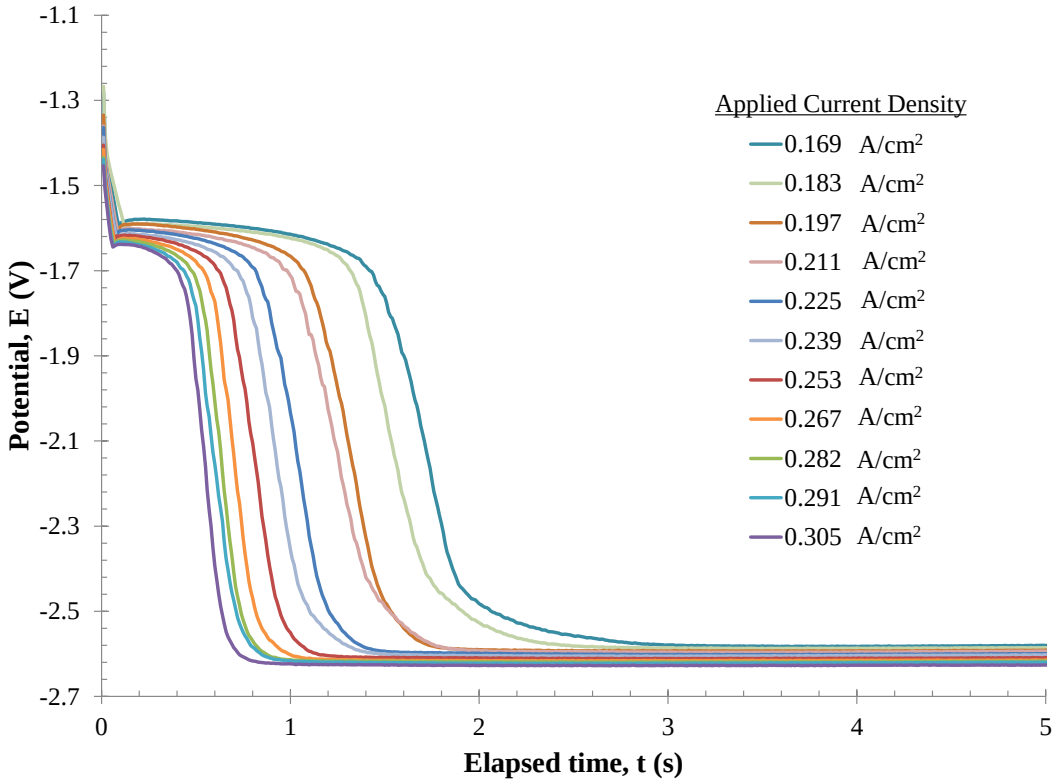

Figure D.3 Chronopotentiograms of 5.00 wt% UCl_3 in LiCl-KCl eutectic at 773 K.

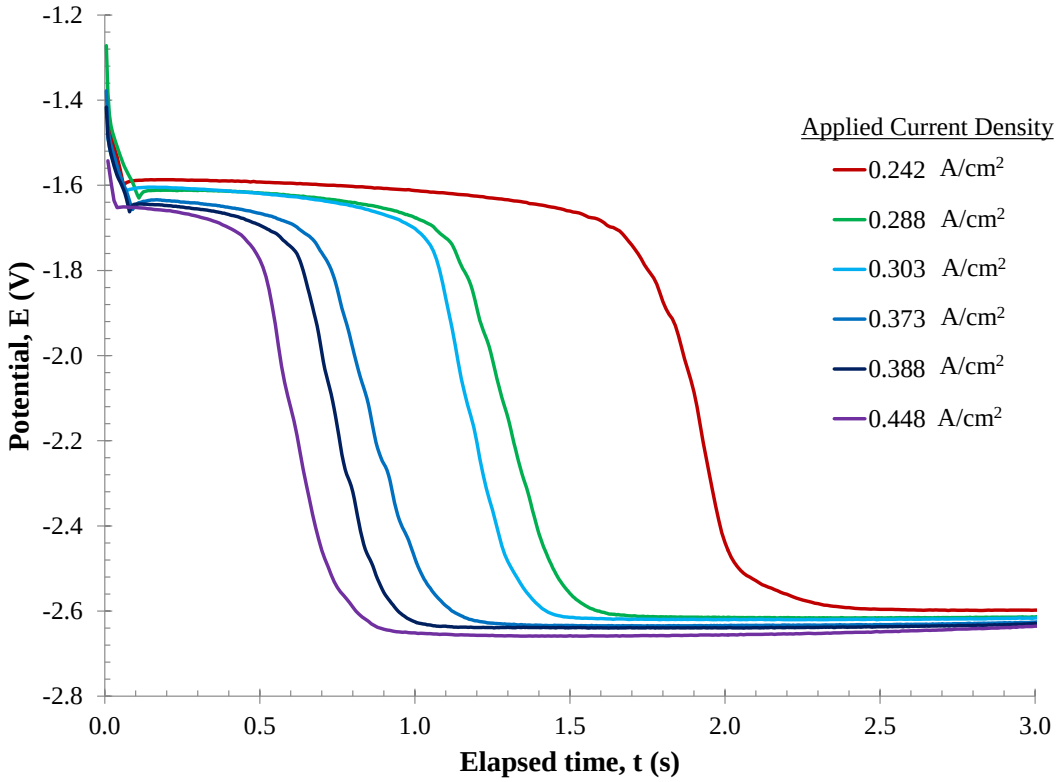

Figure D.4 Chronopotentiograms of 7.50 wt% UCl_3 in LiCl-KCl eutectic at 773 K.

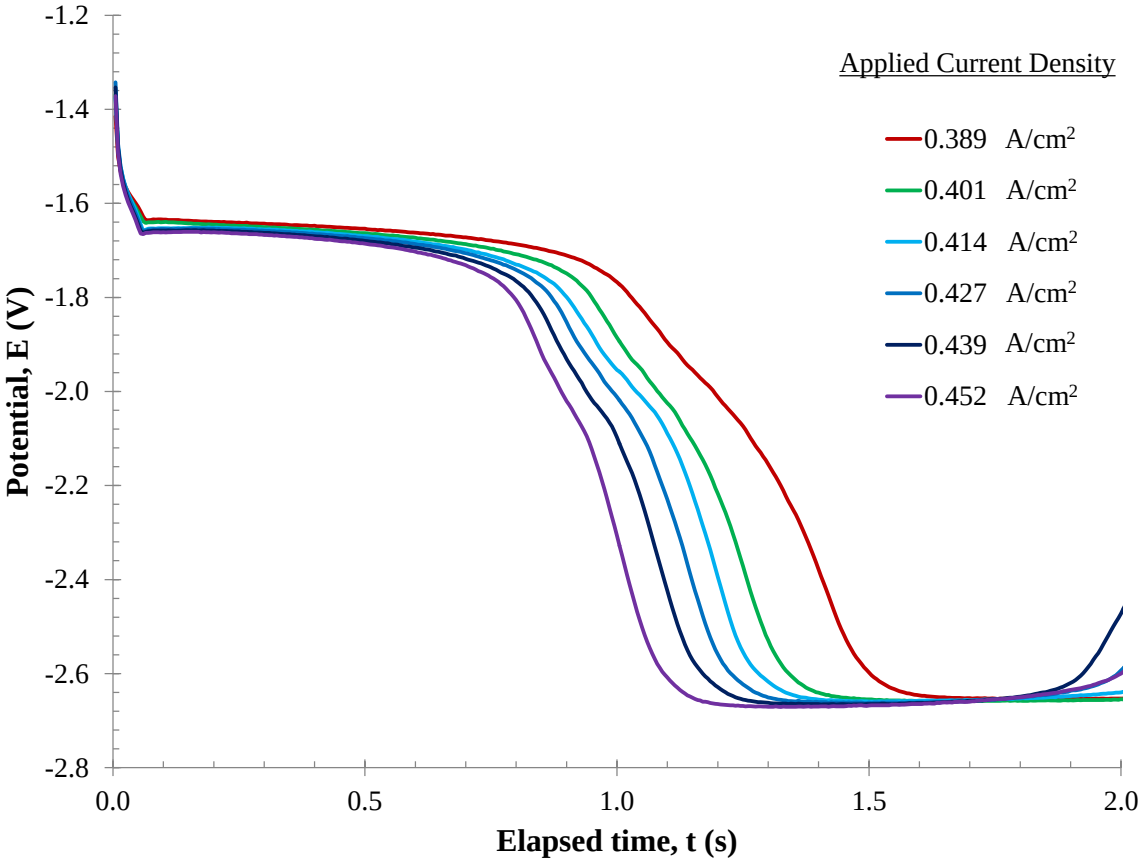

Figure D.5 Chronopotentiograms of 10.0 wt% UCl_3 in LiCl-KCl eutectic at 773 K.

Appendix E

Uranium Anodic Stripping Voltammograms (ASV)

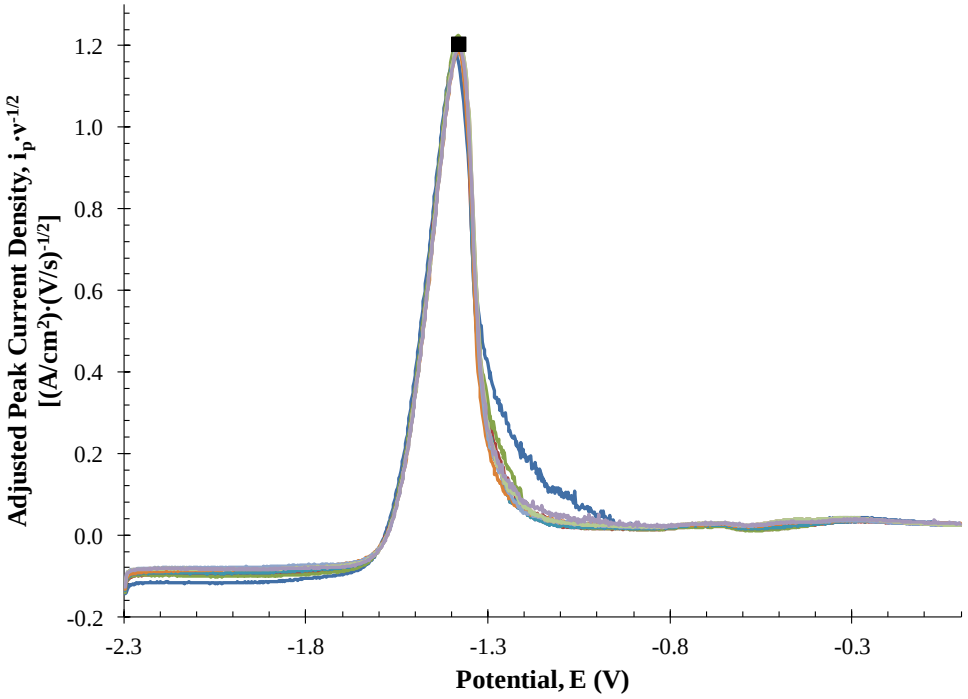

Figure E.1 ASV peaks of 1.00 wt% UCl_3 in LiCl-KCl eutectic at 773 K with 60 second deposition time. The average peak height and potential are marked along with their STD.

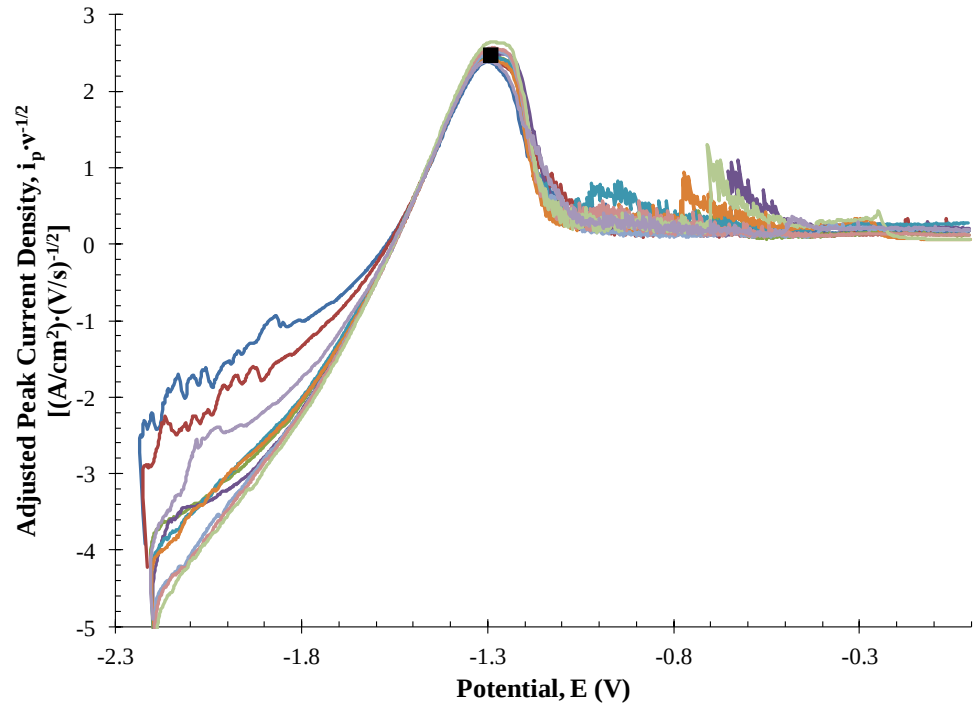

Figure E.2 ASV peaks of 2.50 wt% UCl_3 in LiCl-KCl eutectic at 773 K with 60 second deposition time. The average peak height and potential are marked along with their STD.

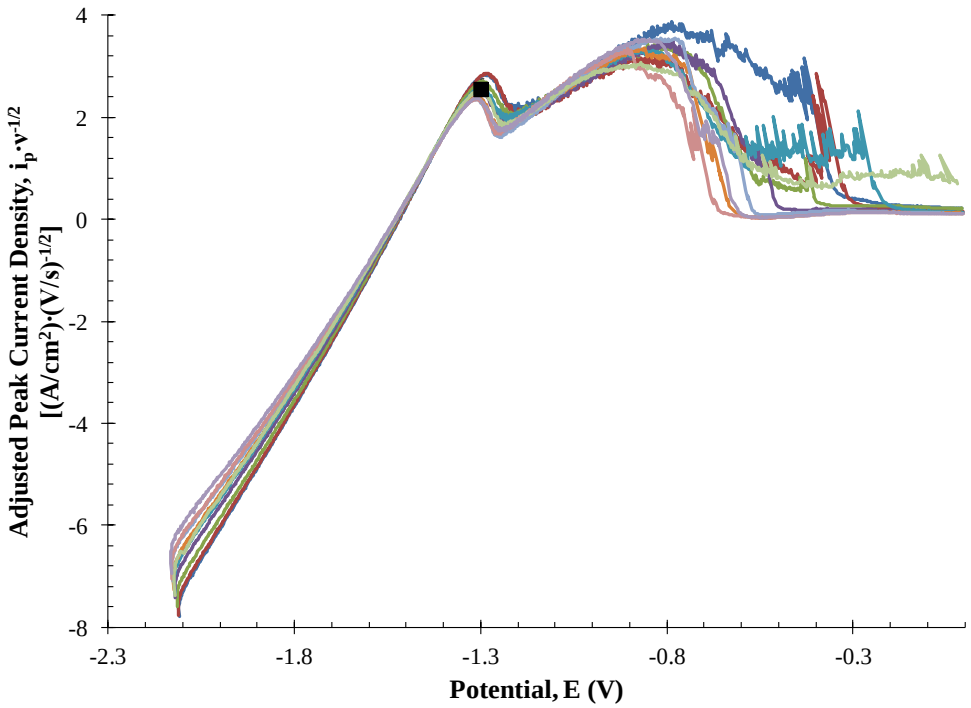

Figure E.3 ASV peaks of 5.00 wt% UCl_3 in LiCl-KCl eutectic at 773 K with 60 second deposition time. The average peak height and potential are marked along with their STD.

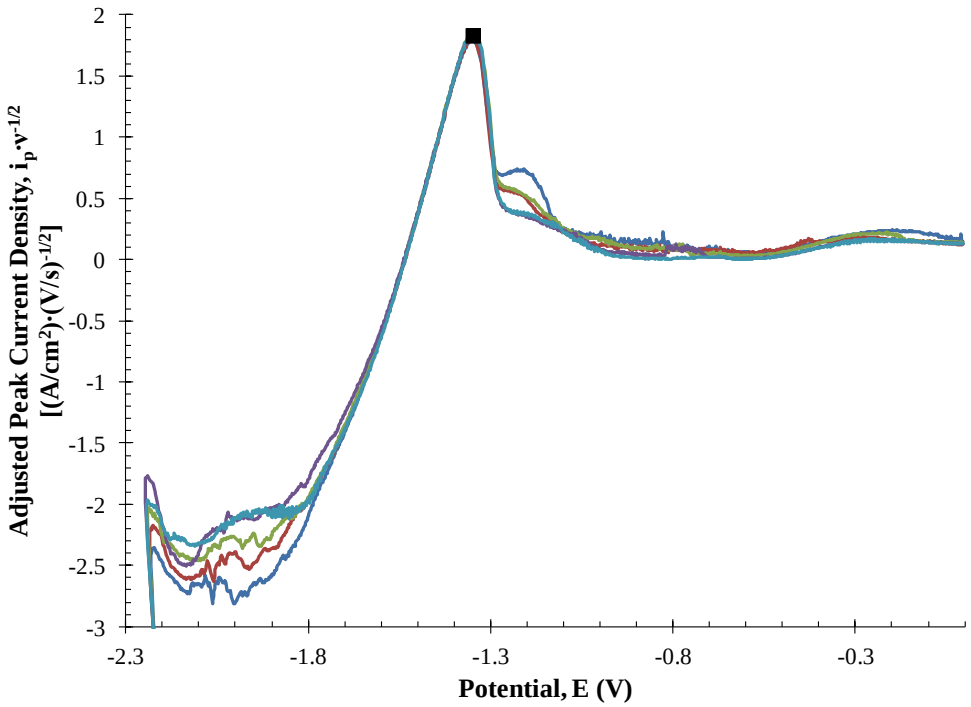

Figure E.4 ASV peaks of 5.00 wt% UCl_3 in LiCl-KCl eutectic at 773 K with 5 second deposition time. The average peak height and potential are marked along with their STD.

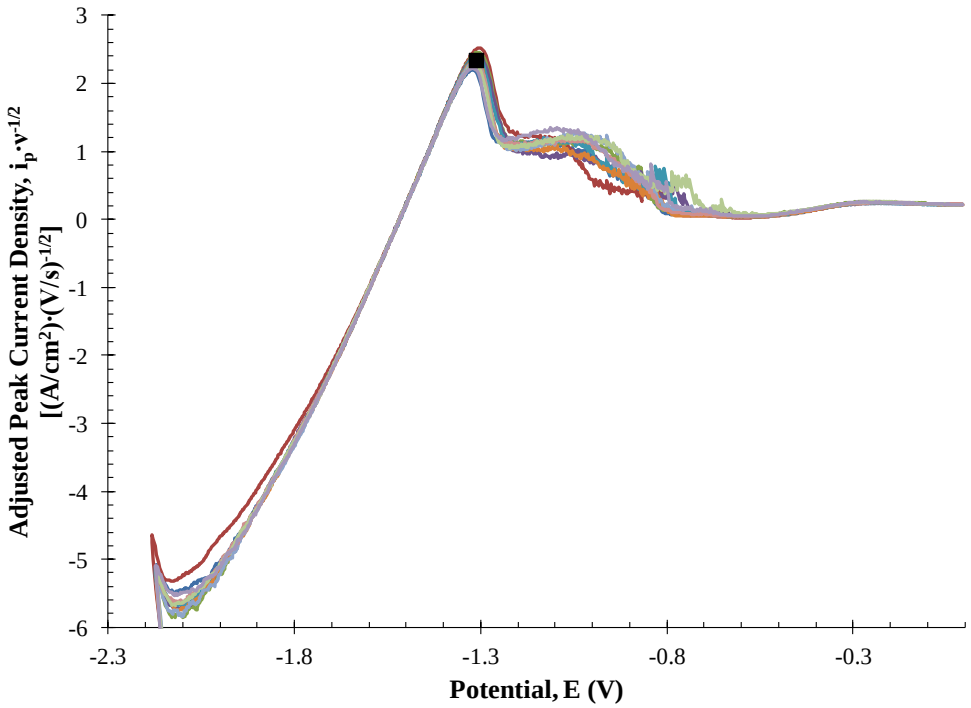

Figure E.5 ASV peaks of 7.50 wt% UCl_3 in LiCl-KCl eutectic at 773 K with 5 second deposition time. The average peak height and potential are marked along with their STD.

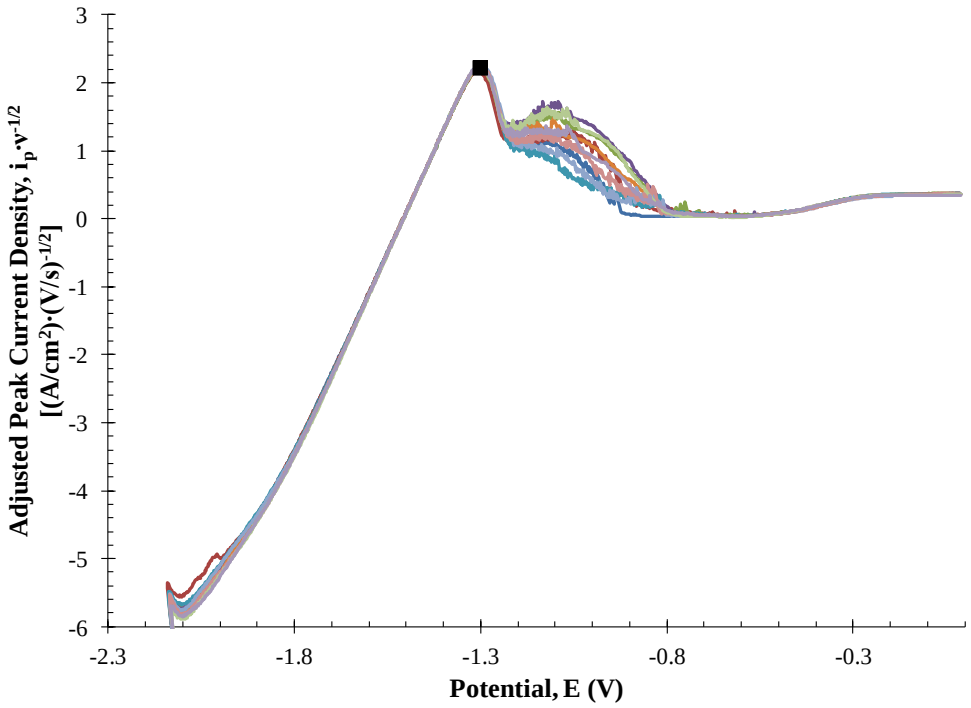

Figure E.6 ASV peaks of 10.0 wt% UCl_3 in LiCl-KCl eutectic at 773 K with 5 second deposition time. The average peak height and potential are marked along with their STD.

Appendix F

Randles-Sevcik and Delahay Equations for Uranium

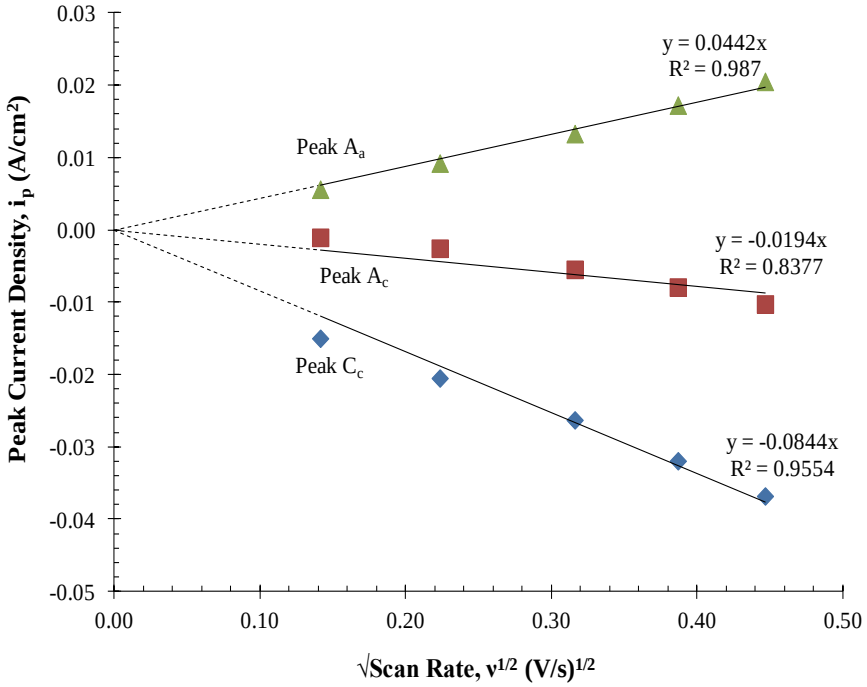

Figure F.1 Peak current versus square root of scan rate for anodic and cathodic peaks in the 1.00 wt% UCl_3 cyclic voltammograms at 773 K.

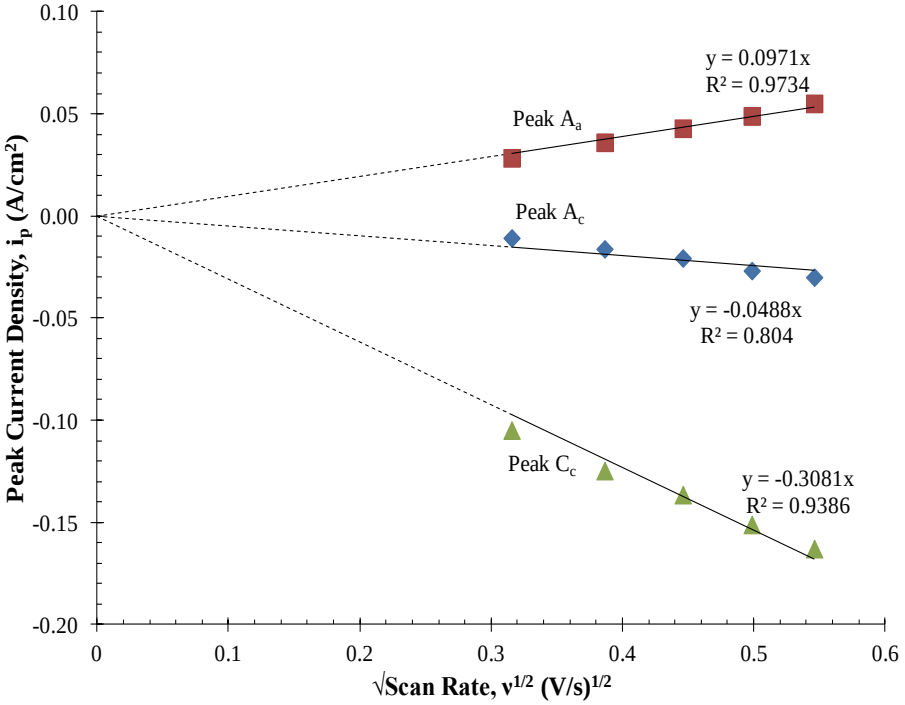

Figure F.2 Peak current versus square root of scan rate for anodic and cathodic peaks in the 2.50 wt% UCl_3 cyclic voltammograms at 773 K.

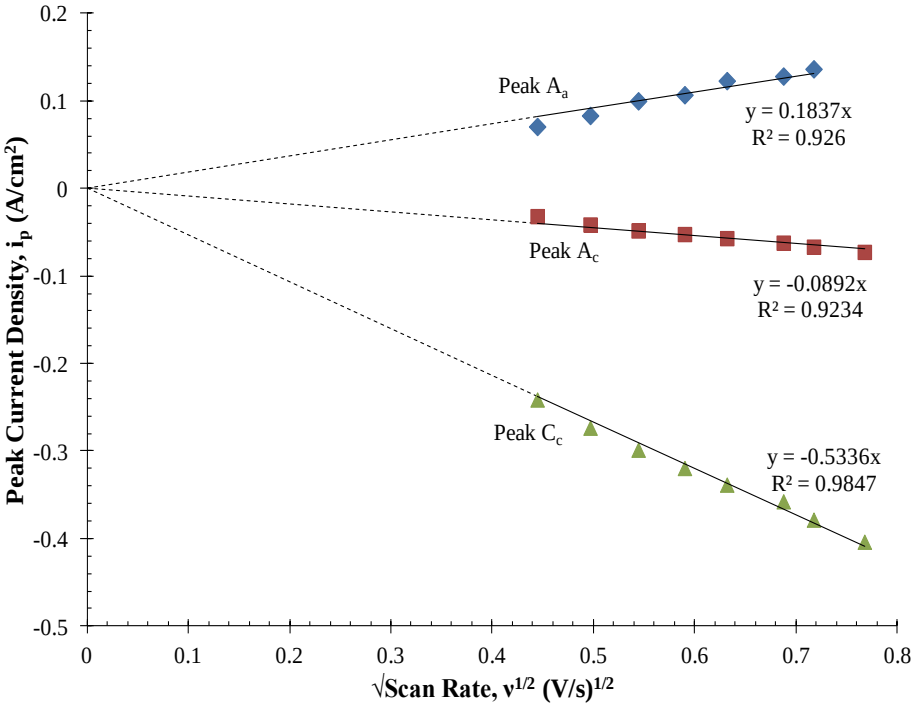

Figure F.3 Peak current versus square root of scan rate for anodic and cathodic peaks in the 5.00 wt% UCl_3 cyclic voltammograms at 773 K.

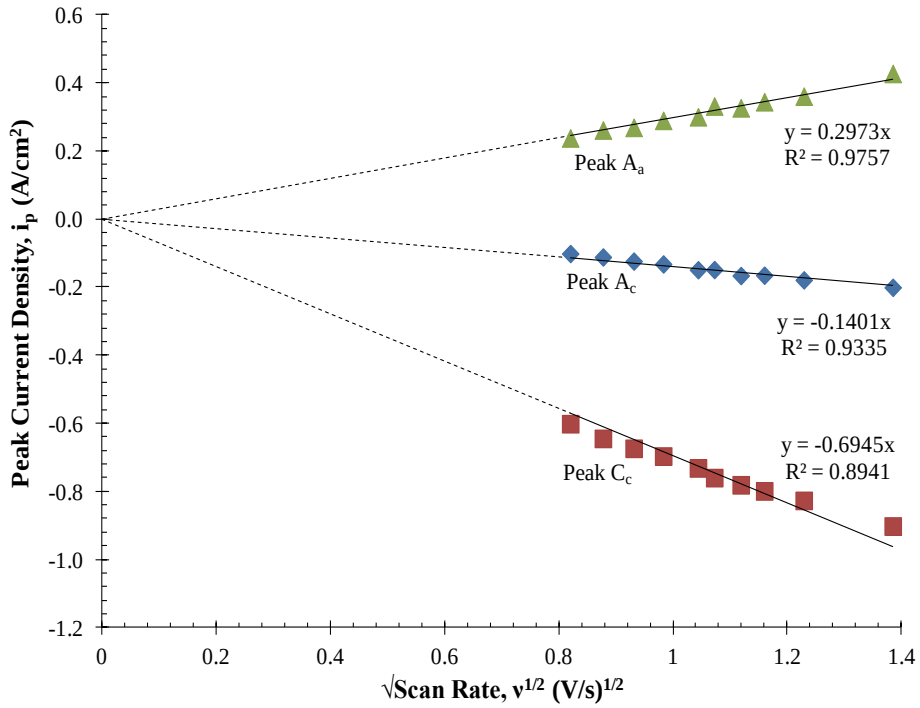

Figure F.4 Peak current versus square root of scan rate for anodic and cathodic peaks in the 7.50 wt% UCl_3 cyclic voltammograms at 773 K.

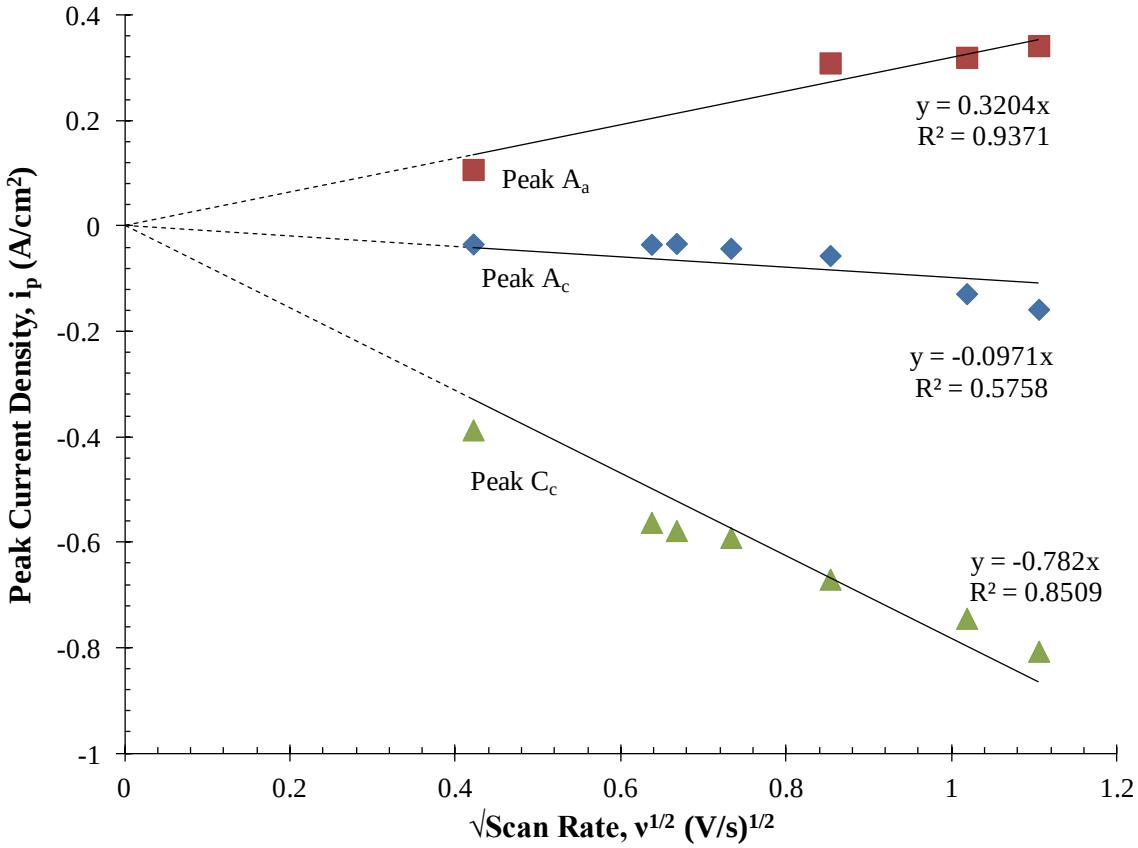

Figure F.5 Peak current versus square root of scan rate for anodic and cathodic peaks in the 10.0 wt% UCl_3 cyclic voltammograms at 773 K.

Appendix G

Zirconium Cyclic Voltammograms (CV)

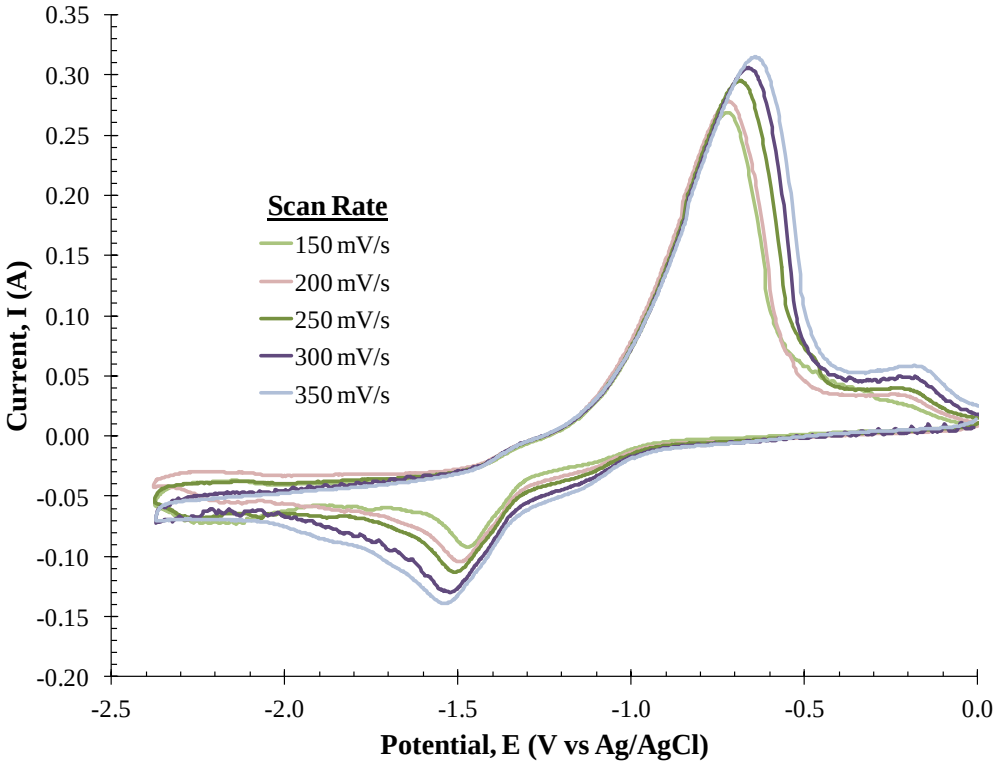

Figure G.1 CVs of 0.57 wt% $ZrCl_4$ in LiCl-KCl eutectic at 723 K.

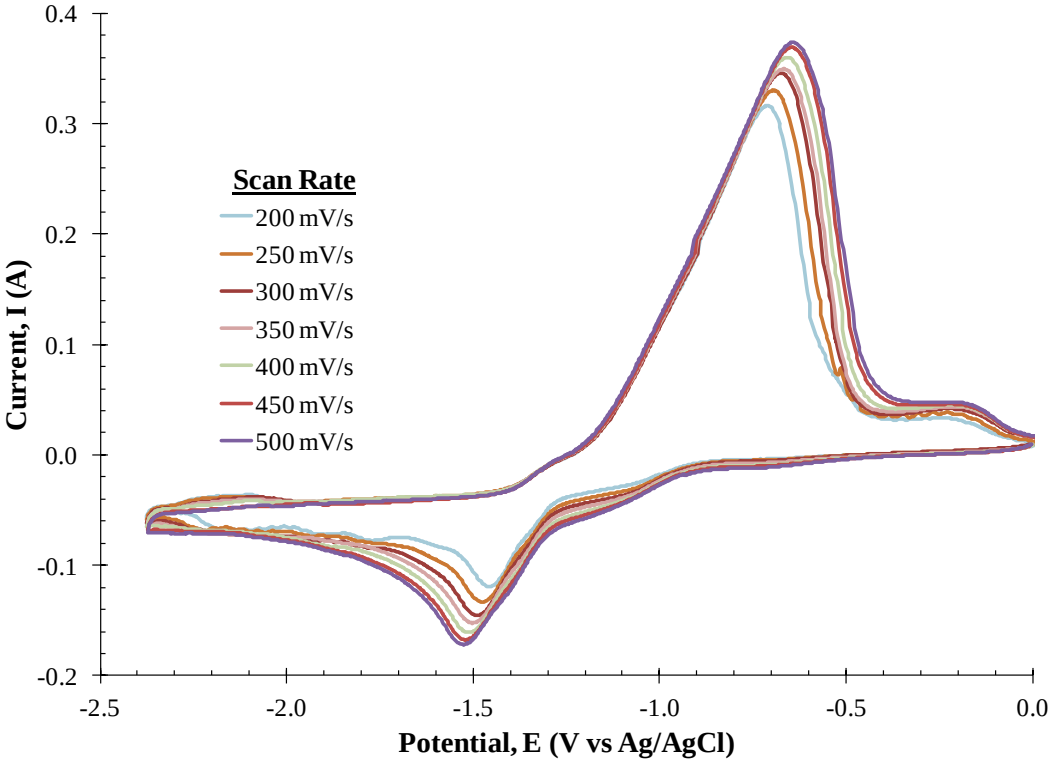

Figure G.2 CVs of 0.57 wt% $ZrCl_4$ in LiCl-KCl eutectic at 773 K.

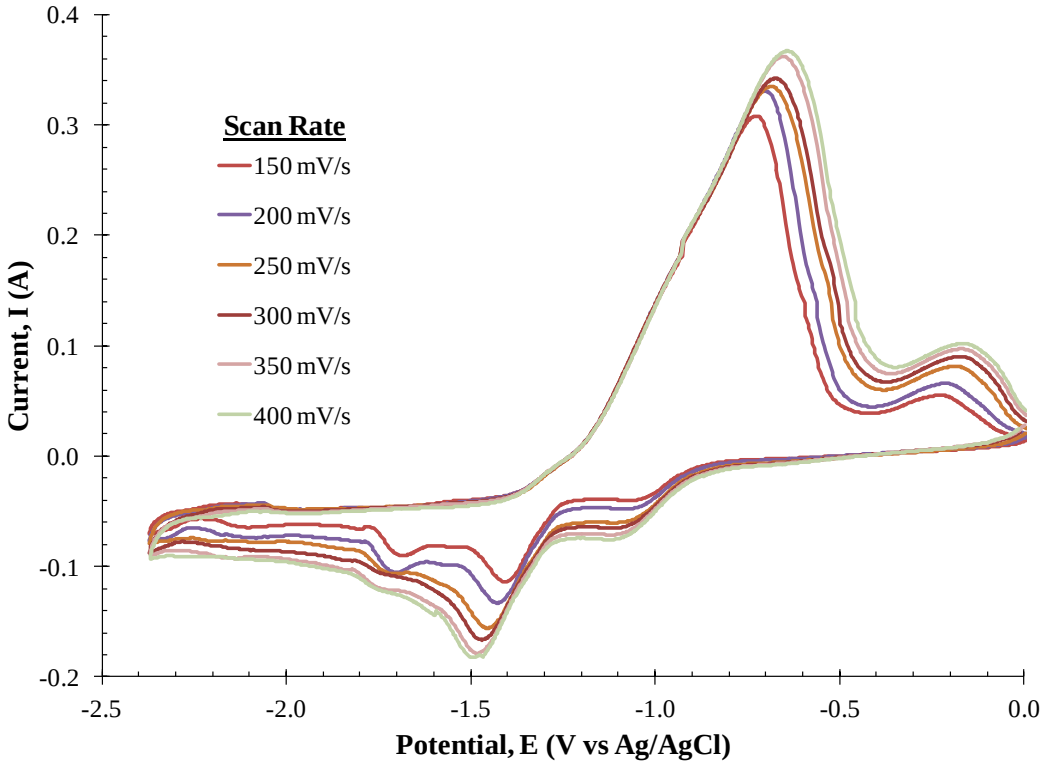

Figure G.3 CVs of 0.57 wt% $ZrCl_4$ in LiCl-KCl eutectic at 823 K.

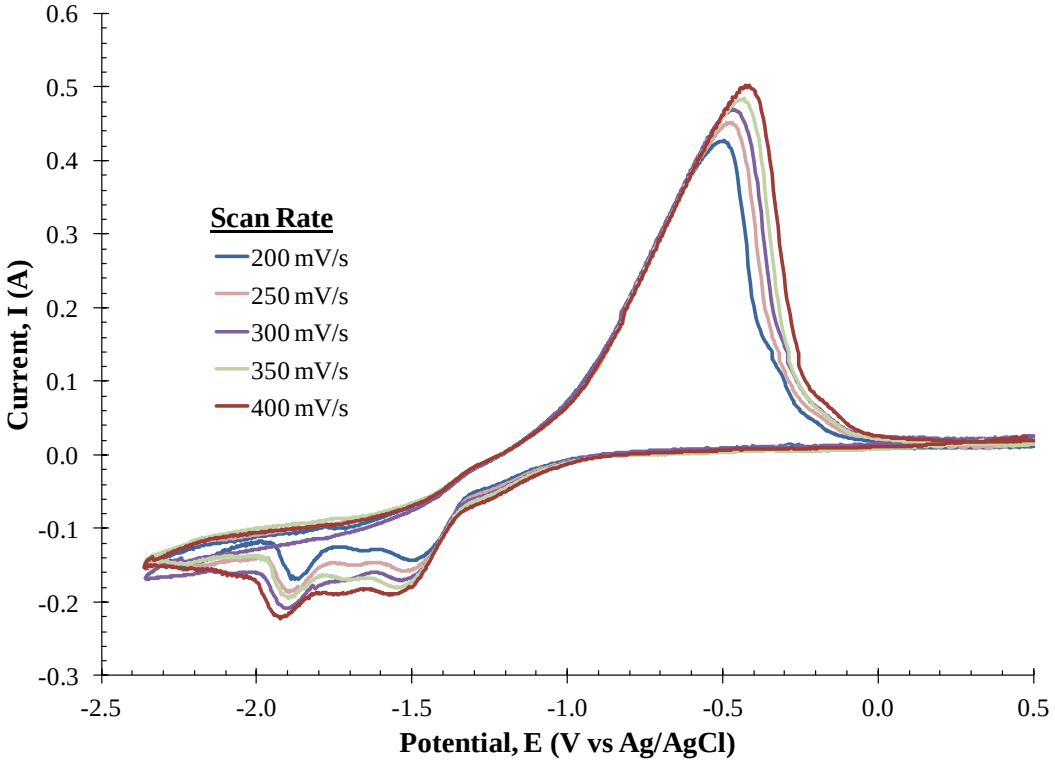

Figure G.4 CVs of 1.07 wt% $ZrCl_4$ in LiCl-KCl eutectic at 723 K.

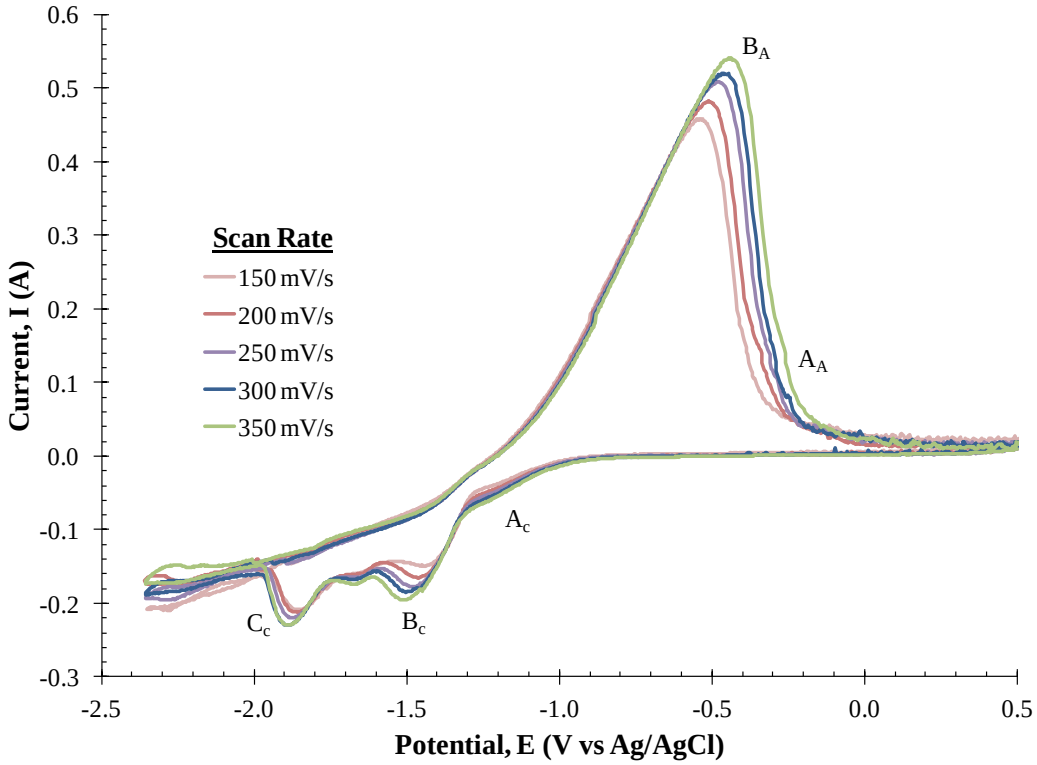

Figure G.5 CVs of 1.07 wt% $ZrCl_4$ in LiCl-KCl eutectic at 773 K.

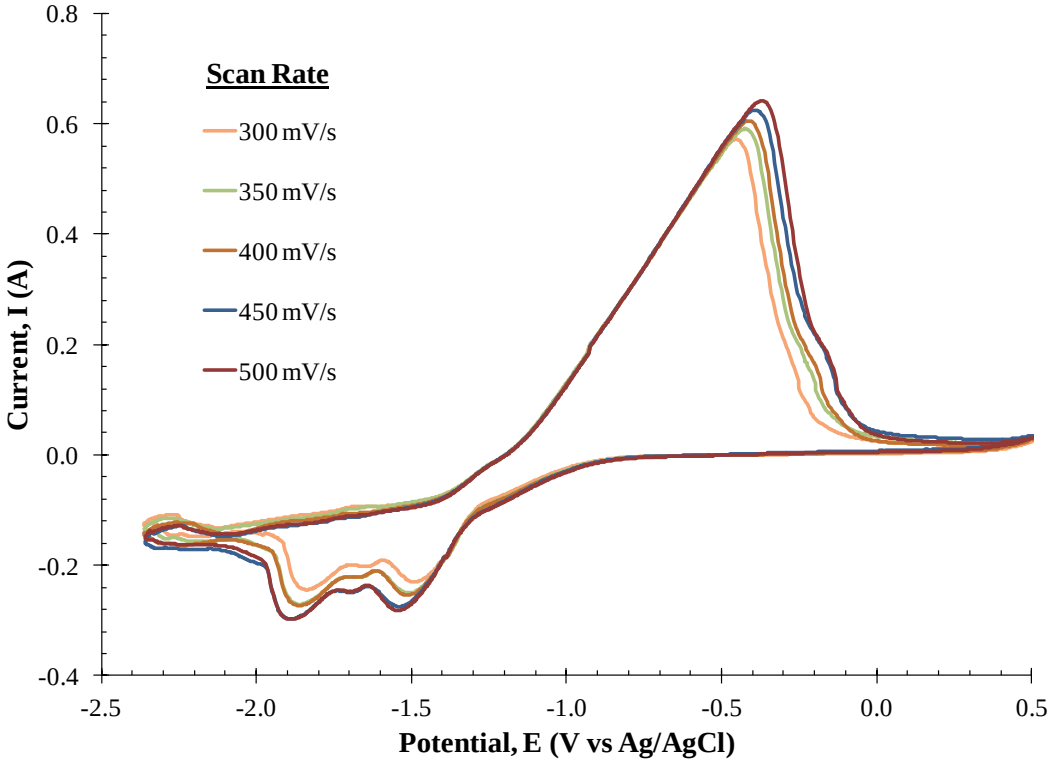

Figure G.6 CVs of 1.07 wt% $ZrCl_4$ in LiCl-KCl eutectic at 823 K.

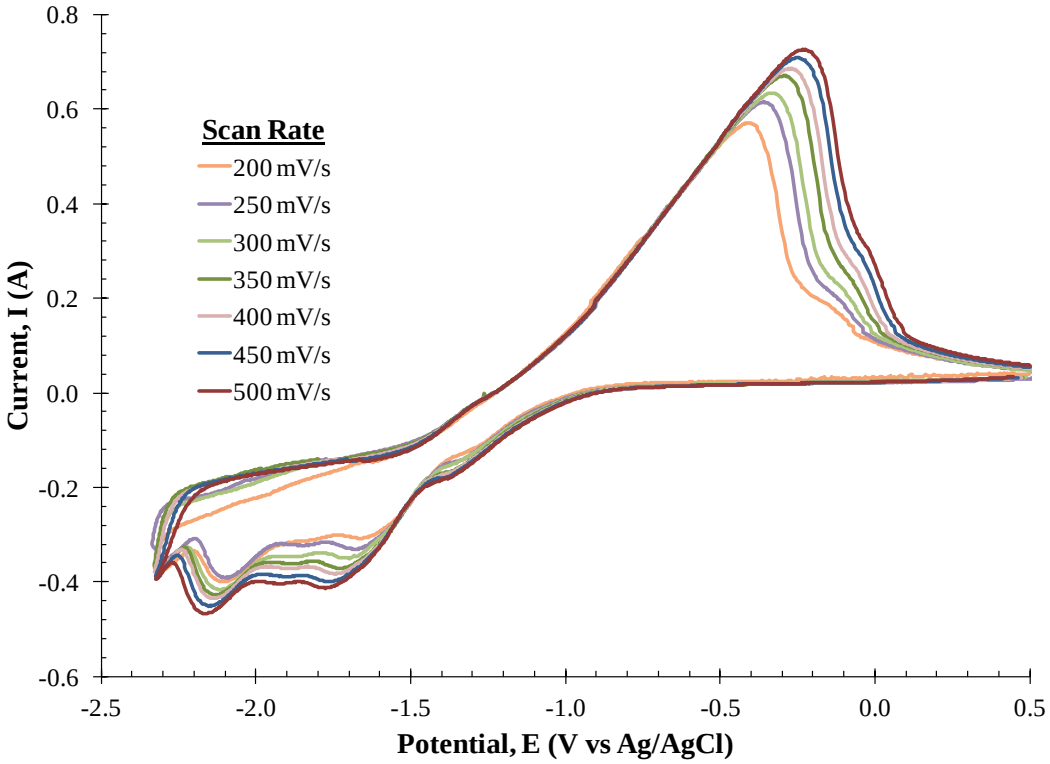

Figure G.7 CVs of 2.49 wt% $ZrCl_4$ in LiCl-KCl eutectic at 723 K.

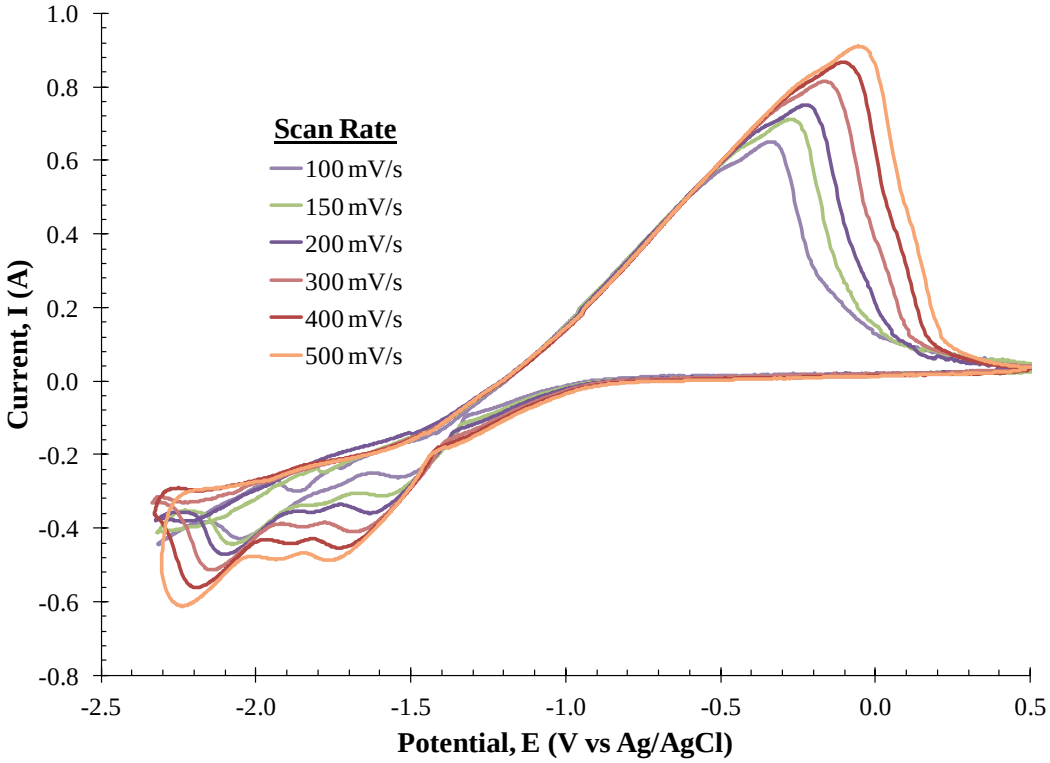

Figure G.8 CVs of 2.49 wt% $ZrCl_4$ in LiCl-KCl eutectic at 773 K.

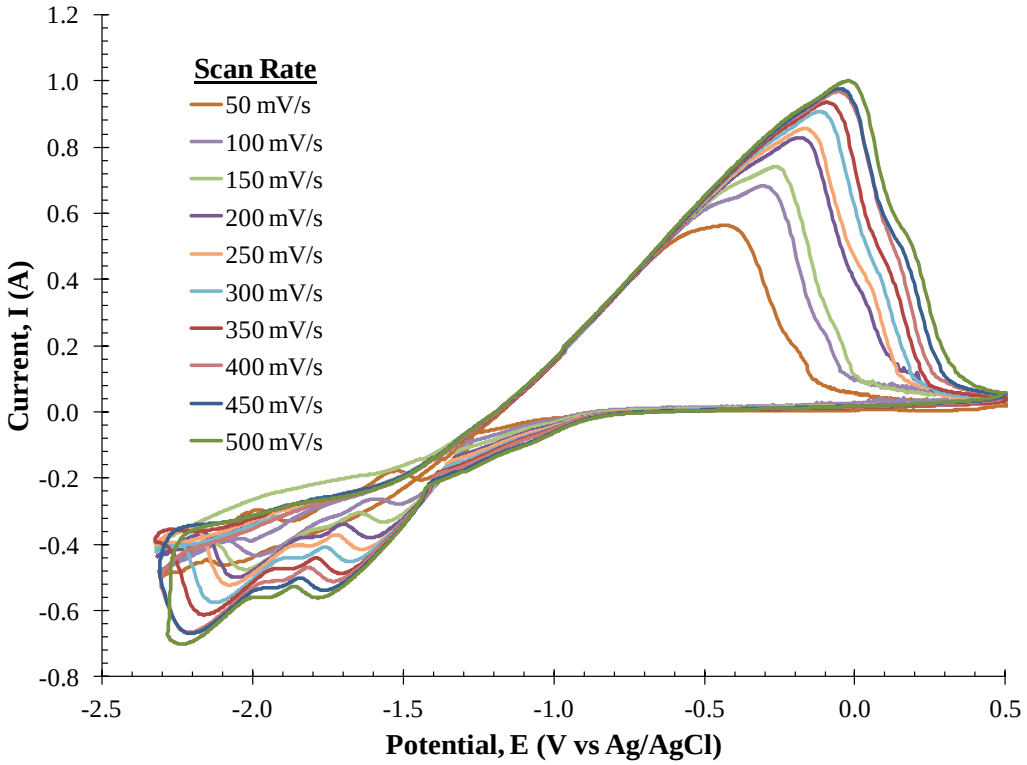

Figure G.9 CVs of 2.49 wt% $ZrCl_4$ in LiCl-KCl eutectic at 823 K.

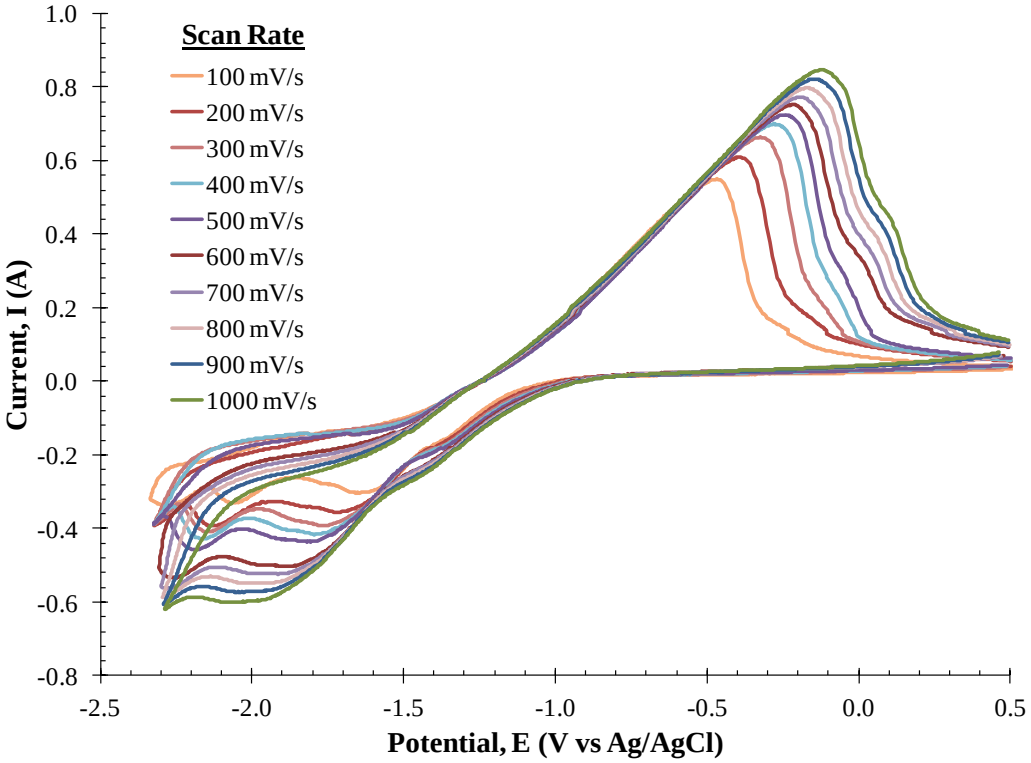

Figure G.10 CVs of 4.98 wt% $ZrCl_4$ in LiCl-KCl eutectic at 723 K.

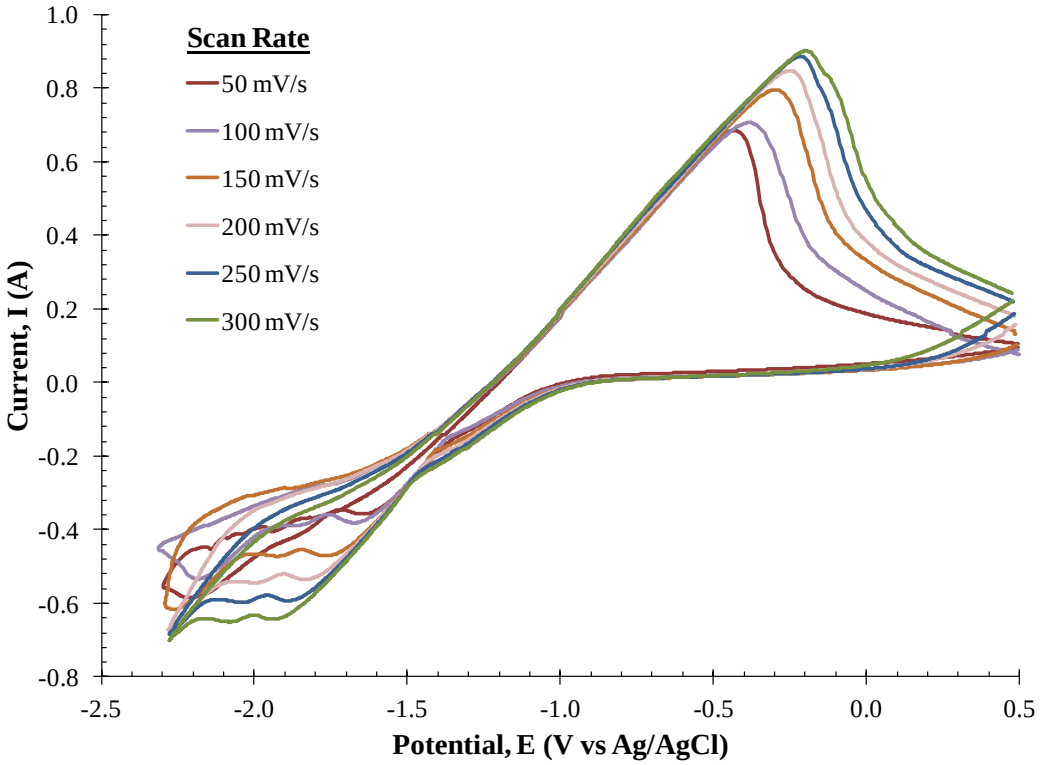

Figure G.11 CVs of 4.98 wt% $ZrCl_4$ in LiCl-KCl eutectic at 773 K.

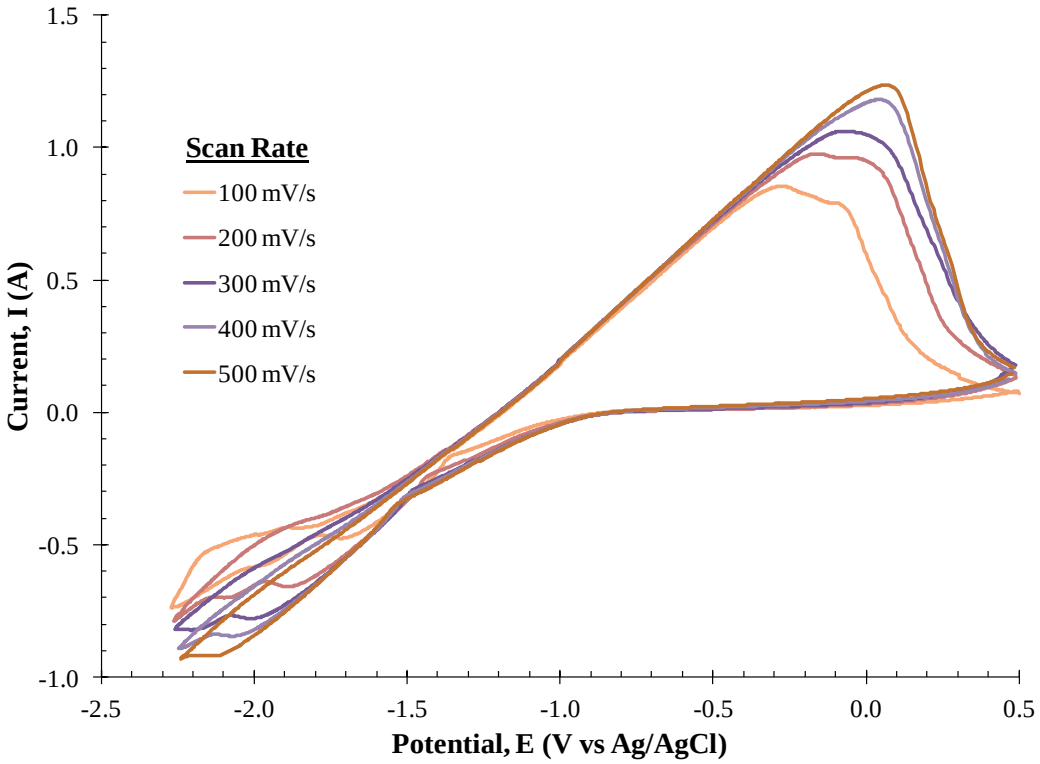

Figure G.12 CVs of 4.98 wt% $ZrCl_4$ in LiCl-KCl eutectic at 823 K.

Appendix H

Zirconium Chronopotentiograms (CP)

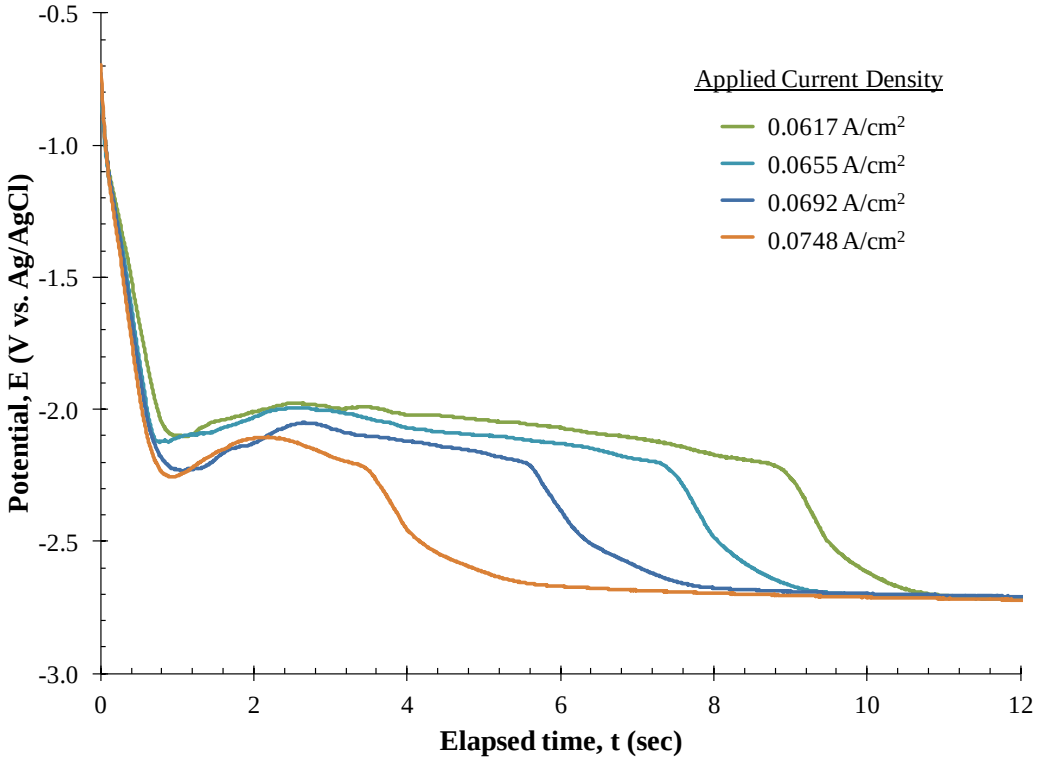

Figure H.1 Chronopotentiograms for 0.57 wt% $ZrCl_4$ in LiCl-KCl eutectic salt at 723 K.

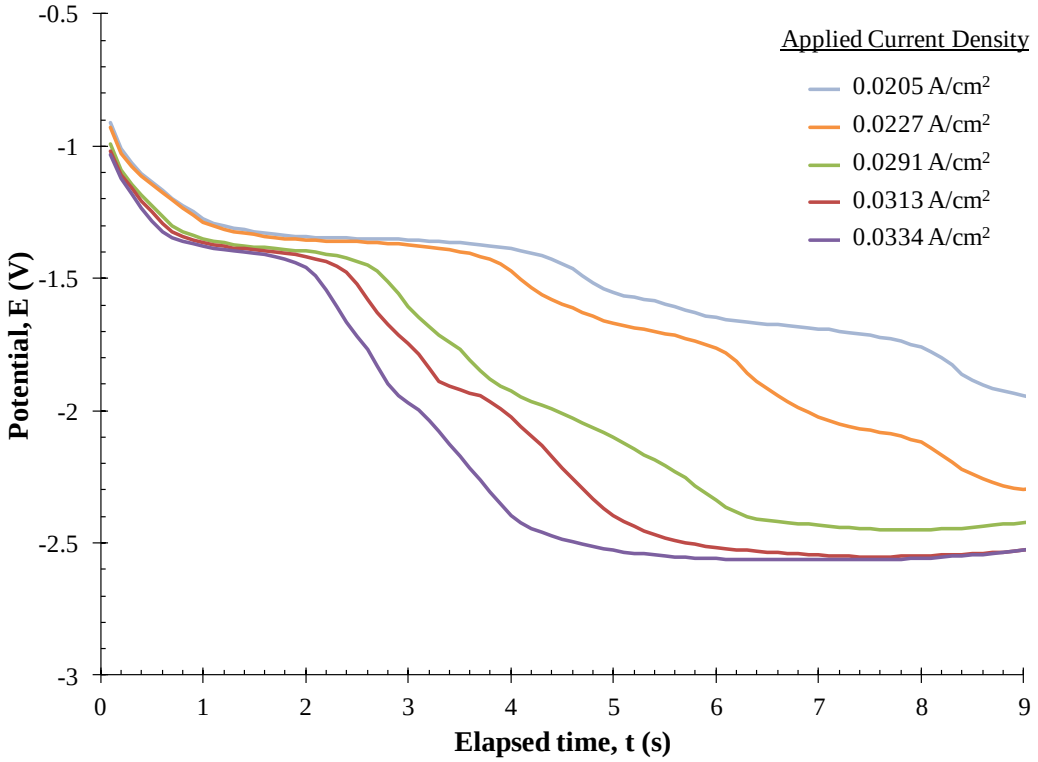

Figure H.2 Chronopotentiograms for 0.57 wt% $ZrCl_4$ in LiCl-KCl eutectic salt at 773 K.

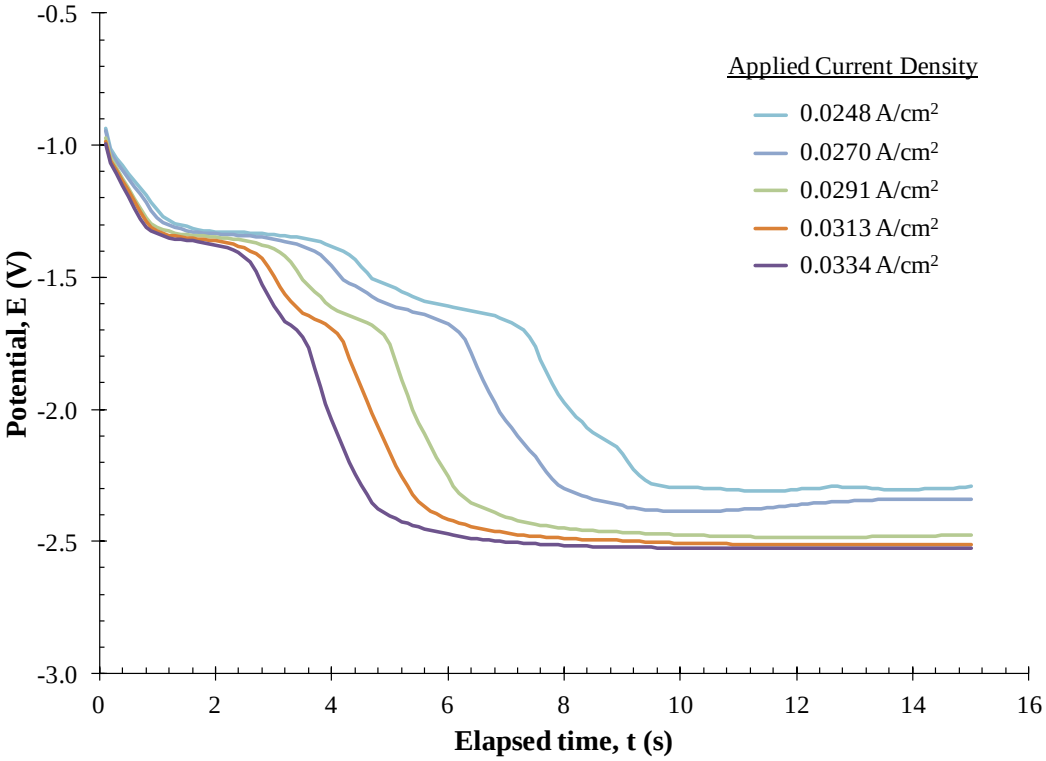

Figure H.3 Chronopotentiograms for 0.57 wt% $ZrCl_4$ in LiCl-KCl eutectic salt at 823 K.

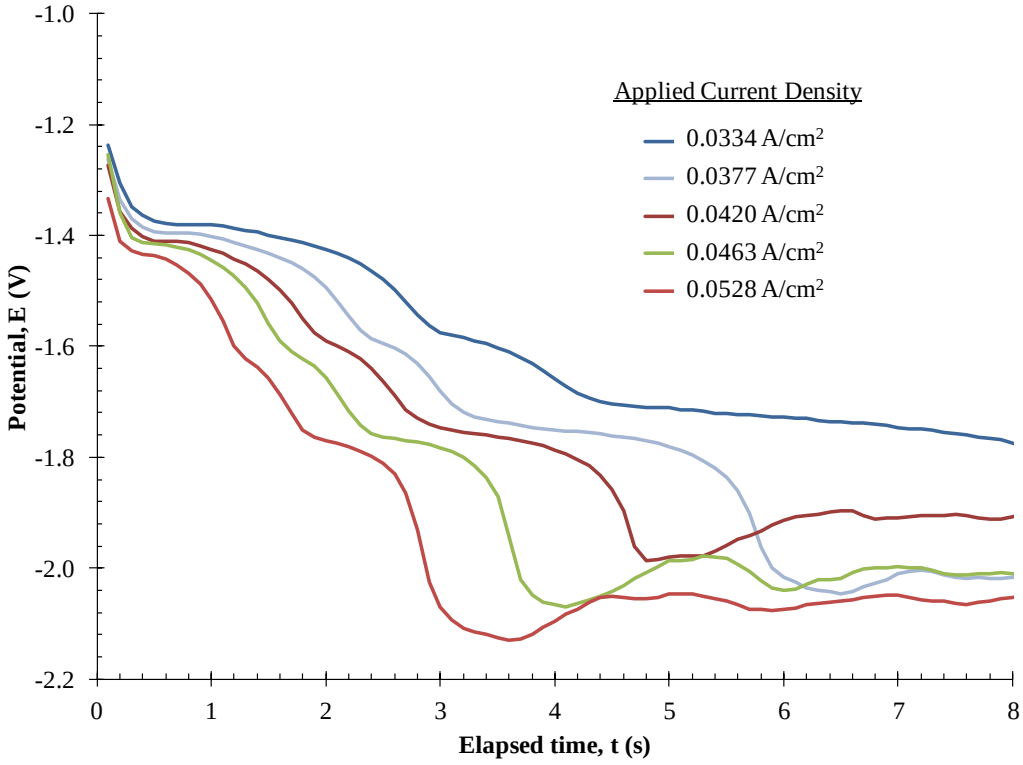

Figure H.4 Chronopotentiograms for 1.07 wt% $ZrCl_4$ in LiCl-KCl eutectic salt at 723 K.

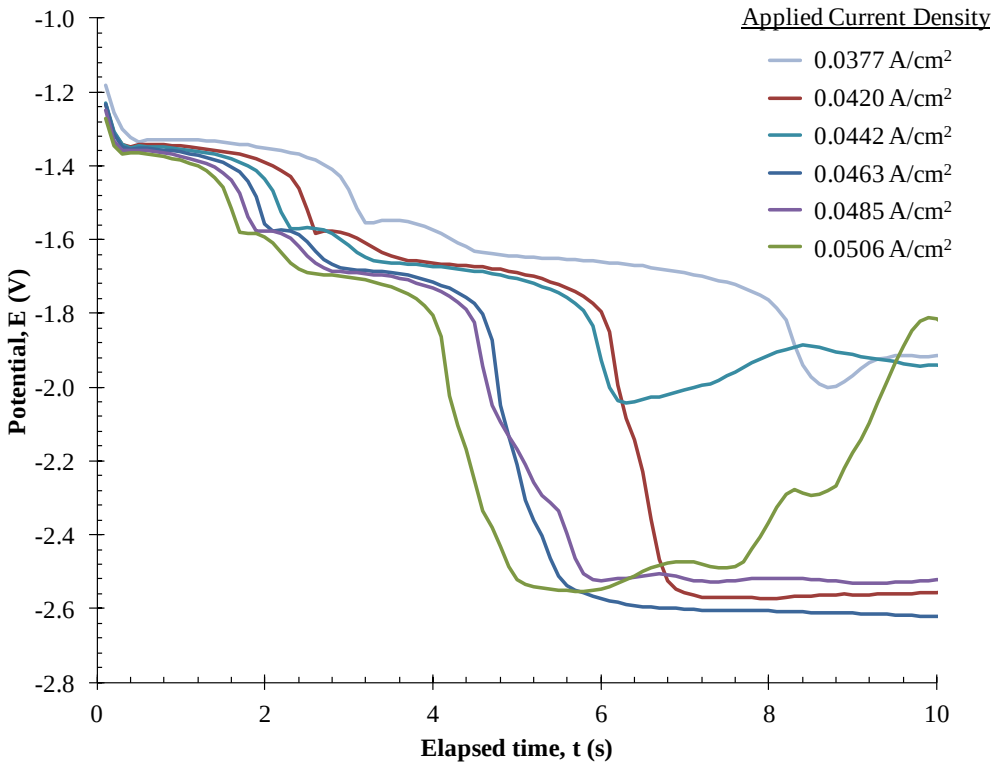

Figure H.5 Chronopotentiograms for 1.07 wt% $ZrCl_4$ in LiCl-KCl eutectic salt at 773 K.

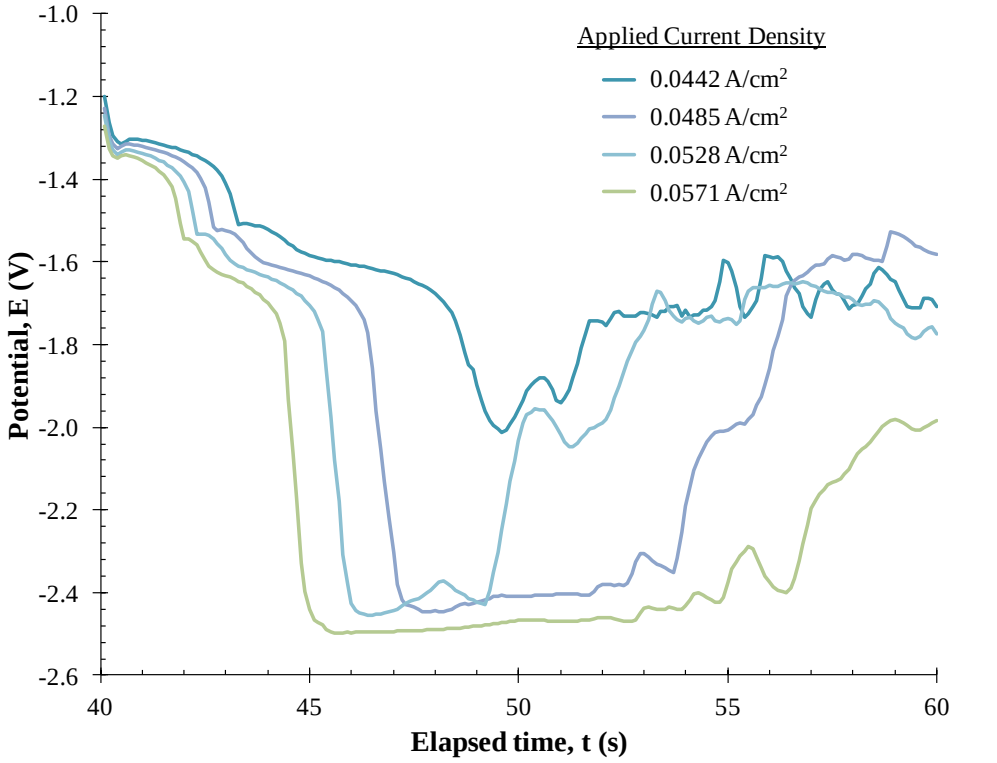

Figure H.6 Chronopotentiograms for 1.07 wt% $ZrCl_4$ in LiCl-KCl eutectic salt at 823 K.

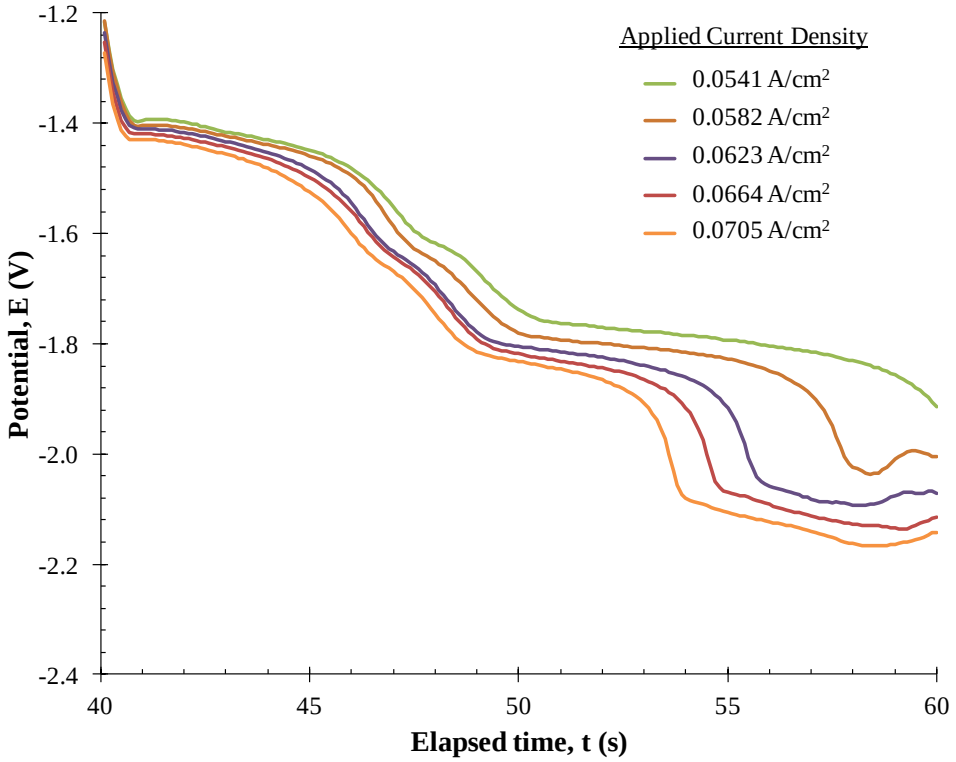

Figure H.7 Chronopotentiograms for 2.49 wt% $ZrCl_4$ in LiCl-KCl eutectic salt at 723 K.

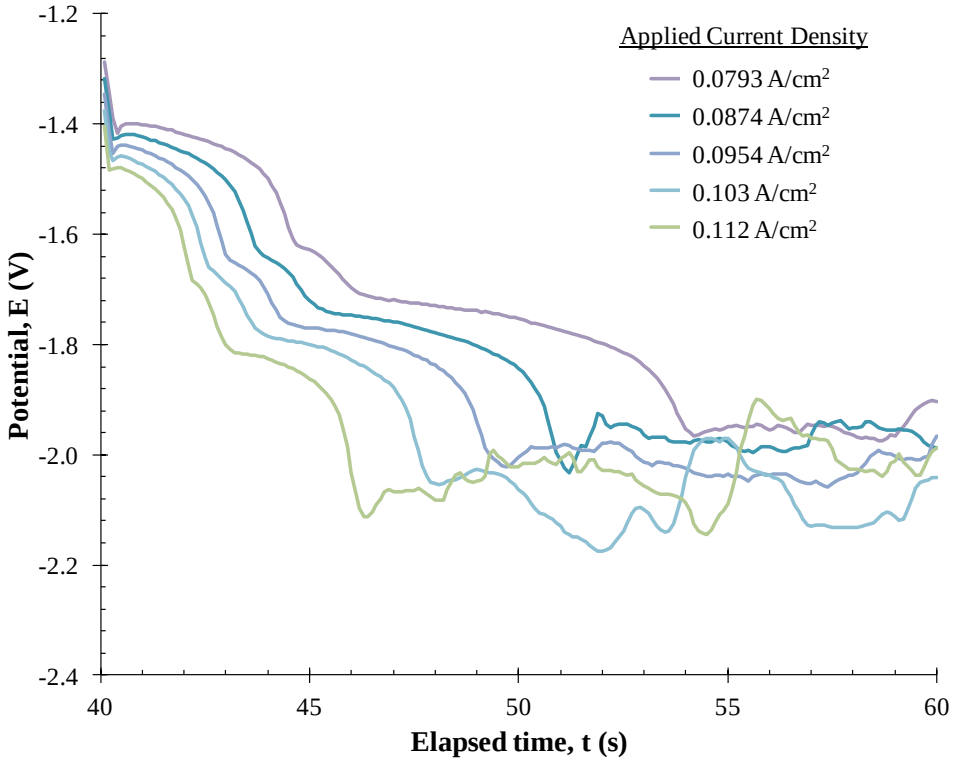

Figure H.8 Chronopotentiograms for 2.49 wt% $ZrCl_4$ in LiCl-KCl eutectic salt at 773 K.

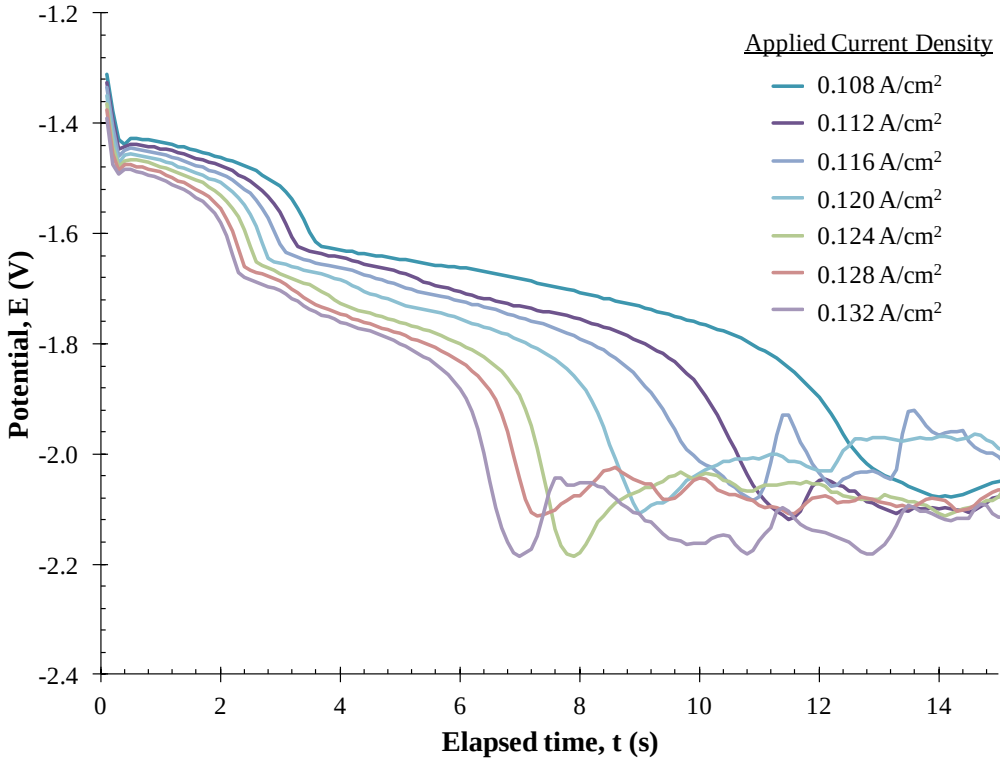

Figure H.9 Chronopotentiograms for 2.49 wt% $ZrCl_4$ in LiCl-KCl eutectic salt at 823 K.

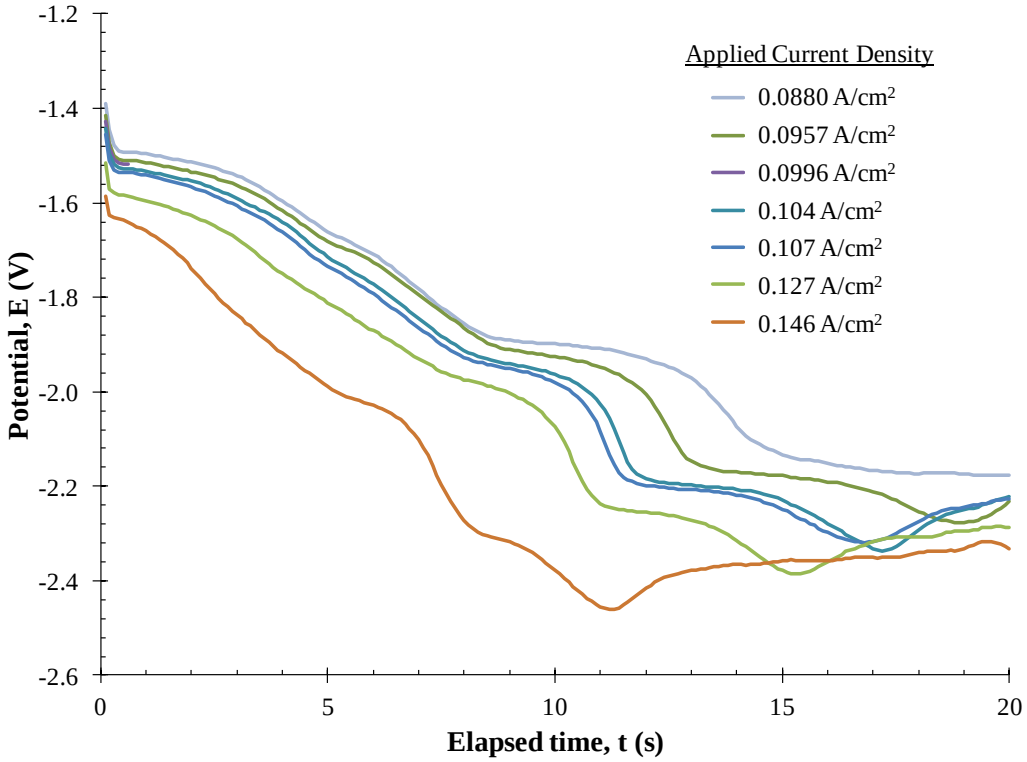

Figure H.10 Chronopotentiograms for 4.98 wt% $ZrCl_4$ in LiCl-KCl eutectic salt at 723 K.

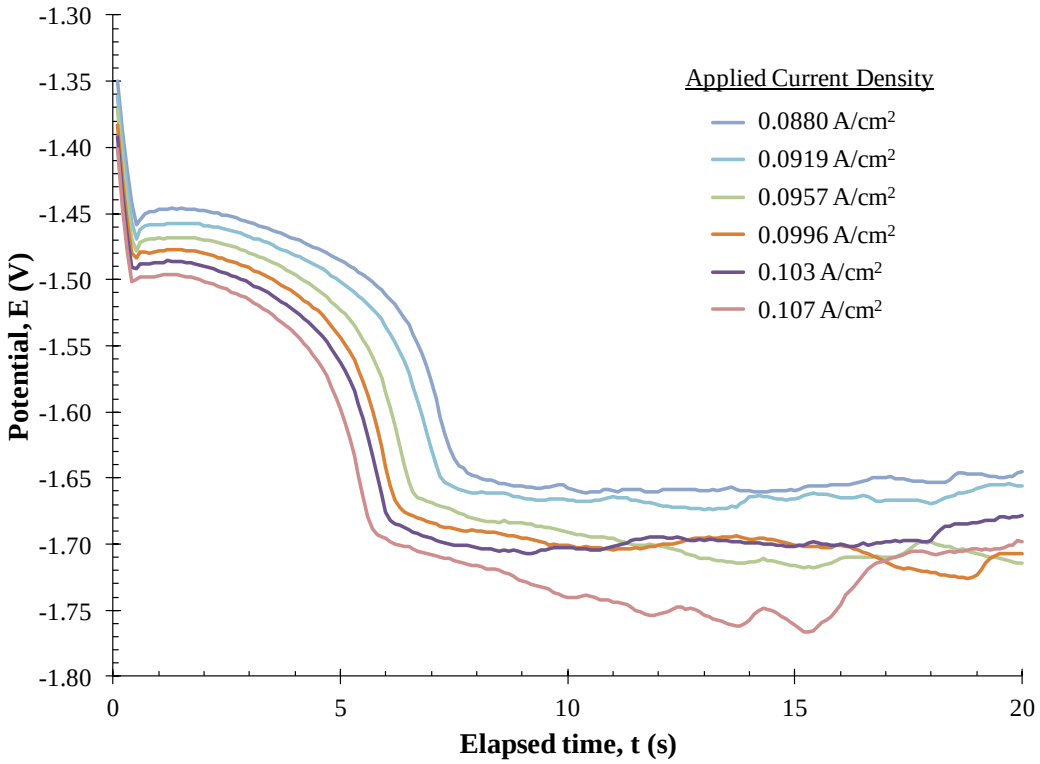

Figure H.11 Chronopotentiograms for 4.98 wt% $ZrCl_4$ in LiCl-KCl eutectic salt at 773 K.

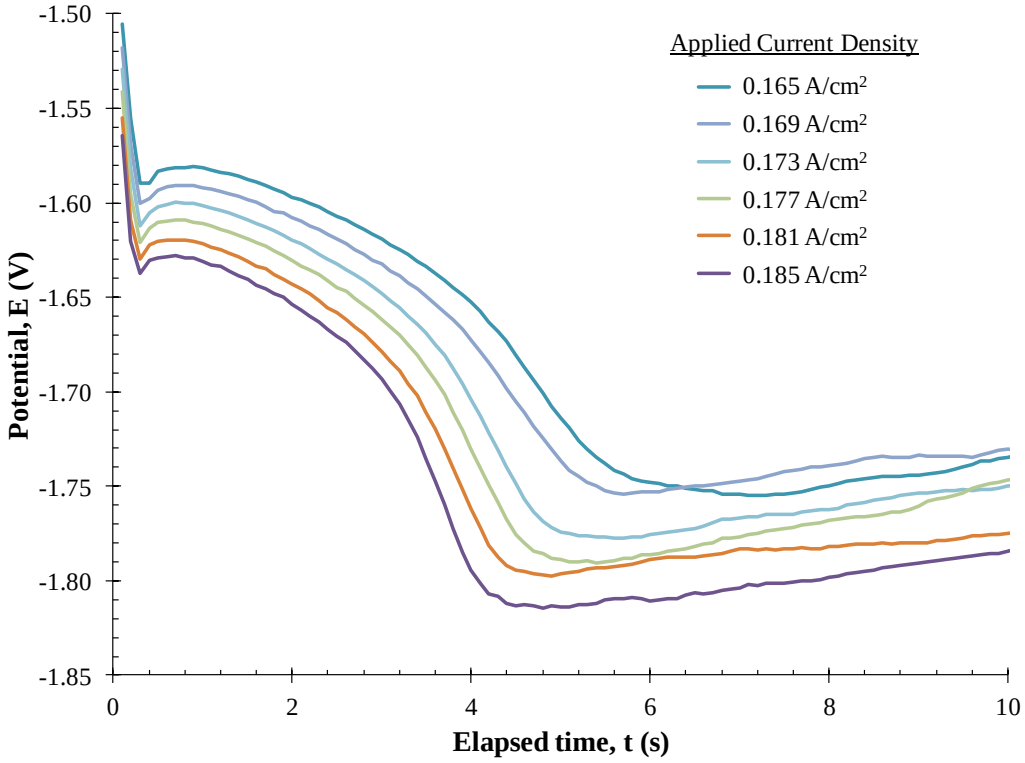

Figure H.12 Chronopotentiograms for 4.98 wt% $ZrCl_4$ in LiCl-KCl eutectic salt at 823 K.

Appendix I

Zirconium Anodic Stripping Voltammograms (ASV)

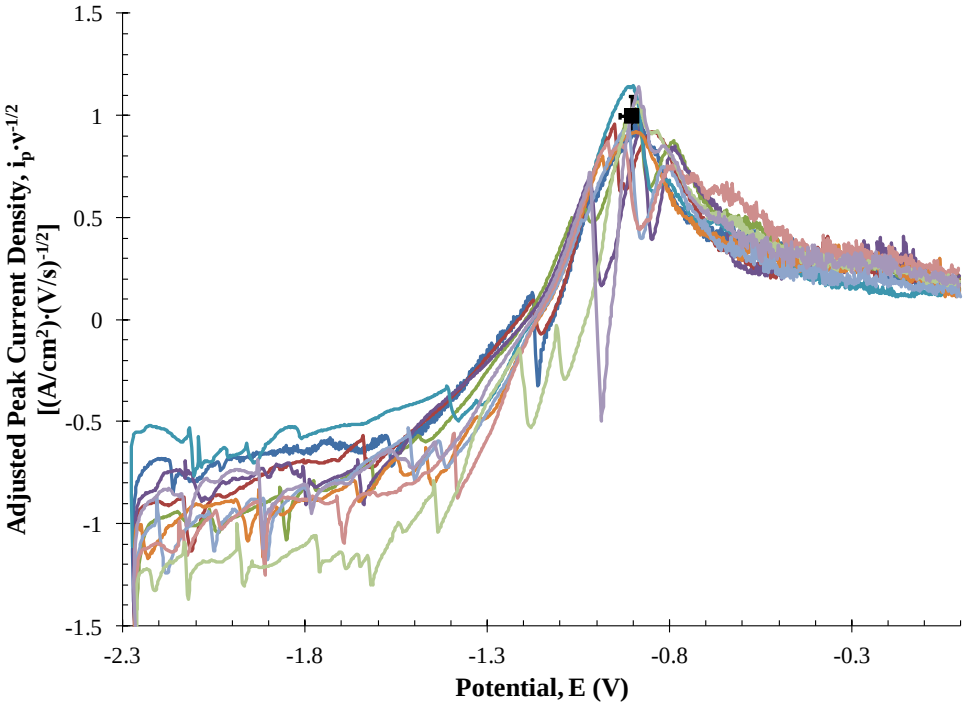

Figure I.1 ASV peaks of 0.57 wt% $ZrCl_4$ in LiCl-KCl eutectic at 773 K. The average peak height and potential are marked along with their standard deviations.

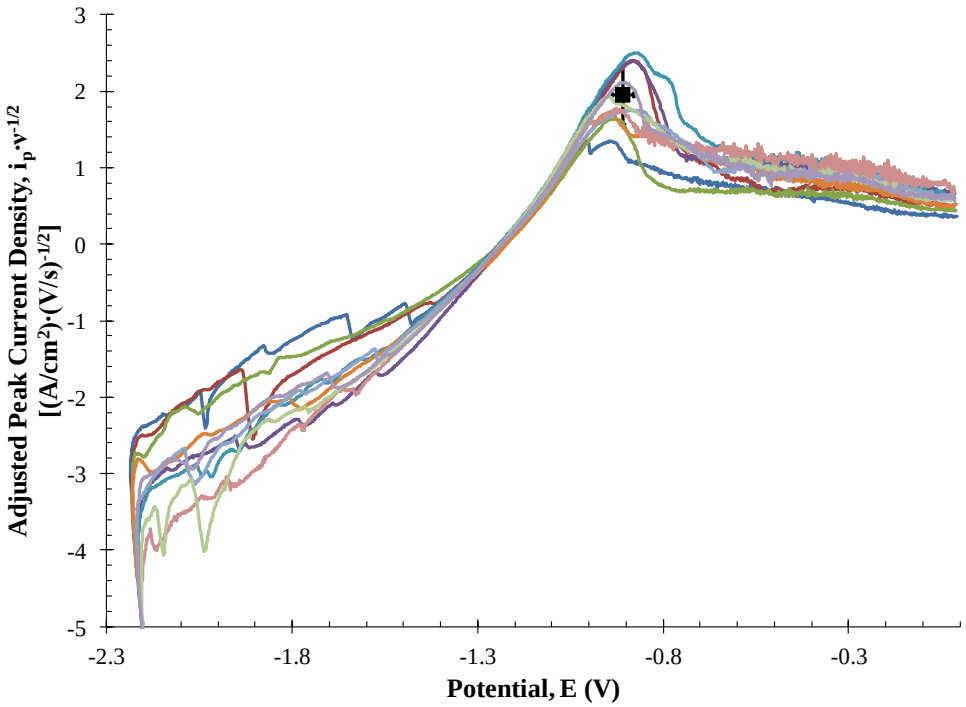

Figure I.2 ASV peaks of 1.07 wt% $ZrCl_4$ in LiCl-KCl eutectic at 773 K. The average peak height and potential are marked along with their standard deviations.

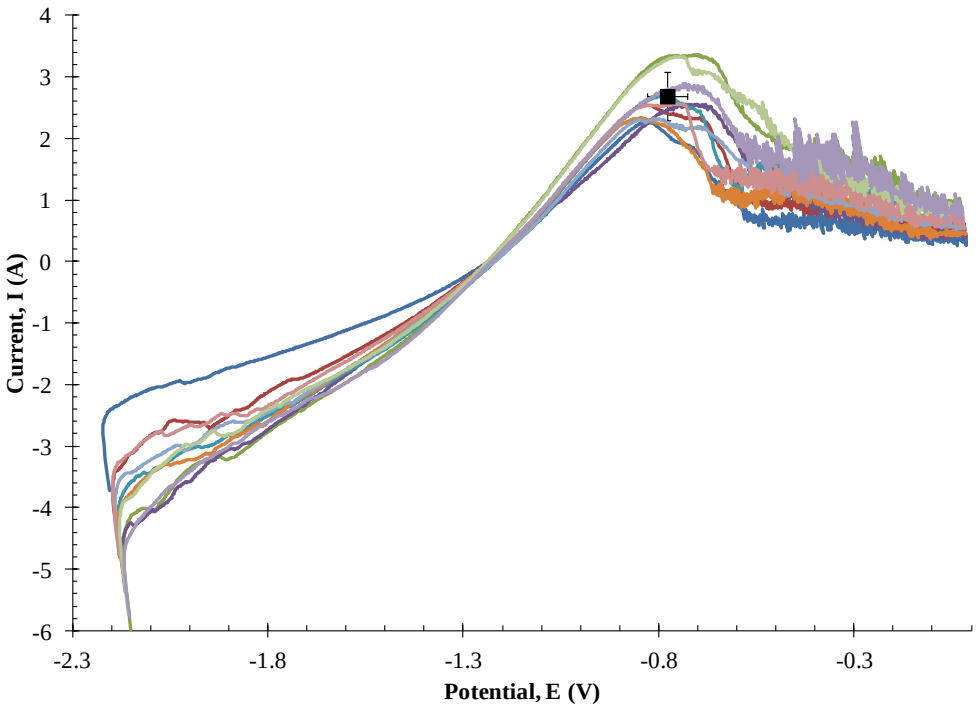

Figure I.3 ASV peaks of 2.49 wt% $ZrCl_4$ in LiCl-KCl eutectic at 773 K. The average peak height and potential are marked along with their standard deviations.

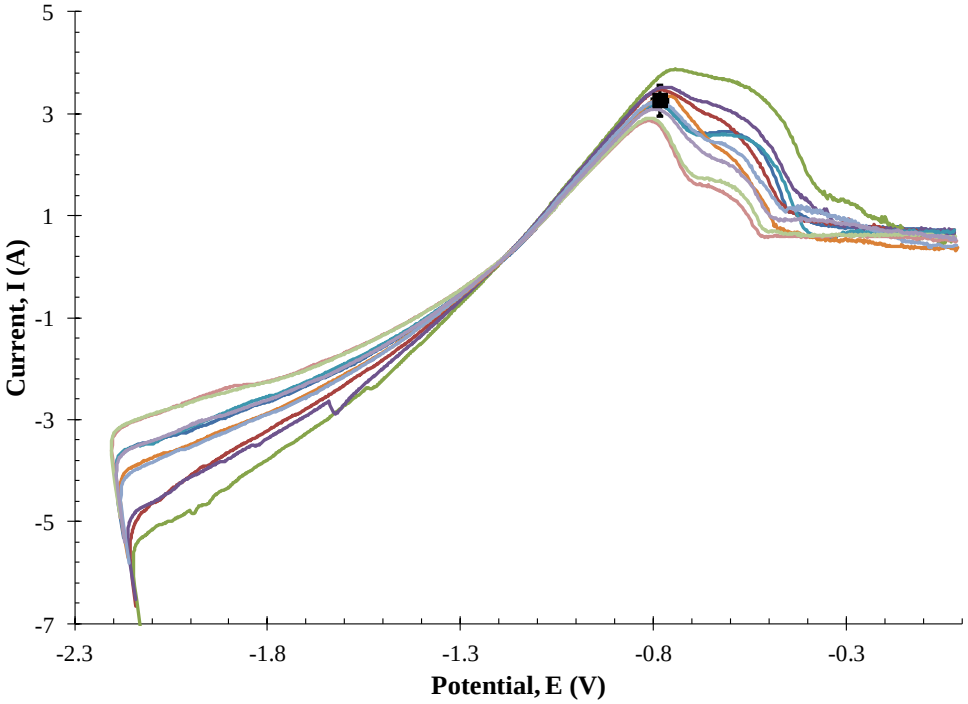

Figure I.4 ASV peaks of 4.98 wt% $ZrCl_4$ in LiCl-KCl eutectic at 773 K. The average peak height and potential are marked along with their standard deviations.

Appendix J

Randles-Sevcik and Delahay Equations for Zirconium

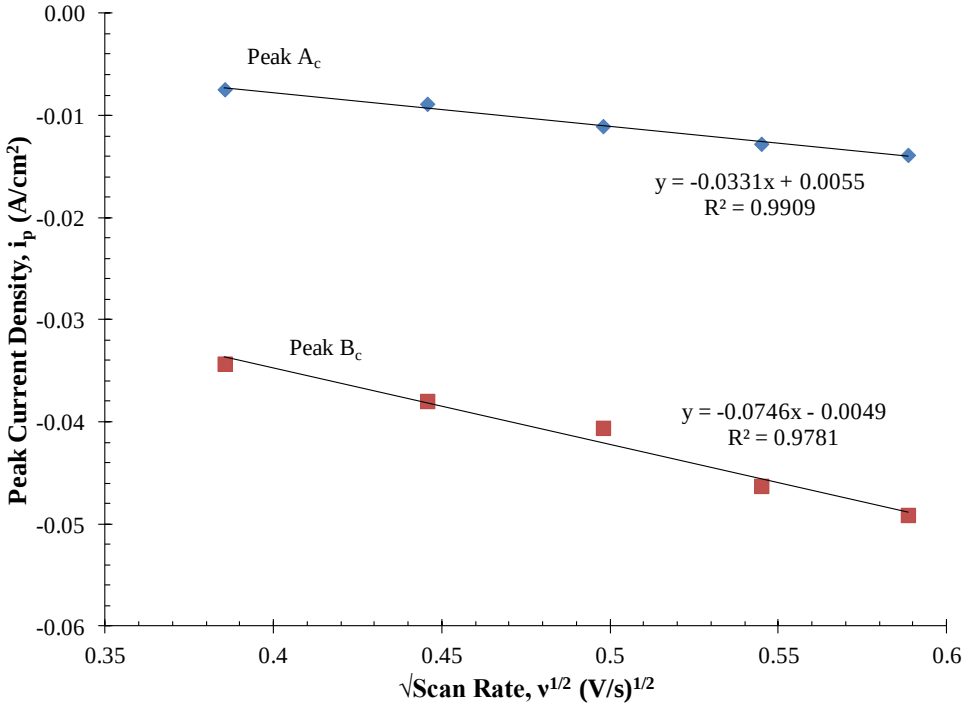

Figure J.1 Peak current versus square root of scan rate for cathodic peaks in the 0.57 wt% $ZrCl_4$ cyclic voltammograms at 723 K.

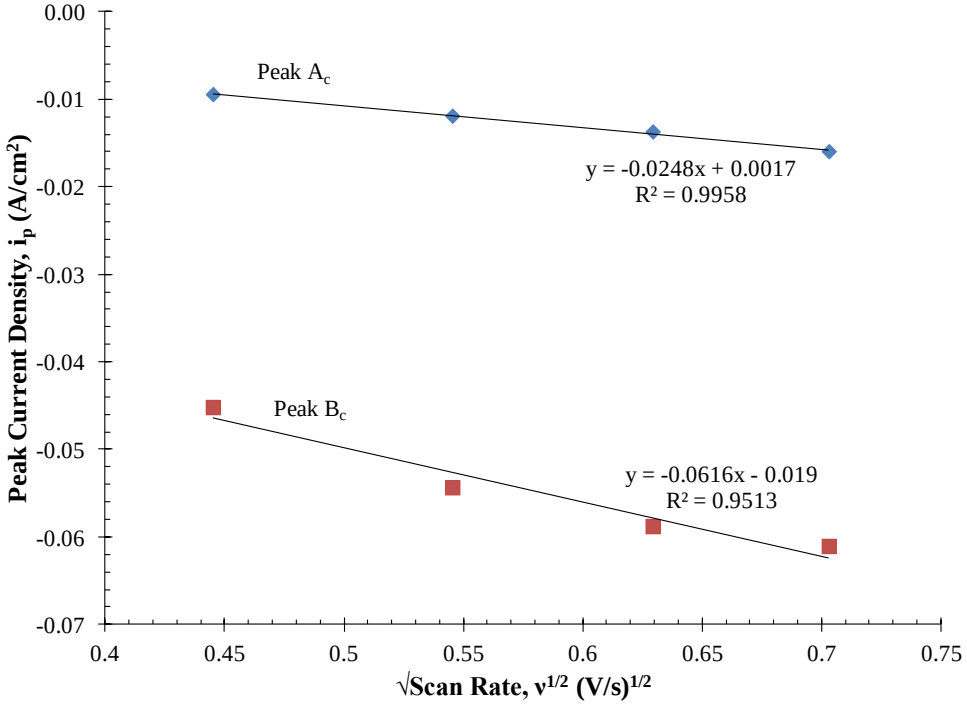

Figure J.2 Peak current versus square root of scan rate for cathodic peaks in the 0.57 wt% $ZrCl_4$ cyclic voltammograms at 773 K.

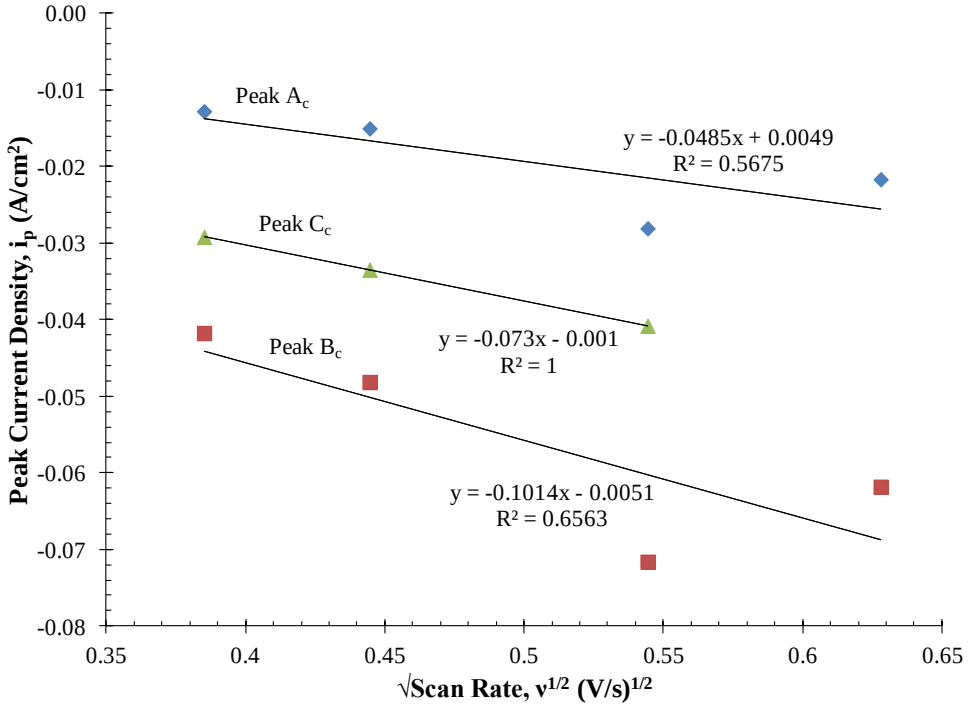

Figure J.3 Peak current versus square root of scan rate for cathodic peaks in the 0.57 wt% $ZrCl_4$ cyclic voltammograms at 823 K.

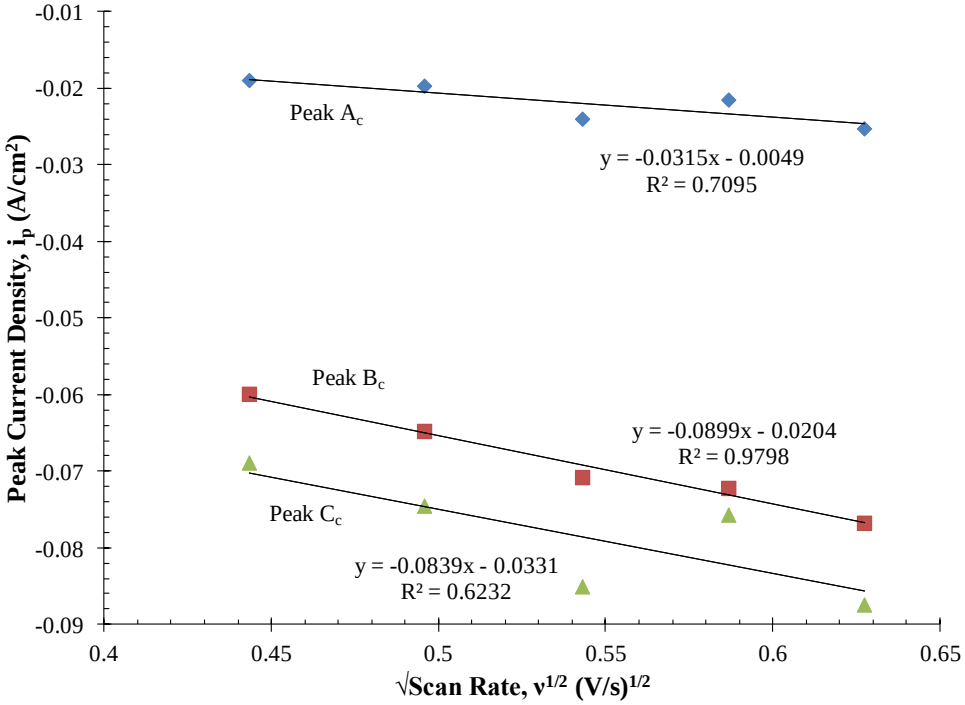

Figure J.4 Peak current versus square root of scan rate for cathodic peaks in the 1.07 wt% $ZrCl_4$ cyclic voltammograms at 723 K.

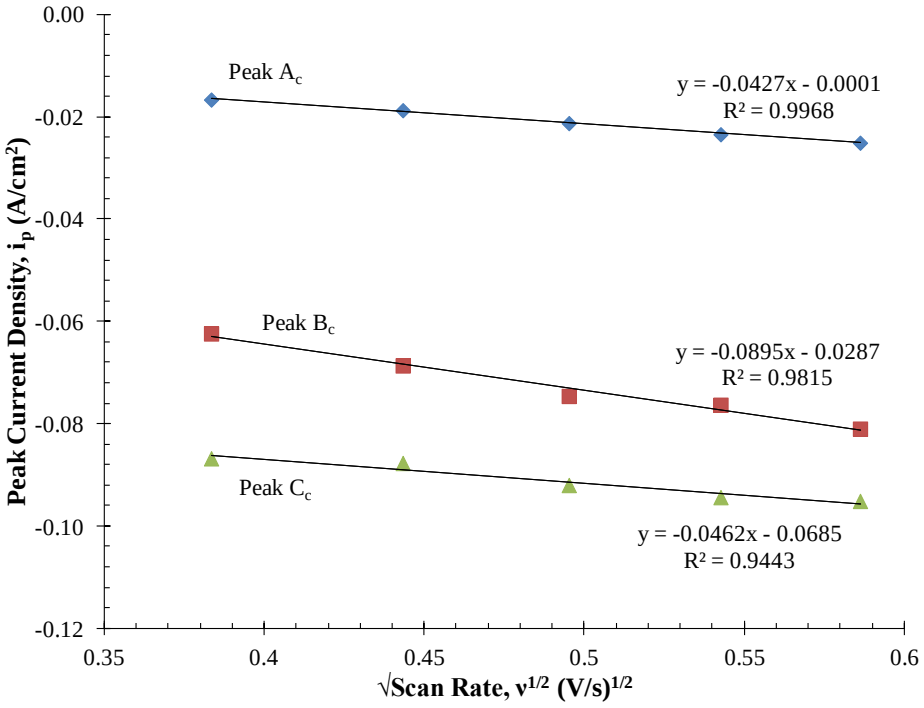

Figure J.5 Peak current versus square root of scan rate for cathodic peaks in the 1.07 wt% $ZrCl_4$ cyclic voltammograms at 773 K.

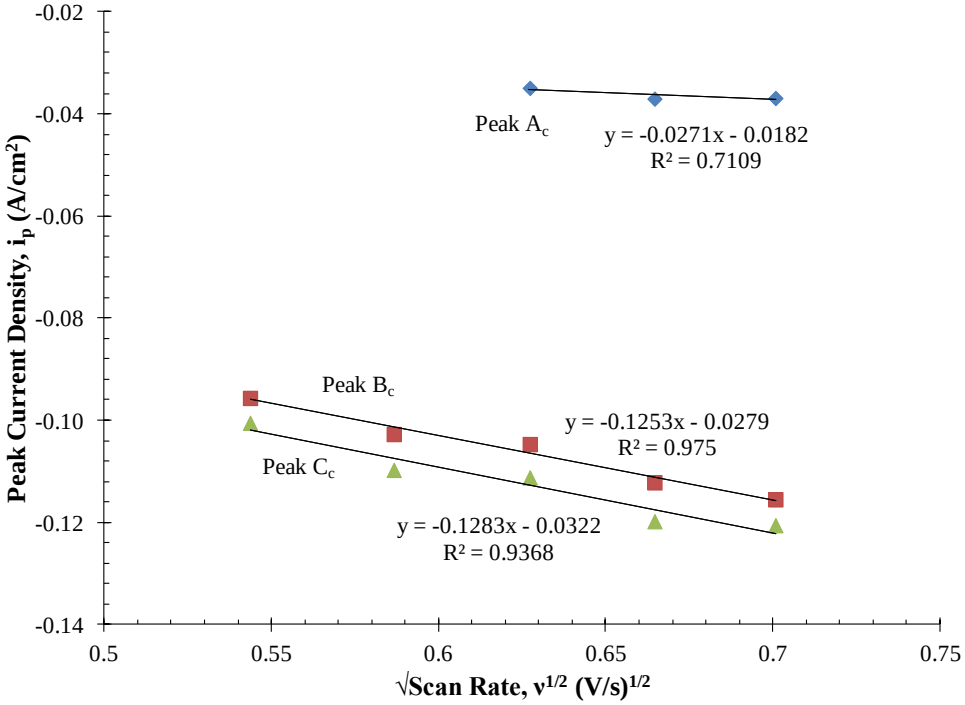

Figure J.6 Peak current versus square root of scan rate for cathodic peaks in the 1.07 wt% $ZrCl_4$ cyclic voltammograms at 823 K.

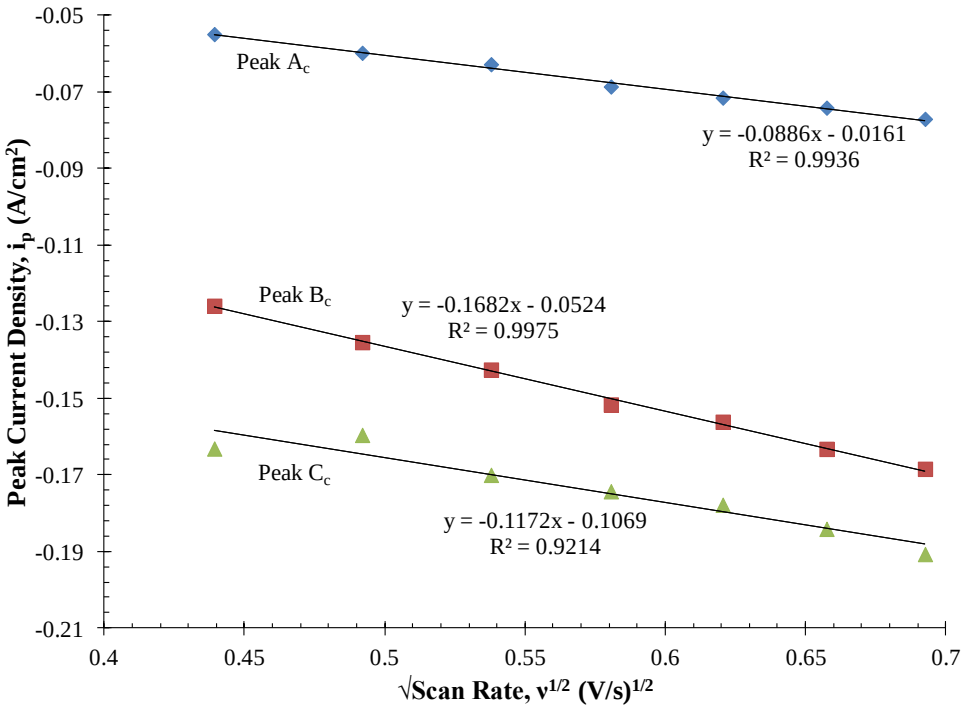

Figure J.7 Peak current versus square root of scan rate for cathodic peaks in the 2.49 wt% $ZrCl_4$ cyclic voltammograms at 723 K.

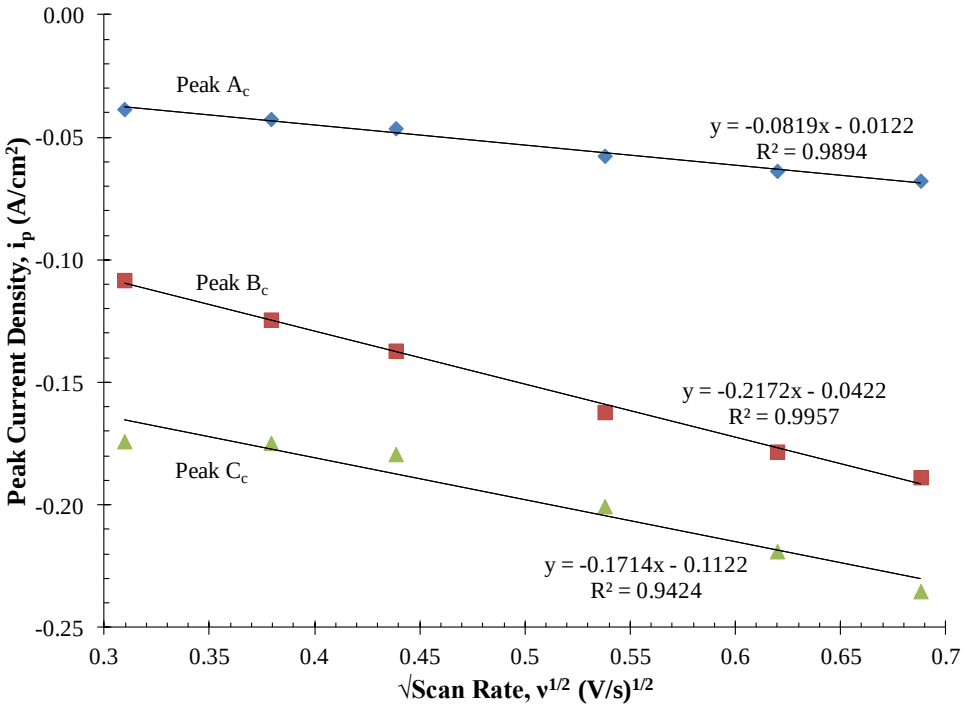

Figure J.8 Peak current versus square root of scan rate for cathodic peaks in the 2.49 wt% $ZrCl_4$ cyclic voltammograms at 773 K.

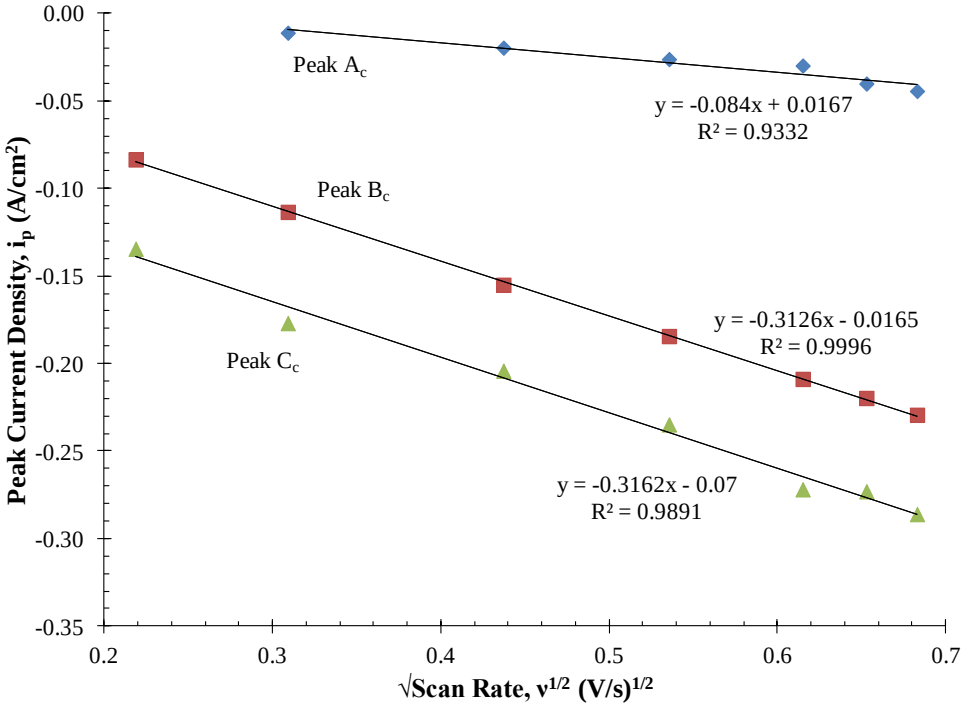

Figure J.9 Peak current versus square root of scan rate for cathodic peaks in the 2.49 wt% $ZrCl_4$ cyclic voltammograms at 823 K.

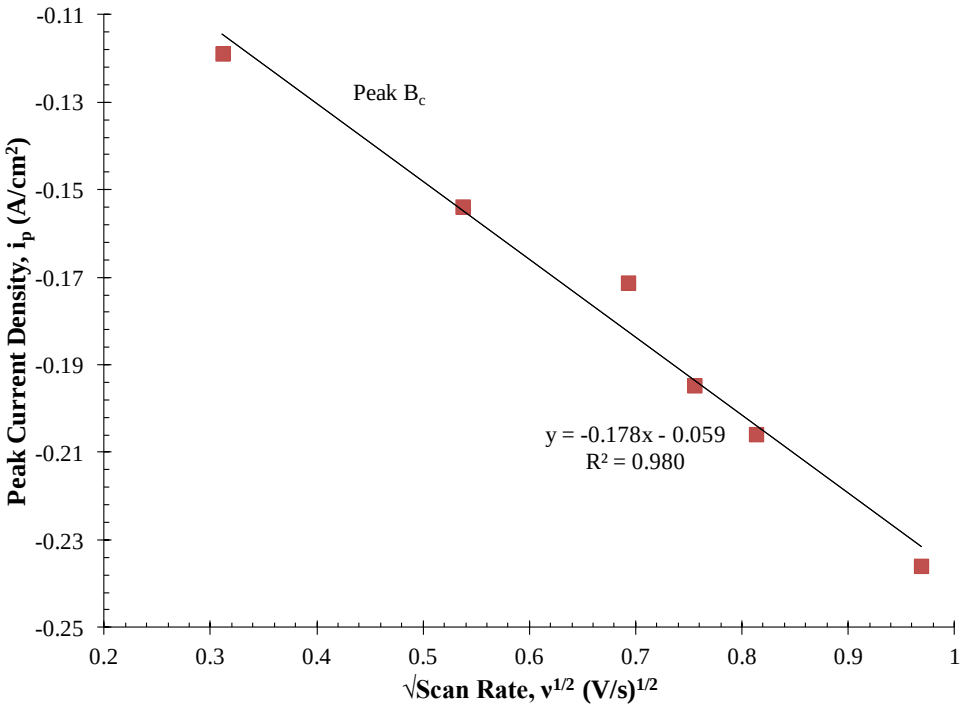

Figure J.10 Peak current versus square root of scan rate for cathodic peaks in the 4.98 wt% $ZrCl_4$ cyclic voltammograms at 723 K.

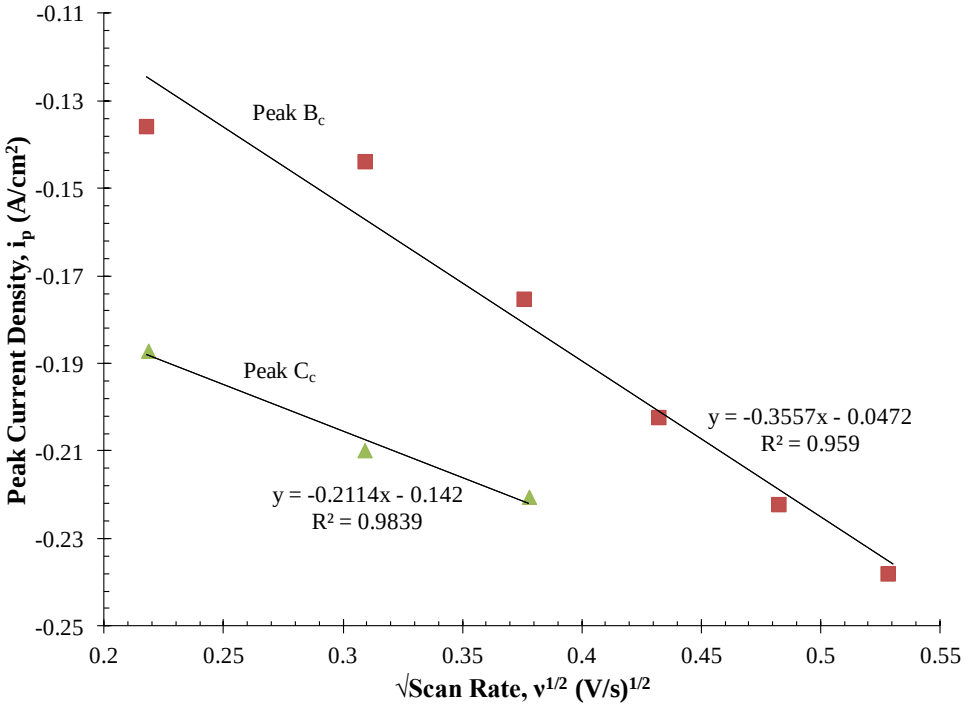

Figure J.11 Peak current versus square root of scan rate for cathodic peaks in the 4.98 wt% $ZrCl_4$ cyclic voltammograms at 773 K.

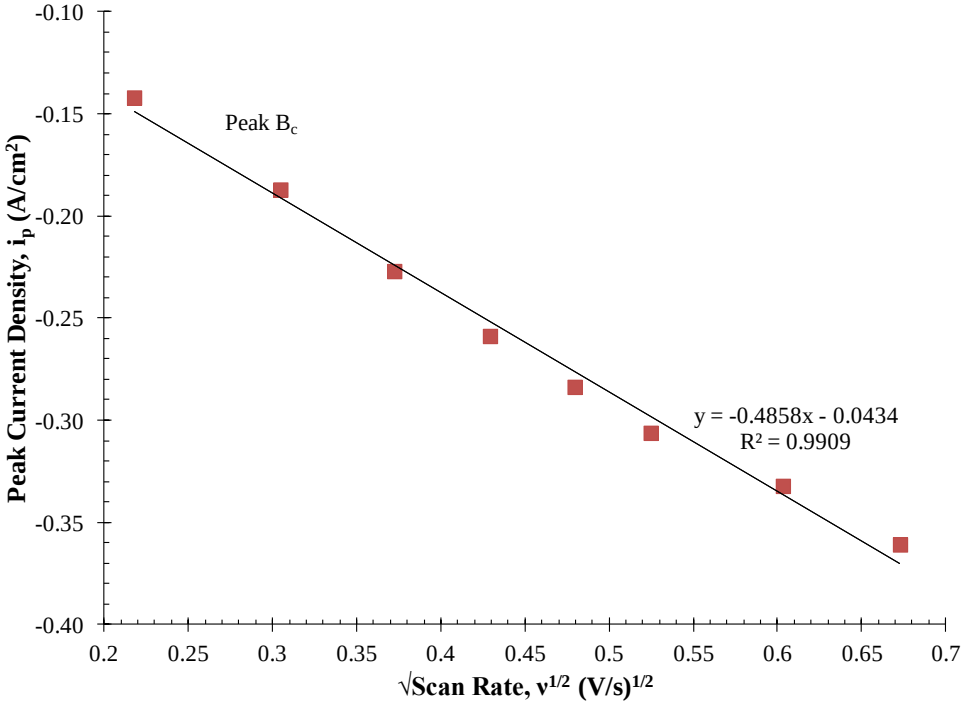

Figure J.12 Peak current versus square root of scan rate for cathodic peaks in the 4.98 wt% $ZrCl_4$ cyclic voltammograms at 823 K